CRPP

CENTRE DE RECHERCHES EN PHYSIQUE DES PLASMAS
FACULTÉ DES SCIENCES DE BASE
ASSOCIATION EURATOM - CONFÉDÉRATION SUISSE

ÉCOLE POLYTECHNIQUE
FÉDÉRALE DE LAUSANNE

ANNUAL REPORT

2006

Table of content

1 Introduction

1.1 *International situation*

The year 2006 was characterised by the signature of the ITER Agreement by the seven parties (China, the European Union, India, Japan, Korea, Russia and the United States of America). The event took place at the Palais de l'Elysée in Paris on November 21st. In parallel, the directorate of ITER was nominated and the team is being formed. Many activities, including a design review of the project, are now on going.

In parallel, the negotiation between Japan and the European Union on a cooperation agreement aimed at accelerating the construction of a demonstration power plant, DEMO, was also completed. The resulting agreement, known as the "Broader Approach", includes many elements. The present Japanese tokamak JT-60 will be upgraded into a superconducting device, called JT-60 SA. JT-60 SA will be jointly exploited by Japanese and European teams and will serve as a "satellite tokamak" to ITER. Research in view of DEMO will be the second theme of the Broader Approach. Activities in the frame of the Broader Approach also include R&D for the neutron source IFMIF (International Fusion Material Irradiation Facility), material science and technology and the conceptual design of DEMO itself. Finally, a centre for fusion energy will be established in Rokkasho (Japan) and will be equipped with a large computing facility.

In 2006 China started the commissioning of its new superconducting tokamak EAST, located in Heifei, underlying a very strong commitment to fusion research. China was also the host of one of the most important fusion conferences, the IAEA Fusion Energy Conference FEC, which took place in the fall in Chengdu. The 2008 IAEA FEC will be hosted by Switzerland, in Geneva.

The budget of the European fusion programme was decided at the end of 2006. It amounts to 1.95 billion Euros for the period 2007-2011. About 900 million Euros will be devoted to research activities within laboratories, the remainder to ITER construction. The structure of the programme is being adapted to take into account the commitment of the EU to the construction of ITER and its involvement in the Broader Approach.

A new "Joint Undertaking", called Fusion for Energy will be formally established at the beginning of 2007. Preparations for its staffing have started. In parallel, the European Fusion Development Agreement (EFDA), which has permitted the joint work of the whole European fusion community in the past year, will also be amended to take into account the new structure of the Programme.

1.2 *The CRPP in 2006*

In 2006, the signature of ITER Agreements and the conclusion of the "Broader Approach" negotiations gave very high visibility to fusion at the Swiss political level. The Swiss government decided to contribute to the Broader Approach, a decision confirmed by the Parliament in December.

In April 2006, the CRPP Director, Prof. M.Q. Tran ended his term as EFDA Leader and returned full time to the CRPP.

In June 2006, Prof. A. Fasoli was nominated Deputy Director of the CRPP when Dr. K. Appert retired. The CRPP and its Direction would like to take this opportunity to express their gratitude to Dr. Appert for his commitment to the laboratory, especially during the last few years when Prof. M.Q. Tran was sharing his time between his European duties as EFDA leader and those as Director of the CRPP.

On the academic ground, an important decision was taken by the EPFL to open a Faculty position in Theoretical Plasma Physics at the CRPP. The search and selection process is still ongoing, with an expected nomination in the second half of 2007.

Research activities of the CRPP continued to give a wealth of interesting results, which are detailed in the following pages of the Annual Report. They cover the main domains of competence of the laboratory:

- experimental plasma physics using the tokamak TCV and the specialized device TORPEX
- theory and numerical modelling, a domain which benefits from the availability of high performance computing (HPC) facilities, such as the Blue Gene HPC
- development of electron wave systems for ITER heating and current drive, and of diagnostics
- superconducting cable R+D for ITER
- material science and technology in view of DEMO and ITER
- participation in the enhancement of JET and its scientific exploitation
- development and characterization of plasma processes for industrial applications

The CRPP is also actively in involved and benefits from collaboration with many other European and international laboratories.

Education and training remain a high priority of the CRPP. Some 40 PhD candidates are preparing their thesis at CRPP. This number is a quarter of the total staff of the CRPP (160 persons). In 2006, CRPP was also selected for two specific European Fusion Training Programmes to train engineers for ITER, one in the field of electron cyclotron wave systems and one in the area of superconductivity.

1 Introduction

1.1 *Situation internationale*

L'année 2006 a été marquée par la signature du Traité ITER par les sept parties (Chine, Corée, Etats-Unis, Inde, Japon, Russie, Union Européenne). L'évènement a eu lieu le 21 novembre au Palais de l'Elysée à Paris. Parallèlement, le directorat d'ITER a été nommé et l'équipe est en train de se constituer. Beaucoup d'activités sont en cours, y compris le passage en revue de la conception du projet.

En parallèle, les négociations entre le Japon et l'Europe sur le traité de coopération visant à l'accélération de la construction d'une centrale de démonstration DEMO ont été finalisées. L'accord qui en résulte, connu sous le nom de 'Broader Approach' ou 'Approche Elargie', inclut de nombreux éléments. L'actuel tokamak japonais JT-60U sera transformé en une machine supraconductrice, appelée JT-60SA. Ce tokamak sera exploité conjointement par des équipes japonaises et européennes et servira de 'tokamak satellite' d'ITER. Les recherches en vue du réacteur DEMO formeront le second volet de cette approche élargie. Les activités dans le cadre de l'approche élargie incluent aussi de la R&D pour la source de neutrons IFMIF (International Fusion Material Irradiation Facility), la science et la technologie des matériaux ainsi que de conception du réacteur DEMO lui-même. Finalement, un centre de recherche en Fusion sera établi à Rokkasho (Japon) et sera doté d'un important centre de calculs

En 2006, la Chine a commencé la mise en service de son nouveau tokamak supraconducteur EAST, ce qui souligne le très fort engagement de la Chine dans la recherche en fusion. Par ailleurs, la Chine a été l'hôte de l'une des plus importantes conférences sur la fusion, l'IAEA Fusion Energy Conference (FEC) qui s'est déroulée en automne à Chengdu. En 2008, cette même conférence sera accueillie par la Suisse, à Genève.

Le budget du programme européen en fusion a été décidé à la fin 2006. Il se monte à 1.95 milliards d'Euros pour la période 2007-2011. Environ 900 millions d'Euros seront dédiés aux activités de recherche dans les laboratoires, le reste allant à la construction d'ITER. La structure du programme est adaptée pour prendre en compte l'engagement de l'Europe dans la construction d'ITER ainsi que dans l'Approche Elargie.

Un nouveau 'projet commun', 'Joint Undertaking', appelé 'la Fusion pour l'Energie' (Fusion for Energy) sera établi formellement au début 2007. Les préparatifs pour former l'équipe ont débuté. En parallèle, l'Accord Européen de Développement de la Fusion (EFDA), qui a permis les activités communes de l'ensemble de la communauté de la fusion en Europe ces dernières années, sera aussi modifié pour prendre en compte la nouvelle structure du Programme.

1.2 *Le CRPP en 2006*

En 2006, la signature du traité sur ITER et la conclusion des négociations pour l'Approche Elargie a donné une très forte visibilité de la fusion au niveau politique Suisse. Le Gouvernement Suisse a décidé de contribuer à l'Approche Elargie, une décision confirmée par le Parlement en décembre.

En avril 2006 le Directeur du CRPP, le Prof. M.Q. Tran terminait son mandat en tant qu'EFDA Leader et retournait à plein temps au CRPP.

En juin 2006, le Prof. A. Fasoli a été nommé Vice-directeur du CRPP alors que le Dr. K. Appert partait à la retraite. Le CRPP et sa Direction aimeraient profiter ici de l'occasion pour exprimer leur gratitude au Dr K.Appert pour son engagement pour le laboratoire, en particulier durant les quelques dernières années pendant lesquelles le Prof. M.Q. Tran partageait son temps entre ses charges européennes à la direction de l'EFDA avec celles de Directeur du CRPP.

Sur le plan académique, l'EPFL a pris la décision importante d'ouvrir une chaire en Théorie de Physique des Plasmas au CRPP. Le processus de recherche et de sélection des candidats est en cours, avec une nomination attendue pour la 2e moitié de 2007.

Les activités de recherche du CRPP continuent de générer une abondance de résultats intéressants, qui sont présentés en détail dans les pages qui suivent du Rapport Annuel. Ils couvrent les principaux domaines de compétence du laboratoire :

- physique expérimentale des plasmas avec le Tokamak TCV et l'installation spécialisée TORPEX
- théorie et modélisation numérique, un domaine qui bénéficie de la disponibilité d'ordinateurs très performants, comme le 'Blue Gene HPC'
- développement de systèmes d'ondes cyclotronique électronique pour le chauffage et la génération de courant pour ITER, ainsi que des diagnostiques
- R&D sur les câbles supraconducteurs pour ITER
- science et technologie des matériaux en vue de DEMO et ITER
- participation aux travaux de développement des capacités de JET ainsi qu'à son exploitation scientifique
- développement et caractérisation des procédés plasmas en vue d'applications industrielles

Le CRPP bénéficie aussi d'un fort engagement dans la collaboration avec de nombreux autres laboratoires européens ou internationaux.

L'enseignement et la formation sont toujours une haute priorité du CRPP. Environ 40 étudiants doctorants préparent leur thèse de doctorat au CRPP. Ce nombre correspond au quart du total du personnel du CRPP (160 personnes). En 2006, le CRPP a été sélectionné pour deux Programmes Européens de Formation en Fusion pour la formation d'ingénieurs pour ITER, l'un dans le domaine des systèmes d'ondes électroniques cyclotroniques, l'autre dans le domaine de la supraconductivité.

1 Einleitung

1.1 Die Fusionsforschung im internationalen Rahmen

Ein bedeutendes Ereignis im Jahre 2006 war die Unterzeichnung des ITER-Vertrags durch die sieben Partner (VR China, Europäische Union, Indien, Japan, Korea, Russische Föderation und die USA) am 21. November im Elysée-Palast in Paris. Ausserdem wurde das ITER-Direktorium ernannt und das ITER-Team zusammengestellt. Zur Zeit sind vielseitige Aktivitäten im Gange, u.a. eine Ueberprüfung und Aktualisierung des Baukonzepts von ITER.

Gleichzeitig wurden die Verhandlungen zwischen Japan und der Europäischen Union mit einem Vertrag zur Zusammenarbeit zum Abschluss gebracht, der eine Beschleunigung beim Bau eines Reaktor-Prototyps (Projekt DEMO) zum Ziel hat. Das unterzeichnete Abkommen umfasst eine Reihe von Elementen, die das sogen. "erweiterte Programm" darstellen. Dazu gehört der Ausbau des japanischen Tokamak-Experiments JT-60 zu einer Maschine mit supraleitenden Spulen, die den Namen JT-60 SA erhalten soll. Diese Maschine soll gemeinsam von japanischen und europäischen Teams betrieben werden und als "begleitendes Experiment" für ITER dienen. Eine zweite Thematik im Rahmen des erweiterten Programms ist die Forschung zur Vorbereitung von DEMO einschliesslich der Entwicklungs- und Forschungsarbeiten zum Bau einer Neutronenquelle für Materialstudien (IFMIF, International Fusion Material Radiation Facility). Schliesslich ist noch geplant, im japanischen Rokkasho ein Zentrum für Fusionforschung einzurichten, das mit einem Hochleistungsrechner ausgestattet werden soll.

Im Jahre 2006 ging in Hefei, in der VR China, der neue, mit Supraleitern ausgestattete Tokamak EAST in Betrieb. Dadurch bekräftigte die VR China ihr Engagement auf dem Gebiet der Fusionsforschung. China organisierte ausserdem im Herbst 2006 in Chengdu die IAEA Fusion Energy Conference (FEC), eine der bedeutendsten Konferenzen zur Kernfusion. Im Jahre 2008 wird die nächste Konferenz dieser Serie in Genf in der Schweiz stattfinden.

Zum Jahresende 2006 wurde das Budget des europäischen Programms der Fusionsforschung für den Zeitraum 2007 bis 2011 verabschiedet. Es beläuft sich auf insgesamt 1.95 Millarden Euro. Davon sind ca. 900 Millionen Euro für die Forschung in den einzelnen Instituten der Mitgliedsländer bestimmt, der Rest ist für den Bau von ITER vorgesehen. Die Struktur des Programms trägt der Tatsache Rechnung, dass sich die EU (Europäische Union) für den Bau von ITER verpflichtet hat und gleichzeitig am sogen. "erweiterten Programm" beteiligt ist.

Zu Beginn des Jahres 2007 soll unter dem Namen "Fusion for Energy" ein neues gemeinschaftliches Unternehmen gegründet werden. Vorbereitungen zur Stellenvergabe sind bereits im Gange. Gleichzeitig wird die Struktur von EFDA (European Fusion Development Agreement), unter deren Leitung im vergangenen Jahr die gemeinsame Forschungsarbeit innerhalb der EU durchgeführt wurde, den Erfordernissen des neuen Programms angepasst.

1.2 Das Jahr 2006 am CRPP

Die Unterzeichnung der ITER-Verträge und der erfolgreiche Verhandlungsabschluss zum "erweiterten Programm" hat der Fusion auch auf der politischen Ebene in der

Schweiz gesteigertes Interesse eingebracht. So entschied sich die Schweizerische Bundesregierung für eine Beteiligung am erweiterten Programm. Diese Entscheidung wurde im Dezember vom Parlament bestätigt.

Im April 2006 beendete Prof. M.Q. Tran sein Mandat als EFDA-Leiter und kehrte vollamtlich zu seiner Hauptaufgabe als Direktor des CRPP zurück.

Im Juni 2006 wurde Prof. A. Fasoli zum stellvertretenden Direktor des CRPP ernannt, nachdem Dr. K. Appert in den Ruhestand eingetreten war. Direktorium und Mitarbeiter möchten an dieser Stelle Dr. Appert für seinen langjährigen, intensiven Einsatz zum Wohl des Instituts herzlich danken. Er hat insbesondere während der vergangenen Jahre zusätzliche Aufgaben auf sich genommen, als Prof. Tran gleichzeitig zur seiner Funktion als Direktor des CRPP mit europäischen Verpflichtungen als EFDA-Leiter belastet war.

Im akademischen Bereich ist die Entscheidung der EPFL zugunsten einer zusätzlichen Professorenstelle für Theoretische Plasmaphysik hervorzuheben. Das Auswahlverfahren ist zur Zeit noch im Gange und man rechnet mit einer Entscheidung in der zweiten Jahreshälfte 2007.

Die Forschungsprogramme am CRPP haben auch im Jahr 2006 vielfältige und bedeutende Ergebnisse hervorgebracht, die in diesem Jahresbericht näher beschrieben werden. Sie geben einen Einblick in die Gebiete, auf denen am CRPP vertiefte Kenntnisse vorhanden sind :

- experimentelle Plasmaphysik unter Verwendung der beiden Maschinen TCV und TORPEX
- theoretische Studien und numerische Modellrechnungen, unter Einsatz von Hochleistungsrechnern, wie dem "Blue gene" HPC
- Entwicklung von Ausrüstung für ITER zur Plasmaheizung und zum nicht-induktiven Stromtrieb mit Hilfe von Elektron-Zyklotronwellen, sowie zu Diagnostikzwecken
- Entwicklung von supraleitenden Kabeln für den Einsatz an ITER
- Materialforschung im Hinblick auf die technologischen Anforderungen von ITER und DEMO
- Beträge zum experimentellen Programm und zur Verbesserung der technischen Ausstattung von JET
- Forschung und Entwicklung auf dem Gebiet der Plasmatechnologie für industrielle Anwendungen.

Das CRPP pflegt weiterhin enge und erfolgbringende Kontakte mit anderen Forschungsinstituten im europäischen und internationalen Rahmen.

Ausbildung und Weiterbildung geniessen am CRPP hohe Priorität. Davon zeugt die Zahl von 40 Doktoranden, die am CRPP ihre Dissertation vorbereiten. Sie stellen damit ein Viertel des wissenschatlichen Personals am CRPP (insgesamt 160 Mitarbeiter).

Seit 2006 übernimmt das CRPP auch Aufgaben zur Ausbildung von zukünftigen Ingenieuren für ITER auf dem Gebiet der Elektron-Zyklotron Wellen and der Supraleitung. Damit leistet das CRPP einen wichtigen Beitrag zu einem neu geschaffenen europäischen Trainingsprogramm.

1   Introduzione

1.1   *La situazione internazionale*

Il 2006 è stato caratterizzato dalla firma dell'Accordo internazionalee ITER da parte dei sette partners (la Cine, l'Unione Europea, l'India, il Giappone, la Corea, la Russia e gli Stati Uniti d'America). L'evento ha avuto luogo al palazzo dell'Eliseo a Parigi il 21 Novembre. La struttura direttiva di ITER è stata nominata, e parte del personale è stato selezionato. Diverse attività, fra le quali una revisione completa del progetto, sono in corso.

Parallelamente agli sviluppi di ITER, un negoziato fra l'Unione Europea ed il Giappone è stato concluso con un accordo di cooperazione, noto come il *Broader approach*, teso ad accelerare la costruzione della prima centrale a fusione di dimostrazione, DEMO.
Questo accordo include diversi elementi. L'attuale tokamak giapponese JT-60U sarà rinnovato con bobine magnetiche superconduttrici e prenderà il nome di JT-60SA. Tale installazione sperimentale sarà utilizzata congiuntamente da gruppi giapponesi ed europei, come tokamak satellite rispetto ad ITER. Sviluppo e ricerca nella direzione di DEMO sarà il secondo tema del *Broader approach*, ed includerà R&D per la sorgente di irradiazione neutronica IFMIF (*Intenational Fusion Material Irradiation Facility*), scienza e tecnologia dei materiali, ed un design preliminare dello stesso DEMO.
Infine, un centro per l'energia di fusione sarà stabilito a Rokkasho, in Giappone, e sarà equipaggiato con sistemi di super-computers.

La Cina ha rinnovato il suo impegno nel campo della fusione intraprendendo nel 2006 l'ultima fase di test del suo nuovo tokamak superconduttore, EAST, ad Hefei. La Cina ha anche ospitato a Chengdu, in autunno, la conferenza piu' importante sulla fusione, la *Fusion Energy Conference* (FEC) dell'IAEA. La FEC del 2008 sarà ospitata dalla Svizzera, ed avrà luogo a Ginevra.

Il budget del programma europeo di fusione è stato deciso alla fine del 2006, ed ammonta a 1.95 miliardi di euro per il periodo 2007-2011. Circa 900 milioni di euro finanzieranno la ricerca nei laboratori delle Associazioni dei vari paesi europei, mentre il resto sarà utilizzato per la costruzione di ITER. La struttura del programma europeo incorporerà le attività legate ad ITER ed al *Broader approach*.

Un nuovo *Joint Undertaking*, denominato *Fusion for Energy*, sarà stabilito formalmente all'inizio del 2007. Parallelamente, l'EFDA (*European Fusion Development Agreement*), sarà adattato alla nuova struttura del programma europeo.

1.2   *Il CRPP nel 2006*

Gli avvenimenti che hanno caratterizzato la comunità della fusione nel 2006, in particolare la firma dell'accordo ITER ed il lancio del *Broader approach*, hanno conferito grande visibilità alla fusione nel quadro politico svizzero. Il governo svizzero ha deciso di contribuire direttamente al *Broader approach*, una decisione confermata dal Parlamento in Dicembre.

In aprile 2006, il Prof. M.Q.Tran ha terminato il suo mandato di *EFDA Leader* ed ha fatto ritorno al CRPP a tempo pieno.

In giugno 2006, il Prof. A.Fasoli è stato nominato Vice Direttore del CRPP, in seguito al pensionamento del Dr. K.Appert. Il CRPP e la sua Direzione colgono l'occasione per esprimere la loro gratitudine al Dr. Appert per il suo impegno ed il suo contributo alla direzione del laboratorio, in particolare durante il periodo in cui il Prof. Tran divideva il suo tempo fra il ruolo di *EFDA Leader* e quello di Direttore del CRPP.

Dal punto di vista accademico, una decisione importante è stata presa dall'EPFL di mettere a concorso un posto di professore di fisica del plasma teorica. Il processo di selezione è in corso e la nomina è prevista per la seconda metà del 2007.

Le attività di ricerca al CRPP hanno continuato a fornire un gran numero di risultati interessanti, descritti in dettaglio in questo Rapporto Annuale, distribuiti sulle varie aree di competenza del laboratorio:

- fisica del plasma sperimentale sul tokamak TCV e sull'esperimento di base TORPEX
- teoria e simulazione numerica, un'area che usufruisce delle infrastrutture di *High Performance Computing* (HPC) dell'EPFL, come il Blue Gene HPC
- sviluppo di sistemi di riscaldamento e di generazione di corrente in ITER tramite onde elettroniche, e di sistemi diagnostici
- cavi superconduttori per ITER
- scienza e tecnologia dei materiali per DEMO ed ITER
- attività e sviluppo di nuovi sistemi al JET
- sviluppo e caratterizzazione di applicazioni industriali dei plasmi.

Il CRPP è implicato attivamente in un gran numero di collaborazioni a livello europeo ed internazionale.

Insegnamento e formazione continuano a costituire un'area prioritaria per il CRPP. Circa 40 dottorandi studiano al CRPP, un quarto di tutto il personale nel 2006. Il CRPP è stato selezionato per due specifici programmi europei di formazione nella fusione, per preparare giovani ingegneri per ITER nel campo dei sistemi ad onde ciclotroniche elettroniche e in quello dei magneti superconduttori.

2   Research achievements of the CRPP in 2006

2.1   *The TCV tokamak*

The operation of TCV in 2006 covered three main periods, between February and mid-March, between mid-April and July, and from the end of September onwards. The involvement of key personnel with a number of external activities, including ITER developments and JET operations, limited the average rhythm of operation to somewhat less than five days a week.

During the two short shutdowns of March-April and August-September a 7th Electron-Cyclotron (EC) horizontal launcher was installed for Electron Bernstein Wave (EBW) studies, an EC launcher was repaired, an X2 gyrotron system was refurbished and put back into operation, and a new ion arc source for the diagnostic NBI was installed and commissioned.

During most of the campaigns discussed in this report, only one EC gyrotron system at the third harmonic was available for the experiments, providing a maximum X3 power of 0.5MW, and up to four EC gyrotron systems at the second harmonic could be used, corresponding to a total X2 power of 2.0MW. On the other hand, significant progress in the preparation of further full power campaigns was made, including the developments of suitable target plasma scenarios, for example for H-mode physics studies, as well as feasibility and design studies for diagnostic upgrades (see Technical achievements section). In addition, disruptive discharges were identified within the wide TCV operational domain, and analysed in terms of the variables required by the international disruption database, to which a data set of about thirty disruptions was sent.

The campaigns were conducted according to the scientific missions defined and agreed during general discussions in December 2005 - January 2006. These missions address specific problems within a few themes of relevance for ITER and for the improvement of the tokamak operation and concept in general, including electron heat, particle and impurity transport, electron internal transport barriers (eITBs), H-mode, edge physics, plasma control, Electron-Cyclotron Heating (ECH) and Electron-Cyclotron Current Drive (ECCD), and performance improvement through high density operation, including questions related to EB waves. The highlights of the results obtained recently on these themes are reported below.

2.1.1   *Scenarios with internal transport barriers*

Electron Internal Transport Barriers (eITBs) are obtained on TCV in a variety of experimental conditions, with strong ECCD in nearly or fully non-inductive scenarios, in cases with comparable ohmic and non-inductively driven currents, and, transiently, by strong heating during current ramps. Fully non-inductive scenarios involve an appropriate distribution of ECCD sources to sustain a hollow current profile, further enhanced by the bootstrap current centred in the high gradient barrier region. Depending on the details of the discharge parameters and conditions, these scenarios may evolve to steady-state, lasting several current redistribution times and up to hundreds of electron energy confinement times. A significant (up to a factor of 6) improvement in confinement compared to TCV L-mode scaling and strongly correlated barriers in n_e and T_e characterise all these

conditions. The highest performance discharges also display high bootstrap current fractions and high poloidal β. Higher enhancement factors are obtained in non-stationary conditions, and the bootstrap fraction reaches 90% transiently during early current ramps.
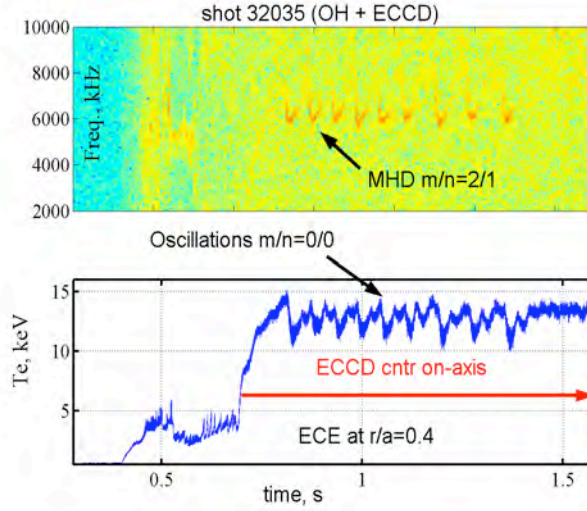
Fig. 2.1.1   *Example of low frequency global (m=n=0) plasma oscillations in the eITB regime, with ohmic heating and counter-ECCD on axis.*

Global plasma oscillations in eITB regimes

Both in non-inductive and inductive eITB scenarios, slow oscillations of the electron temperature, with frequency ~10Hz and full poloidal and toroidal symmetry (m=n=0), are observed, coexisting with MHD modes (Fig. 2.1.1). This phenomenon appears akin to the O-regime on the Tore Supra tokamak, occurring in fully or nearly non-inductive discharges with lower hybrid current drive and negative central magnetic shear. The oscillations affect the whole plasma column, as the total plasma current oscillates (with a 45° phase shift with respect to the temperature oscillations) and the magnetic axis shifts radially by up to 3cm. A feedback mechanism therefore appears to be at play, in which the MHD mode degrades the confinement, which in turn reduces the gradients and the MHD instability drive, so that a regular oscillatory pattern is established.

eITB diffusion coefficients in Argon puff experiments

The injection of Argon gas puffs in a steady state eITB has been employed as a tool to study density transients and evaluate diffusion coefficient and pinch velocity separately. This data is used as an input in a radial transport code (ASTRA) to reproduce the measured evolution using a particle diffusion equation without sources and a model for the pinch velocity. The agreement between the simulation and the initial phase of the transient after one Argon puff indicates that the estimated (anomalous) value of the diffusion coefficient is consistent with the data, while the neoclassical diffusivity would predict too slow an evolution inside the barrier. This supports the hypothesis that turbulence is still active inside the eITB, although at lower levels than in standard monotonic q-profile scenarios. The estimated particle diffusion coefficient is 5-10 times smaller then the diffusivity of standard positive shear scenarios, but is still 10 times higher than the neoclassical predictions (Fig. 2.1.2).
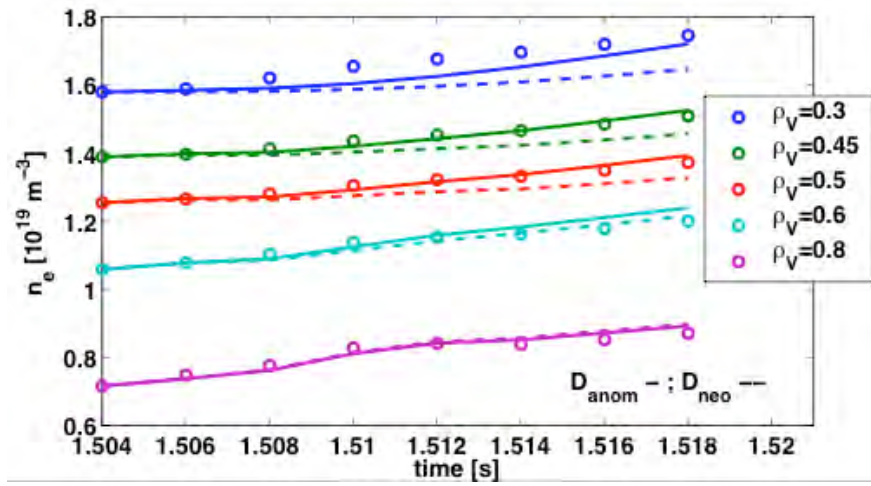
Fig. 2.1.2   *Density vs time plot illustrating the evolution of the particle diffusion coefficient after a rapid Argon gas puff. Circles are the experimental values and the lines are the simulation of the time evolution with the different D values inserted in ASTRA. D_{anom} (solid line) is the anomalous level, which is about 5-10 smaller than the usual level, but still 10 times higher than the neoclassical value evaluated within the ITB, D_{neo} (dashed line).*

2.1.2   Plasma edge characterisation and modelling

Tokamak scrape-off layer (SOL) parallel flows are increasingly recognised as one of the principal driving forces for the material migration observed in all diverted tokamaks in which such migration has been studied. This migration may ultimately be responsible for unacceptable levels of tritium retention in ITER and future reactors. These plasma flows have been measured in several tokamaks, almost exclusively using fast reciprocating Langmuir probes equipped with Mach probe measuring capability. This has now also been performed on TCV for the first time.

Probe reciprocations have been made just below the plasma midplane into standard single null lower ohmic discharges at fixed current (260 kA) but varying density and for both forward (FWD-B) and reversed (REV-B) toroidal field. The result, shown in Fig. 2.1.3a, is an extremely clear demonstration of a number of key aspects associated with these flows: the high absolute magnitude (as high as M=0.6, where M is the parallel Mach number of the flow – the flow velocity normalised to the ion sound speed), especially at low density and near the separatrix; the strong decrease with increasing density; the net flow from outer to inner divertor for forward toroidal field; and the "offset flow" towards the outer divertor. The latter can be seen more clearly by computing the "mean flow" as the average of the FWD-B and REV-B field measurements at fixed density. These are also shown in the lower part of Fig. 2.1.3a. It is evident that at all densities, there is a net, field direction independent flow into the outer divertor. Such a flow is just what would be expected in the case of enhanced perpendicular transport into the outboard (unfavourable magnetic curvature) SOL, given the location of the fast probe below the outer midplane. Using comparisons between two dimensional fluid turbulence simulations using the ESEL code developed at Risoe in Denmark and experimental turbulence measurements (using the same reciprocating probe), this transport has been shown unambiguously on TCV to be due to interchange motions in the SOL (as described in the 2005 Annual Report). Employing a simple ansatz for the parallel flow driven along these interchange filaments, density fluctuation time series from the ESEL

code and from experiment can be analysed to estimate the parallel flow that would be driven by the radial transport. The result is shown in Fig. 2.1.3c, where the measured, field direction independent flow offset profile for a series of densities is plotted in comparison with the ESEL estimate computed from a high density simulated case. Agreement is clearly reasonable, demonstrating that the interchange motions can account for much, if not all, of the field independent component observed in the TCV parallel flow.
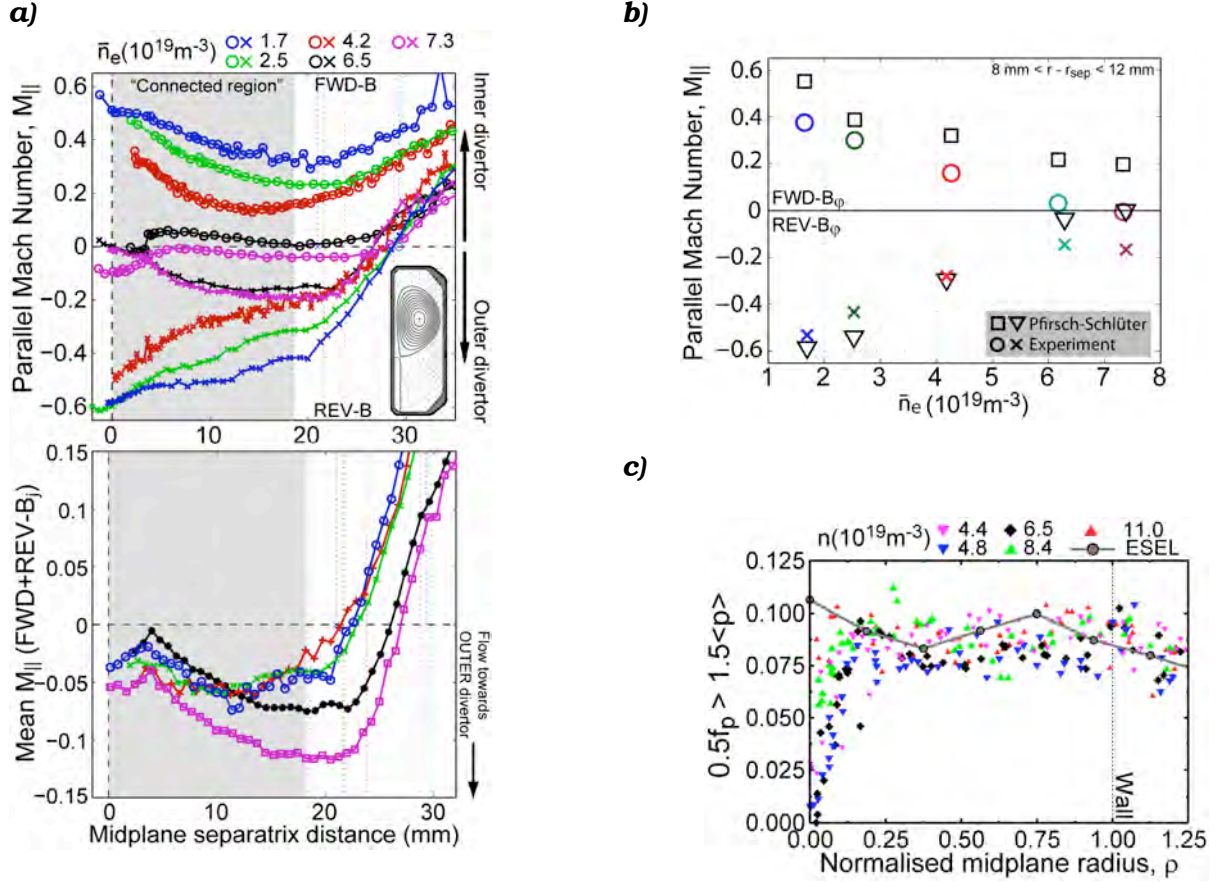
Fig. 2.1.3   (a) Top: radial profiles of parallel fluid flow Mach number for forward and reversed toroidal field and varying density in ohmic SNL TCV discharges. Bottom: mean of FWD and REV-B flows for each density. (b) Density dependence of measured and computed Pfirsch-Schlüter parallel flows averaged over an interval of 4 mm in the central region of the midplane SOL. (c) Estimated radial profiles of the field independent flow offset from both experiment and ESEL code. The profiles are generated assuming that plasma blobs (filaments) transiently increase the local pressure as they cross the SOL and drive parallel flows which exhaust along the field. The normalized midplane radius is defined such that $\rho=0$ at the separatrix and $\rho=1$ at the point where a flux surface from the outer divertor intersects the outboard midplane wall.

Meanwhile, the field dependent part of the flow in the outboard midplane vicinity can be described very well on TCV in both magnitude and direction by classical Pfirsch-Schlüter (P-S) flows in the SOL, which are return parallel flows driven by poloidal drifts, themselves driven by radial electric fields and pressure gradients. This is clearly seen in Fig. 2.1.3b, where for a given range of radial distance from the separatrix, the experimental Mach flow data are compared with an analytic

approximation to the P-S flow. This now represents a serious test of the coupled fluid-Monte Carlo neutral codes, such as SOLPS5, which are known to consistently underestimate the experimentally measured flows by large factors on other tokamaks. Simulations of this TCV data with drift terms activated are currently being pursued using SOLPS5.

This code is now also being used to simulate the SOL and divertor plasma of ELMing (ELM = Edge Localised Mode) H-mode on TCV, beginning first with a time independent model of the inter-ELM phase without drifts activated. The steep gradients in the H-mode pedestal region mean that the assumption of constant perpendicular particle ($D_\perp$) and heat ($\chi_\perp$) transport coefficients across the simulation grid often employed in L-mode code runs is no longer valid and radial variation must be included if experimental data are to be satisfactorily matched. An example is shown in Fig. 2.1.4, in which the SOLPS5 simulations are compared with radial profiles of T_e and n_e compiled from edge Thomson scattering (pedestal and near SOL) and fast reciprocating Langmuir probe (SOL) measurements. This favourable match also yields reasonable agreement between simulation and experimental profiles at the divertor targets. Drifts are now being incorporated into these simulations and time dependent simulations of the ELM itself have begun.
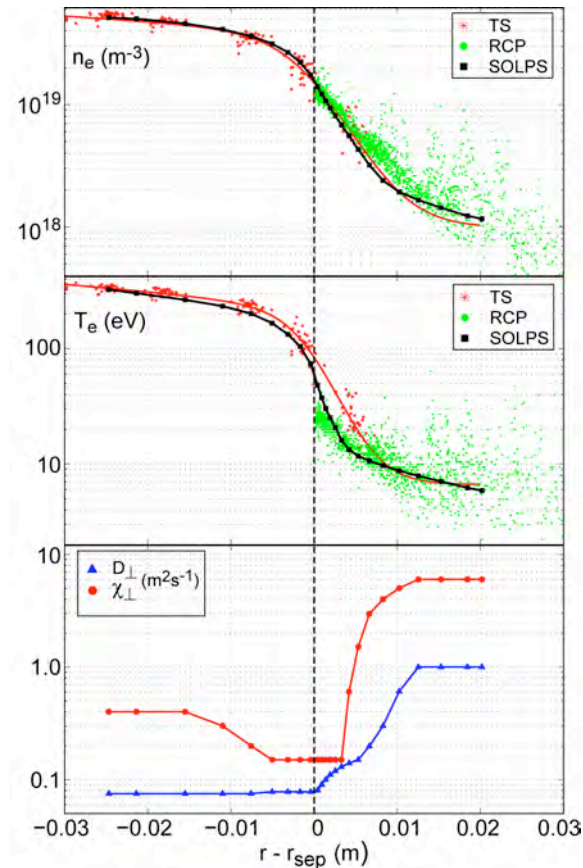
Fig. 2.1.4 *Measured pedestal and SOL radial profiles during an ohmic Type III ELMing H-mode together with SOLPS5 simulations showing the assumed radial profile of anomalous $D_\perp$ and $\chi_\perp$.*
TS: Thomson scattering
RPC: reciprocating probe

2.1.3   H-mode physics

Stationary ELM-free H-mode with strong electron heating

During the first six months of 2006 the analysis of the results of high power X3 heating experiments was completed. Using an ohmic H-mode as target and three X3 gyrotrons it was possible to obtain an X3 absorption up to ≈90%. With 1.3MW of

coupled X3 power, two H-mode regimes were obtained: a regime resembling a Type I ELMy H-mode and a quasi-stationary ELM-free H-mode. Despite the ELM-free nature of this second regime, both the electron density and the diamagnetic energy remain approximately constant. Normalised values are rather high, $\beta_N \approx 2.0$, with good confinement enhancement factors HIPB98(Y,2)$\approx$1.4. During the quasi-stationary ELM-free H-mode, ion heating is observed, together with spontaneous plasma rotation. At mid-radius the Carbon ion temperature increases from 500eV, in the ohmic H-mode phase, to 1keV during the quasi-stationary X3 heated phase, the most significant ion heating observed on TCV to date. At the same time T_e rises from 1keV to 3keV and Carbon ion rotation increases dramatically, from 5kms^{-1} to 50kms^{-1}.

ELMy H-mode in discharges with favourable drift direction

The ohmic ELMy H-mode regime has regularly been obtained in TCV with the ion ∇B drift directed away from the X-point, the so-called 'unfavourable direction'. In order to decrease the H-mode threshold power and access large ELM regimes with ECH X3 heating, the direction of the main toroidal field was changed. In this configuration, experiments performed several years ago showed a direct transition to an ELM free H-mode. The search for a stationary ELMy H-mode, the ideal target for X3 heating, was performed with the same strategy as for the unfavourable direction. Plasma density and current were simultaneously varied from shot to shot to follow the L-mode to H-mode (LH) transition, and the effect of small changes in plasma shape was explored. A regularly ELMing H-mode was found at the low density/high current end of the investigated range, as shown in Fig. 2.1.5. These results were obtained for plasmas with their magnetic axis located at the vertical position z=0.23cm, but an ELMy H-mode regime was recently obtained also at z=0, a position that is of practical interest for diagnostic access and coverage.
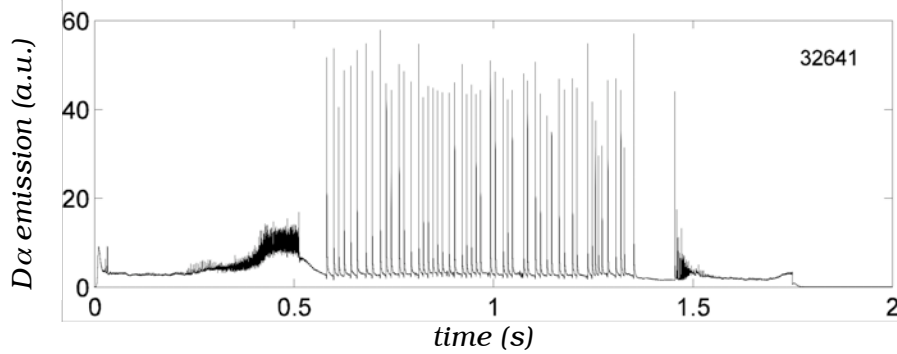
Fig. 2.1.5 *Regularly ELMing H-mode in ohmic plasma with favourable ion ∇B drift. I_p=350kA, n_e=5.4x10^{19}m^{-3}, κ=1.68, δ=0.46.*

2.1.4 Plasma rotation, electron energy, particle and impurity transport in shaped plasmas

Plasma rotation

The question of plasma rotation in toroidal devices is receiving increasing attention due to its impact on the stability of resistive wall modes, neoclassical tearing modes and micro-instabilities causing anomalous transport. TCV provides unique insight into the mechanisms generating and regulating plasma rotation, and the related interplay between particle, energy and momentum transport, using its Ohmic and

EC heated discharges with minimum external momentum injection. These investigations use the diagnostic neutral beam, which induces a small rotation (~1km/s, compared to ~20km/s in other tokamaks), due to a combination of quasi-orthogonal injection angle and a modest average deposited power (20kW).

Stationary toroidal rotation profiles have been studied in steady-state Ohmic L-mode discharges as a function of plasma current and electron density. For currents $I_p<380kA$ and central densities n_{e0} up to $8\times10^{19}m^{-3}$ the plasma rotates in the counter current direction (the electron diamagnetic drift direction), with absolute values of the angular frequency $\omega_\phi=v_\phi/R$ up to 40krad/s at the plasma centre, decreasing towards zero at the edge. As observed in other tokamaks, the toroidal rotation profile is strongly linked to the ion transport. Outside the inversion radius, the stationary rotation profile follows the T_i profile. (By expressing the toroidal rotation in angular units, results from difference plasma devices may be directly compared).

The study of intrinsic toroidal plasma rotation in L-mode confinement regimes was extended from limited to diverted magnetic configurations. A comparison of the dependence of rotation on n_e was performed in two cases using a sequence of steady state plasma discharges with a range of plasma densities with the same plasma current. In limiter configurations, with $I_p=155kA$, the ω_ϕ profile is always negative and depends weakly on n_e (Fig 2.1.6, left). In particular, the rotation at $\rho\sim0.9$ appears to be independent of n_e, with values ~10krad/s. The increase of ω_ϕ may at least partly be ascribed to the increased T_i from the enhanced thermal coupling to electrons at higher plasma densities.
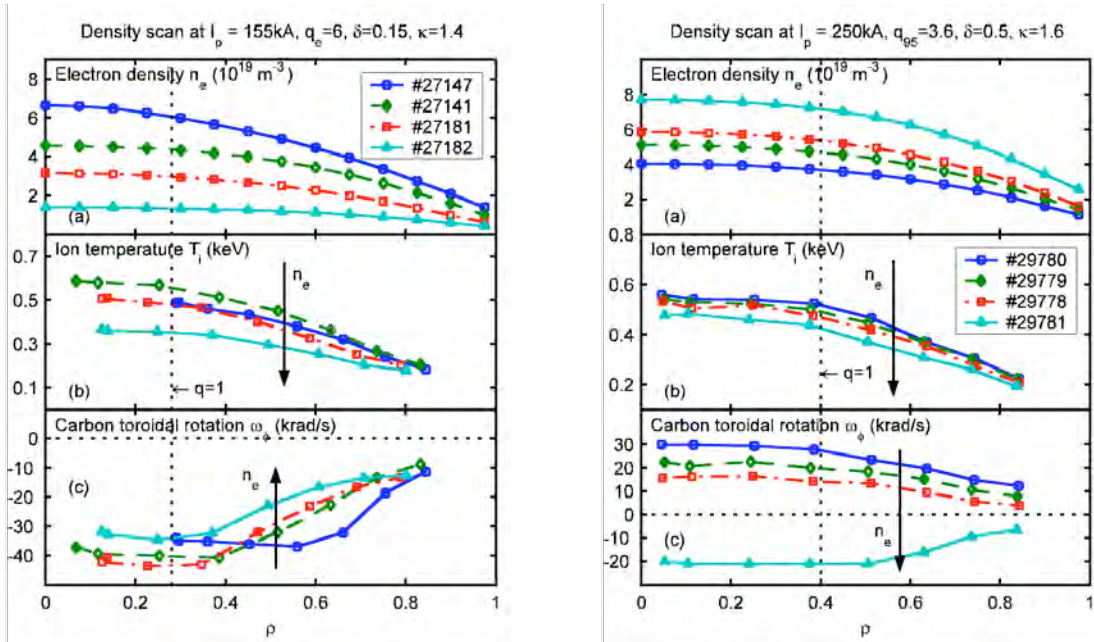
Fig. 2.1.6   *Stationary radial profiles of electron density, ion temperature and toroidal rotation for discharges in limited (left) and diverted (right) configurations.*

A different behaviour is found for diverted discharges. The right column of Fig. 2.1.6 shows the results of a shot by shot plasma density scan for $I_p=255kA$, with the ion ∇B drift directed away from the X point. For central densities up to $n_{e0}=6\times10^{19}m^{-3}$, the plasma column rotates in the current direction, with $\omega_\phi\approx20krad/s$. The outer CXRS measurement at $\rho=0.85$ indicates a positive rotation

with values of ω_ϕ=7-12krad/s. Edge measurements where the plasma has been vertically displaced inside the TCV vessel confirm a positive rotation >10krad/s up to ρ=1, for n_{e0}=4×10^{19}m^{-3}. With increasing density, the entire rotation profile slows down, maintaining the same profile shape. In particular, a decrease in the edge rotation of 12 to 5krad/s, for n_e increasing from 4 to 8×10^{19}m^{-3} on axis, is observed in divertor configuration. This effect is not observed in limited plasmas, where the plasma wall interaction stops the edge plasma rotation.

In diverted configurations, the edge rotation is found to no longer be constrained to near zero values, and may now evolve freely with the ω_ϕ profile. The parallel fluxes present in the scrape off layer and the shape of rotation profile are now determined by the internal generation and transport of toroidal momentum, which is again found to depend on the main plasma parameter profiles (n_e, T_e, T_i). Increasing the density further to n_{e0}=8×10^{19}m^{-3} results in a new inversion of the rotation profile, which now, somewhat surprisingly, becomes similar to that measured in the low density limited configurations.

Figure 2.1.7 compares the stationary toroidal rotation, for two radial positions normalised to the limited L-mode scaling law :

$$V_{\phi Max}[km/s] = -12.5\ T_{0i}[eV]/I_p[kA]$$

that expresses the empirically observed dependence of the maximum axial velocity as a strong function of the central ion temperature and the plasma current. The figure shows an example of the toroidal rotation as a function of plasma density for limited and diverted configurations, demonstrating the transition to a counter current rotation for n_{e0}>6×10^{19}m^{-3} for the diverted configuration. This observation appears to be in agreement with the Alcator C-mod results, where similar ω_ϕ values in the core are measured for high density plasmas in limited and diverted ohmic L-mode discharges. The wide range of toroidal velocity scaling observations in other configurations clearly indicates that both the sources and the transport of toroidal momentum are still far from understood in this relatively simple ohmic case. It is interesting to note that on ITER, in spite of the seemingly high planned neutral heating power, the toroidal momentum balance may be quite close to the TCV ohmic configurations. If on ITER the observation of the dependence of other plasma phenomena such as MHD activity and particle and energy transport are also found to depend of the toroidal velocity, an understanding of the natural TCV rotation behaviour could be particularly relevant for the future.
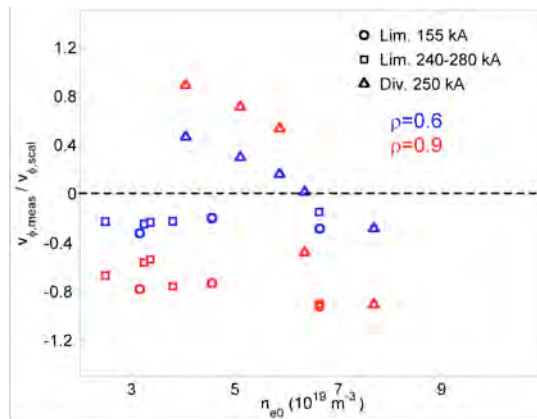
Fig. 2.1.7   *Stationary toroidal rotation normalised to the limited L-mode scaling law, taken at two radial positions, for discharges in limited (squares and circles) or diverted (triangles) magnetic configuration.*

Reconstruction of ion temperature profiles using a Neutral Particle Analyser

The charge exchange spectrum recorded by Neutral Particle Analysers (NPAs) is used to determine parameters of light plasma ions, such as the ion temperature and/or neutral particle emission density of hydrogen, deuterium or helium. Neutralisation of ions occurs throughout the plasma volume, so the measurement consists of an integral along the line of sight of the diagnostic and local properties (e.g. T_i in the plasma core) are not readily available.

In order to measure the ion temperature profile of an ohmically heated plasma discharge on TCV, the plasma was vertically displaced across the horizontal view line of the compact NPA, which is located on an equatorial port. A second vertically orientated NPA was used to monitor the plasma ion population to ensure that this displacement did not, itself, affect the neutral particle emission. The highest particle energy contribution to the spectrum was assumed to come from the observed region closest to the plasma core and the scan of the vertical plasma cross section was used to reconstruct an experimental ion temperature profile (Fig. 2.1.8, left).

The measured neutral energy spectrum was modelled with a combination of codes for the neutral plasma transport (kinetic transport algorithm KN1D or Monte Carlo algorithm DOUBLE-TCV), the ion neutralisation and the attenuation of the neutrals from their birth place to the edge. Together with the main plasma parameters, these codes require an ion temperature profile as input.
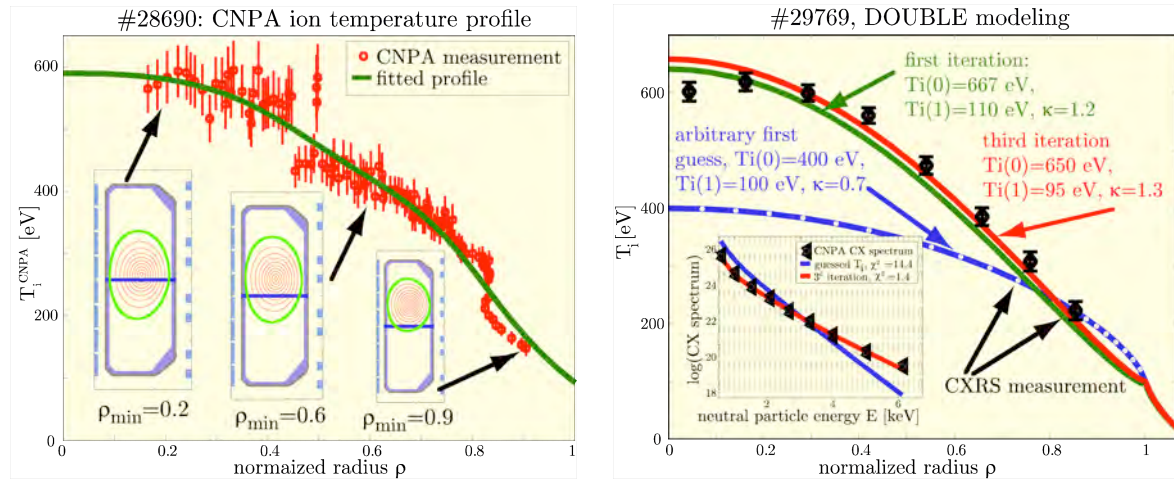
Fig. 2.1.8   *Left: Experimentally reconstructed ion temperature profile by vertically displacing the plasma in the TCV vessel across the Compact NPA with fixed line of sight (the blue line in the insets showing the equilibrium reconstruction of the magnetic flux surfaces at t=0.1, 0.9 and 1.5s of discharge #28690). The red circles represent the temperature inferred from the CNPA data and the green curve is a weighted fit of the measurement. Right: Reconstruction of the ion temperature profile by iteratively modelling the measured NPA charge exchange spectrum (inset) for discharge #29769. This discharge has a good CXRS measurement of the carbon ion temperature profile (black diamonds), which is used to validate the reconstructed profile from the NPA measurement. The initial "guess" of the T_i profile (red curve) was chosen to be far from the CXRS profile to demonstrate the rapid convergence (generally within three executions of DOUBLE-TCV, blue curves in the figure) of the algorithm. The iteratively adjusted ion temperature profile is consistent with the Carbon T_i profile measured by CXRS.*

The T_i profile is reconstructed without requiring a sequence of plasma displacements from iterative calculations based on the measured charge-exchange spectrum and on the adjustment of the parameters of an initially unknown functional ion temperature profile. The model for the neutral flux is verified for discharges with thermalised ion populations, where the modelled T_i-profile coincides with the experimentally determined Carbon ion temperature profile measured by Charge eXchange Recombination Spectroscopy (CXRS).

The core ion temperature may be recovered as long as the neutrals emitted in the plasma core are not completely re-ionised (as is the case for high density plasmas) before reaching the NPA. The 1-5ms integration time of the NPA measurement is ~20 times faster than the CXRS system and provides insight into fast changes of the ion distribution function during one measurement from the CXRS system. This recovery algorithm breaks down for plasmas with non-thermal ion populations as observed during experiments with strong electron cyclotron heating.

In general, modelling of NPA measurements improves the understanding of the physics of plasma ions and neutrals and gives insight into particle transport mechanisms and confinement properties (spatial resolution and time scales), isotopic plasma composition (measurement of multiple isotopes) and the influence of turbulence (anomalous ion heating leading to a distortion of the ion velocity distribution function).

Electron heat transport dependence on plasma shape and collisionality

As the shape of the plasma cross-section influences a number of important plasma properties, experiments that can vary the plasma shape in a controlled way over a large range can lead to a better understanding of the physics determining these properties and, in practice, to identifying ways to control them. In 2006, the database on the dependence of the core energy confinement and electron heat transport on the plasma shape was further expanded. The data includes low-density EC heated plasmas with localized EC deposition just outside the q=1 surface, and a wide range of plasma collisionalities, v_{eff} (~0.15-2). This study was restricted to L-mode conditions, with a plasma configuration limited on the central column, to avoid a strong influence of the plasma edge stability and parameters on the results.

Practically no plasma current is driven by the EC system, as the injection geometry is adjusted to be perpendicular to the field line at each value of plasma triangularity. The electron heat transport is quantified experimentally via the electron heat diffusivity χ_e defined from a power balance relation, in which the heat flux accounts for the contributions of the EC heating, the ohmic, and the electron-ion equipartition power, quoted in order of importance.

Figure 2.1.9 confirms that for the large values of normalised temperature gradient characteristic of these experiments (R/L_{Te}>10), χ_e ape, and as the plasma triangularity is decreased (δ from +0.4 to -0.4). The measured scaling of χ_e with T_e, density and effective charge is compatible with χ_e depending on these parameters only through v_{eff}.
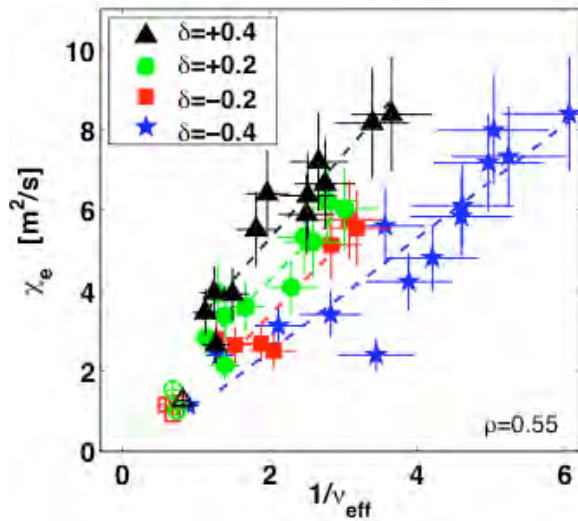
Fig. 2.1.9 *Experimental electron heat diffusivity at mid-radius as a function of plasma effective collisionality at four different values of plasma triangularity. Full symbols refer to EC-heated L-mode plasmas, while open symbols indicate ohmic plasmas, in which electron transport seems unaffected by plasma triangularity.*

No significant MHD activity is detected in these discharges and the sawtooth activity is observed to have only a minor effect on the pressure profile around mid-radius, where the experimental points are taken. In addition, the variations of the safety factor profile with triangularity are only minor, and are not observed to influence χ_e.

On the other hand, an important role of Trapped Electron Modes (TEM) in electron heat transport is suggested by linear gyro-fluid and gyro-kinetic models, which predict TEM to be the most unstable modes in these plasmas. Their stability and the transport that they cause are expected to depend on ν_{eff} and δ in a similar way as the measured electron heat transport.

Particle and impurity transport

The shape of the density profile will have a significant impact on the performance of ITER and fusion reactors. Peaked profiles can increase the fusion power, but may also lead to a deleterious impurity accumulation in the reactor core. The behaviour of particle and impurity density profiles is investigated in a number of different scenarios, including ECH and ECCD L-modes, eITBs and H-modes, with a view to improving our physics understanding and predictive capability for electron heated, ignited reactor conditions.

Fully ECCD sustained discharges in TCV show that density profiles can be peaked even in the absence of the Ware pinch. Similarly, helium discharges, in which neutral penetration by successive charge exchange reactions is quenched because of the low cross section for double charge exchange, show that density profiles peak without a core particle source. In addition, neutral penetration calculations using the KN1D and DOUBLE-TCV codes confirm that the experimental density profiles are too peaked, even in deuterium plasmas, to be explained by edge fuelling and diffusive particle transport alone. The combination of these observations provides the experimental proof that peaked density profiles may only be explained by anomalous processes.

Parametric scalings were obtained in L-mode, in which a wide range of operating conditions is easily achieved. The density peaking is found to scale with the peaking of the current profile and with the minor radius of ECH deposition for $P_{ECH}>0.5MW$. The density profile is observed to flatten with additional core electron heating, but this effect saturates for a total power exceeding the ohmic power by more than a

factor of three, as shown in Fig. 2.1.10. In contrast to L-modes, regimes characterised by reversed magnetic shear profiles and steady-state eITBs (see Section 2.1.1) do not show this profile flattening, even with central ECH. These results suggest that in a burning plasma, with strong core electron heating from fusion produced α's, the density profiles may remain peaked both with monotonic and reversed q-profiles, improving the fusion power output.

A concern for a reactor is that the large core electron heating by α's may destabilise TEMs, driving a thermo-diffusive outward particle flux, which may lead to partial or complete flattening of the density profile. This cannot be tested at JET, because purely ICRH heated H-modes in JET can only reach $\beta_N \sim 1$. However, purely electron heated H-modes with $\beta_N \cong 2$ and $T_e/T_i \cong 2$, recently obtained in TCV using 1.5MW of ECH (see Section 2.1.3), show only partial profile flattening and that significantly peaked profiles ($n_{e0}/\langle n_e \rangle \sim 1.5$ in TCV ELMy H-modes) persist in electron heated regimes at reactor relevant values of β_N, even when T_e is significantly larger than T_i.
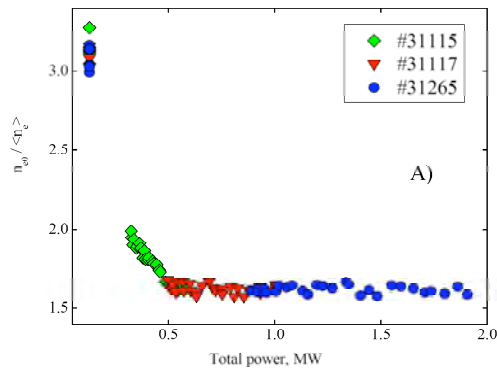
Fig. 2.1.10   *Density peaking as a function of the total power, indicating a clear saturation of flattening at high power. The plasma elongation, the minor radius and the toroidal magnetic field value are kept constant at $\kappa=1.6$, $a=0.25m$ and $B_T=1.44T$.*

Carbon ion density profiles were measured using the calibrated active TCV charge exchange spectroscopy system. Although the peaking of Carbon density profiles scales similarly to the peaking of the electron density profiles, for $\langle j \rangle/(q_0 j_0)<0.25$ (corresponding approximately to $q_{95}>4$), the Carbon ion density profiles, are notably more peaked than the electron density profiles, hence the normalized gradients $R\nabla n/n$ at mid-radius are more pronounced (Fig. 2.1.11). This effect, although reminiscent of neoclassical impurity accumulation, requires transport coefficients, which are clearly anomalous, for modelling using the STRAHL code.
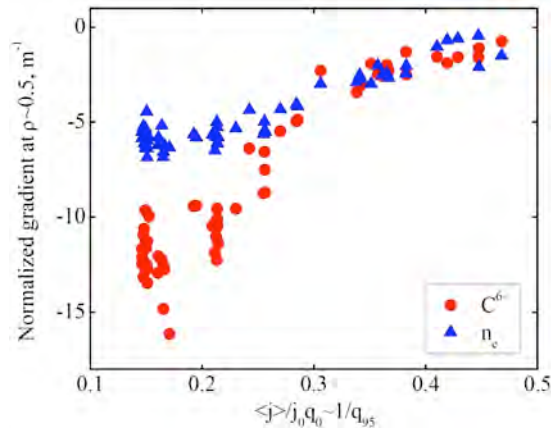
Fig. 2.1.11   *Comparison between the normalised gradients at mid-radius of electron and Carbon ion densities for different q_{95} values.*

2.1.5 Physics of ECH and ECCD, including Electron Bernstein Waves, and of suprathermal electrons

During the 2006 campaigns, the ECH and ECCD physics studies were slowed down due to some missing gyrotrons, particularly the third harmonic system. The main focus was the investigation of the physics of suprathermal electrons, generated by ECH/ECCD as well as by sawtooth crashes, and Electron Bernstein waves.

Suprathermal electron physics

The dynamics of suprathermal electrons is investigated thoroughly in TCV, as it is intrinsically related to the efficiency of the main heating and current drive systems, based on EC wave-particle interactions. A distinct suprathermal electron population is observed not only during strong EC heating, but also following sawtooth crashes. Different ECH-ECCD scenarios, including X3 vertical injection, are used to manipulate the electron distribution and study its dynamics. Low duty cycle EC bursts and coherent averaging of the relevant signals provide information on EC wave induced diffusion of fast electrons, their collisional slowing-down and pitch angle scattering in velocity space, as well as on their real space transport.

High field side measurements of the electron-cyclotron emission are interpreted assuming a simple bi-*Maxwellian* electron distribution, and that the relatively tenuous suprathermal component is optically thin. They provide the suprathermal density profile. The broadening of the profile due to radial transport and the decay in time, due to collisional momentum scattering, are clearly distinguished. By applying a simple diffusive model, a suprathermal diffusion coefficient and a typical decay time are extracted from the data. Very fast diffusion ($D>10m^2/s$) is generally found, although more complete (Fokker-Planck) modelling of the phase space transport of the suprathermal component is needed to fully unfold the system dynamics.

Suprathermal electrons are also observed in TCV in the absence of ECH and ECCD, during magnetic reconnection at the sawtooth crashes. Insight into the suprathermal electron dynamics and the magnetic reconnection process itself can be obtained by a careful analysis of this effect. These investigations were conducted in ohmic plasmas, without auxiliary heating, as well as with second harmonic ECH, but without ECCD, which would affect the generation of fast electrons by the reconnection process. In these experiments Low Field Side (LFS) ECE signals originate from the thermal bulk plasma, while High Field Side (HFS) ECE can detect the emission from a non-thermal electron population. The parameters of the fast electrons responsible for the non-thermal ECE are reconstructed by modelling the HFS ECE spectra using a bi-maxwellian electron distribution function, under the constraints imposed by the measured LFS ECE spectra.

Figure 2.1.12 shows the ECE profiles corresponding to times before and just after a sawtooth crash. The HFS and LFS ECE profiles coincide within experimental uncertainties before the crash, while after the crash the HFS ECE profile clearly exceeds the LFS profile just outside the sawtooth inversion radius. Since both radiometers view the same plasma volume, this deviation indicates the existence of non-thermal electrons, shortly after the crash, in the region close to the sawtooth inversion radius.
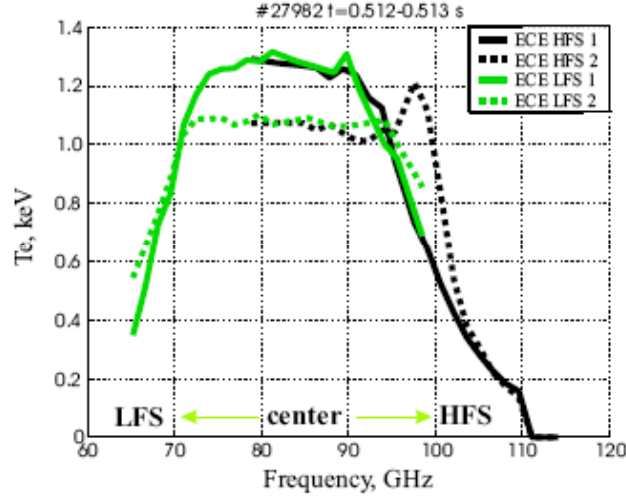
Fig. 2.1.12 *ECE profiles before (solid line) and just after (broken line) the sawtooth crash. In the latter case, HFS ECE exceeds the level of thermal ECE in the region close to the inversion radius.*

This conjecture is supported by soft X-ray measurements with different energy filters, shown in Fig. 2.1.13. At the top, the signal corresponds to photons in the energy range 1-10keV (47μm thick Beryllium foil), while at the bottom the signal corresponds to photons with energies 15-30keV (308μm thick Aluminium foil +350μm Beryllium foil). Naturally, high-energy photons are only emitted after each sawtooth crash, while during the ramp-up phase of sawtooth the signal is not higher than the noise level. The deviation of the non-thermal ECE from the thermal level exhibits a nearly linear dependence on the sawtooth crash amplitude, varied using ECH power.
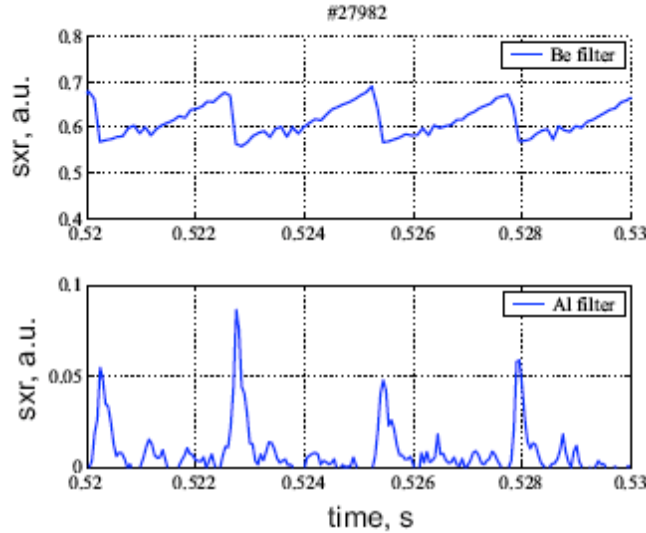
Fig. 2.1.13 *Soft X-ray signals obtained with different energy filters. At the top 47μm Beryllium foil, at the bottom 308μm Aluminium foil. Non-thermal spikes are visible after each crash.*
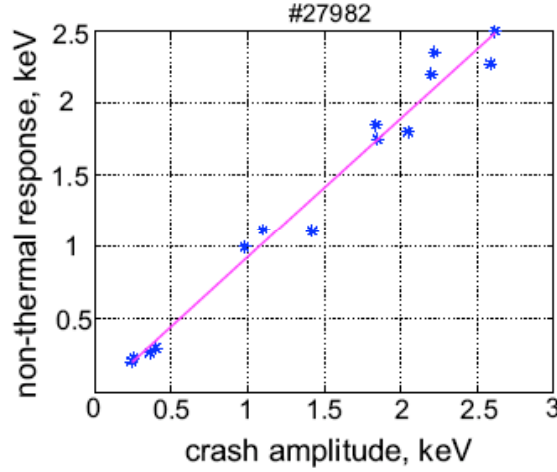
Fig. 2.1.14 *Nearly linear dependence of the deviation of the non-thermal ECE from the thermal level on the crash amplitude. Crashes with amplitude <500eV correspond to the ohmic plasma, while the crashes with larger amplitude correspond to the ECH plasma.*

Using Faraday's law, the change of the poloidal field flux provides an estimate of the toroidal electric field that can be created during the crash, which amounts to about 30V/m. According to the classical Dreicer formulation, this value is sufficient to create the measured number of non-thermal electrons and accelerate them to the energy of 15-30keV during 40μs, as observed.

TCV data demonstrates that the kinetic energy in the suprathermal electrons represents a significant part of the magnetic energy lost during reconnection associated with the sawtooth crash. Finally, the time evolution of the ECE spectra provides information about the effective radial diffusion of the fast electrons. The broadening of the suprathermal density profile during the crash and the decay of the non-thermal population after the crash give similar numbers for the effective radial diffusion coefficient, $D^{eff}_{st} \sim 25 \mathrm{m}^2/\mathrm{s}$. Radial diffusion dominates over slowing down, as the latter would give much longer characteristic relaxation times (1-2ms).

Destabilisation of MHD activity with modulated ECCD experiments

Preliminary experiments had been carried out on TCV in 2004 to study the dependence of the electron diffusivity on magnetic shear, which would be varied periodically using periodically alternated co- and counter-ECCD (a technique dubbed "Swung ECCD", or SECCD). In these discharges, in which low-amplitude sawteeth with a q=1 surface inside the normalized radius ρ_{inv}=0.03 were observed, a local decrease (≈40%) in the magnetic shear was associated with a decrease of the same amount (≈40%) in the electron thermal diffusivity at the normalized EC deposition radius ρ_{dep}=0.22.

New experiments were performed in 2006 with the goal of extending this study to a variety of deposition radii and amplitudes of the magnetic shear oscillations. Contrary to the old experiments, for these new discharges the q=1 surface (given by the inverse equilibrium code LIUQE) is located almost exactly on the deposition radius ρ_{dep}≈0.22. This prevents us from drawing direct conclusions on the effect of magnetic shear on transport, due to the interplay with the MHD effects associated with sawteeth. At larger deposition radii, most of the new discharges with ρ_{dep}=0.45 show an intermittent MHD activity, synchronous with the SECCD. Figure 2.1.15

shows a spectrogram from magnetic probes, in which an oscillation (5÷10kHz) appears during the co-injection period of SECCD with 2 gyrotrons in each cluster (shot #30675).

Although the effect of the MHD island on transport masks that of the shear, the details of destabilization/stabilization could provide very useful information on the mechanisms of Tearing Modes (and Neoclassical TM) stabilization by ECH/ECCD, which is of great importance for ITER applications.
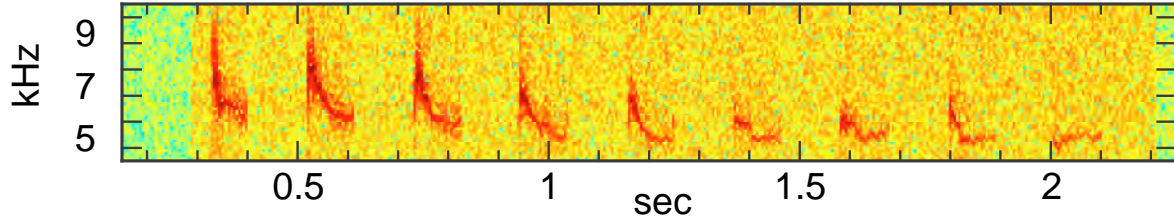
Fig. 2.1.15   *Frequency spectrum evolution in time of a MHD signal (Mirnov coils combination) for shot #30675. A mode is detected (frequency 5-10 kHz) during the co-injection period of SECCD.*

Electron Bernstein Wave Heating

Heating plasmas at densities above the second harmonic X-mode cut-off can lead to increasing both the plasma confinement and the pressure. The means to achieve high-density electron heating on TCV include quasi-vertically launched X3 ECH, and low field side injected Electron Bernstein wave heating (EBH). EB waves are not subject to X2 cut-off, hence can be used to circumvent the limitation to the plasma density that can be accessed by O- and X-mode EC. The O-X-B scheme is used on TCV, where the large densities and density gradients necessary for the O-X conversion are obtained in diverted H-modes with specific values of triangularity and edge safety factor, $\delta \sim 0.55$ and $q_{95} \sim 2.5$.

A 7th EC launcher was recently installed on an equatorial port, with a preliminary narrow-band polariser, and connected to the radiometer via a waveguide, allowing to sweep the angles during a discharge, hence a fast determination of the angular window for the EB emission (EBE) and for EBH. EBE measurements were obtained with the new launcher used in reception mode. The EBE appears on different frequency radiometer channels as the density increases, first on the low frequency channels, then on the higher frequency ones. MHD signatures like ELMs or sawteeth confirm the spatial origin of the signals. In a density rise (ELM-free) followed by a density drop (the first big ELM crash), the EBE signal first appears, then disappears, as expected.

The optimum injection angle for the O-X-B conversion is determined experimentally by varying the injection angle of EC waves modulated at a low duty cycle (6%) and measuring the microwave stray radiation. The measured value of the optimum angle is in good agreement with the predictions of the ART ray tracing and double mode conversion code.

EC waves modulated with a higher duty cycle (46%) are injected to measure the global and local EBH power deposition. An average absorbed power fraction of about 60% is obtained from diamagnetic measurements for densities well above the cut-off. The spatial distribution of the power absorption is determined experimentally from a Fourier analysis of the soft X-ray emissivity. The deposition radius is observed to be well inside the plasma cut-off and to match the value

predicted by ART to within the experimental uncertainties (Fig. 2.1.16). These modulated power deposition measurements are performed with a far off-axis deposition (ρ=0.7), to avoid strong sawtooth perturbations.
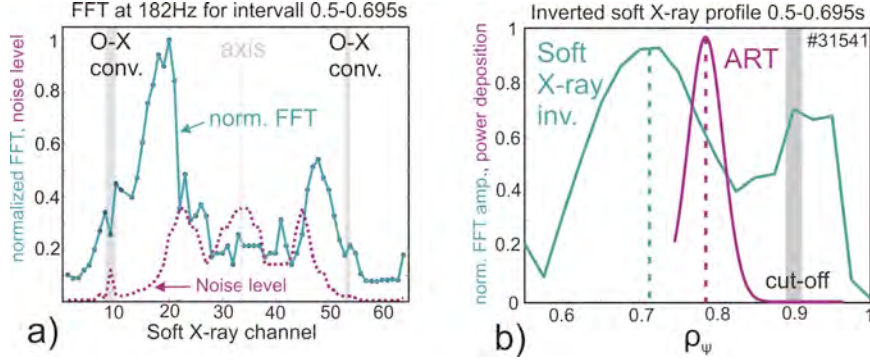
Fig. 2.1.16   *a) Profile of the normalized FFT amplitude of the line-integrated soft X-ray time traces at the modulation frequency of the injected EC waves at 182Hz (green). The noise level, due to sawteeth, is shown for reference (violet). b) Local soft X-ray emissivity oscillation amplitudes at the modulation frequency, derived by inverting the line-integrated soft X-ray chords signals (green). The resulting deposition profile (peaked at ρ~0.71) is compared with that of the deposited beam power calculated by the ART code (peaked at ρ~0.78). The residual power deposited outside the cut-off, visible in the edge soft X-ray signals, is presumably due to 2nd harmonic X-mode absorption of non-converted wave power subject to multiple wall reflections.*

To demonstrate EBH over periods longer than the confinement time, long pulses and a more central power deposition scheme (ρ=0.4) are used. A central temperature increase of up to 80eV is measured consistently by Thomson scattering and the soft X-ray absorber method. These results constitute the first demonstration of heating by O-X-B double mode conversion in an overdense, conventional aspect-ratio tokamak and motivate further investigations of the potential of using EBH or EBCD in H-modes of large tokamak devices.

2.2   *Theory and numerical simulation*

Theory and numerical modelling activities have been pursued in the areas of *ab initio* simulations of turbulence, analysis of tokamak MHD stability and transport, application of RF waves to tokamaks and stellarators, and characterisation of 3D magnetic confinement configurations.

2.2.1   *Physics underlying anomalous transport*

Nonlinear global gyrokinetic simulations

The global nonlinear gyrokinetic code ORB5 has been further upgraded and intensively tested for its noise-reduction capabilities and for its adaptation to massively parallel platforms of several thousand processors. A double parallelisation scheme has been implemented using domain decomposition in the

toroidal direction and domain cloning. The Poisson's equation field solver has been modified to treat only the discrete Fourier transform components that are retained in the field-aligned filter, resulting in a decrease by orders of magnitude of the required memory storage and a better scalability of computer performance for larger physical system sizes. The code performance has been tested on the EPFL IBM Blue Gene BG/L with up to 4096 processors and 6 billion particles, showing almost perfect scalability. Numerical convergence with the number of particles has been verified for various quantities: the time evolution of the turbulent heat flux, the energy spectrum of the modes and energy conservation. Comparisons of linear and nonlinear results of ITG turbulence for the "Cyclone" base case have been made with results previously obtained by other authors. These test results are very promising for further developments on the physics, in particular for the inclusion of non-adiabatic electron response and for simulations of larger plasma sizes. A global simulation of a "Cyclone" case with the ORB5 code (Figs. 2.2.1, 2.2.2) code takes about 5 hours on 1024 processors of BG/L and can also be run on smaller computer platforms such as PC Linux clusters using 32 processors in 2-3 days.
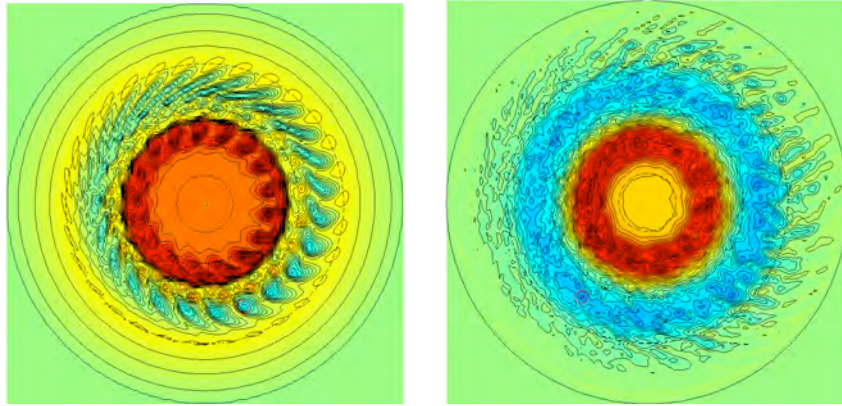
Fig. 2.2.1   *Poloidal cross-sections of ITG turbulence in a "Cyclone" case, showing the development of zonal flows that break the toroidal-ITG elongated radial structures. Contours of the perturbed electrostatic potential. Early (left) and late (right) in the simulations.*
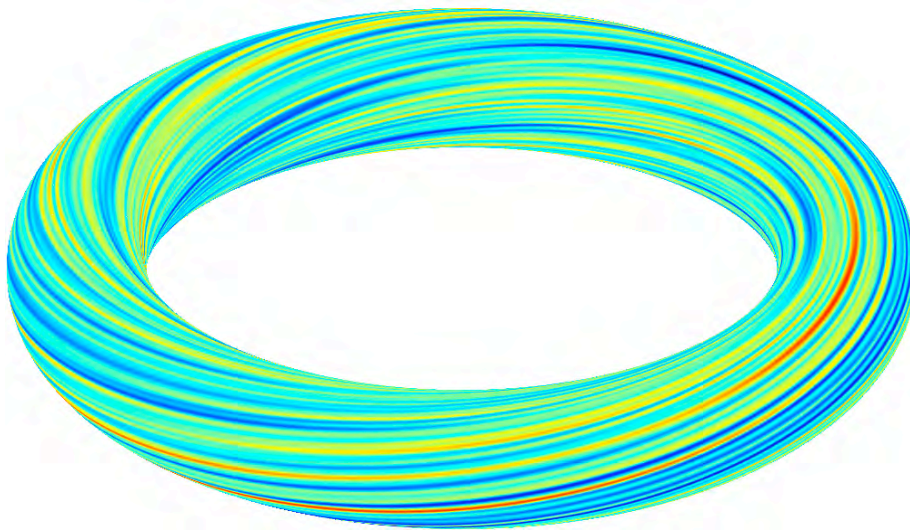
Fig. 2.2.2   *Contours of perturbed electrostatic potential for a "Cyclone" ITG turbulence case. View on a magnetic surface. The perturbations tend to align with the equilibrium magnetic field.*

The ORB5 code has been used for the investigation of zonal flow and geodesic acoustic mode physics in ITG driven turbulence and for ETG simulations. The scaling of ITG driven heat flux with the inverse plasma current has been confirmed in longer simulations using the optimised loading technique for numerical noise reduction. Verification of the analytical theory of Rosenbluth - Hinton for the residual zonal flow, geodesic oscillations frequency and damping rates have been successfully made. In collaboration with IPP Garching, ETG simulations in which numerical noise has been monitored and kept under control have been achieved. Global results show that heat diffusivity is comparable to that predicted by eulerian flux tube simulations. Work has started to include source terms in the global simulations which evolve consistently the temperature and its gradient profiles. The aim is to perform long time simulations with temperature gradients maintained well above marginality in a quasi steady state.

Two-dimensional simulations of the Kelvin-Helmholtz (K-H) instability have been carried out using different Semi-Lagrangian (S-L) algorithms. Various high order time integration schemes have been formulated and tested. This exercise has clearly illustrated the challenge of applying the S-L scheme to cases where time-splitting is not applicable, and for which the integration back in time along the trajectories must be carried out self-consistently in multi-dimensions.

A second order accurate leap-frog (L-F) time integration method was included in the 4-D gyrokinetic semi-lagrangian global code CYGNE in cylindrical geometry. This has shown somewhat better numerical accuracy (reduced overshoot effect, improved energy conservation) compared to the previously used predictor-corrector scheme. However, at later stages of the simulations this L-F integration led to a numerical instability. It is presently being investigated whether coupling of odd and even time steps solves the problem. Other numerical improvements in the S-L code CYGNE include the development of more general software modules for working with splines.

The alternative of considering a purely eulerian approach to solving gyrokinetic equations has been investigated. In this case, space and time discretisations are carried out separately (method of lines). In particular, the ENO (Essentially Non-Oscillatory) scheme, which tends to reduce the overshoot problem, has been studied for handling the space discretisation. While successful in a simple 2-D case, this study has pointed out the serious challenges of generalizing this type of spatial discretisation to the curvilinear tokamak geometry. It was thus concluded that the semi-lagrangian approach was to be pursued, despite its own difficulties.

Electron transport and current profile modelling

Electron confinement and plasma current density profile were found to be strongly related in a variety of dedicated experiments in several tokamaks. In TCV, it was shown that the electron confinement improves by modifying the steady-state current density from peaked to hollow. Such behaviour is believed to be due to the suppression of plasma turbulence in the presence of a negative magnetic shear and a finite Shafranov shift. Switched ECCD has been done in TCV L-mode plasmas, i.e. driving alternatively co- or counter-ECCD at constant total input EC power during a single discharge. The idea is to decouple the contributions of specific heating oscillations from those of the current density tailoring, so that any modification in the transport properties of the plasma is to be ascribed only to the shear profile modulation realized by the ECCD switching. Modelling of the plasma current density profile has been carried out with the ASTRA code employed in both

interpretative and predictive modes, with two shear-dependent transport models. In this approach the modulation of ECCD is the only actuator for the transport properties modifications. The plasma response has thus been studied in the presence of Switched ECCD to understand the differences in time scales and transient behaviours between the various models employed and with different experimental conditions, such as changes in period and deposition location, confirming the synergy between electron transport and magnetic shear, both of which are modulated around the EC deposition region. This modelling also allows us to completely decouple the effects of the current profile modification from those of slight plasma heating imbalance or non-constant plasma elongation.

Particle transport modelling

Various theoretical models for particle transport have been analysed in order to help understanding the behaviour observed experimentally. In particular the role of trapped electron modes (TEM) has been investigated. TEMs tend to decrease density peaking through an increase of an outward thermodiffusive type transport. At this stage, the aim is to understand the main mechanisms responsible for inward or outward density pinch effects.

Electron internal transport barriers (eITB) in TCV have been analysed from the point of view of particle transport to study the behaviour of the density profile in these advanced scenarios. The main result is that the normalized density gradient scales as 0.5 times the normalized electron temperature gradient, with no clear dependence on the q profile. Therefore a peaked density profile is observed despite the strong electron heating, contrary to what is normally observed in ohmic L-mode plasmas. Transient phenomena in eITB have been analysed and the particle diffusivity has been estimated as 10 times higher than the neoclassical prediction, indicating that anomalous transport is still active, although at lower levels, i.e. 5-10 times smaller than diffusivity in ohmic L-modes. Modelling with gyrofluid and gyrokinetic codes show that the mechanism that sustain this thermodiffusive particle transport might come from the non-adiabatic passing electron response to parallel electrostatic fluctuations.

Characterisation of bursty behaviour in the tokamak edge

Excellent agreement has been found between TCV and 2D fluid interchange simulations of plasma fluctuations, and especially the bursty behaviour of plasma "blobs", in the scrape-off layer. Analysis of the time series from the simulations demonstrate the density and temperature fluctuations conform closely to the Gamma probability density functions (pdf), over a wide range of parameters. The reason why the experiment and simulations conform to Gamma statistics is not yet understood, but the results provide important evidence of universality in the plasma edge.

2.2.2   RF waves

Alfvén and ICRF waves in 2D and 3D configurations

The development of the LEMan code for the investigation of low frequency wave propagation and absorption in magnetically confined plasmas including warm plasma effects in the limit of small Larmor radius is continued. The exact computation of the parallel wave vector in 2D and 3D systems is complicated due to

its dependence on position and mode spectrum. An initial comparison with the 2D PENN code has been explored for different approximations for the parallel component of the wave vector. Improved matrix construction and storage algorithms have been implemented in LEMan that significantly reduce the memory requirements to allow calculations in the ion cyclotron frequency range in stellarator geometry to become tractable.

2.2.3   Operational limits

Kinetic effects on MHD modes

Studies continue to identify kinetic modifications to modes which are essentially of MHD origin. Pressure anisotropy has recently been considered in the equilibrium, in linear fluid perturbations and in the drift orbits of particles (see 2.2.4). While pressure anisotropy in the equilibrium and fluid perturbations have been treated analytically, an analytical treatment of the average orbit drifts in an anisotropic equilibrium had until recently not been undertaken. The new solution for trapped particles demonstrates a significant difference in the drift frequency for the following three cases: isotropic, parallel anisotropic, or perpendicular anisotropic. In parallel to this the VENUS code has recently been generalised to include pressure anisotropy following the hamiltonian formulation described in Section 2.2.4. Early comparisons between the equilibrium analytical work and the VMEC code, as well as the orbit analytical work and VENUS, are encouraging. The ultimate aim of this work is to develop a delta-f code which can evaluate linear and non-linear kinetic corrections to MHD modes in realistic equilibria.

Sawtooth behaviour and internal kink mode

The bi-maxwellian model employed in VMEC and TERPSICHORE has been compared favourably with the Fokker-Planck code SELFO used to post-process ICRH distributions of fast ions in JET discharges. A scheme has been implemented which obtains a best fit of the SELFO data in terms of the model distribution function. Very good fits are obtained for JET demonstration discharges which are of particular interest for testing sawtooth control in the presence of energetic trapped ions in the core. The fits of the distribution function, together with current drive profiles obtained from SELFO simulations, have enabled reproduction of the sawtooth period over ICRH and localised ICCD discharges.

Analytical techniques have been advanced in order to accurately evaluate the stability of the ideal internal kink mode. This long-standing problem, of particular difficulty in realistically shaped tokamak geometry, has been undertaken within the frame of the integrated tokamak modelling group, and a collaboration with the University of Uppsala. Accurate calculations of the internal kink mode stability are required, over a large number of time varying parameters, within transport codes in order that sawtooth oscillations can be correctly included. Improvements have been made to terms responsible for the effects of plasma cross section, inverse aspect ratio, beta, and the collisionless kinetic effects of energetic ions - especially alpha particles.

Edge Localised Modes (ELMs)

The ideal MHD global stability code KINX, which treats the plasma consistently up to the magnetic separatrix, has been applied to the analysis of edge-localised

instabilities in the TCV tokamak. The studies have focused on plasmas in which a high resolution Thomson diagnostic provided good quality data in the pedestal region, in ohmically heated discharges. The results indicate that the experimental profiles in between ELMs are such that the plasma is below the pressure limit set by high-n ballooning ideal MHD modes and the current limit set by edge localised external kink modes. This is an indication that in TCV ohmic discharges the ELM triggering mechanism is probably not due to ideal MHD limits.

The stability of edge localised modes in TCV and Asdex-Upgrade proposed experiments with applied boundary deformation and different patterns of plasma movements was analysed using the free boundary code SPIDER integrated with the discharge evolution code DINA-CH. The stability boundaries of edge kink/ballooning modes have been found to be mostly affected when the deformation of the plasma boundary has a large local curvature on the outboard side of the plasma cross-section.

In support of planned JET experiments aiming at ELM stabilization the ideal MHD stability was investigated for several optimized shear equilibria having a large current density at the separatrix. The results are in agreement with the general scaling for the current driven edge kink modes: the modes with toroidal wave number n>5 were found to be unstable due to the large values of the normalized current density at the separatrix $J/<J>$, where $<J>$ is the current density average over the plasma cross-section.

Neoclassical tearing modes (NTM)

A detailed study of the various effects of NTMs expected on ITER and a discussion of the best strategies for NTM control has been done. The present values of the upper launcher design have been used as baseline values for the studies, that is a deposition width $w_{cd}{\sim}5cm$ and a value of $\eta_{NTM}\,w_{cd}=6.3$. We have used a recent paper on cross-machine comparison of ECCD stabilized NTMs to calibrate the various free parameters in the modified Rutherford equation. Then, we have analysed the effects of varying the expected marginal island width, from 2 to 6cm, the main stabilizing model, CW versus modulation, for w_{cd} values of 2.5, 5 and 10cm. It showed that in most cases 13MW should be sufficient to fully stabilized NTMs in ITER.

The impact on the value of Q has also been analysed. The main result is that a viable scenario requires that less than about 10MW should be used for NTMs control. For larger values of the power, the Q values decreases as much due to the additional auxiliary power as due to the loss of confinement caused by the NTM. It was also shown that partial stabilization might be useful.

The time to stabilize the mode and the relation to the sawtooth period has been discussed, since the sawtooth crashes are expected to be the main cause for NTM trigger. If the time to detect and act on the mode is too long, it is as efficient to just keep a continuous small island in the plasma. Another important factor which results from this study is that one needs to be clearly above marginal to fully stabilize the mode. Indeed, if the power is just sufficient to stabilize the mode, dw/dt will be negative but small for a range of island widths, typically around 10cm. Therefore if the initial island width is larger or equal to this range, there will be a certain time with |dw/dt| small, which can result in a delay of more than 100s in ITER to fully stabilize the mode.

2.2.4 *Optimization of 3D configurations*

Neoclassical transport in 3D stellarators

Further improvements in the VENUS delta-f code have been undertaken in the investigation of neoclassical transport properties in stellarators. Several ideas dealing with the problem of lost particles with growing weights in the long mean free path regime have been explored. Test of implicit symplectic[*] integration techniques have also been evaluated.

3D anisotropic pressure stellarator equilibria

The implementation of an anisotropic pressure model based on an energetic particle bi-maxwellian distribution function in a fixed boundary version of the 3D VMEC code has been applied to a 10-field period Heliotron and a 2-field period quasi-axisymmetric stellarator. For parallel pressure much larger than its perpendicular counterpart, the corresponding pressures do not vary significantly around the magnetic surfaces. For off-axis hot particle deposition with large perpendicular anisotropy, the energetic particle density structure correlates more closely with the perpendicular rather than the parallel pressure.

Ballooning stability in stellarators with fluid and non-interacting energetic particle models

The local stability modules of the TERPSICHORE code have been adapted to model the effects of hot particles using the Kruskal-Oberman energy principle formulation (fully interacting hot particle model) and the rigid non-interacting hot particle energy principle formulation. In the absence of hot particles, the ideal MHD stability results are recovered. For equal hot particle temperatures, the rigid energetic particle model predicts, as expected, more stable ballooning eigenvalues than the fully interacting model.

J-parallel optimised quasi-isodynamic stellarators with poloidal quasi-symmetry

Further optimization of a N=12 field period quasi-isodynamic stellarator configuration has been achieved with MHD stable beta values near 20%. The configuration retains good long-time collisionless confinement of alpha-particles, small neoclassical transport in the long mean free path regime and small bootstrap current. A N=6 period configuration has also been identified with aspect ratio 12 and a beta limit of 8.5%. Work is under way to calculate free boundary equilibria and coil parameters for some optimized stellarator configurations.

Guiding centre drift orbits for energetic particles

A relativistic hamiltonian guiding centre drift orbit formulation has been developed to treat energetic particles in the background of an anisotropic pressure equilibrium state. Perturbed electromagnetic fields constrained to have only a finite component of the vector potential along the equilibrium magnetic field lines are allowed together with small but arbitrary electrostatic perturbations. A direct evaluation of

---

[*] symplectic: phase-space area preserving

the relativistic drift velocity recovers the equations of motion obtained from the hamiltonian formalism except for ignorable higher order terms.

Kinetic ballooning stability with anisotropic energetic electron layers

Kinetic ballooning mode equations have been derived from the gyrokinetic equation in the intermediate frequency regime of fluid ions, adiabatic thermal electrons and rigid hot electrons. In the fluid MHD limit, the thermal pressure gradients dominate the instability dynamics and the equation obtained combines features of the fluid equations derived from the Kruskal-Oberman and rigid hot particle energy principles.

2.2.5   *Tokamak discharge simulation*

A tokamak discharge simulator which consists of a free-boundary evolution code, DINA-CH, and an advanced transport modelling code, CRONOS, have been developed for the study of free-boundary plasma evolution. In the combined tokamak discharge simulator, DINA-CH calculates plasma current diffusion and controls plasma current, position and shape. The diffusion of plasma current is self-consistently calculated, considering the movement of deformable plasma and the electro-magnetic responses between the plasma and surrounding toroidal conducting structures. The plasma current, position and shape are actively controlled by an integrated controller which actuates input voltage signals to the poloidal field coils. CRONOS calculates particle and heat transport using its advanced transport and source models. The equilibrium required for the transport calculation of CRONOS is directly substituted by a free-boundary equilibrium of DINA-CH. This method is more efficient and stable than the equilibrium reconstruction method applied at the beginning of this work. After resolving another problem, additional time-step delay in data exchange between two codes, ITER H-mode and hybrid mode are simulated for the flat-top phase of tokamak operation.

During the simulation of the ITER hybrid mode, sudden vertical jumps of the plasma magnetic axis are observed, when the plasma has a more delicate condition such as a high bootstrap current at the edge region of plasma. This is a numerical instability and can be suppressed at the expense of computational performance by decreasing computational grid size. For the improvement of computational performance, the control of the time-step which determines the update interval of external plasma heating and driven current profiles is suggested. When the time-step is controlled, however, unphysical changes of plasma heating and driven current profiles are observed in some modules. The examination of this problem is in progress with the collaboration of the CRONOS authors.

Recently, the effect of free-boundary equilibrium on plasma heating and driven current profiles is studied for the ITER hybrid mode. ICRH, LH and NBI powers are stepped up or down and the feed-back controls for plasma position and shape are turned on. The resultant disturbances are not large enough for the controller to fail. Therefore, the free-boundary effect which non-linearly coupled with the plasma heating and current drive does not seem to be significant for the ITER plasmas.

A control algorithm is tested for the control of plasma shape using an identification method of linear plasma model from repeated simulations. A similar and more refined control algorithm was already tested by the other group for the kinetic profile control of JET plasmas and showed that it works for the reference plasma state. In both cases, however, the constant control matrix generated from a

stationary state of certain plasma may not work correctly for different plasma states. [Kurchatov Inst., Moscow, RU; TRINITI Inst., RU; CEA Cadarache, F]
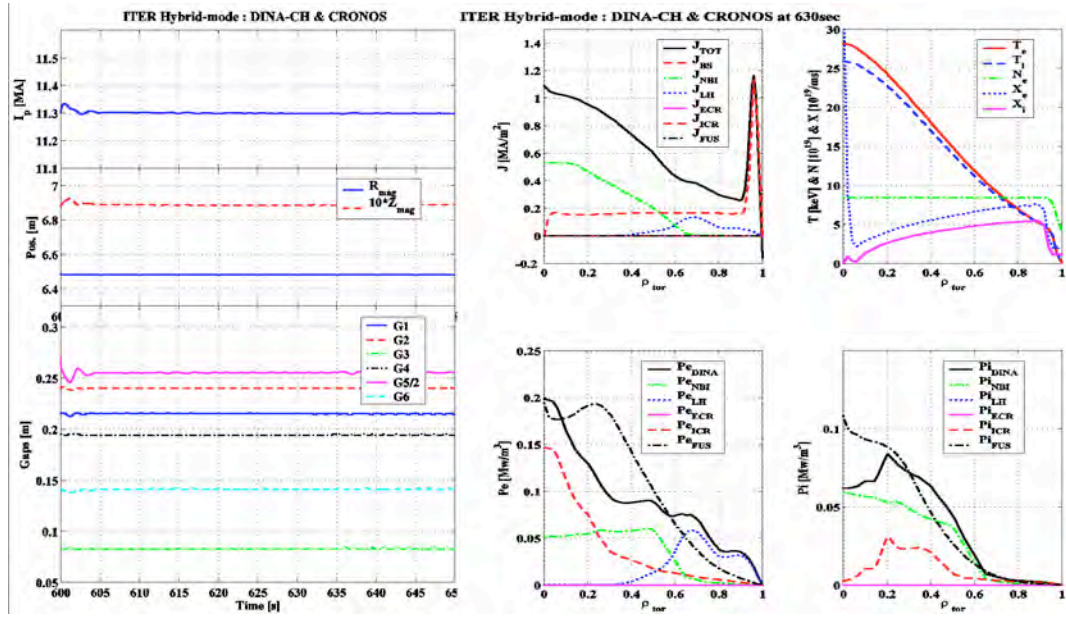
Fig. 2.2.3   *Simulation results of ITER hybrid mode plasma. Time traces of plasma current, magnetic centre position and gap measurements (left) and profiles of plasma currents, densities, temperatures and heating at 630 sec (right) for 6 independently controlled gaps G1…G6.*
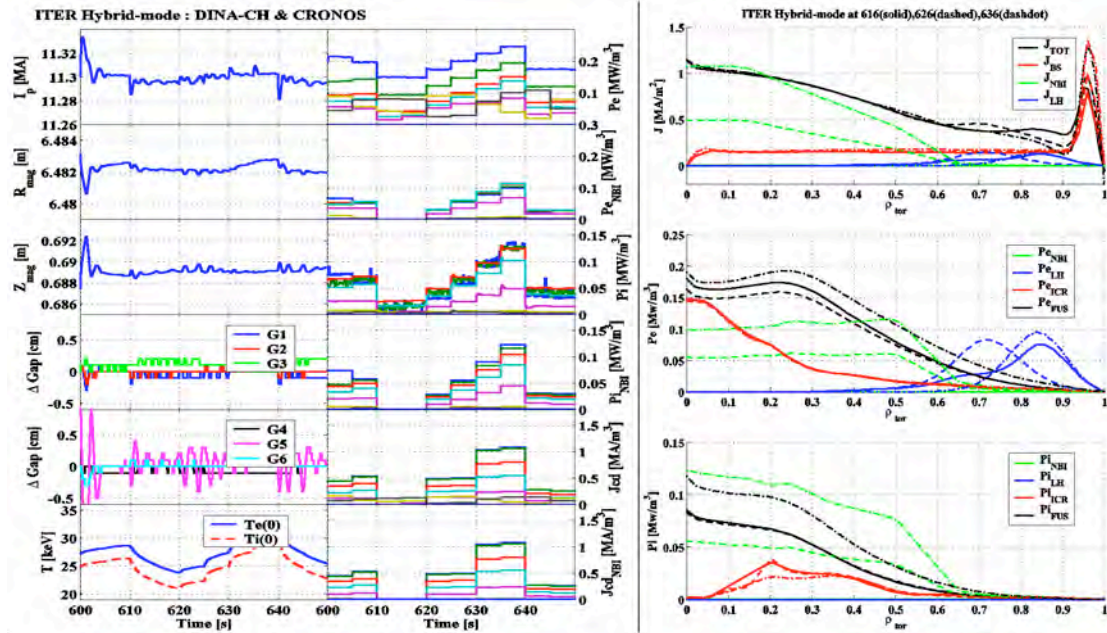
Fig. 2.2.4   *The effect of free-boundary equilibrium on plasma heating and driven current profiles. NBI power is stepped up or down (33MW@610s, 33MW@620s, 66MW@630s and 16.5MW@640s). Time traces of plasma current, magnetic centre position, gap changes, central temperatures, heating and driven current (left) and the profile changes of plasma heating and driven current at different power levels (right).*

2.2.6   Integrated Tokamak Modelling

The CRPP has contributed to the EU-ITM Task Force activities in the Projects CPP (Code Platform Project), DCP (Data Coordination Project) and IMP#1 (Equilibrium and stability). Activity has continued at a reduced level on the development of the data schemes. The generic definition of ITER in the EU ITM TF data was used to generate all the electromagnetic parameters for DINA-CH simulations and a time slice was loaded into the EU ITMTF data structures. These data were analysed in collaboration with CEA Cadarache, resulting in a full reconstruction of this simulated ITER discharge. The loop was therefore closed for the first time. This mechanism is presently being used to populate a database with a wide variety of ITER simulations using the DINA-CH code.

We have progressed in the integration of the equilibrium codes CHEASE and CAXE, and in the ideal MHD stability code KINX using the MDS+ data tree structure for the interfacing with the ITM database. Issues related to the necessary accuracy of equilibrium magnetic surface coordinates and mapping have been identified. The need of a unified plasma surface geometry description was recognized.

Work is in progress to test the integration of ITER equilibrium and stability computations. Contributions have also been made to the problem of internal kink stability in the presence of fast ions (see 2.2.3).

2.3   Operation of a specialised basic plasma physics device, TORPEX

The activities of the CRPP Basic Plasma Physics group are focused on fundamental aspects of the physics of fluctuations and turbulence, and related transport phenomena in toroidal magnetised plasmas. The experiments are conducted on the TORPEX (TORoidal Plasma Experiment) device, characterized by low plasma densities and temperatures, allowing high-resolution measurements of plasma parameters and wave fields throughout the plasma cross-section. Plasmas are confined by a toroidal magnetic field up to $B_T=0.1T$, and a smaller vertical component, $B_v \leq 50mT$, corresponding to a simple configuration incorporating the main ingredients for drift wave instabilities and turbulence, namely pressure gradients and magnetic field line curvature. Highly reproducible discharges of Argon, Hydrogen and Helium with density and electron temperature in the range $n_e \sim 10^{16}\text{-}10^{17}m^{-3}$ and $T_e \sim 5\text{-}10eV$ are driven during more than 2s by microwaves at f=2.45GHz, in the electron cyclotron (EC) range of frequencies. Up to 50kW of microwave power is injected from the low field side in the ordinary mode and can be modulated at frequencies up to 60kHz. Parameters such as the neutral gas pressure, the location of the EC resonance and the amount of injected power can be varied to control density and temperature profiles.

Progress was made in 2006 in a number of areas, mostly in the simple magnetised plasma configuration (in the absence of rotational transform), including:

- completion of the study of the plasma production mechanisms by investigating the phase space distribution of suprathermal electrons;
- first attempts at measuring different orders of cross-field particle fluxes;
- a complete identification of the character of the naturally occurring fluctuations, namely in terms of their dispersion relation;

- investigation of the nonlinear development of the instabilities, and its link with spectral cascade processes;
- the demonstration of the possibility of a controlled excitation of drift waves using an electrostatic antenna;
- an investigation of the universal properties of the time series of turbulent fluctuations;
- the development and application to TORPEX data of a method for the probabilistic analysis of turbulence structures based on 2D plasma imaging data.

In addition, we obtained the first characterisation of the transition in the turbulence properties as the flux surfaces are closed in the plasma by using an ohmic transformer, driving a toroidal plasma current.

During the year, part of the team effort was dedicated to conducting design and preparatory work for physics activities to investigate the interaction between suprathermal ions and drift wave turbulence, and for upgrades to the machine control software and to the diagnostics, in particular to improve spatial resolution in the instability source region and to develop a fully non-perturbative optical imaging system. A fast framing visible camera (Ultima APX-RS by Photron, with up to 250kframes/s) was purchased, for combined use on TORPEX and TCV. Initial preparations were undertaken for the implementation of Laser Induced Fluorescence, which could add ion velocity resolution to the reconstruction of snapshots in time of the spatio-temporal fluctuations and turbulent structures. A Java based interface has been developed to control the TORPEX discharge cycle, including the data acquisition. The new interface, dubbed TorpControl, is faster than the Matlab based control system and is now routinely used in the daily operation of the device.

The results obtained in the different research areas and the main technical developments are highlighted below.

2.3.1 *Measurements of electron distribution function and suprathermal electron dynamics*

The local properties of the electron energy distribution function are investigated both to complete a reconstruction of the details of the plasma production mechanisms by waves in the electron cyclotron frequency range, and to test the assumptions usually made to interpret electrostatic probe data. The electron energy distribution function is measured by means of a time-resolved electrostatic energy analyser. The measurements indicate that suprathermal electrons are accelerated to different energies at the electron-cyclotron and upper-hybrid resonances (see Fig. 2.3.1). Electrons from the upper-hybrid resonance have higher energies and can be represented by a secondary maxwellian energy distribution function.

The electron distribution function is found to be invariant with respect to experimental parameters such as the neutral gas pressure, the magnetic field configuration and the injected microwave power. The effects of the suprathermal electrons on the measurements performed with Langmuir probes is explored. We find that the electron temperature may be over-estimated by up to 50% when a few percent of electrons are in the high energy tail produced by the plasma-wave interaction occurring at the upper-hybrid resonance.
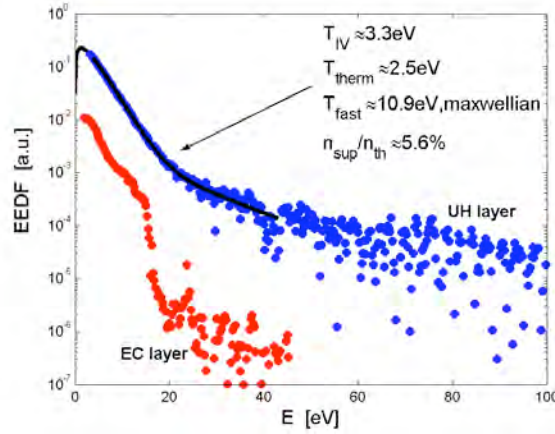
Fig. 2.3.1 *Electron energy distribution function (EEDF) measured at two different radial locations at the midplane, corresponding to the electron-cyclotron (EC) and upper-hybrid (UH) resonances. Note the enhanced tail in the EEDF produced by the interaction of the injected microwaves with the plasma at the UH resonance, which is not observed at the EC resonance, indicating that different plasma-wave mechanisms are at play in the two resonant regions.*

2.3.2   Particle transport studies

Techniques based on the Fourier analysis of the plasma response to a sinusoidal modulation of the injected microwave power are applied to quantify the particle flux responsible for the particle loss. The spatial profile of the plasma response to the modulated power is interpreted in terms of a continuity equation for the perturbed density based on a convective model. The results are related to the fluid drifts originating from the magnetic field curvature and from the finite pressure gradients, estimated from the time average plasma profiles.

The relevant terms in the continuity equation are identified from a Laplace analysis of the plasma response to a fast square modulation of the injected power. It is found that the density perturbation mainly arises from a localised increase of the ionisation term. A perturbation of the convective velocity term is observed for a steep increase of the injected power, due to the transient modification of the plasma potential.

A dedicated experimental programme has been initiated to identify and quantify the different contributions to the particle cross-field flux. The particle fluxes associated with the creation of the quasi-equilibrium are compared with those related to fluctuating density and potential, both locally and in conjunction with macroscopic fluctuation structures. These measurements are complemented by a 2D reconstruction of the heat flux from measurements of the plasma potential and electron temperature fluctuations, performed using Conditional Average Sampling (CAS).

With a convenient choice of the trigger condition, the CAS technique is also used to investigate events that lead to the detachment of high density, macroscopic plasma structures that propagate across the magnetic field carrying particles and heat. The link with similar phenomena observed in the tokamaks scrape-off-layer can thus be investigated.

To achieve these goals, the hardware control of the microwave source installed on TORPEX has been conveniently modified. A feedback loop, which enhances the stability properties of the microwave source, has been introduced in the original control system. The discharge duration has been increased, and a safe continuous operation of the microwave source is now possible.

2.3.3   Identification of drift-interchange instabilities

Low frequency electrostatic instabilities have been extensively studied in a variety of different experimental scenarios and characterized using 2D profiles of frequency and amplitude of density and potential fluctuations. They generally develop in the bad curvature region, at the position of maximum pressure gradient and are observed to propagate in the laboratory frame along the **E×B** direction. Their phase velocity in the plasma frame, when the Doppler effect is taken into account, is consistent with the direction and magnitude of the electron diamagnetic velocity, as shown in Fig. 2.3.2.
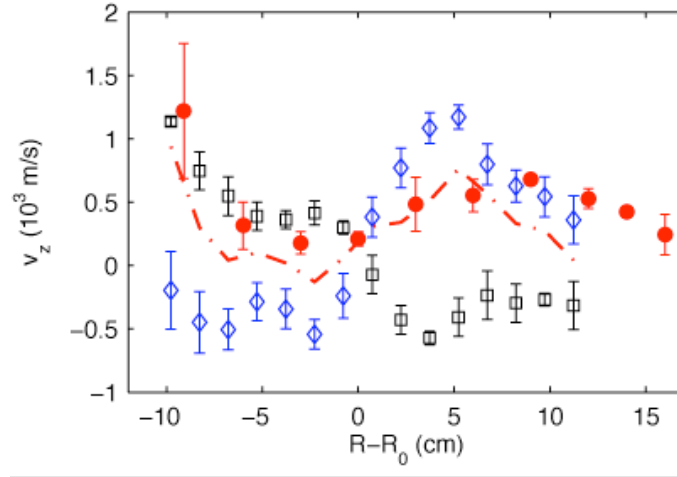
Fig. 2.3.2   *Measured phase velocity of the instability, ω/k_z (red circles), compared to diamagnetic velocity, $v_d=T_e/BL_n$ (black squares) and the E×B velocity, $v_E=E/B$ (blue diamonds), measured at midplane. The dashed-dotted line is the (vector) sum of v_d and v_E.*

An unambiguous identification of the nature of instabilities was obtained in an experimental configuration with low level of fluctuations, where the frequency spectrum is dominated by coherent modes. The dispersion relation, measured in direction parallel and perpendicular to the ambient magnetic field, is consistent with that calculated on the basis of a linear, kinetic model for drift-waves in slab geometry. It is proven that the curvature of the magnetic field is the dominant mechanism for the destabilization of these modes, which can therefore be identified as drift-interchange instabilities.

2.3.4   Nonlinear development

Measurements performed across the whole plasma cross section indicate that the wavenumber and frequency spectra are relatively narrow at the location where the instabilities are generated, but tend to broaden significantly during propagation, leading to the development of turbulence. Initial results obtained using high order

spectral analysis, performed at different positions along the convection of the instabilities, indicate that the transition from a coherent to a turbulent spectrum may be due to three-wave interaction processes. At the location where instabilities are generated, the dominant nonlinear coupling appears to be between the fundamental mode and higher order harmonics. Along the convection path, the spectral regions in between harmonics are rapidly filled in and the range of nonlinear interactions extends to fluctuations with frequency much larger than the fundamental. As the measured dispersion relation along the direction of propagation of instabilities is linear, these observations can be extended from the frequency to the wavenumber domain. The observed direction of power transfer can therefore be interpreted as a forward cascade in wavenumber, from large to small scales, as illustrated in Fig. 2.3.3. Work is in progress to identify the nature of the underlying nonlinear coupling mechanism.
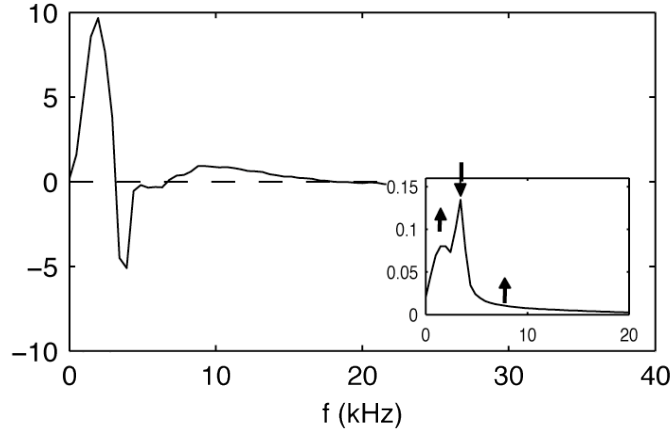
Fig. 2.3.3   *Variation of spectral power of density fluctuations, due to quadratic coupling, measured at midplane, at R-R_0=10cm, with two probes with vertical separation 0.6mm. The insert shows the power spectrum measured at the same position. Arrows indicate an increase or loss of energy due to quadratic coupling at the corresponding frequency.*

2.3.5   *Antenna excitation of drift waves*

Experiments on drift wave excitation have been conducted as a first step toward controlling drift wave dynamics on TORPEX. The excitation is performed using an antenna consisting of four identical rectangular metallic electrodes (30mm along B and 8mm high) lying in the vertical (poloidal) direction and driven with the same frequency and a relative phase that can be chosen in the $[-\pi, +\pi]$ range. This antenna is mounted on a movable system that allows for radial positioning. The vertical separation between each adjacent electrode is 20mm.

A multi-peak density response is detected using arrays of Langmuir probes covering the whole plasma cross-section, whose signal is detected synchronously with the antenna drive. Using the electrostatic dielectric function and the antenna k-spectrum, one of the peaks of the density response to the antenna excitation is identified as a weakly damped drift wave mode (Fig. 2.3.4). The other strongly damped peaks are compatible with the plasma dielectric response, but do not correspond to roots of the drift wave dispersion relation.
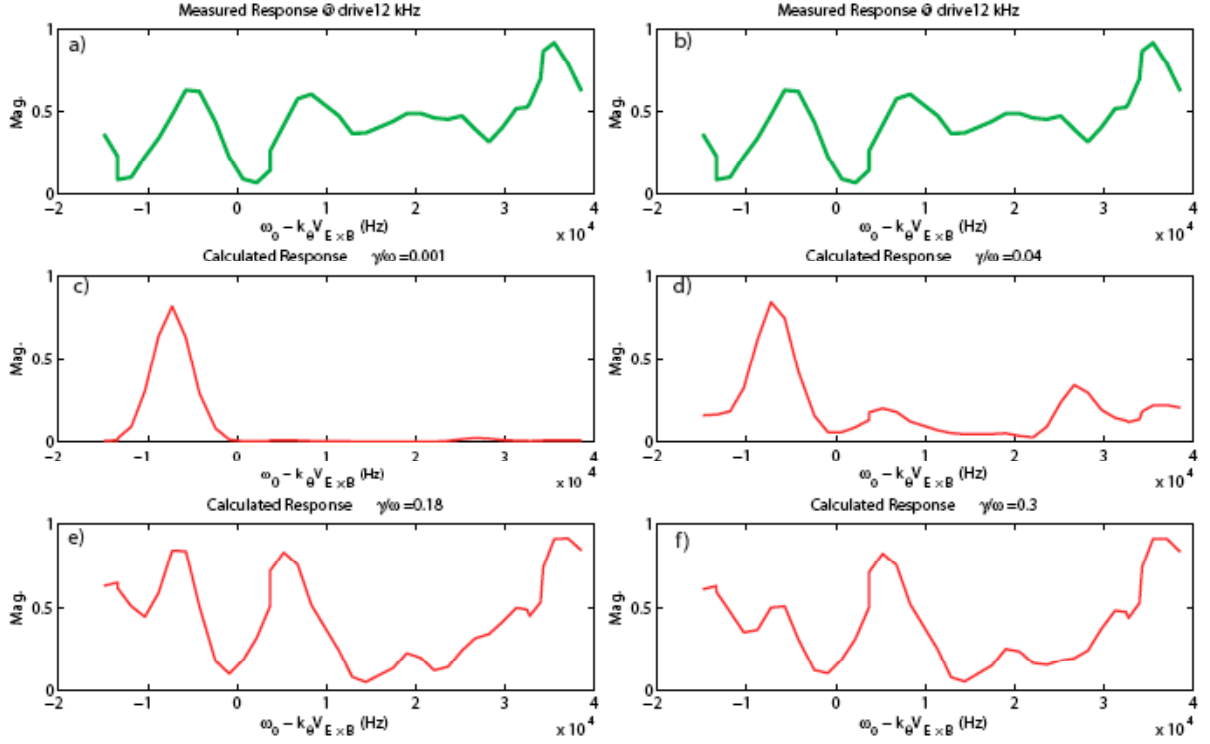
Fig. 2.3.4 *Measured and calculated density responses to the antenna excitation. Figures a) and b) represent the observed density response. Figures c) through f) show a summary of the calculated response function for various damping rates. Note that these figures show the normalized responses. The largest peak in amplitude is 10dB greater than the background fluctuation. We refer to this background fluctuation as the naturally occurring coherent fluctuation when no drive is applied to the antenna.*

2.3.6 Universal statistical properties of drift-interchange turbulence in toroidal plasmas

A significant effort is dedicated in plasma physics to finding universal aspects in the statistical description of plasma turbulence, to improve our understanding of the impact of different types of micro-instabilities on the macroscopic plasma behaviour and to generalise the results obtained on different individual machines. We have addressed this question by looking at statistical properties, like the probability density function (PDF), that are common to a large number of electron density signals (~10000), taken across the entire plasma cross-section and over a broad range of experimental conditions. For all the signals, the skewness (third moment of the PDF) and the kurtosis (fourth order moment of the PDF) are estimated and plotted against each other (see Fig. 2.3.5). An important result is that a significant fraction of the signals (~30%) are characterized by a negative skewness. In TORPEX, measurements extend to regions where fluctuations may result in a depletion of density, yielding experimental distributions with a negative skewness, conversely to tokamak plasmas where measurements with Langmuir probes can only be done at the edge.

A first universal feature is the unique and precise relationship that links the experimental skewness and kurtosis. The data in Fig. 2.3.5 is least-square fitted by

the quadratic polynomial: K=(1.502±0.015)S^2+(2.784±0.019). This relation allows us to rule out all PDF families that cannot provide such a quadratic poynomial together with these coefficients. As a consequence, a second universal character of drift-wave turbulence is identified: all the PDF of the density fluctuations at all locations can be described by the same analytical distribution. This is a special case of the general Beta distribution, akin to the form of the Gamma distribution, depending on the sign of the signal skewness. Having established the existence of a universal PDF shape, we addressed the question of the existence of a specific frequency range of density fluctuations contributing more significantly than others to the formation of such universal distributions. We find that the density fluctuations contained in the measured frequency range of drift-wave turbulence (1kHz<f<10kHz) must be retained to recover this Beta distribution .
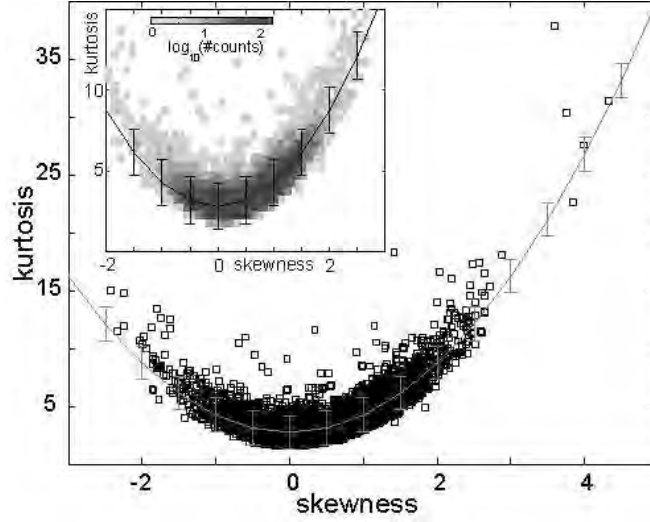
Fig. 2.3.5   *Kurtosis versus skewness computed for the 9824 experimental signals. The fitting second order polynomial (solid grey line) is also plotted. Inset: Joint probability of K and S for the experimental signals.*

2.3.7   *Probabilistic analysis of turbulent structures from 2D plasma imaging*

A method to construct object-related structure observables, such as size, mass, shape, and trajectories from 2D plasma imaging data was developed on TORPEX. The probability distributions of these observables, deduced from measurements of many realizations, provide a robust framework in which the fluctuations, the turbulence, and the related transport are characterised. In particular, a quantitative assessment of the structure-induced transport becomes possible. The method is used on measurements from a hexagonal turbulence imaging probe (HEXTIP), an 86-tip Langmuir probe array covering the whole poloidal cross section.

For each time frame, the signal function is obtained by a linear interpolation on the triangulated measurement grid. Positive and negative structures are defined as regions where the magnitude of the signal exceeds an appropriately chosen threshold value, typically the overall signal variance. Bounding polygons of structures are delineated where the signal coincides with the chosen threshold value. Structure observables such as the structure area, centre of mass and total mass are defined by integral moments over the structure bounding polygon. Second order geometrical moments characterise the orientation of the structure. Structures

are followed during their time evolution, and trajectories can be fully reconstructed, along with the structure birth and death, and splitting and merging events.

The example shown in Fig. 2.3.6 illustrates the use of this method for a hydrogen plasma discharge made from a neutral gas pressure of 2×10^{-5}mbar with low (<1kW) microwave power. In this case about 3000 realisations of trajectories longer than 50 time frames, corresponding to 0.2ms, are selected and binned into a spatial grid of 60×60 bins (Fig. 2.3.6). The ensemble averaged velocity field is also indicated.
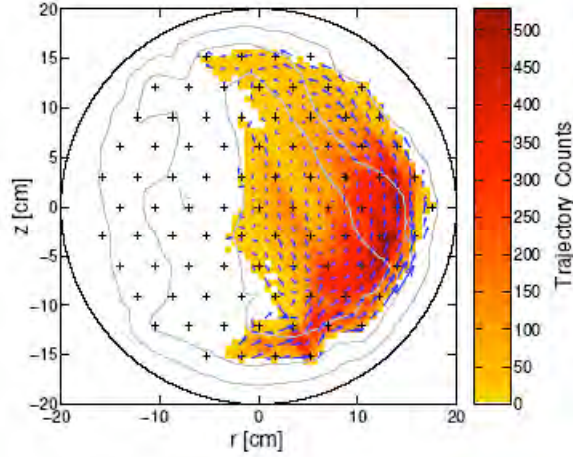
Fig. 2.3.6   *Spatial distribution of structure trajectories and average velocity field. Contours of the time averaged density profile are shown at 25% (outermost), 50% and 75% of the maximum.*

The statistical properties of structure motion are addressed in a pilot chart representation (Fig. 2.3.7), in which the velocity directions are binned into octants and the average speed is evaluated for each octant. The result is represented by a rhumb-card in the centre of each region. For each rhumb-card, the lengths of the eight arrow shafts are proportional to the probability that the velocity direction falls into the corresponding octant. The number of feathers, each standing for 250m/s, indicates the average speed for each direction. The area of the circle in the centre of each rhumb-card is proportional to the number of realizations. The superimposed L-shaped symbols indicate the average orientations and extensions.
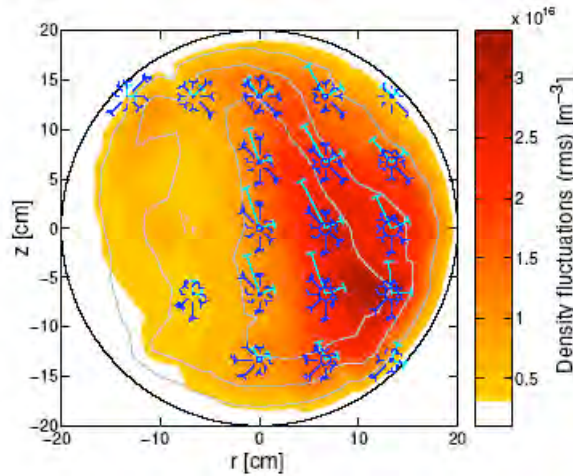
Fig. 2.3.7   *Pilot chart of the structure velocity random field (rhumb-card) and average structure orientations and extensions (L-shaped symbols) on top of the time-series standard deviation profile.*

Structures are primarily observed on the LFS, in the source region for drift-interchange instabilities, characterized by large amplitude peaks in local frequency spectra and a rms fluctuation level of more than 60% of the local time-average value of the density. The structure velocities fluctuate significantly, and average values lie in the range of 500–1000m/s, similar to velocity measurements of structures in the tokamak SOL. The overall structure flow pattern is similar to the general **E**×**B** drift pattern derived from the time-averaged plasma potential profiles.

In Fig. 2.3.8, the overall joint probability distribution of structure speeds and occupied areas is shown for two values of the neutral gas pressure. It is clearly visible that the probability of measuring large structures decreases with the neutral gas pressure. A similar effect was observed previously in terms of an increased width of the wavenumber spectrum, corresponding to a reduction of spatial coherence. For both pressures, the distributions of structure speeds are observed to be mostly independent of the structure sizes, down to the limit of validity of the tracking approach.
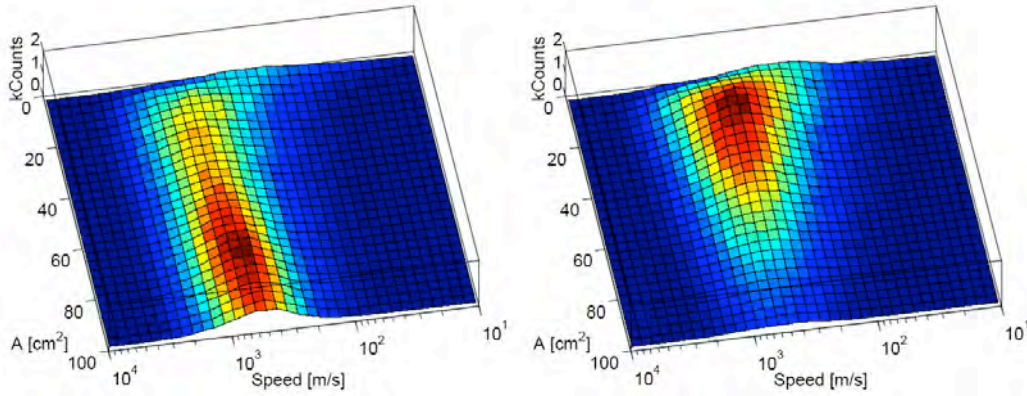
Fig. 2.3.8   *Histogram estimates of the joint probability distribution of structure speeds and occupied areas for a neutral gas pressure of 2×10^{-5}mbar (left) and 1.1×10^{-4}mbar (right).*

To address the structure-induced transport, one of the consequences of turbulence, a grid of macroscopic radial and poloidal surfaces is introduced well inside the domain covered by physical measurement points. Transport events are characterized by the time when a structure centre of mass crosses a surface and by the number of particles transported through it. The particle transport resulting from the imbalance between positive and negative structures can be evaluated throughout the poloidal cross section. We observe that such an asymmetry is present only in the top and bottom regions. Positive structures dominate on the top, giving rise to a positive net poloidal transport, and negative structures, or holes, dominate on the bottom, where the direction of transport is opposite to the direction of motion.

2.3.8   First results with a transformer induced plasma current

In the confined region of toroidal devices, the magnetic field lines lie on flux surfaces which are topologically equivalent to nested tori. This leads to the so-called field line connection, which ensures a finite parallel response of disturbances (turbulence and/or waves) propagating in the plasma. In contrast in the scrape-off

layer (SOL), the field lines end on divertor plates and are therefore not closed, breaking this constraint and allowing the existence of convective cell modes.

To investigate the influence of the magnetic field topology (open versus closed field lines) on fluctuations and turbulence, preliminary experiments have been done on TORPEX using the ohmic system that has recently been optimized against the parasitic vertical field. Such a system induces a loop voltage of approximately 8V, which drives a toroidal current of up to ~1kA, thus closing the magnetic field lines over a substantial portion (~10cm radius) of the poloidal cross section. Figure 2.3.9 shows the time evolution of (a) the plasma current from a Rogowski probe and (b) the central electron density for a typical ohmic discharge. A total plasma current of ~700A is sustained for ~3ms with an increased electron density of up to $3 \times 10^{18} \mathrm{m}^{-3}$ during the flat top.
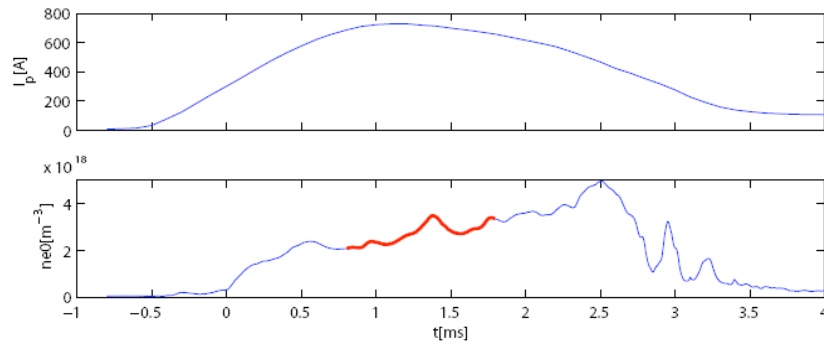
Fig. 2.3.9   *Time evolution of (top) plasma current and (bottom) central electron density during an Ohmic discharge. The Ohmic system is switched on at t=0. The red section corresponds to the current flat top.*

Systematic measurements of the 2D spatial distribution of the fluctuations of the electron density and plasma potential together with magnetic fluctuation measurements show the presence of coherent electromagnetic modes in the frequency range 7-15kHz. Unlike the open field line case, where purely electrostatic drift-interchange modes are observed which are localized at the maximum gradient density position on the low field side, in the ohmic case electromagnetic modes are observed at the position of maximum density gradient on both high and low field sides. The nature of the observed modes is currently under investigation.

2.3.9   Investigation of the interaction of turbulence with suprathermal ions

In tokamak reactors, highly energetic ions can exert a strong influence on the plasma properties via direct heating, by exciting instabilities or by interacting with existing instabilities. This problem can be addressed in TORPEX in a relatively simple experimental environment.

For this investigation the suprathermal ions will be produced by a small fast ion source which will be directly placed inside the vacuum vessel. The beam will be generated by an aluminosilicate Li-6+ ion emitter (6mm diameter, 10-30μA current). Ions will be accelerated in the toroidal direction with energies between 100eV and 1keV by two grids (see Fig. 2.3.10, left).

In order to optimize the construction of the source, a calculation of electric field and ion trajectories inside the source was done in collaboration with the University of California at Irvine. To measure the beam ions, a scheme with two detectors in one casing was chosen (Fig. 2.3.10, right).

Fig. 2.3.10   *The TORPEX fast ion source (left) and double detector (right).*

In the experiment, the spreading of the beam will be measured by a gridded energy analyser, using coherent detection. Both the source and the detector will be installed on 2D poloidally moving systems, using sliding seal feedthroughs with differential pumping, based on a steel ball allowing angular excursion of up to 65° (Fig. 2.3.11).
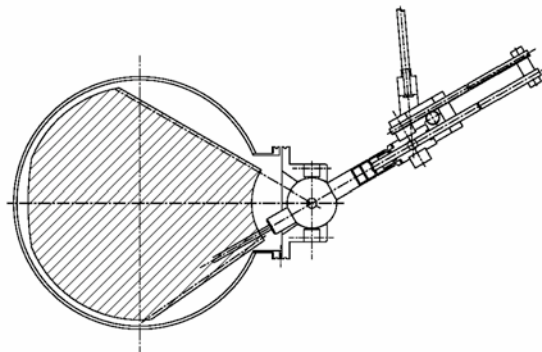
Fig. 2.3.11   *The 2D moving system.*

After injection, the beam tends to diverge due to at least six mechanisms: particle drift, space charge, classical transport, poloidal electric field, turbulent transport, and interaction with alfvénic modes. A simulation of the ion orbits was performed, showing that the fast ion trajectories could be controlled by a small vertical magnetic field and also that the beam temperature (spreading in fast ion energy distribution) leads to the beam spreading along the vertical axis, in which case TORPEX works as a big magnetic energy analyser.

2.4   *Materials research*

The main objective of the Fusion Technology Materials (FTM) group is to investigate the effects of the damage produced by irradiation in a variety of materials, in particular candidate materials for structural components of the future fusion

reactors, but also pure metals and model alloys. This group is located at the Paul Scherrer Institute (PSI) in Villigen.

In fusion reactors, the high-energy fusion neutrons will produce atomic displacement cascades and transmutation nuclear reactions within the irradiated materials. From the point of view of materials science, atomic displacement cascades induce the formation of point structure defects, i.e. vacancies and interstitial atoms, while transmutation nuclear reactions yield the production of impurities, e.g. helium or hydrogen gas atoms.

Key parameters for the first wall in fusion power reactors with a fusion power of 3 to 4GW and in quasi-continuous operational mode include a total neutron flux of 10 to $15 \times 10^{14} ncm^{-2}s^{-1}$, a neutron wall loading of 2 to $3MW/m^2$, an integrated wall load of 10 to $15MWy/m^2$, a surface heat load of 0.1 to $1MW/m^2$ and a volume power density of 20 to $30W/cm^3$. The accumulated dose will amount to 20-30dpa/year in steels, while the gas produced by transmutation nuclear reactions will amount to 10-15appm He/dpa and 40-50appm H/dpa, also in steels.

The final microstructure of the irradiated material results from a balance between radiation damage and thermal annealing. It may be formed of small defect clusters, dislocation loops, precipitates, stacking-fault tetrahedra, voids and/or helium bubbles (Fig. 2.4.1, left). This microstructure has a strong impact on the physical and mechanical properties of the irradiated material. It may engender important hardening (Fig. 2.4.1, right), loss of ductility, fracture toughness and creep strength, as well as macroscopic swelling of the material. These effects are the main factors limiting the choice of candidate materials. The residual radioactivity of a large amount of exposed material is also a concern and will govern the handling methods, dictate the storage periods and the overall waste management and recycling scenarios. The development strategy that takes into account these limitations has led to the development of the so-called low activation materials.

The efficiency of a reactor is proportional to the temperature of the coolant, which is imposed by the upper temperature of use of the structural materials. Then, from the technological point of view, the temperature window of operation of fusion reactors is mainly limited by the mechanical properties of structural materials. Candidate structural materials for plasma facing and breeding-blanket components have a chemical composition that is based on low activation elements (Fe, Cr, V, Ti, W, Si, C, Ta). They include mainly reduced activation ferritic/martensitic (RAFM) steels, oxide dispersion strengthened (ODS) RAFM and RAF steels, vanadium-based alloys, tungsten-based materials, and fibre reinforced SiC/SiC ceramic composites. Each alternative alloy class exhibits specific problems arising from radiation damage. For the time being, the most promising class of alloys are the RAFM steels for which the greatest technology maturity has been achieved, i.e. qualified fabrication routes, welding technology and a general industrial experience are already available.

As no intense source of 14MeV fusion neutrons is presently available on earth, it is necessary to simulate experimentally the effects of 14MeV neutrons, by using for instance fission neutrons. Until December 2003, the FTM group used preferably the high-energy (590MeV) proton beam of the PSI accelerator, through the Proton Irradiation Experiment (PIREX) facility. Since April 2004, most irradiation experiments have been performed with a mixed spectrum of high-energy protons and spallation neutrons by using a combination of the PSI proton accelerator and the target of the Swiss Spallation Neutron Source (SINQ).

Like 14MeV neutrons, 590MeV protons produce atomic displacement cascades and transmutation nuclear reactions within the irradiated materials. One of the main

advantages of the 590MeV protons is to generate high rates of production of impurities, which cannot be achieved with any other currently available irradiation source. While proton irradiations in PIREX were producing about 130appm He/dpa and 800appm H/dpa (in steels), irradiations in SINQ produce about 50appm He/dpa and 450appm H/dpa (in steels). However, in order to investigate the material properties changes and degradation under different irradiation conditions, the FTM group is also involved in specific neutron irradiations performed in reactors in the USA, the Netherlands and Hungary.
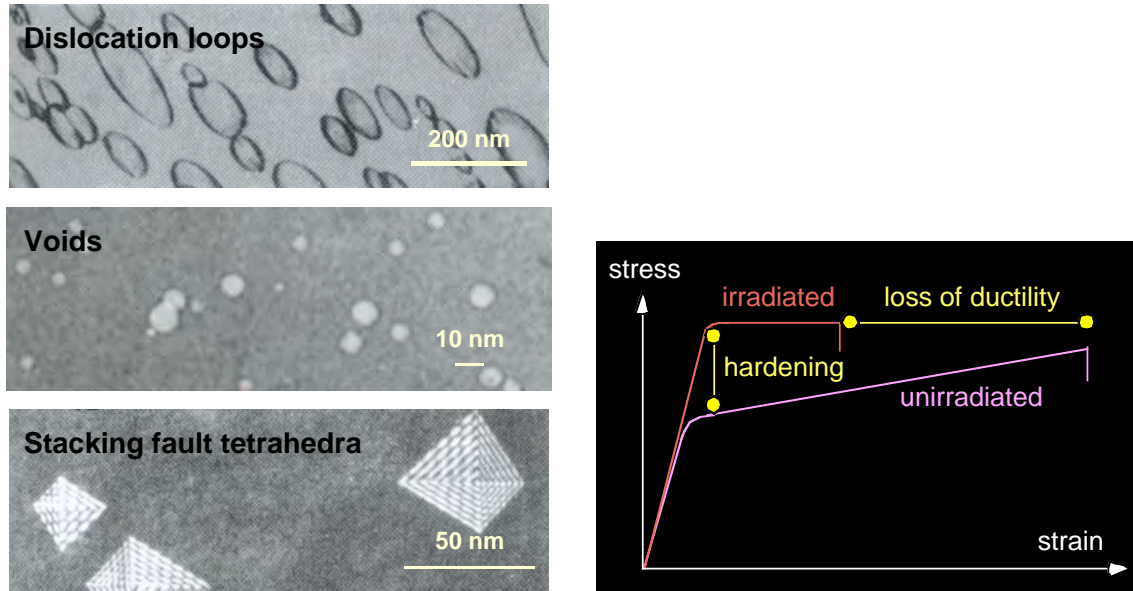
Fig. 2.4.1 *Left: examples of transmission electron microscopy images of irradiation-induced structure defects. Right: schematic of irradiation-induced hardening and loss of ductility, as measured in tensile tests on irradiated specimens.*

The scientific approach adopted by the FTM group to understand the fundamentals of radiation damage in metals and alloys is based on investigating the structure/mechanics relationships at different length scales (micro-, meso-, and macroscopic). A range of experimental and numerical tools is used to reach these objectives. The main experimental tools include mechanical testing on sub-sized and standard specimens, scanning and transmission electron microscopy (SEM, TEM), small angle neutron scattering (SANS) and corrosion resistance experiments. The main numerical tools include ab-initio calculations, molecular dynamics (MD), Monte-Carlo (MC) and dislocation dynamics (DD) simulations, and finite element modelling (FEM).
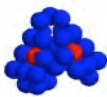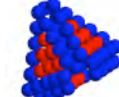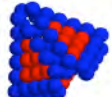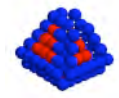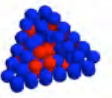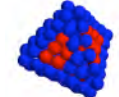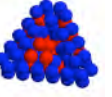
2.4.1 Underlying Technology Tasks

Modelling of radiation damage in face centred cubic (fcc) and body centred cubic (bcc) metals

This work is aimed at simulating numerically the precipitation in binary systems that are prone to phase separation, with the aim of simulating the behaviour of RAFM steels under irradiation. The resulting phase separation in this case is the precipitation of α', which is a chromium-rich phase. Two approaches are proposed: (1) molecular dynamics (MD) simulations to study the stability and precipitation of

Cr precipitates in Fe under a displacement cascade, (2) kinetic rate theory to predict the long term evolution of α'. Empirical interatomic potentials for the Fe-Cr system are being developed within the EFDA programme for investigation of the damage accumulation processes under irradiation by MD simulations. However, there is still a lack of knowledge on the parameters needed for the simulation of the long-term evolution of the irradiated microstructure, which is achievable by kinetic rate theory developed in an analytical way. These needed parameters include for instance the migration energies of the various point defect species present in the Fe-Cr system.

As a consequence, we first considered the binary Ni-Al system, for which well-developed empirical potentials exist. The study of such a system provides insight into the mechanisms of damage accumulation in the presence of two different species, akin to the Fe-Cr system. The particularity of the Ni-Al system is the large difference in atomic radii of the two different atomic species. In addition, its fcc structure presents the particularity to host stacking fault tetrahedra (SFTs) following irradiation, as in a number of fcc metals, such as Cu, Ni and Pd. Their formation under irradiation is however still unclear. It may depend on the stacking fault energy and the shear modulus. Stainless steels, however, although they present favourable formation conditions with a low stacking energy and a high shear modulus, do not exhibit SFTs, or, if present, their number density is low. There is still a lack of knowledge on this phenomenon. The first step of the present study consisted in reproducing the formation of a SFT from a triangular vacancy platelet. Following the Silcox-Hirsch (1962) mechanism, it collapses to a SFT. A 15 vacancy-triangular platelet has been first relaxed at 800K for 3ps, in pure Ni and in Ni-5at.%Al. Both materials allow the platelet to collapse to a perfect SFT. On this basis preliminary runs were performed on platelets containing 6, 15, 21 and 66 vacancies, annealed for 3ps at a temperature of 10, 400 and 800K. Table 2.4.1 present the cases of 6 and 15 vacancies. It appears that only in a few cases do the platelets collapse to perfect SFTs. The phenomenon is still being investigated. The next step will consist in producing atomic displacement cascades in these systems to study the evolution and possible destruction or formation of SFTs and to understand the influence of material properties on the damage formation and accumulation in fcc metals.

T [K]	6 vacancies			15 vacancies		
	pure Ni	Ni-5Al	Ni-10Al	pure Ni	Ni-5Al	Ni-10Al
10	imperfect	imperfect	imperfect	imperfect	imperfect	imperfect
400	imperfect	imperfect	imperfect	imperfect	imperfect	imperfect
800	imperfect	imperfect	imperfect	perfect	perfect	imperfect

Table 2.4.1   *Resulting atomic configurations, showing stacking fault tetrahedra, after an anneal of a vacancy-triangular platelet for 3ps in pure Ni, Ni containing 5at.% Al and 10at.%Al. Red atoms: hcp coordinated atoms, blue atoms: non-fcc, non-hcp, non-bcc atoms.*

Study of heat-treatments on the impact and tensile behaviour of Fe-Cr-C model alloys

Two Fe-Cr-C model steel alloys, referred as to A9 and A12, have been investigated. The chemical composition of the model alloys are: Fe-9wt.%Cr-0.1wt.%C for A9 and Fe-12wt.%Cr-0.1wt.%C for A12. Four different heat-treatments were selected to vary both the prior austenite grain size during the austenization and the annealing/recovery during the tempering. The details of these heat-treatments are the following:

HT1: austenizing at 980°C/25min, air quenched, tempering at 590°C/80min
HT2: austenizing at 980°C/230min, air quenched, tempering at 590°C/80min
HT3: austenizing at 980°C/25min, air quenched, tempering at 760°C/80min
HT4: austenizing at 980°C/230min, air quenched, tempering at 760°C/80min

In Fig. 2.4.2, the absorbed energy measured by Charpy impact tests is plotted against test temperature for the alloy A12 in two different annealed conditions. The ductile-to-brittle transition temperature (DBTT) is defined at the half of the upper shelf energy minus the lower shelf energy. Interestingly, the DBTT value is not strongly affected by either the Cr content or the heat-treatment. All the measured DBTT values are in the range 185-200K. However, the shape of the transition depends mainly on the tempering level. Indeed, quite a sharp transition is observed for the 760°C/80min tempering condition, while a much more extended transition was systematically found for the 590°C/80 min tempering condition, independently of the Cr content (see Fig. 2.4.2). This result clearly indicates that the prior austenite grain size has only a limited effect on the DBTT value, if any. Charpy impact test results are summarized in Table 2.4.2. Note that the Charpy impact properties of the EUROFER 97 RAFM steel have also been determined and the DBTT value was found to be equal to 197K with a sharp transition.
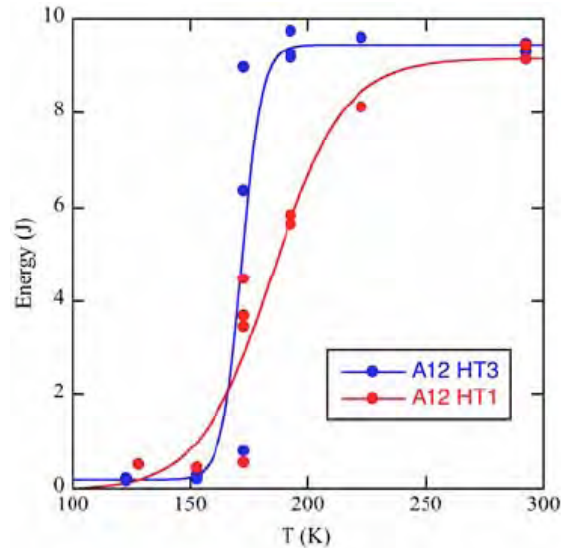
Fig. 2.4.2   *Absorbed energy versus test temperature measured by Charpy impact tests.*

Alloy	Heat-treatment	DBTT [K]	DBTT character
A12	HT1	185	smooth
A12	HT3	172	sharp
A12	HT2	201	smooth
A12	HT4	168	sharp
A9	HT1	186	smooth
A9	HT2	186	smooth

Table 2.4.2   *Results of Charpy impact tests on model steel alloys.*

2.4.3 Supporting research

Small angle neutron scattering analysis of irradiation-induced defects in pure metals and alloys

Nano-scale irradiation-induced defects are believed to significantly contribute to the hardening and/or embrittlement of metallic materials under irradiation, along with the microscopic defects. Transmission electron microscopy (TEM) allows direct observations of defects whose size is larger than about 1nm in weak beam imaging but other techniques have to be used to reveal ultra-fine scale microstructures. Small angle neutron scattering (SANS) is an effective technique to characterize nano-scale distributions of features in terms of number density, size distribution and chemical composition.

SANS measurements
SANS measurements were performed in a strong saturating magnetic field perpendicular to the incident neutron beam with the aim to separate nuclear and magnetic contributions to the scattered intensity.

Results of the most recent measurement campaign confirmed results of previous campaigns. Assuming that the irradiation-induced scattered intensity arises from a dilute distribution of a single type of scattering spherical features, it was found that the mean ratio of the irradiation-induced defects peaks at about 0.6nm, a value well below the TEM resolution limit. The number density of irradiation-induced defects was found to increase with accumulated dose and to decrease with increasing irradiation temperature.

Simulations of the SANS signal
A variety of nano-sized irradiation-induced defect clusters may contribute to the additional scattered intensity exhibited by the irradiated specimens. These include small, unidentified defect clusters (of vacancy or interstitial type), voids, helium bubbles, small dislocation loops (of vacancy or interstitial type), carbides and/or precipitates. The ratio of the nuclear plus the magnetic scattering intensity to the nuclear scattering intensity indicates that the irradiation-induced defects could be $CrHe$ or Cr_2FeHe_3 complex defect clusters or a combination of He bubbles and Cr_3C chromium carbides, for instance. In order to clarify the situation, specimens of pure Fe have been produced by molecular dynamics (MD) simulations, which contain either of the possible irradiation-induced defects. In addition, the Electron Microscopy Software (EMS), originally destined to simulations of TEM images, has been modified to simulate the SANS signal of the specimens generated by MD. Systematic simulations are in progress.

Fracture mechanics: 2D Finite element simulation of the stress fields at the crack tip. Comparison between compact tension specimens and small scale yield condition

Research activities were mainly focused on the calibration of a local critical stress state to trigger quasi-cleavage in the ductile-to-brittle transition of the RAFM steel EUROFER 97. This critical stress condition is then used to model the fracture toughness-temperature curve, K(T), in the transition with finite element simulations of compact tension, C(T), specimens. First, the fracture toughness in the transition of the EUROFER 97 was determined by testing pre-cracked 0.4T C(T) specimens in the lower ductile-to-brittle transition.

More than 90 specimens were tested to assess the amplitude of the scatter as a function of temperature. The data are plotted in Fig. 2.4.3 with indication of the 1% failure probability bound. The temperature dependence of fracture toughness can be modelled by determining a critical stress/strain state ahead of the crack tip, which triggers quasi-cleavage as soon as it is reached under the application of external remote load. This critical stress state is assumed to be temperature independent and is defined as the attainment of a critical stress value σ^* (maximum principal stress) over a critical area A^*. In this study, we focused our attention on modelling the 1% lower bound of the K(T) data by using the local criterion σ^*-A^*. The main motivation to reconstruct the lower bound resides in the fact that the loading and deformation level is small, and thus quasi plane-strain conditions prevail all along the crack front. Under such conditions, 2D finite element modelling (FEM) of in plane-strain conditions for C(T) specimens can be regarded as representative of an actual specimen. Linear elements with reduced integration were used for FEM. The modelled specimen was deformed by imposing a rigid body displacement at the level of the C(T) specimen pin hole. The load-displacement curve is readily obtained by extracting the reaction force acting on the pin and plotting it against the displacement. The applied stress intensity factor at any step of the simulations was determined with the J-integral calculated from many closed line stress contours around the crack.

A FORTRAN program has been written, which reads the FEM ABAQUS output file, to calculate the areas encompassed by any given σ^*. It was found that the lower bound is the best fit for σ^* equals to 2150±50MPa (see Fig. 2.4.3), which leads to a critical area A^* of 50 to 270µm^2. This A^* value corresponds to a cross sectional area of only 1 to 2 prior austenitic grains.
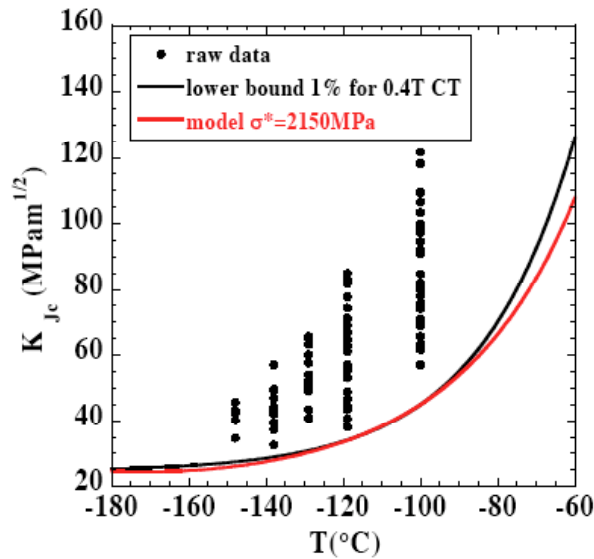
Fig. 2.4.3   *K_{Jc} data versus temperature for the EUROFER 97 RAFM steel. The 1% failure probability curve is indicated (black curve). The σ^*-A^* modelled curve of the 1% bound is also shown (red curve).*

EXTREMAT Integrated Project (IP) of the Sixth European Framework Programme

Activities within the EXTREMAT Project are aimed at:
- Modelling the radiation damage and radiation effects on pure W.
- Developing reduced activation, radiation resistant, oxide dispersion strengthened (ODS) ferritic steels for structural applications in the future fusion reactors.

- Developing ductile, radiation resistant W-base materials for structural applications in the future fusion reactors.

Modelling of radiation damage and radiation effects on pure W

Two long-range (equilibrium) Embedded Atom Method (EAM) potentials have been used to describe tungsten atoms at low energies in the past. As these two long-range interatomic potentials seem to fail to reproduce the correct energy of defects in body centred cubic (bcc) transitions metals, a new potential has been developed by UKAEA (England).

For short range two universal potentials can be used. As previous studies have shown no difference, we selected one of them fort he present study.

The short and long-range potentials have to be smoothly connected so that the value of pair-interaction and its first derivative are continuous. The connecting procedure is more complicated in the case of the new long-range potential (3, see table 2.4.3), as there is a bigger mismatch between this potential and the universal potential and also the embedding term is more important than it is for long-range potentials (1) and (2). In the case of the new long-range potential (3) the connection is achieved by shifting the universal potential by $+\sqrt{\rho_{max}}$, where ρ_{max} is the maximum and constant electron density at small distances. This value is obtained by performing electron density truncating. In the case of the new long-range potential (3) this truncating is necessary, as otherwise densities reach too high values at short distances.

Point defect formation and migration energies have been calculated with the new long-range potential and compared to the values obtained with the older two potentials (see Table 2.4.3). The values are close to each other, with the exception of the migration energy of interstitial atoms in the <111> direction, E^m_{111}, which is much smaller when calculated with the new potential than with the older two potentials. This discrepancy still has to be solved.

Long-range interatomic potential	E^f_v [eV]	E^f_{111} [eV]	E^f_{110} [eV]	E^m_v [eV]	E^m_{111} [meV]
Finnis, Sinclair (1)	3.631	7.810	8.441	1.442	30.67
Ackland, Thetford (2)	3.632	8.889	9.613	1.449	26.70
Derlet, Nguyen-Manh, Dudarev (3)	3.557	9.476	9.771	2.054	9.78

Table 2.4.3 *Formation and migration energies of vacancies and interstitial atoms in the <111> and <110> directions, calculated with three different interatomic potentials.*

Atomic displacement cascades have been generated by molecular dynamics (MD), using the new interatomic potential and primary knock-on atom (PKA) energy of 10keV, in a tungsten specimen containing 250'000 atoms. Preliminary results showed that the defect production is slightly lower with the new potential, as compared to the Finnis-Sinclair potential. This result is in agreement with the higher displacement threshold energy obtained with the new interatomic potential as compared to the value calculated with the Finnis-Sinclair potential. Vacancies cluster at a smaller rate with the new interatomic potential than with the Finis-

Sinclair one, although the vacancy-vacancy interaction is almost the same. On the contrary, more than 50% interstitials are found in the form of clusters when using the new interatomic potential, which is more than twice the ratio obtained with the two old potentials. This might be due to the higher mobility of <111> interstitials using the new potential. However, interstitial-interstitial interaction still has to be investigated in detail.

Development of advanced, radiation-resistant ODS ferritic steels

The aim of this work is to develop reduced activation, radiation-resistant ODS ferritic steels by powder metallurgy techniques. Such materials are expected to be used as structural materials in fusion reactors up to about 800°C. In addition, the numerous interfaces engendered by the presence of oxide particles are expected to act as sinks for the irradiation-induced defects. This work is complementary to the EFDA Long Term Technology Task TW5-TTMS-006/D4, in terms of manufacturing route and characterization of irradiation resistance.

Two ODS ferritic steels, with the composition Fe-14Cr-1.2W-0.3Ti-0.3%Y_2O_3, have been prepared by mechanical alloying and Hot Isostatic Pressing (HIPping) at 1100°C for 4 hours, in the shape of a small cylindrical ingot, and by mechanical alloying and hot extrusion at 1100°C under a pressure of 250 tons, in the shape of a cylindrical bar (700mm in length and 11mm in diameter), respectively. Hot extrusion was performed at the CEA (Commissariat à l'Energie Atomique) in Saclay (France). The small, hipped ingot has been characterized. The extruded bar has been sent to the ARC company in Seibersdorf (Austria) for severe plastic deformation (SPD) by equal channel angular pressing (ECAP). A new batch of ODS ferritic steel powder is now being produced by mechanical alloying, which will be compacted by hot extrusion at the CEA. Series of specimens from both HIPped and hot extruded materials will then be prepared for Charpy impact tests, tensile tests, small ball punch testing, TEM observations, SANS measurements and high heat flux testing. A part of them will be irradiated with neutrons in the High Flux Reactor (HFR) in Petten (The Netherlands) at about 600 and 900°C to a dose of 3-5dpa.

Development of ductile, radiation resistant W-based materials

The aim of this work is to develop nanocrystalline W-based materials by severe plastic deformation (SPD). Such materials are expected to show improved ductility and better resistance to radiation damage, as the grain boundaries should act as sinks for the irradiation-induced defects.

Three commercial materials have been selected and purchased from the Plansee company (Austria): pure W powder (99.99% purity), pure W rod (30mm in diameter, 200mm in length (99.97% purity), and W-1%La_2O_3 rod (40mm in diameter, 200 mm in length). They have been sent to the Technical University in Warsaw (Poland) where their microstructure will be made nanocrystalline by SPD using high-speed hot extrusion. Following SPD, series of specimens will be prepared for Charpy impact tests, tensile tests, small ball punch testing, TEM observations, SANS measurements, high heat flux testing and thermal conductivity measurements. A part of them will be irradiated with neutrons in the High Flux Reactor (HFR) in Petten (The Netherlands) at about 600 and 900°C to a dose of 3-5dpa.

PERFECT Integrated Project (IP) of the Sixth European Framework Programme

This project is aimed at investigating the possibility to identify by means of transmission electron microscopy (TEM) observations nano-sized irradiation-induced defects as well as nano-sized secondary phase precipitates in pressure vessel steels used in classical fission reactors. This is being done by means of TEM image simulations of defects in Fe, in order to identify the appropriate TEM imaging conditions for the identification of voids and Cu precipitates in Fe. This work is being performed in collaboration with the University of Helsinki, Finland and with the University Autonoma de Barcelona, Spain.

Series of samples were produced for molecular dynamics (MD) simulations, which contain a spherical defect in the centre (2nm in size). The defects are divided into three categories: (1) Cu atoms in Fe, (2) vacancies in Fe, (3) Cu atoms with a complement of vacancies. Each category had four samples, in which the defect was constructed by changing an amount of randomly located Fe atoms within the defect volume into Cu atoms (categories 1 and 3) or vacancies (category 2) in 20% increments. In category 3, the remaining Fe atoms within the defect volume were completely removed. In addition, 2nm pure Cu precipitates and 2nm pure void defects were investigated. MD simulations were performed using the Embedded Atom Method (EAM) and periodic boundary conditions. The relaxations were done using the conjugate gradient method. The atomic interactions were dealt by the Ackland many-body interatomic potentials for Fe-Cu alloys. The samples were first slowly heated from 0 to 800K, annealed for 100ps, and finally cooled down to 0K.
TEM image simulations were performed using the Electron Microscopy Software (EMS) programme and the multislice technique. The diffraction vectors were g={200}, close to a <100> zone axis, and g={110}, close to a <011> zone axis. The imaging condition, or excitation of the imaging vector (g), was $g(3.1g)$ for all TEM image simulations.
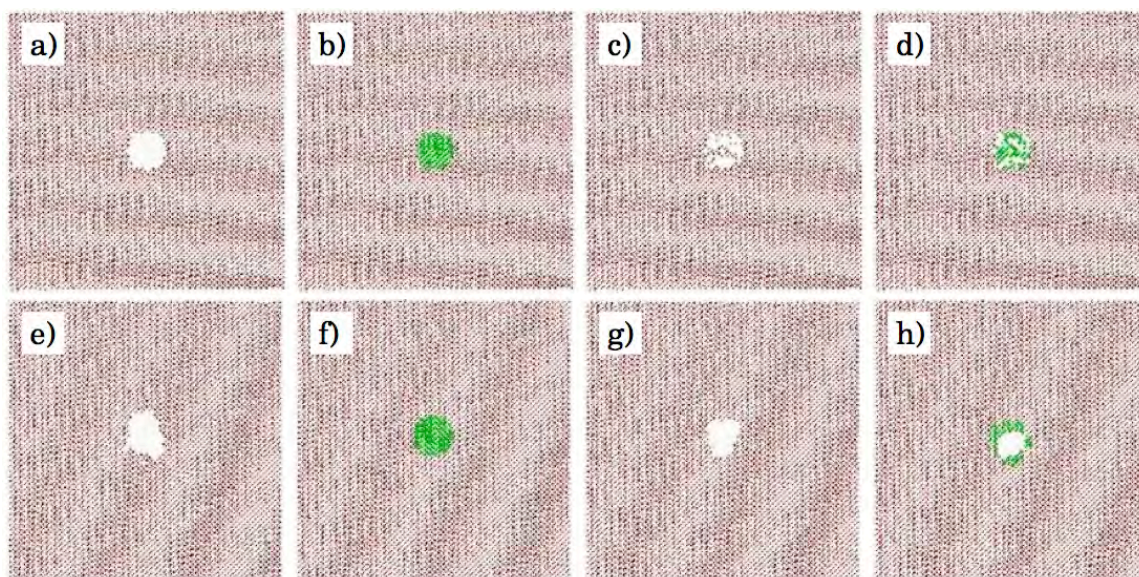
Fig. 2.4.4 *Atomic cross-sections of the specimens used in the simulations, containing a 2nm defect made of (a) 100% vacancies (unrelaxed void), (b) 100% Cu atoms (unrelaxed precipitate), (c) 60% vacancies (unrelaxed defect), and (d) 60% Cu atoms with a complement of vacancies (unrelaxed defect). Figures (e) through (h) are the same specimens, but relaxed.*

The relaxation of samples containing vacancies had a tendency to merge the randomly placed vacancies and arrange them in such a way as to minimize the surface energy of an empty void (Fig. 2.4.4), leading to the formation of a void coated with Cu atoms. In some cases, depending on the amount of missing atoms, this meant a spherical or near-spherical shape, but in other cases, a relaxed shape with straighter edges was prevalent. In the Cu/vacancy samples, the Cu atoms drift to the inner surface of the merged void. In samples without vacancies, an investigation of the atomic positions showed little or no change in the location of the Cu defects.
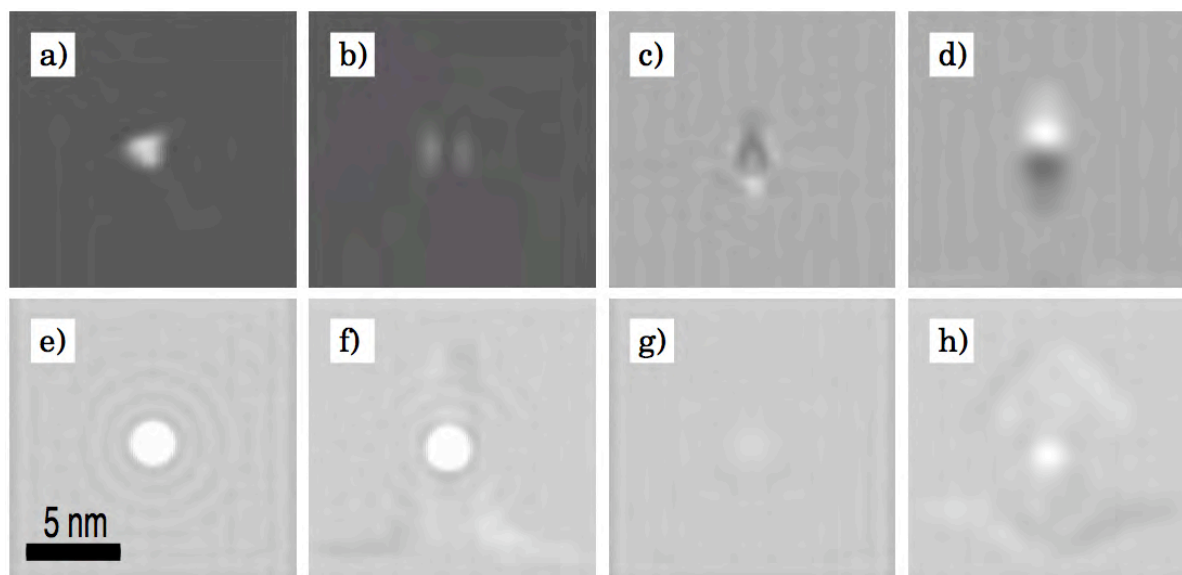
Fig. 2.4.5   *TEM simulated images of specimens containing a 2nm defect made of (a) 100% vacancies (unrelaxed void), g={200}, (b) 100% Cu atoms (unrelaxed precipitate), g={200}, (c) 60% vacancies (unrelaxed defect), g={200}, (d) 60% Cu atoms with a complement of vacancies (unrelaxed defect), g={200}, (e) 100% vacancies (unrelaxed void), g={110}, (f) 100% vacancies (relaxed void), g={110}, (g) 100% Cu atoms (unrelaxed precipitate), g={110}, and (h) 100% Cu atoms (relaxed precipitate), g={110}.*

Results of TEM image simulations seem to indicate that the g(3.1g) imaging condition with g={200} favours the detection of voids, while the g(3.1g) imaging condition with g={110} favours the detection of Cu precipitates. The relaxation of the void had little effect on the TEM image contrast, as can be seen in Fig. 2.4.5. In fact, voids were easily visible in all simulated images. Relaxation of the Cu defects had, relative to the voids, a strong effect on the TEM images. Unrelaxed Cu precipitates were not visible at all in certain diffraction conditions. Relaxation increased significantly the image contrast. In addition, it appears that it is possible to use a combination of different sample orientations to distinguish between vacancy- and Cu-base defects, in order to analyse samples more fully. The image contrast for Cu precipitates increases with the relative amount of Cu atoms within the defect volume, while the contrast for void defects only increases when using g={200}. Contrasts of this type in TEM are due to the diffraction of the electron beam from local variations in the positions of the atoms. If there is a lattice distortion, it causes a slight change in the deviation parameter, which strongly affects the image intensity in weak beam imaging. It is clear that the more Cu atoms within a Fe lattice, the more strain-induced distortions due to the large

differences in lattice parameters and bulk crystal structures between the two metals. With void defects, however, the image contrast is more dependent on the actual geometry of the defect, and as such, is not as reliable an indication of the defect size. It has been ascertained both computationally and experimentally that Cu precipitates in a bcc lattice such as Fe can maintain a stable bcc structure only up to a diameter of about 6nm. Beyond that point the fcc structure of Cu will dominate, giving rise to displacements that will modify the strain around the defect. It is therefore likely that quantitative analysis of Cu precipitate size of larger defects cannot be safely extrapolated from contrast data obtained from smaller defects such as the ones investigated in this study, and thus, requires further research.

2.4.4   EFDA Technology Tasks

Tasks Long Term

TW1-TTMS-001 deliverable 3: Proton irradiation of EUROFER 97 up to 1dpa of plate, for He effect testing
Tensile testing of specimens of the RAFM steel EUROFER 97, which have been irradiated with high-energy protons in the PIREX facility to various doses ranging between 0.3 and 2dpa and at various irradiation temperatures ranging between 50 and 350°C, has been completed.

The tensile specimens were of the flat type (0.2 to 0.3mm thick) and were specially designed for the PIREX irradiation facility. The geometry of these PIREX specimens is shown in Fig. 2.4.6 along with that of the usual standard round DIN specimens. In order to verify that the results obtained with PIREX specimens are consistent with those obtained with standard specimens both specimen geometries were tensile tested at room temperature. A very good agreement between the results was found, as shown in Fig. 2.4.7 (upper left) where the true stress-strain curves of both specimens are plotted up to the onset of necking.
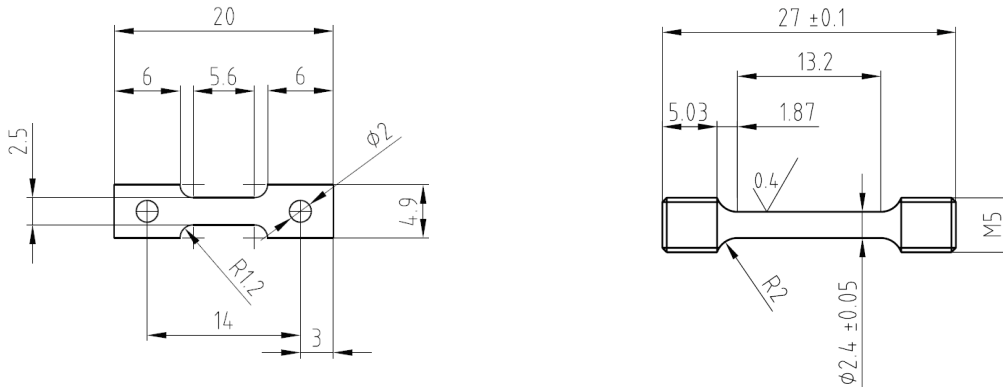
Fig. 2.4.6   *Left: Flat PIREX specimen. Right: Round DIN specimen.*

As an example, the effect of irradiation at 50°C on the increase in flow stress and on the reduction of uniform elongation is shown in Fig. 2.4.7 (upper right). The tensile curves of the two specimens irradiated up to 0.62 and 1.27dpa clearly show that the uniform elongation is strongly reduced even at these moderate dose levels. In fact, above 1dpa, the uniform elongation practically coincides with the conventional 0.2% plastic strain defining the yield stress. The effects of accumulated dose and irradiation temperature are illustrated in Fig. 2.4.7 (lower left). Note that the temperatures of the tests were the same as those of the irradiations. It is common

to plot the irradiation hardening, $\Delta\sigma_y$, defined as the irradiation-induced increase in yield stress, as a function of the square root of the dose. Despite a significant scatter in the experimental data, a clear decrease of the irradiation hardening at a given dose with increasing irradiation temperature was found. An extrapolation of the temperature dependence of the slope of the fits to higher temperature indicates that the irradiation-hardening disappears for temperatures slightly above 400°C. Note also that the origin of the scatter resides in the uncertainty in the dose estimations and in the usual scatter of the yield stresses of both the unirradiated and irradiated specimens, which are used to calculate $\Delta\sigma_y$.
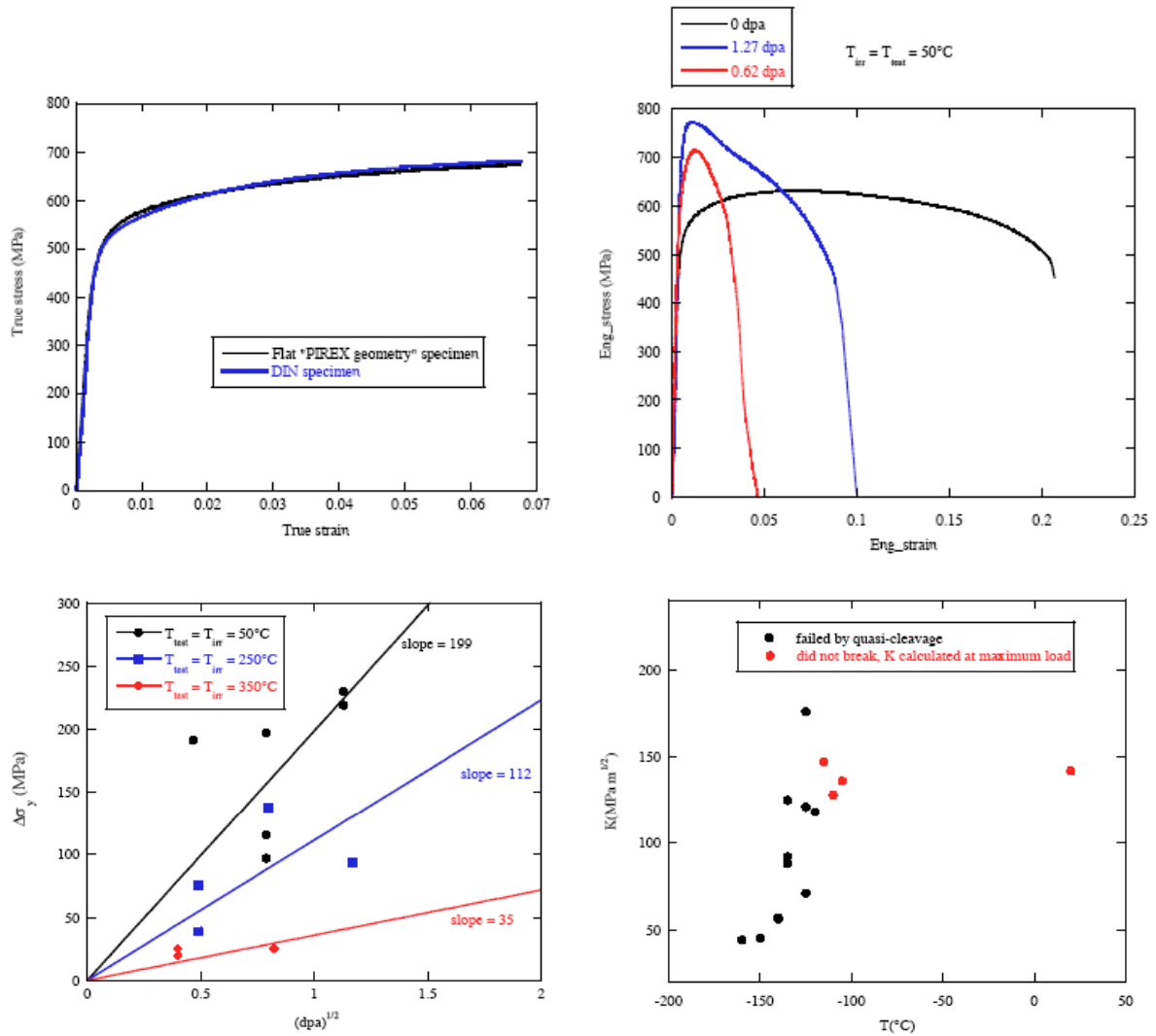
Fig. 2.4.7   *Upper left: Comparison of the tensile stress-stress curves σ(ε) for a PIREX specimen and a DIN specimen. Upper right: Effect of irradiation on tensile tests, $T_{test}=T_{irr}=50°C$. Lower left: Irradiation hardening versus $dpa^{1/2}$ at different irradiation temperatures. Lower right: Effective fracture toughness versus test temperature.*

In a next step it is planned to characterise the fracture toughness-temperature curve, K(T), of the EUROFER 97 RAFM steel, using mini-bend bars with a 1mm x 1mm cross-section which have been proton-irradiated in the PIREX facility at 300°C to 1dpa. Such mini-bend bars have already been tested in the unirradiated state. The specimens were tested statically in three-point bending at a machine traverse velocity of 0.5mm/min. In total fifteen mini-bars were tested over the

temperature range [-160°C; 20°C]. A very steep ductile-to-brittle transition was found, as shown in Fig. 2.4.7 (lower right). Below -120°C all the specimens failed by quasi-cleavage while above this temperature the specimens did not break. The fracture toughness data reported in Fig. 2.4.7 (lower right) above 120°C were then calculated at the maximum load reached on the load-displacement curve. The median effective fracture toughness at 125°C is around 120MPa.m$^{1/2}$ and the fracture toughness falls down to about 40MPa.m$^{1/2}$ at -150°C. Such a steep transition, if also observed for the irradiated specimens, will facilitate the estimation of the irradiation-induced shift of the fracture toughness-temperature curve.

TW2-TTMS-004b deliverable 3: Development and testing of coatings to improve the corrosion resistance vs Pb17Li at T>450°C

Eighteen specimens of the RAFM steel EUROFER 97 have been sent to three different European companies for deposition of pure W coatings using three different techniques. Six specimens have been coated with a 10µm-thick hard W coating using a galvanic technique. Six specimens have been coated with a 18-22µm-thick W coating using a physical vapour deposition (PVD) technique. Six specimens have been coated with a 120µm-thick W coating using a plasma spraying technique. Twelve small corrosion devices have been constructed. They are destined to test the resistance of the three types of W coatings as protection barriers for the EUROFER 97 RAFM steel against corrosion in molten Pb-17Li. In such a device a cylindrical specimen is screwed to the bottom part of a rod connected to a small motor. Features of the motor allow the specimen to rotate in a bath of molten Pb-17Li at a speed between 1mm/s and 5m/s and a bath temperature between 300°C and 800°C. Corrosion testing of reference specimens (uncoated EUROFER 97) and W coated specimens is being performed at a specimen rotation speed of 1cm/s and a bath temperature of 550°C, for various corrosion times ranging between 500 and 10'000 hours. Corrosion experiments for corrosion times of 500 and 1'000 hours have been completed. Corrosion experiments for corrosion times of 2'500, 5'000 and 10'000 hours are still ongoing.

TW3-TTMS-007 deliverable 8: Irradiation in SINQ

Irradiation was completed in December 2005. Analysis of the irradiation parameters, (e.g. doe and temperature) versus location of the specimens inside the SINQ target, is ongoing.

TW5-TTMS-001/D7: Assessment of irradiations performed on EUROFER97

A comparative assessment of the microstructures of the F82H and EUROFER 97 RAFM steels was performed in order to find an explanation for the observed differences in the mechanical properties, in particular the fracture properties, between these two materials. Optical, scanning and transmission electron microscopy observations were carried out, and the results were compared to those of previous investigations. Studies were focused on the prior austenite grain (PAG) size and the distribution and nature of carbides and inclusions. The most striking differences that were found between the two steels can be summarized as follows:

- A significant difference in the Ta content: 0.7wt.% for the EUROFER 97 against 0.02-0.4wt.% for the F82H-mod 9741 and 9753 heats, respectively.
- The PAG size of the EUROFER 97 steel is about 10µm while it is of the order of 80-90µm for the F82H-mod steel.
- Large non-spherical inclusions, 7-15µm in size, which seem to be mainly Ta, Ti, and Al rich-mixed oxides, have been found in the F82H-mod steel.

It seems that the difference in Ta content plays a role in the PAG size. It must be emphasized that, in the F82H steel, Ta mainly combined with Al, Ti and O leads to the formation of undesirably large inclusions. Some of them are as large as the mean PAG size for the EUROFER 97. As a consequence, fewer TaC carbides to pin the PAG boundaries during the normalization process are present in the F82H steel with respect to the EUROFER 97 steel, leading to a larger final grain size in the F82H steel. The formation mechanism of these large inclusions is not well understood for the time being. The role of these inclusions on the fracture behaviour is likely to be very detrimental, and they are suspected to be the origin of the low fracture toughness values that are obtained at relatively high temperatures in the ductile-to-brittle transition and that lie well below the 1% lower bound of the Master-Curve.

TW5-TTMS-005/D2: SSTT: Model the brittle transition region - continuation of TW2-TTMS-005b/D6

Having obtained a fairly large fracture database for 0.4T C(T) specimens of the EUROFER 97 RAFM steel in the lower ductile-to-brittle transition region, it was possible to analyse in detail the amplitude of the scatter in the fracture toughness data and its temperature dependence in the transition. We just recall that the scatter is an intrinsic feature of brittle fracture whose origin resides in the probability of finding a 'crack initiator' in the process zone surrounding a loaded crack. We were particularly interested in knowing whether an approach of the Master-Curve type, like the ASTM-1921 standard used to index the median fracture toughness-temperature curve, $K_{med}(T)$, of reactor pressure vessel (RPV) steels on an absolute temperature scale, yields a satisfactory statistical description of the EUROFER 97 data.
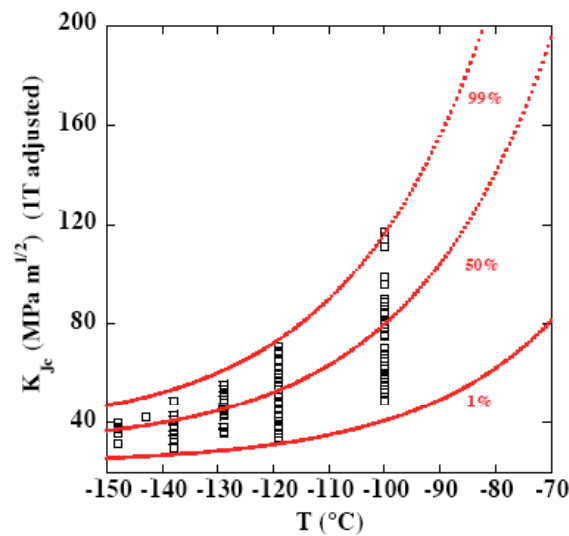
Fig. 2.4.8   *Fracture toughness data for EUROFER 97 in the transition region.*

Lower bound [%]	Data below	Upper bound [%]	Data above	Total data out of the bounds	Expected data out of the bounds
1	0	99	2	2	2
5	4	95	7	11	9
10	8	90	11	19	18
20	19	80	17	36	36

Table 2.4.4   *Numbers of data related to the bounds shown in Fig. 2.4.8.*

The main findings of the modelling activities associated with this task are manifold. First, there is a need to consider a significant change of the $K_{med}(T)$ curve shape for RAFM steels with respect to that for RPV steels. The transition for RAFM steels appears much steeper than that for RPV steels. Second, the overall approach of the Master-Curve provides a very good statistical description of the scatter. Ninety-one data are plotted in Fig. 2.4.8 along with the 1%, 50% and 99% failure probability curves. As expected, all the data fall between the 1% and 99% bounds. In Table 2.4.4, the number of points lying out of the bounds for various failure probabilities is also indicated. The number of experimental data out of the bounds is in excellent agreement with the theoretical number. This result gives strong support to the use of a modified Master-Curve to characterize the scatter of fracture toughness data for RAFM steels. Third, a local approach for cleavage (fast fracture) in terms of a critical stress value σ* (maximum principal stress) encompassing a critical area A* or volume V* has been discussed in the context of a statistics description of the data. On the one hand, we postulated that the σ*-V* model is well suited to model the main features of 'initiation-controlled' fracture. Size effects predicted by the σ*-V* model agree with the predictions of the weakest-link approach. On the other hand, we postulated that the σ*-A* model is well suited to model the main features of 'propagation-controlled' fracture. In this perspective, the σ*-A* model is therefore the appropriate tool to model the lower bound.

TW5-TTMS-005/D10: Support in development of design rules for structural materials with low ductility

It was shown experimentally that the uniform elongation defined at the maximum load is not necessary the best criterion to characterize the stability of the plastic flow in tensile testing for materials with low strain hardening. Indeed, it was found for the EUROFER 97 RAFM steel that the plastic deformation may continue steadily at a low strain rate by keeping the specimen under a constant load smaller than the maximum load.

The stress-strain curve (expressed in terms of engineering and true units) is shown in Fig. 2.4.9 (left). It was obtained for a test in which the load was maintained constant from a strain that was about 2.5% lower than the uniform strain. The evolution of the true strain rate during the transient at constant load as a function of time is reported in Fig. 2.4.9 (right), in which the onset of the instability can be clearly seen. In order to explain this somewhat unexpected behaviour, we developed a model to account for the evolution of the plastic strain-rate with plastic strain of a specimen kept under constant load. The model is based on the Orowan's equation that relates the plastic strain-rate to the product of the mobile dislocation density and the dislocation velocity. The model assumes an exponential decrease of the mobile dislocation density from that existing during the tensile test at constant strain-rate, down to a saturation level that characterizes the steady state reached under the constant load condition. This contributes to a strong decrease of the plastic-strain rate. On the contrary, the increase in the true stress during the constant load transient results in a constant increase in the dislocation velocity. The stress dislocation velocity dependency was described as a power law. Therefore, the product of the mobile dislocation density and the dislocation velocity must pass through a minimum. The model we developed is able to reconstruct the evolution of the plastic strain-rate with the plastic strain during the transient using three parameters reflecting the exhaustion rate of the mobile dislocation density, the saturation level of the mobile dislocation density and the power exponent in the velocity power law.
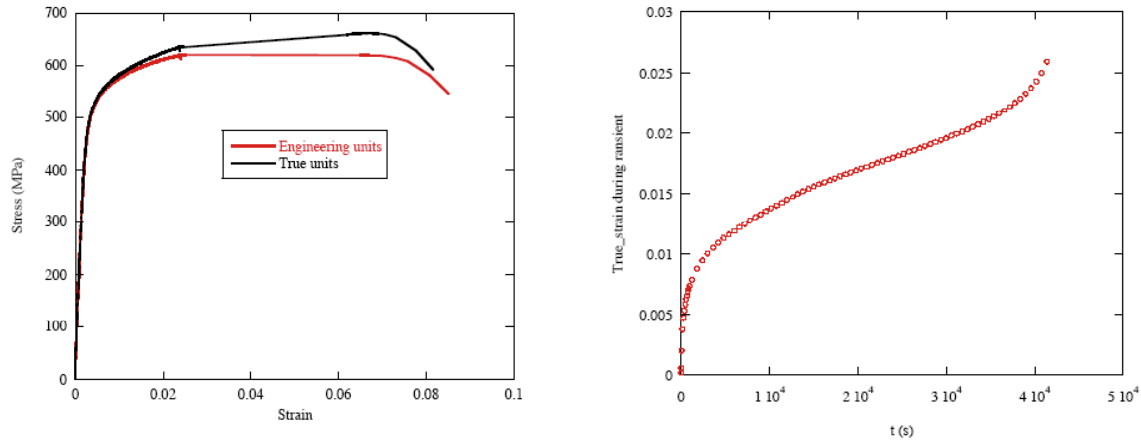
Fig. 2.4.9 *Left: Tensile stress-strain curve at room temperature with a constant load transient experiment. Right: Evolution of the true strain with time during the constant load transient.*

TW5-TTMS-005/D11: Experiments in support of TW5-TTMS-005/D2
The testing of all the unirradiated fracture specimens has been completed. Modifications of the shielded testing machine were performed for allowing the testing of 0.2T C(T) and 0.4T C(T) specimens of the F82H RAFM steel irradiated in the KFKI reactor in Budapest (Hungary). This includes the set-up of a low temperature environmental chamber and the production of series of adaptors for compact tension, C(T), specimens and bend bars.

TW5-TTMS-006/D2: Characterisation of reference EU ODS-EUROFER batch
The objective of this task was to assess the mechanical properties of the reference EU ODS-EUROFER batch, made of the EUROFER 97 RAFM steel reinforced with Y_2O_3 (yttria) particles, produced by the Forschungszentrum Karlsruhe (FZK) together with the Plansee Company. Mechanical tests included Charpy impact tests between -100 and 300°C, in order to evaluate the ductile-to-brittle transition temperature, and uniaxial tensile tests between room temperature and 800°C.

Pieces of ODS-EUROFER, cut out from two different products (17mm thick plate and 20mm diameter rod), have been received from FZK in September 2005. In order to save material, it was decided to perform tensile tests on miniaturized cylindrical specimens with a diameter of 2.4mm and Charpy impact tests on KLST specimens (3x4x27mm^3). The received quantities allowed the manufacturing of 48 tensile specimens (8x3 specimens per product) and 90 Charpy impact specimens (15x2 specimens from the rod, 15x2 specimens from the plate in the rolling direction and 15x2 specimens from the plate in the transverse direction).

The temperature dependence of the yield strength and ultimate tensile strength for the two products is shown in Fig. 2.4.10 (left). The temperature dependence of the uniform and total elongation for the two products is shown in Fig. 2.4.10 (right). It can be seen that both products exhibit similar tensile properties. However, one observes slightly larger total elongation values for the rod, with respect to the plate, in the temperature range 300-700°C.
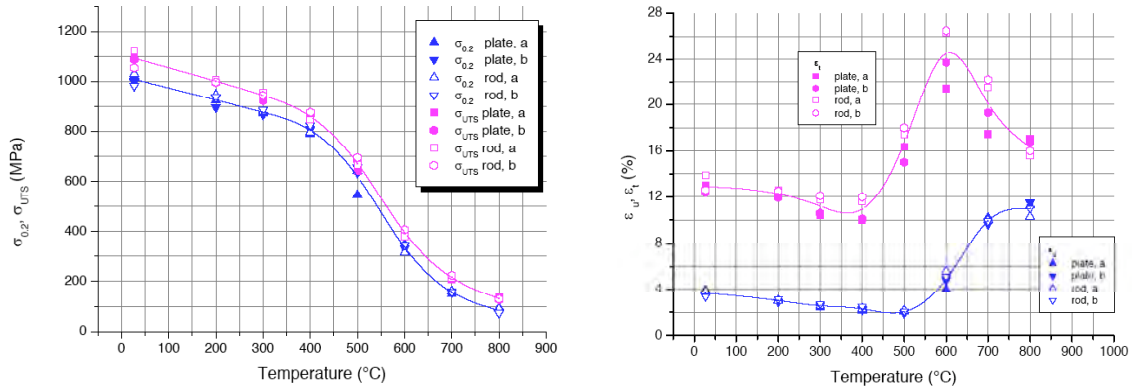
Fig. 2.4.10   *Left: Yield strength and ultimate tensile strength versus temperature for tensile specimens extracted from the plate and the rod. Right: Uniform and total elongation versus temperature for tensile specimens extracted from the plate and the rod.*

Results of Charpy impact tests on specimens extracted from the rod and the plate are shown in Fig. 2.4.11. The ductile-to-brittle transition temperature (DBTT) is defined as half the upper shelf energy minus the lower shelf energy. It appears that the DBTT is slightly lower for the rod (-30°C) than for the plate. Specimens cut out from the plate in the rolling and transverse directions exhibit similar DBTT values, of about -15.9°C and -17.4°C, respectively. The rod exhibits significant upper shelf energy in the ductile region. Therefore, it can be concluded that the rod presents a better Charpy impact behaviour with respect to the plate. There is no difference in the fracture mode between the plate and the rod materials. The fracture mode seems to be intergranular in nature in all cases.

The plate and the rod materials exhibit similar microstructures in transmission electron microscopy. The microstructure consists of tempered martensite, which is characterized by the presence of martensite lathes and chromium carbides, which are of the type $Cr_{23}C_6$. These carbides have sizes ranging from 100 to 200nm. Yttria particles with sizes ranging from 10 to 30nm are observed. They are homogeneously distributed in the matrix made of EUROFER 97. The yttria particles are at most semi-coherent with the matrix.
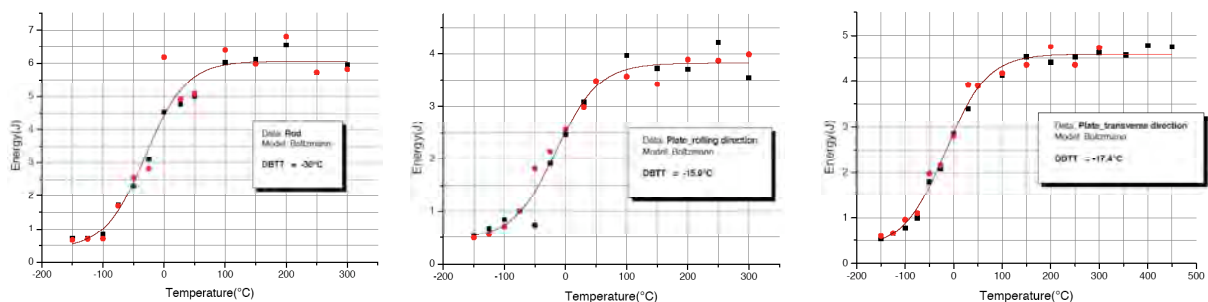
Fig. 2.4.11   *Absorbed energy versus temperature for KLST specimens extracted from (left) the rod, (centre) the plate in the rolling direction, and (right) the plate in the transverse direction.*

TW5-TTMS-006/D4: Nanocomposited ferritic steels for HT application
The aim of this project is to develop reduced activation, radiation-resistant ODS (i.e., nanocomposited) ferritic steels by powder metallurgy techniques. Such materials are expected to be used as structural materials in fusion reactors up to

about 800°C. The numerous interfaces engendered by the presence of oxide particles are expected to act as sinks for the irradiation-induced defects.

Small cylindrical ingots of Fe-12Cr-2W-(0.1-0.3-0.5)Ti-0.3Y_2O_3 and Fe-14Cr-2W-(0.1-0.3-0.5)Ti-0.3Y_2O_3 ODS ferritic steels (six compositions, in weight percent) have been prepared by mechanical alloying of pure Fe, Cr, W, Ti and Y_2O_3 powders in a planetary ball mill of the type Retsch PM100, in an argon atmosphere, and compaction of the milled powders by hot isostatic pressing (HIPping) at 1100°C for 4 hours in argon (see Fig. 2.4.12, left). The density of the ingots was found to be 99.3-99.5% of the theoretical density. All ingots contain a homogenous distribution of fine (below 5nm in size) oxide particles, as shown in Fig. 2.4.12 (right).

Charpy impact tests showed that the compacted materials exhibit very low impact energy at all temperatures. Significant improvement in fracture behaviour was obtained by annealing 12Cr ODS ferritic steels at 850°C for half an hour in vacuum. The resulting ductile-to-brittle transition temperature (DBTT) was found to be close to 0°C, associated with an upper shelf energy of 3.3J. The fracture behaviour of 14% ODS ferritic steels was found unaffected by thermal annealing. Transmission electron microscopy (TEM) observations revealed that following annealing 12Cr ODS ferritic steels contain a more homogenous distribution of smaller grains of tempered martensite. Following annealing the microstructure of 14% ODS ferritic steels appears unchanged: the materials contain a bimodal distribution of coarse grains, a few microns in size, with oxide and carbide impurities, and smaller grains, about 500nm in size. In these materials the dislocation density varies from dislocation-free areas to very dense tangles located especially at the grain boundaries.

Optical and scanning electron microscopy (SEM) observations of both groups of ODS ferritic steels showed that very small, spherical pores, located mainly at the grain boundaries, are present in some regions of the specimens. The observed pores, as well as carbon and oxide impurities concentrated at the grain boundaries, may have a detrimental influence on the mechanical properties of ODS ferritic steels. The main issue of the manufacturing route relates to the high oxygen content of the mechanically alloyed powder. Chemical analyses revealed that the elemental ODS powders contain about 0.27wt% oxygen, which cannot be reduced by milling in an argon atmosphere. It will be attempted to reduce the oxygen content by mechanically alloying either elemental powders in a hydrogen atmosphere or a master powder, prepared by gas atomization of a master alloy made of Fe-Cr-W-Ti, with Y_2O_3 particles.
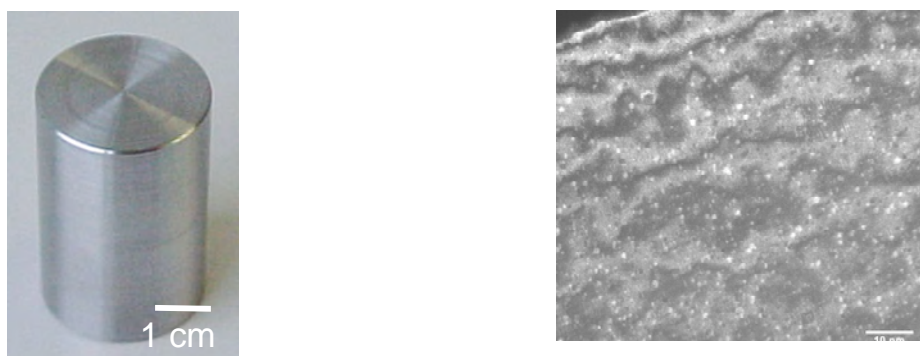
Fig. 2.4.12 *Left: Optical micrograph of an ingot of ODS ferritic steel manufactured by mechanical alloying and HIPping. Right: TEM image of the homogeneous distribution of oxide particles with a size up to 5nm.*

<u>TW5-TTMS-007/D11: Ion irradiations for verification analyses on thin foils of Fe-Cr-C model alloys</u>
In order to close the gap between modelling of radiation damage in Fe(Cr,C) model alloys and actual experiments, in view of understanding the response to irradiation of ferritic and ferritic/martensitic steels, it is proposed to irradiate two Fe-9Cr-C model alloys and one Fe-12Cr-C model alloy with ions and to investigate the resulting microstructure by transmission electron microscopy (TEM).

Materials were prepared from high purity casts. Further heat treatments were applied to obtain the desired microstructure, either ferritic or martensitic. Table 2.4.5 summarizes the preparation conditions for the six prepared types of materials.

Cast ID	Material	Ferritic structure heat treatment	Martensitic structure heat treatment
785	Fe-12Cr	1h at 950°C, 24h at 800°C	-
786	Fe-9Cr	1h at 950°C, 24h at 800°C	-
787	Fe-12Cr-0.1C	1h at 940°C, 1h at 760°C	1h at 940°C, WQ
788	Fe-9Cr-0.1C	1h at 940°C, 1h at 760°C	1h at 940°C, WQ

Table 2.4.5 *Matrix of the ferritic and martensitic model alloys. WQ: water quench.*

About 10 TEM disks, 3mm in diameter, were punched from each material. Ion implantations with 350MeV Au ions were conducted at the Hahn Meitner Institute in Berlin (Germany) at room temperature, to a dose of 0.05dpa, at 7μm below the surface. Implantation of pure Fe is still pending, due to the overload of the ion accelerator. TEM observations are in progress.

<u>TW5-TTMS-007/D15: Dislocation-defect interaction and the evolution of the deformed microstructure in Fe (development of dislocation dynamics methods)</u>
This work is aimed at simulating the effects of irradiation-induced defects like dislocation loops and/or cavities, such as voids or helium bubbles, on the plasticity of Fe by dislocation dynamics simulations.

The code microMegas from LEM-ONERA was successfully compiled and implemented in our computers. It is based on the so-called lattice model. In a first step, irradiation-induced defects were successfully simulated as a population of locked, short dislocation segments. It was observed that in the presence of obstacles in the matrix, deformation occurs by junction formation and cross slip events at the beginning of deformation and then by increase in the dislocation density as a result of forest hardening.

The next step consisted in implementing defects that are closer to a proper description of irradiation-induced defects, such as cavities and dislocation loops. A completely different approach was selected, which is based on the so-called nodal model. A new software is being developed, with a scaled down approach, in collaboration with the CEMES, France. While the lattice model allows simulations of large strains, up to a few percents of deformation, for samples that are tens of μm^3 in size, the nodal model developed in this study allows simulations of samples only up to a few μm^3 in size for strains that are negligible. However, in this latter approach the displacement step is 0.1nm while in the lattice approach it is typically tens of nanometres. In addition, the lattice model implies that the dislocation line is composed of segments that can be of only 3 types: edge, mixed and screw. In the nodal approach, segments can have any orientation, which permits for example to finely describe the interaction between an edge dislocation and a void, down to the nanometric level or below. It would allow eventually the match to molecular

dynamics (MD) simulations, which would implicitly validate the dislocation dynamics modelling approach in a self-consisting way. The MD simulations in turn will provide in a reliable way the requested information for the lattice model that allows to simulate large strains.

<u>TW5-TTMI-003/D7: Development of the test rig technology for in situ creep-fatigue measurements in the MFTM</u>
The International Fusion Materials Irradiation Facility (IFMIF) target facility and the irradiation modules will be located in a common volume called the 'test cell'. The test cell will accommodate the lithium target, a lithium tank, and the two vertical test and irradiation assemblies VTA-1 and 2, which will all be located inside a vacuum liner. The components will be surrounded by a massive gas-cooled shielding system. This project is aimed at presenting a concept for the realization of in situ creep-fatigue experiments in the medium flux test module (VTA-2) of IFMIF and also at making a first design step in producing a miniaturized actuator for axial loading of specimens. This mechanical actuator will be one of the main components of this new experiment. It will incorporate the latest developments in high quality mechanical components such as ball screw spindles, harmonic drives and electro-servo motors. One of the main difficulties relates to the very limited size of the IFMIF test modules and to the very high requirements in displacement accuracy and power.

The on-going development takes advantage of our experience in the design and operation of *in situ* experiments. An in situ actuator has been operated for many years in the PIREX facility, near the proton beam, and accumulated a high dose. Based on the history of the dismantled PIREX facility, neutronics calculations are being run to determine the integrated dose at the level of the load cell. This calculation will serve as a basis to assess the life of components in VTA-2. A technology identical to the one used for the PIREX actuator is being used for the new actuator that consists of a ball screw spindle, an anti-torsion guide, a harmonic drive and an electro-servo motor. The whole device including the actuator, a specimen and the instrumentation will be placed as a new unirradiated component into the VTA-2 module and will be used only for one experiment.

The actuator is shown in Fig. 2.4.13. All detailed drawings of the actuator have been produced and the parts and components are being manufactured. The system should be put together and tested in 2007. At the level of the specimen the dose rate will attain 10dpa per year. Due to the rapid decrease of the irradiation flux along the vertical axis, the neutron flux is expected to be much lower at the level of the electro-servo motor. Nevertheless, other components like the load cell and the strain transducer will be located close to the specimen. The survival of these components is not guaranteed in the high neutron flux of IFMIF.
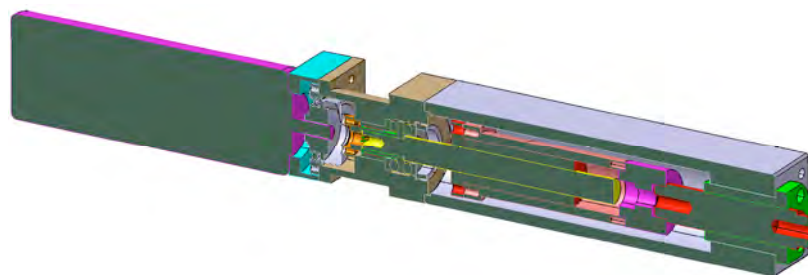
Fig. 2.4.13   *Cross sectional schematic view of the actuator drive for IFMIF. From left to right: the electromotor, the harmonic drive and the ball screw.*

TW6-TTMS-007/D9a: Molecular dynamics simulation of the dislocation-defect interaction in Fe and its dependence on the Fe empirical potential

The interaction of an edge dislocation in Fe with various types of defects has been investigated by means of molecular dynamics (MD) simulations. The defects studied were: helium, either as a gas in solid solution or in cavities (helium bubbles), voids, $a_0[100]$ dislocation loops, all 2nm in size.

Results showed that helium in solid solution up to 1.0at % has little effect on the dislocation mobility. Conversely, voids and $a_0[100]$ dislocation loops are strong obstacles to the passage of the edge dislocation. Interestingly, voids are stronger obstacles than helium bubbles at low helium contents. The bubble strength first decreases with increasing helium content, up to 2 helium atoms per vacancy, where it reaches its weakest obstacle strength of 350MPa. The release strain is also reduced to about half the value needed for the voids. With more than 2 helium atoms per vacancy, the bubble strength and release strain increase with further increase in helium content. At 5 helium atoms per vacancy, the obstacle strength of the bubbles of 800MPa overcomes the one of the voids.

Figure 2.4.14 shows snapshots from a sequence of the interaction of an edge dislocation in Fe with a 2nm helium bubble containing 5 helium atoms per vacancy. It appears that a phenomenon of loop punching takes place, in the form of emission of short dislocation segments attached to the cavity, rendering it larger than the original 2nm sphere. It occurs already during the relaxation of the sample, before straining (Fig. 2.4.14a). As the dislocation approaches, there is a dislocation reaction that repels the impinging dislocation (Fig. 2.4.14b). Finally, the dislocation can go through and escapes with significant jogs along its line (Fig. 2.4.14c). More in detail, as the dislocation approaches, the dislocation reaction triggers the formation of a dislocation segment, B, that repels the impinging dislocation, A. This can be seen in the cross-sectional view in Fig. 2.4.14d, showing segments A and B and the inside of the helium bubble, which is deformed by the internal pressure. The loop punching and subsequent mechanisms explain the extreme obstacle strength presented by helium bubbles.
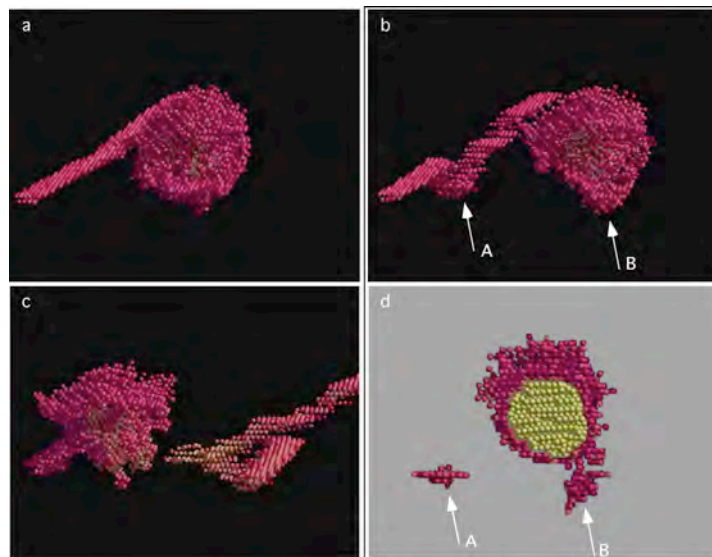
Fig. 2.4.14   *Four snapshots of the time evolution of the MD simulated interaction in Fe at 10K of an edge dislocation with a 2nm helium bubble containing 5 helium atoms per vacancy (see details in the text).*

TW6-TTMS-007/D12: Selection of experimental methods in JANNUS for 2007

This work is aimed at preparing a detailed scientific programme of ion implantation of ferritic/martensitic materials, in collaboration with a number of other European partners, in view of validating the European effort of modelling radiation damage and radiation damage effects on fusion materials using the future JANNUS facility at the CEA, France. A 20 pages common document has been issued in December 2005. It contains a literature survey of past and on-going experiments of ion implantation of ferritic/martensitic steels. The characteristics of ion implantations and the main results obtained are described. It also contains some advice on the potential use of the French facility JANNUS for investigating the resistance to irradiation of fusion materials as a function of irradiation temperature, accumulated damage and damage rate. Fifteen topics have been defined, which are distributed over four main topics: point defects, microstructural evolution under irradiation, phase stability under irradiation, and mechanical properties under irradiation.

Preliminary investigations are in progress to provide a more detailed frame for the scientific programme sketched in the 20 pages document. In particular, Infra-Red (IR) spectroscopy is being assessed as a tool to probe irradiation-induced damage in ferritic/martensitic materials, in collaboration with Prof. J. Humlicek from Masaryk University in Brno (Czech Republic). Fe(Cu) alloys will be measured to calibrate and evaluate the precision of IR spectroscopy measurements relatively to results of electrical resistivity measurements performed at CEA by Dr A. Barbu. The advantage of IR spectroscopy is that it is a non-destructive technique.

Tasks Next Step

TW4-TVM-CUSSPIT: Testing of irradiated CuCrZr/SS joints produced under different blanket manufacturing conditions

CuCrZr/SS (SS = stainless steel) joints, where CuCrZr refers to a precipitation strengthened Cu-base alloy and SS to the 316LN austenitic stainless steel, are part of the current ITER design. Their final applicability in ITER will depend on their mechanical properties before and after neutron irradiation, with respect to those of the base materials. This project is aimed at investigating the effects of different heat treatments on the mechanical properties (joint strength, fracture toughness) of unirradiated and neutron irradiated CuCrZr/SS joints and base materials. It is being performed by three European Associations: SCK-CEN (Belgium) is responsible for the neutron irradiations, the joints will be tested by VTT Manufacturing Technology (Finland) and the fracture toughness of the base materials will be measured at the CRPP. Specimens have been irradiated with neutrons at SCK/CEN to three different doses of 0.001, 0.01 and 0.1dpa. All specimens have been delivered to the Risoe National Laboratory (Denmark) and from there to VTT. The specimens are now being stored in a hot cell in VTT and will be forwarded to CRPP as soon as the radioactivity of the specimens will be low enough. Testing of neutron-irradiated base materials should take place in summer 2008 via three point bend fracture experiments.

TW5-TVM-COMADA: Investigation of the effect of creep fatigue interaction on the mechanical performance and lifetime of CuCrZr

The CuCrZr alloy is a candidate heat sink material for the first wall of ITER. Therefore, extensive research was conducted in the past on the fatigue properties of the CuCrZr alloy, under relevant ITER operating conditions. Unfortunately, only few data exist on its creep-fatigue behaviour, mainly due to the very costly testing involved, as the tests may run for months. This project is aimed at checking if a

prediction method based on pure fatigue and creep tests only can be found or eventually modified to fit the results. The project consists of two different parts: (1) a literature survey with an analysis of the existing data, (2) an experimental part in which selected data points will be measured in order to verify the suitability of life prediction for the creep-fatigue tests.

The first part of this project has been completed according to the program schedule. It consisted in reviewing the mechanical properties of CuCrZr alloys in fatigue, creep and creep-fatigue testing conditions. A collection of ITER data files, reports, review articles and papers on fatigue and creep-fatigue behaviour of CuCrZr alloys, has been provided by the EFDA. Three materials files on the creep, fatigue and creep-fatigue properties of CuCrZr have been revised. These files are now part of the ITER Materials Properties Handbook (MPH), which is the materials database for the design of ITER. The collected data have been analysed using the time-based approach, as proposed by the French RCC-MR design code, to verify the suitability of the linear damage accumulation rule for lifetime predictions in creep-fatigue tests. This method assumes that fatigue and creep damages are linearly additive and that a lifetime prediction can be made on the basis of the partition of pure creep and pure fatigue lifetimes. It requires knowledge of the relevant fatigue life equations, the cyclic hardening curve and the creep equation. The method can be applied with more accuracy if the particular relaxation curve at the holding point is known, which of course requires the completion of at least one partial creep-fatigue test. Creep-fatigue data are very scarce. On the basis of the few data available it was found that fatigue and creep damages are actually not linearly additive and that the above method needs to be improved before it can be applied to CuCrZr alloys.
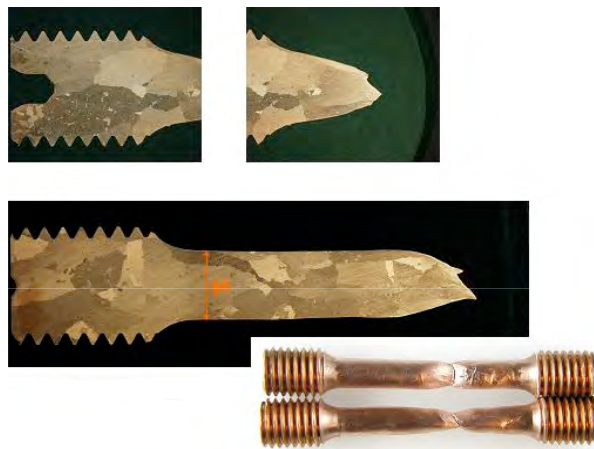
Fig. 2.4.15   *Cross sectional micrographs of specimens with a microstructure made of very large grains.*

As a result of the first part of this project, an experimental testing program was prepared with the aim of producing the additional data points needed to make reliable predictions for the first wall of ITER. The material necessary for the experimental part of the project has been ordered by CEA (Grenoble), The material was delivered by the KME company and heat treated to reproduce the manufacturing route for the first wall sections of ITER. Unfortunately the resulting grain size was up to 20mm (see Fig. 2.4.15) and then of the order of the size of the test specimens. As a consequence, the testing program had to be stopped. It was decided to re-order new material and to repeat the heat treatments, using a lower annealing temperature. Mechanical testing shall be achieved in 2007. After the experimental part is completed and the French partners have also delivered their results, a final analysis will be done, in terms of lifetime prediction.

TW6-TVM-LIP3: Modification of ITER materials documents

Over the past few years, a number of ITER Materials Properties Handbook (MPH) files have been created. Some of the existing files on the mechanical properties (fatigue, creep, creep-fatigue) of unirradiated CuCrZr have been produced by the CRPP. ITER MPH files need to be constantly updated. The available data will be reduced to data produced under well-accepted standards and for which a good traceability exists. The new produced data, when available, will be introduced into the datasets, the Figures of the MPH files will be updated, mean curves and data equations will be re-calculated, and new recommendations for the designers will be proposed. This project will consist in revising the documentation available on the production of joints of the following types: SS to SS (stainless steel), SS to CuCrZr and Be to CuCrZr. New MPH files will be written, focused on the main properties of interest: fracture toughness, tensile and fatigue properties. The results of the project TW4-TVM-CUSSPIT will be directly inserted into the corresponding MPH files.

2.5 Superconductivity

In 2006, the conductor test in SULTAN was well publicised, with the disappointing performance of the ITER-type cable-in-conduit samples and the successful test of the alternative conductor layout developed at CRPP. The assignment of the Dipole test facility to CRPP was also the source of intense activities, both for planning of the new plant and for tests of the dipole conductors in SULTAN. For ITER as well as for the Dipole, the SULTAN test results in 2006 are the drivers for the 2007 work programme not only in the CRPP Superconductivity group, but also in the whole magnet community of fusion.

The activity on high temperature superconductors (HTS) continued, but the priority has been shifted. The test campaigns in the JORDI test facility are completed, providing a unique, experimental database for the analysis of current imbalance on ITER conductors. Studies and analysis activities are carried out in the field of ac losses, conductor to coil comparison and hydraulic behaviour in dual channel conductors.

2.5.1 Underlying Technology

Transverse heat transfer coefficient between bundle and central channel

A superconducting sample ("Low Cost Joint", LCJ) was instrumented at CRPP with the specific aim to investigate the thermal hydraulic properties of its conductor, an ITER-type dual channel cable-in-conduit conductor (CICC) in which the coolant flows in parallel in the central channel and in the annular bundle region. The LCJ sample was tested in the CRPP SULTAN Facility. Thanks to the special instrumentation for thermal hydraulic (TH) measurements, the transverse heat transfer coefficients were assessed using a new method.

The TH measurements are performed at zero SULTAN background magnetic field, zero current in the sample, and mass flow rate from 2g/s to 8g/s, see Fig. 2.5.1. Special runs are performed using the heater H0 to calibrate the thermometers on the jacket, i.e. to offset the effect of inadequate thermalisation of the sensor leads due to severe space restrictions. The heat transfer coefficients in the azimuthal

direction h_{BB} (between subcables in the bundle) and in the radial direction h_{BH} (between bundle and central channel) are assessed by a steady state analysis. This is possible because there are enough thermometers along the jacket circumference and along the sample axis so that they can be reliably calibrated.

The temperature sensors are placed along the conductor jacket with a periodic pattern, see Fig. 2.5.1, and the Fourier analysis is applied to analyse the measurements. The first Fourier coefficient ($A1_i$) corresponds to the average temperature variation in the bundle, and the module of the second coefficient ($A2_i$) is proportional to the temperature difference among subcables in the bundle. The heat transport is modelled assuming that this takes place in 6 parallel cooling channels, located under the thermometers in the cable bundle, and in the central hole, with steady state conditions, incompressible flow, negligible transverse flow, and constant thermophysical and transport properties. The radial heat transfer coefficient is $h_{BH}=C1\ k_{BH}$ and the azimuthal heat transfer coefficient is $h_{BB}=C2\ k_{BB}-C3\ h_{BH}$, where C1, C2 and C3 depend on conductor geometry and helium properties and k_{BH} and k_{BB} are obtained from the exponential fit of the Fourier coefficients along the sample axis, i.e. $A1_i=ae^{-kBH X}$ and $A2_i=be^{-kBB X}$. The analysis results for h_{BB} and h_{BH} are plotted in Fig. 2.5.2.
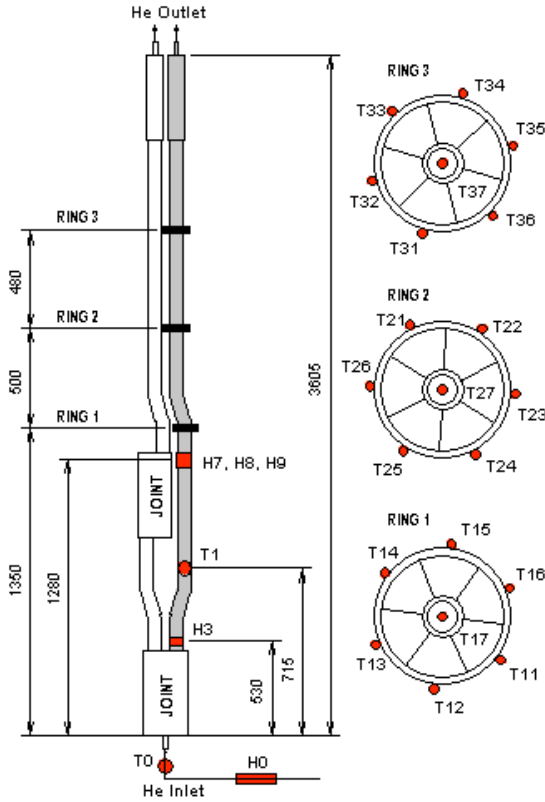
Fig. 2.5.1 *Schematic experimental set-up of the LCJ sample in SULTAN. Only the right leg is used for TH measurements. Helium enters the sample from the bottom, is heated up by 5 resistive heaters producing a variety of heat slugs (H0, H3, H7, H8, H9) and the warm front propagates along the sample length. The heater H7 is inside the central channel, H8 is a local heater on the jacket. There are 21 temperature sensors at three rings along the sample (Ring 1, Ring 2 and Ring 3).*
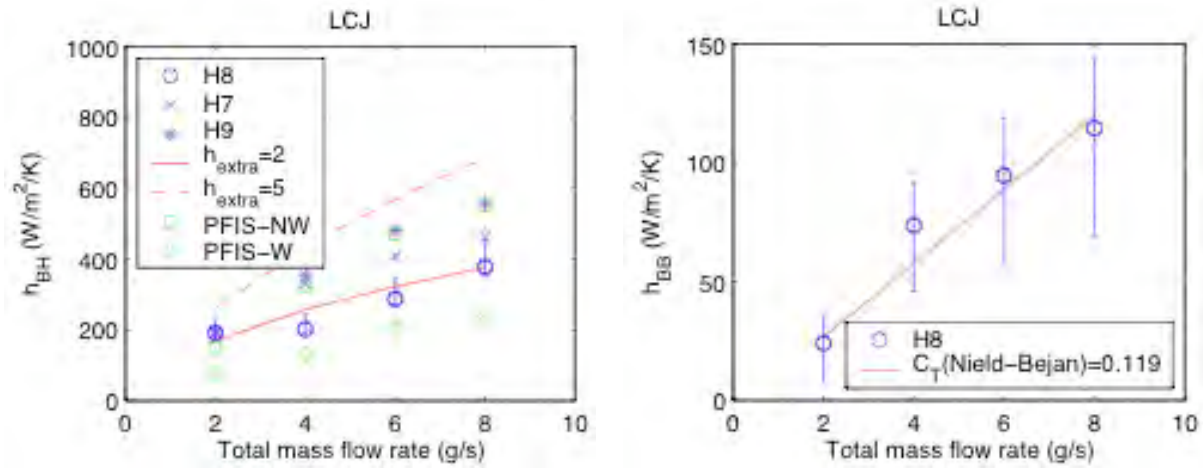
Fig. 2.5.2   *Left: Azimuthal heat transfer coefficient between subcables in the bundle using the heater H8. The fit of the experimental data using the porous media correlation by Nield-Bejan is also shown. Right: Radial heat transfer coefficient between bundle and hole using the heaters H7, H8 and H9. The results of the PFIS conductor, also tested in SULTAN, are included for comparison (PFIS-NW without subcable wraps, PFIS-W with subcable wraps). The LCJ conductor is without subcable wraps.*

This study, which integrates and concludes the work started with the ITER PFIS conductor, also tested in SULTAN, has shown that: (a) the special instrumentation allows precise measurement of the local temperatures as well as the calibration to obtain reliable steady state values, (b) the analytical solution for heat exchange among parallel pipes in a system with an arbitrary number of channels allows to derive the transverse heat transfer coefficients, and (c) the applied method provides a simple and powerful means to extrapolate and predict transverse heat transfer coefficients of cables.

Development of a react&wind conductor

The sensitivity of Nb_3Sn to longitudinal strain is an issue for the cable-in-conduit conductors (CICC) using a steel jacket, which must be manufactured according to the wind&react method. The mismatch of the thermal expansion of steel and Nb_3Sn between the heat treatment and operation temperature leads to a high compressive strain and a reduction of the current carrying capability by a factor of two. Another drawback of the large Nb_3Sn CICC is the irreversible, transverse load degradation, explained in terms of filament cracking due to local bending of the poorly supported strands in the cable, between two crossovers.

To cure the high compressive, longitudinal strain in steel jacketed conductors, it is mandatory to assemble the steel to the cable after the heat treatment, i.e. to switch from the wind&react to the react&wind method. To minimize the bending strain during manufacturing and winding after the heat treatment, the Nb_3Sn strands must be as close as possible to the neutral bending axis.

The transverse load degradation can be effectively cured limiting the cable displacement under load by means of low void fraction and flat cable geometry. As an ultimate measure, the void fraction of a multistage cable can be filled by a low melting alloy, providing full support to the strands and preventing filament damage from local bending.

An alternative conductor following the above design guidelines and the operating requirement for the ITER TF coils was laid out at CRPP in 2005. The prototype manufacture was completed in February 2006 and the assembly of a SULTAN sample followed in spring 2006. The test in SULTAN was carried out in June 2006, see section 2.5.2 (first subsection).

About 40kg of Cr plated Nb_3Sn strand (two billets) has been procured. The standard strand layout had to be adjusted by the supplier to match the large diameter and the low Cu:non-Cu ratio. The two-stage flat cable is compacted down to about 16% void fraction, with some deformation of the strand shape. The outer layer of soft, Cr plated copper wires is twisted in opposite direction compared to the flat cable. With 42 copper wires, the outer layer is not fully closed and some gap between the copper wires is left to improve the penetration of the low melting alloy. For the heat treatment, three 3.5m long sections of cable are bent at 4.5m radius and straightened after heat treatment to reproduce the procedure for the ITER conductor/coil manufacture. No residual torsion is observed in the cable after heat treatment.

A folded, 2mm thick strip of steel is closed around the cable by a longitudinal weld. Two conductor sections are then impregnated with a defined amount of BiSn alloy in the furnace at 200C, leaving a rectangular cooling channel, $\approx 100mm^2$, underneath the jacket weld. The two 3.5m long conductor sections are connected and assembled to a SULTAN sample, see Fig. 2.5.3. After the first test campaign, the conductor section without BiSn filling is assembled with one of the filled sections for a straight comparison of the beneficial role of the filling.
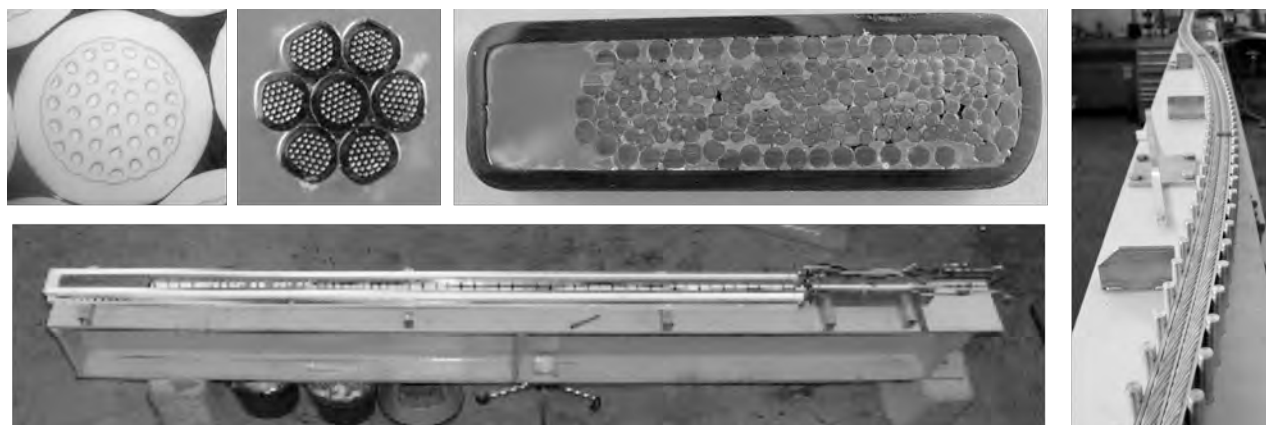
Fig. 2.5.3   *Various steps of conductor manufacture. From top left to bottom right: strand, cable and finished conductor cross section, cable section bent for heat treatment and SULTAN sample, ready for cool down*

The target J_c for the strand at 12T, 4.2K was set at $1000A/mm^2$. Five I_c specimens from two billets have been heat treated together with the cable at 185C/50hrs, 460C/50hrs, 575C/150hrs and 650C/200hrs. At 12T, 4.2K and $10\mu V/m$, the I_c of the five specimens is in the range of 672-845A. The Cu:non-Cu is 0.807 and 0.833 for the two billets respectively. The weighted J_c of the strands used in the cable is $1075A/mm^2$. The n index is 15 and 22 for the two billets.

After heat treatment, the Residual Resistivity Ratio (RRR) of the Cr plated Nb_3Sn strand is 80 (295K/18K). For the Cr plated Cu wires around the flat cable, RRR=260 (295K/4.2K). The Bi52Sn48 alloy (melting point 138C) has a resistivity of

$6.55 \cdot 10^{-8} \Omega \cdot m$ at 4.2K, over one order of magnitude higher than conventional solder alloys and comparable to CuNi5 and CuSn6 alloys.

2.5.2   Technology Tasks

SULTAN operation 2006 (TW6-TMSC-SULTAN)

The operation of the SULTAN facility in 2006 is covered by an EFDA technology task. Only European samples have been tested. In the testing period reported here (October 2005 – October 2006), the following samples have been tested in multiple campaigns:

1. Thermal-hydraulic test of Low Cost Joint (LCJ) sample
2. TFAS1, TF Model Coil type conductor with advanced strands (three campaigns)
3. TFAS2, TF Model Coil type conductor with advanced strands (two campaigns)
4. Plan B, alternative, R&W conductor (two campaigns)
5. SUBSAM I, high field prototype conductor for dipole (two campaigns)
6. SUBSAM II, low field prototype conductor for dipole

The results of 1 were discussed in section 2.5.1. The TFAS results are highlighted under 2.5.2 (under the heading "Use of high temperature superconductors for fusion applications"). The main results of 5 and 6 are attached to section 2.5.2 (under the heading "Two subsize sample manufacture and testing". The results of 4 are given below.

Test results of a react&wind conductor

The dc test in SULTAN includes both current sharing temperature and critical current in the background field of 8, 9, 10 and 11T. At the design operating current of 48kA, the average field over the conductor cross section is enhanced by 0.17T, i.e. the average self-field factor of the sample is $k_{av}=3.5\cdot10^{-3}$T/kA. The take-off electric field at the design operating current is about 25μV/m and decreases below the 10μV/m criterion for current above 60kA. The *n* index is low, about 7 at 48kA ($435A/mm^2$).

The dc test results are gathered in Fig. 2.5.4 as critical current vs. temperature at 11T background field for both the filled and non-filled conductor sections. The performance matches the prediction made starting from the strand results without applying any additional longitudinal strain or transverse load degradation factors. The non-filled conductor has the same performance within the test accuracy of the filled conductor, with fully supported strands. The *n* index at 48kA ($435A/mm^2$) is moderately low, about 7 for the filled conductor and 13 for the non-filled conductor. Even after 1000 load cycles at the nominal operation of 48kA/11T, the performance of the non-filled conductor did not change. This result proves that the target of the development has been fully achieved and that the cable geometry (flat cable with low void fraction and superconductor segregated from copper) is able alone to prevent transverse load degradation, even without the ultimate measure of impregnating the cable with low melting alloy.

The ac loss is, as expected, lower in the non-filled conductor, see Fig. 2.5.5. A much better result can be achieved using an insulating strip as a core of the flat cable. In the prototype manufacturing this measure was skipped for cost and schedule reasons. The large loss reduction in the non-filled conductor after cyclic load

suggests that the transverse load on the cable has been large enough to break the low resistance contact points in the virgin state, but not large enough to cause bending damage to the filaments.
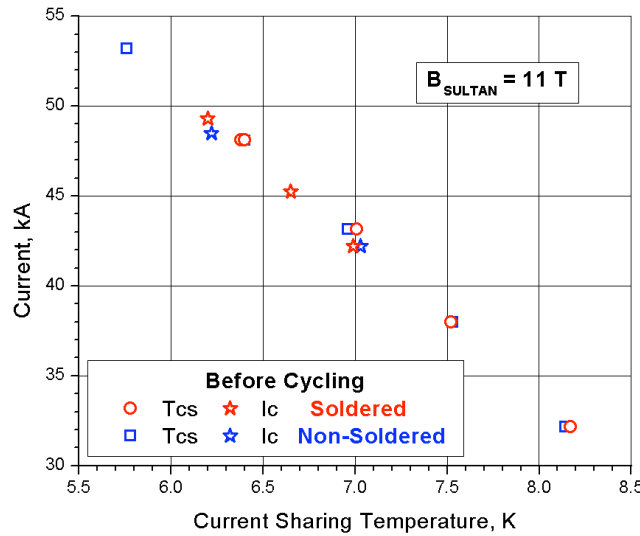
Fig. 2.5.4   *Critical current and current sharing temperature for both filled and non-filled conductors at 11T.*

The non-Cu operating current density, scaled to an average field of 11.15T, is reported in Fig. 2.5.6 as a function of the temperature. The results of the last generation of ITER Nb$_3$Sn CICC (TFAS conductors) and the TF Model Coil conductor (TFMC) are also included for comparison. At the ITER design current density of 286A/mm^2, the new R&W prototype conductor achieves T$_{cs}$=7.9K, while the CICC are in the range of 4.8-5.5K (below the ITER specification of 5.7K). At the operating current density of 435A/mm^2, the new conductor has T$_{cs}$=6.3K. In other words, the ITER specification can be largely exceeded even at 50% higher operating current density, which means a saving of over 180t Nb$_3$Sn strand.
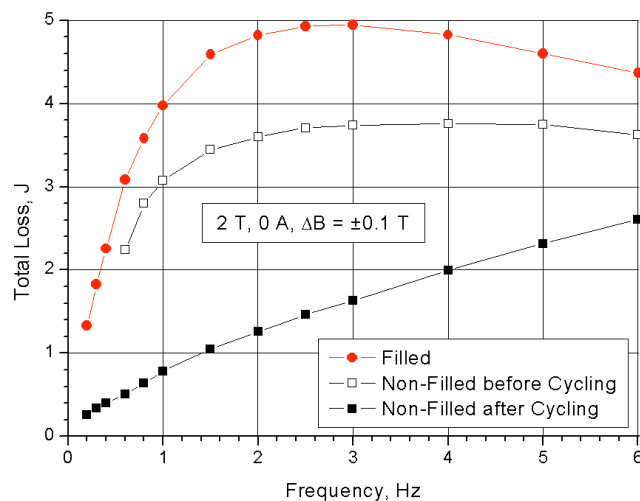
Fig. 2.5.5   *AC loss in superimposed dc and ac fields measured by gas flow calorimetry in both conductors. For the non-filled conductor, the ac loss is also reported after cyclic load.*
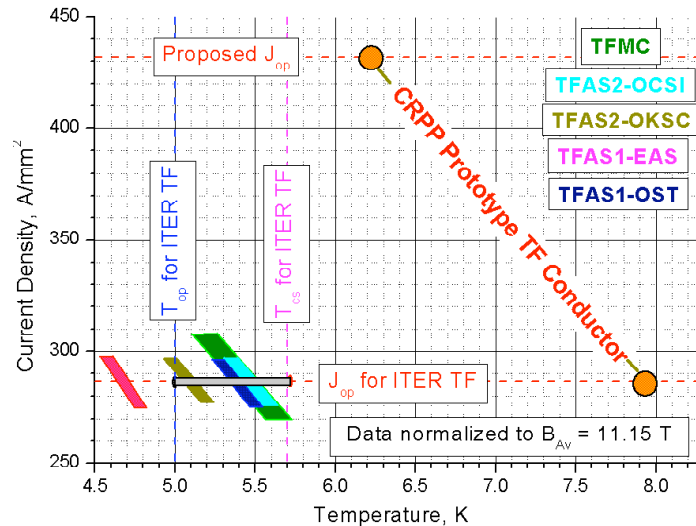
Fig. 2.5.6   *DC performance of the react&wind conductor in comparison with the ITER CICC. The newly developed conductor can work at 50% higher current density with higher temperature margin than the ITER CICC made from similar strands.*

A capacitor bench is discharged on the SULTAN pulsed coils (the same used for the ac loss test) to generate a field transient of about 120ms duration and controlled amplitude. The current in the sample is raised to 48kA and the temperature is adjusted to obtain 0.3, 0.5, 1 and 1.5K margin to the measured T_{cs}=6.35K. The amplitude of the field transient is raised in small steps till a quench occurs in the sample. The quench is driven by the deposited heat (ac loss). As the filled conductor has much higher ac loss than the non-filled one, the transient field stability test is applied to the filled conductor. Despite the large ac loss, the stability is more than satisfactory in the filled conductor. To withstand the field transient of the ITER plasma disruption for TF conductor, $0.12T^2$/s, the required temperature margin, T_{cs}-T_{op}, is negligibly low, in the range of 0.1K.

Preparation of two TF Conductor Qualification samples (TW5-TMSC-NEFSS and TW6-TMSC-TFPRO)

In the task TFPRO, CRPP is committed to assemble a sample from two conductor sections supplied by EFDA. The conductor layout (ITER TF) is identical for both sections, using respectively a strand made by OST and EAS. The conductor sections are expected to be delivered to CRPP by the end of 2006.

In the task NEFSS, CRPP procures two conductor sections from the Russian supplier VNIINM, according to the spec of the ITER TF conductor, made with Russian Nb_3Sn strand. The conductor sections are later assembled at CRPP into a SULTAN sample with the same procedure as for the TFPRO. In September 2006, VNIINM delivered an intermediate report with successful results for the development of high current density Nb_3Sn (J_c @ 12T, 4.2K in the range of 950-1020A/mm^2) and manufacture of dummy cables at the subcontractor VNIIKP.

The sample assembly procedure at CRPP includes the compaction of conductor ends with crimping ring before the heat treatment to prevent any cable/jacket slippage due to the mismatch of thermal expansion of steel jacket and Nb_3Sn cable, see Fig. 2.5.7. Such slippage must be avoided, as it would affect the relevance of the

SULTAN samples with respect to the actual coil manufacture, where slippage does not occur in the wound conductor.
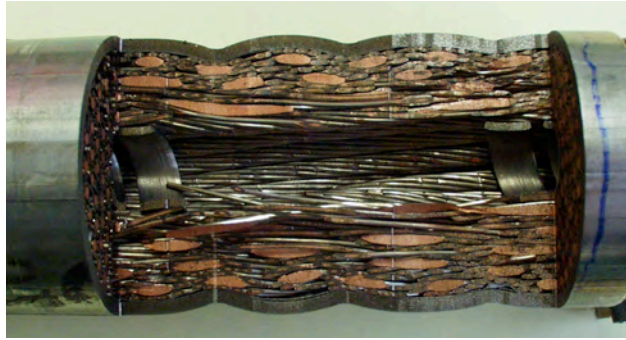
Fig. 2.5.7   *Longitudinal section of a trial compaction using crimping rings of various thickness to prevent cable/jacket slippage during the heat treatment.*

The heat treatment will be carried out in the CRPP furnace. Afterwards, the electrical termination and joint will be assembled according to a procedure proposed by CRPP and adopted by ITER. Clamping, instrumentation and wiring will complete the assembly work. A full set of CATIA drawings has been prepared for all the components. A 3D view of the assembled sample is shown in Fig. 2.5.8.

Fig. 2.5.8   *A SULTAN sample of ITER TF conductor after final assembly.*

Advanced strand test (TW3-TMSC-ASTEST)

In order to study the possibility to counterbalance the performance drop in large Nb_3Sn CICC's observed after cyclic loading by the use of advanced (i.e. high current density) Nb_3Sn strands, two European full size conductors TFAS-1 (EAS, OST strands) and TFAS-2 (OCSI, OKSC strands) were fabricated and tested in the SULTAN facility. As a basis for the comparison of Nb_3Sn strand and CICC performances, the critical current, the residual resistivity ratio, and the copper to non-copper ratio of the recently developed advanced strands supplied by European Advanced Superconductors (EAS), Oxford Superconducting Technology (OST), and Outokumpu Italy (OCSI) have been tested at CRPP. To complete the picture the EAS and the OKSC witness strand (Outokumpu Finland) results from the heat treatment of the TFAS-1 and TFAS-2 full size samples are also presented. For the heat treatment as well as for the critical current measurement, the advanced strands were wound onto Ti6Al4V ITER barrels.

The critical current of the Nb_3Sn strands was measured by the standard four-probe method. An electric field criterion of $0.1\mu V/cm$ was used to define the critical current. The n value, defined by the expression $E = E_c(I/I_c)^n$ (E: electric field, $E_c = 0.1\mu V/cm$, I: current, I_c: critical current) was determined in the electric field range of $0.1 - 1\mu V/cm$. The residual resistivity ratio is defined as the ratio of the

resistances measured at room temperature and 18K, i.e. slightly above the critical temperature of Nb_3Sn. The copper to non-copper ratio was determined by a weighing and etching procedure.

The main results of the strand characterisation are listed in Table 2.5.1. The diameter of each of the advanced strands is 0.81 mm. The critical currents and the n factors, quoted in the table, were measured at 4.2K and 12T. The upper critical fields (B_{c2}) at 4.2K were estimated by means of Kramer plots.

Strand	Cu:non-Cu	RRR, Cr/no-Cr	I_c (A)	n	B_{c2} (T)	Heat Treatment
EAS⁻ NSTT8305-HK002/A1	0.93	95 / 230	215.7	41	29.94	570°C, 250h/620°C, 350h
		95 / 230	189.2	41	30.76	HT-A*, 660°C, 100h
OST-7845	1.12	130 / 285	268.4	34	28.86	HT-A*, 660°C, 100h
OST-7878	-	-	276.0	34	-	HT-A*, 660°C, 100h
OCSI - NS026001	1.52	95 / 240	210.5	16	27.35	HT-B**
OKSC - NT6807	-	-	251.0	16	28.76	HT-B**

*210°C, 50h/340°C, 25h/450°C, 25h/575°C, 100h,
**185°C, 32h/460°C, 48h/575°C, 100h/650°C, 175h

Table 2.5.1   *Main results of strand test*

In Fig. 2.5.9, the critical current densities of the different advanced Nb_3Sn strands are shown as a function of magnetic field for a temperature of 4.2K. The critical current densities found for the OCSI, OKSC and OST strands, fabricated by the internal tin route, reach values well above 1000A/mm^2 at 4.2K and 12T. As expected, the critical current density achieved in the EAS strands, fabricated by the bronze route are considerably smaller than those measured in the internal tin strands. The heat treatment used for the TFAS-1 full-size conductor is considerably shorter than that proposed by the manufacturer (see Table 2.5.1). Consequently, the critical current density of the EAS-TFAS-1 witness strands of 709A/mm^2 at 4.2K and 12T is approximately 12% lower than the value of 808A/mm^2 obtained for the long heat treatment.
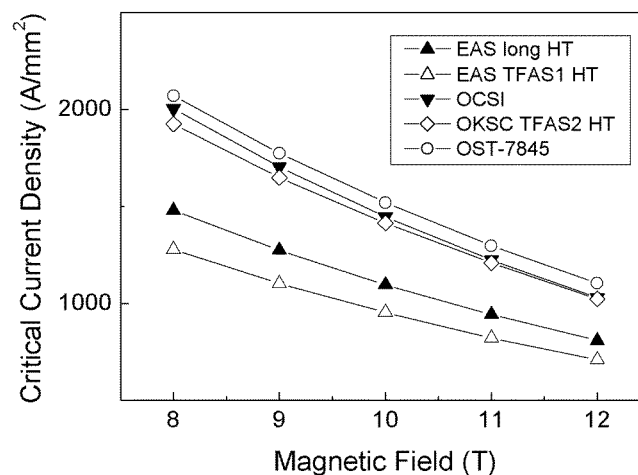
Fig. 2.5.9   *Critical current densities of the advanced Nb_3Sn strands, measured at a temperature of 4.2K, as a function of applied magnetic field.*

For all investigated Nb_3Sn strands, it has been found that different combinations of magnetic field and temperature leading to identical critical current densities resulted in the same n values to a first approximation. This behaviour is illustrated in Fig. 2.5.10. The dependence of the n factors on the critical current density can be well described by an expression of the form $n(J_c)=1+aJ_c^b$, where the critical current density is in A/mm^2. The parameters are gathered in Table 2.5.2.

Strand	a	b	Comments
EAS	4.61	0.328	Long heat treatment
EAS	5.15	0.318	TFAS-1 heat treatment
OST-7845	3.00	0.347	TFAS-1 heat treatment
OCSI	0.33	0.541	TFAS-2 heat treatment
OKSC	2.37	0.277	TFAS-2 heat treatment

Table 2.5.2 *Parameters for the n (J_c) dependence in Nb_3Sn strands.*
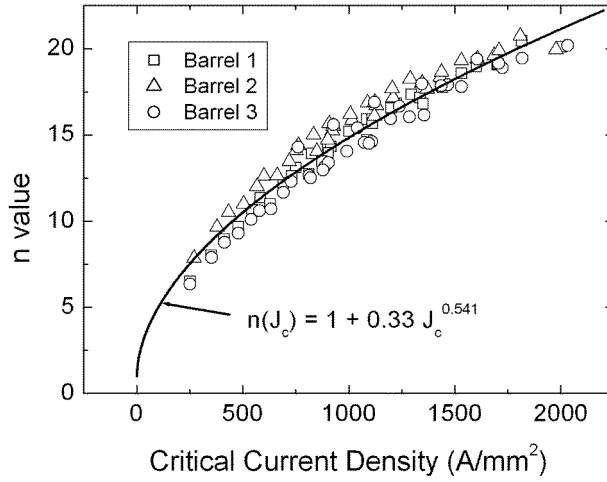
Fig. 2.5.10 *The n values of three advanced OCSI Nb_3Sn strands as a function of the non-copper critical current density. The scatter in the n values of the three OCSI strands is approximately 20%. The dependence of the n values on the critical current density can be well represented by the expression $n(J_c)=1+0.33J_c^{0.541}$.*

Attempts to measure the critical current of the advanced strands in a temperature-variable cryostat proved to be difficult because of the weak thermal contact of the strands to the ITER barrels and the heat generation in the contacts and the current leads. In the case of the OCSI strands the estimated systematic errors in the strand temperature and the corresponding uncertainty in the critical current were low enough that the data can be used to estimate the strand performance at elevated temperatures. In Fig. 2.5.11, the critical current of the OCSI strand is shown as a function of temperature for fields between 8 and 12T. The estimated errors of the strand temperature and the critical current are indicated in the figure. The critical currents, measured at CRPP, are in line with the results of measurements performed at Durham University.
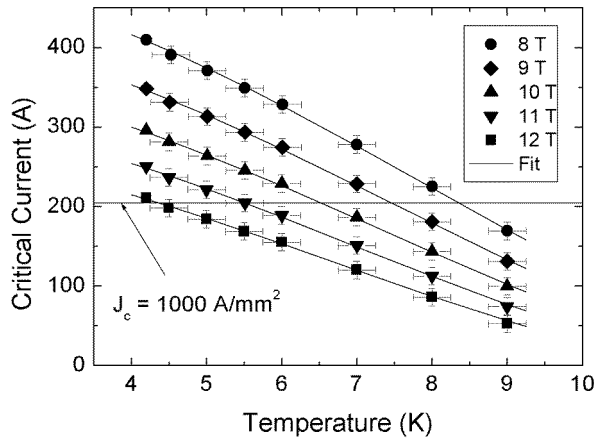
Fig. 2.5.11 *Critical currents of the OCSI Nb₃Sn strands versus temperature for applied magnetic fields between 8 and 12T. The fit lines are based on the constant strain ε_{barrel}.*

Joint resistance distribution (TW1-TMC- JSPREP)

JORDI (JOint Resistance DIstribution) is the CRPP test facility for the measurement of contact resistance distribution in full-size, ITER type conductor terminations. The actual motivation to measure the resistance distribution under imposed current balance in a large, demanding experiment is the possibility to deduce the current distribution in normal operation for a coil working under imposed voltage.

Three samples have been prepared starting from three large size cable-in-conduit conductors (CICC). For samples #1 and #3 the CICC is made from the same NbTi strand and has different cable patterns, see Table 2.5.3. The Nb₃Sn CICC for sample #2 has a braided cable pattern. For sample #1 and #2, the basic current carrying element is made from the first cable stage after cutting the segregated copper, leading to 96 and 42 elements respectively. For sample #3, two 2nd cable stages are bundled to form each of the 60 current carrying elements.

	Sample #1	Sample #2	Sample #3
Strand type	NbTi	int. Sn Nb₃Sn	NbTi
Strand diameter, mm	0.73	0.70	0.73
Strand coating	Ni	Cr	Ni
# of sc strands	864	588	1440
# of Cu wires	96	924	-
Cable pattern	(1+9)x4x4x6	((29x7)+49)x6	3x4x4x5x6
Sub-cable wraps	No	No	Yes
Pitch sequence, mm	45/166/248/350	380/160/390	42/86/122/158/490
Void fraction, %	41	37	33
# of current elements	96	42	60
# of strands/element	9	14	24
Void fraction in joint, %	35	30	25
Joint length, mm	380	392	420
Max. current/element, A	104	238	166
Max. current/strand, A	12	17	7

Table 2.5.3 *Layout of conductors and samples.*
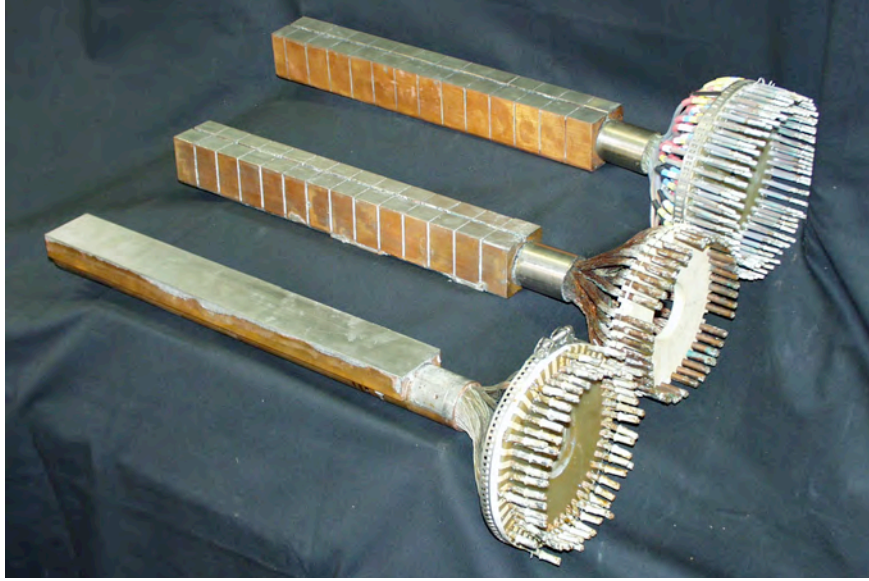
Fig. 2.5.12 *The three JORDI samples (half termination) before installing in the test facility.*

The termination (half joint) for sample #1 and #2 is made according to the CRPP design, also used for the SULTAN short length samples made of the same conductors. The surface of the compacted cable is soldered to segmented copper blocks. For sample #2 the heat treatment is carried out before assembling the joint, with the cable end opened into the 42 elements (braids). Sample #3 is made by cutting a SULTAN sample and opening the short section of cable extending from the joint, which is prepared by swaging the cable into a 5mm thick, high resistivity CuZr sleeve to low void fraction. The three "half joints" are shown in Fig. 2.5.12, before assembling with the return current lead.
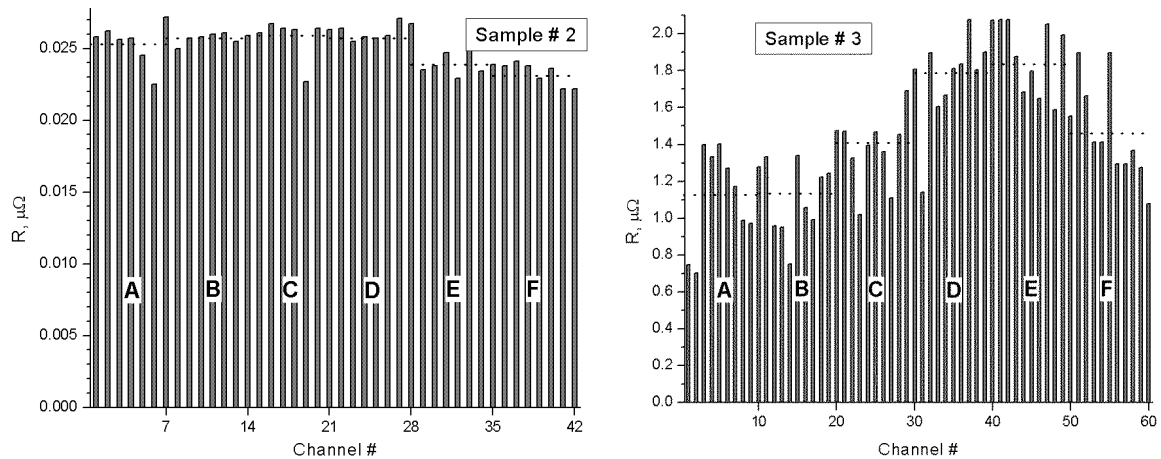
Fig. 2.5.13 *Histograms of channel resistance, R_c, versus channel number (current carrying element) for sample #2 and #3.*

The results of samples #2 and #3 are presented in Fig. 2.5.13 as histograms of channel resistance, R_c, versus channel number (current carrying element). The channels are numbered according to the six main sub-cables (petals) in the CICC, named from A to F. For example, the first 16 channels in sample #1 belong to the

same petal, A. In sample #2 and #3, this is the case for the first 7 and 10 channels respectively. As expected from the SULTAN test results on joints, the average value of R_c is much smaller in sample #1 and #2 (CRPP layout) than in sample #3. The spread of R_c (standard deviation) is much smaller in the Nb_3Sn sample than in the NbTi samples, possibly due to the high resistivity bronze layer around the filaments, which dominates the overall resistance (another possible interpretation is the positive effect of the braided pattern). The impact on R_c of the high resistivity CuZr sleeve of sample #3, practically "in series" with the contact resistance of the cable, can be recognized in Fig. 2.5.13, where the spread of results is large, but the lowest value is still very large, about $0.7\mu\Omega$.

	Sample #1	Sample #2	Sample #3
Av. channel conductance, G_c	22.4MS	40.1MS	0.736MS
Av. conductance per strand	2.5MS	2.8MS	31kS
Max to Av. G_c (OL_c)	3.55	1.12	1.93
Est. joint resistance, R_{jJORDI}	0.47nΩ	0.6nΩ	22.6nΩ
Meas. joint resistance, $R_{jSULTAN}$	0.2nΩ	0.75nΩ	18nΩ
Av. R_p in a sample,	62.9nΩ	24.9nΩ	1.46$\mu\Omega$
Relative Stand. Dev of R_p	54.0%	4.2%	19.2%
Av. R_c in a sample,	0.13$\mu\Omega$	25.0nΩ	1.45$\mu\Omega$
Relative Stand. Dev of R_c	135%	5.7%	25.2%

Table 2.5.4   *Summary of resistance distribution results.*

The overall joint resistance may be described as a parallel resistance of all the channels. In Table 2.5.4, the resistance of half-joint from the short length sample test in SULTAN, $R_{jSULTAN}$, is compared with the resistance calculated from the parallel resistance of all R_c from the JORDI test, R_{jJORDI}. The qualitative agreement is satisfactory. The relative standard deviation (coefficient of variation) is reported for both R_c and R_p (R_p is the mean value of R_c within a petal, dotted lines in Fig. 2.5.13): the spread among the average petal resistance, R_p is actually smaller than the spread of R_c within the individual petals, i.e. the highest level of current imbalance is within the petal, not among the petals.
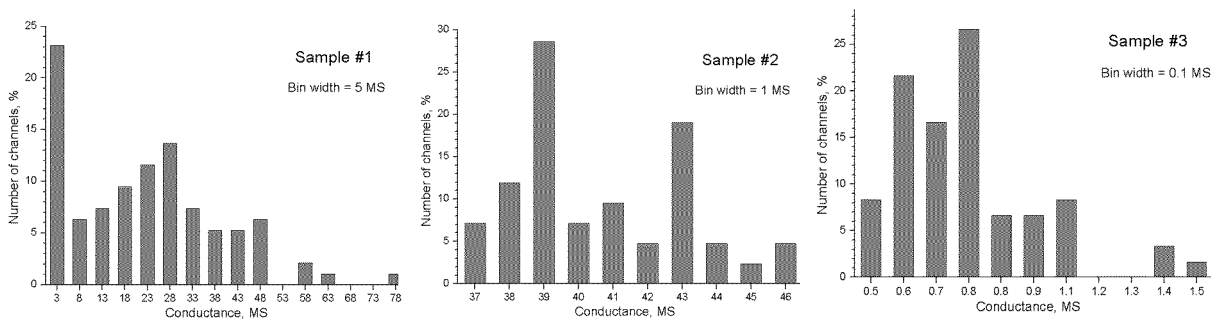
Fig. 2.5.14   *Histograms of G_c (population statistic), normalized to the total number of channels in each sample.*

The distribution of the channel electrical conductance, $G_c=1/R_c$, gives a straight picture of the current distribution in a dc winding connected by similar termination. The plots in Fig. 2.5.14 show the histograms of the G_c distribution in

terms of channel counts, normalized to the total number of channels in each sample (population statistic). Note the different range of G_c and the different bin widths in the three plots. The current overload in a channel, OL_c, is defined as the ratio between the highest and the average G_c in a sample, see Table 2.5.4. In NbTi CICC operating in the range of self-field induced sudden take-off, where current re-distribution cannot take place locally, the OL_c gives a measure of the performance degradation.

Use of high temperature superconductors for fusion applications

The successful test of a 70 kA high temperature superconductor (HTS) current lead demonstrator, reported in 2004, motivated the ITER International Team to foresee the use of HTS current leads for the magnet system of ITER (TF, CS and PF coils). In collaboration with the Forschungszentrum Karlsruhe the final design of HTS current leads for ITER will be elaborated (Task TW4-TDS-CLDES). In the task TW5-TMS-HTSMAG, the limitations of the operating temperature of anisotropic Bi-2223 tapes in future fusion reactors beyond ITER have been studied. Moreover, the performance of industrially fabricated Bi-based HTS has been investigated as a part of the task TW5-TMSC-HTSPER.

Final design of HTS current leads for ITER (TW4-TDS-CLDES)

In the task TW4-TDS-CLDES, the optimum operating conditions for ITER HTS current leads, have been determined, including the possibility of using the design of the 70kA HTS current lead demonstrator also for the CS and PF current leads of ITER, operated in pulsed mode. In the present study, the length of the HTS part has been kept constant at a value of 0.6m independent of the warm end HTS temperature. The design value of the critical current is 95.5kA at the envisaged HTS warm end temperature. The outline design of the 70kA HTS current lead demonstrator provided maximum magnetic fields of 157.4 and 68.1mT parallel and perpendicular to the broad face of the AgAu/Bi-2223 tapes, respectively. The current carrying capacity of the HTS current lead is limited by the field perpendicular to the broad face of the AgAu/Bi-2223 tapes. In the optimization study, a stainless steel support of 50cm^2 cross-section has been considered. For the heat exchanger part, a copper cross-section of 63.6cm^2 and a copper residual resistivity ratio of 50 have been selected.

The heat load at the cold end of the conduction-cooled HTS part as a function of the warm end HTS temperature is shown in Fig. 2.5.15. Due to the rapid decline of the critical current density of the AgAu/Bi-2223 tapes with increasing temperature an enhanced superconductor cross-section is required at higher warm end HTS temperatures. This effect is reflected by the dependence of the required superconductor volume on the HTS warm end temperature also shown in Fig. 2.5.15. The results presented in this figure are based on an engineering critical current density of the AgAu/Bi-2223 tapes of 12kA/cm^2 at 77K and zero applied field. Because of the enlarged integrated thermal conductivity for enhanced warm end temperatures of the HTS module the heat load at 4.5K increases slightly more rapidly than the required superconductor volume with increasing warm end HTS temperatures.

The heat input at the warm end of an optimised heat exchanger part is zero. In Fig. 2.5.16, the dependence of the calculated optimum length of the heat exchanger part of a binary 68kA HTS current lead on the copper temperature at the cold end is presented. The heat input at the warm end and the optimum length of the heat exchanger are very sensitive to the helium mass flow rate. The optimum helium

mass flow rate has been calculated with an accuracy of 0.01g/s leading to some scatter in the calculated optimum length of the heat exchanger part. The optimum lengths of the heat exchanger, provided by Fig. 2.5.16, are average values for a heat flux between 0 and 40W at the cold end. The optimum length of the heat exchanger decreases with decreasing helium inlet temperature, whereas it increases with reduced copper temperature at the cold end of the heat exchanger.
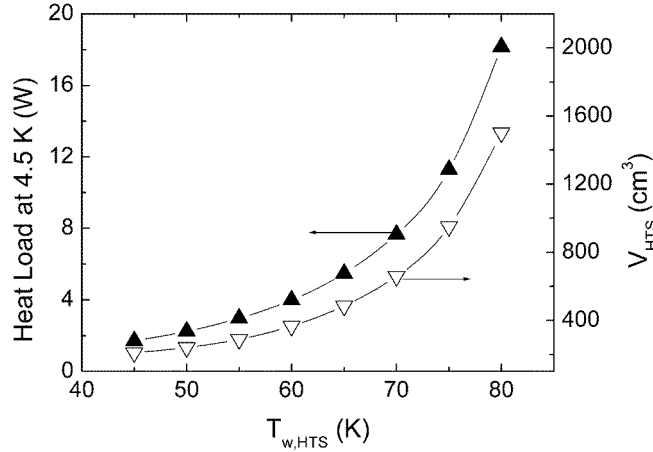
Fig. 2.5.15   *Heat load at 4.5K and the required superconductor volume as a function of the temperature at the warm end of the 0.6m long HTS part.*
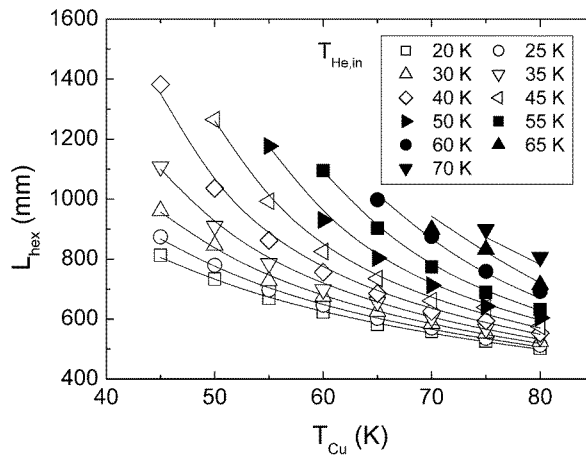
Fig. 2.5.16   *Optimum length of the heat exchanger part of a binary 68kA HTS current lead versus the copper temperature at the cold end for helium inlet temperatures between 20 and 70K.*

In Fig. 2.5.17, the required helium mass flow rate is shown as a function of the helium inlet temperature. In general, the optimum helium mass flow rate is smaller for low helium inlet temperatures and increases rapidly with decreasing difference of copper and helium temperature at the cold end of the heat exchanger.

A detailed analysis of the refrigeration power as a function of inlet temperature and mass flow rate indicate that the optimum cooling conditions are a helium inlet temperature close to 55K and a HTS warm end temperature of $\approx$75K. Only a slightly larger refrigerator input power is required for a helium inlet temperature of 50K and

a warm end HTS temperature of 65K, providing a nearly 50% reduction in the required amount of superconductor, see Fig. 2.5.15.
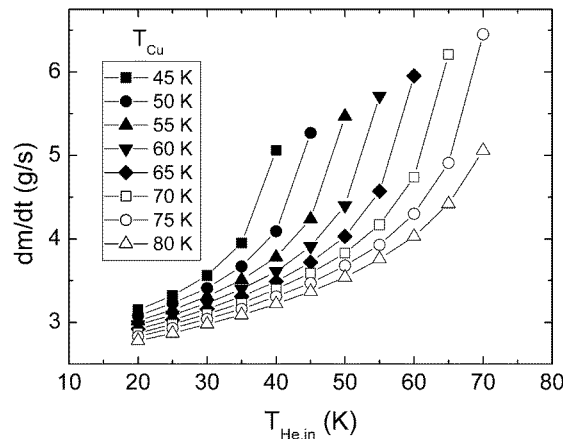
Fig. 2.5.17   *Helium mass flow rate required to cool the optimised heat exchanger part of a binary 68kA HTS current lead*

To evaluate the ac performance, required for CS and PF, the 70kA HTS current lead demonstrator was also tested under pulsed operating conditions at the Forschungszentrum Karlsruhe. After an initial 68kA dc run of 12 minutes, 36 pulses of 68kA were performed with ramp rates of 10kA/s and flat top times of 20s (68kA and 0kA). In spite of a reduced mass flow rate in the heat exchanger, all temperatures measured along the HTS module decreased during pulsed operation compared to steady, full current load. Moreover, no detectable voltage was observed along the superconductor.

Scoping study of HTS fusion magnets (TW5-TMS-HTSMAG)

Having shown the feasibility of a 70kA HTS current lead demonstrator for ITER stimulated the interest in the possibility to use HTS also for the TF magnets of fusion reactors beyond ITER. High temperature superconductors (HTS) are characterised by layered crystal structures leading to a pronounced anisotropy of the physical properties. As a consequence of this anisotropy it is not sufficient to use the absolute value of the peak magnetic field in the design of a HTS magnet. The TF coils of a fusion reactor generate to a first approximation a tangential magnetic field, which is inversely proportional to the radial distance from the centre of the torus. Thus, the magnetic field reaches a maximum at the inboard legs of the TF magnet system. In the windings of the TF coils of a fusion reactor the Bi-2223 tapes may be arranged in such a way that the broad face of the tapes is parallel to the tangential magnetic field (favourable field direction). However, close to and inside the winding pack also non-tangential magnetic fields are present leading to a field component perpendicular to the broad face of the Bi-2223 tapes, which is the unfavourable field direction for the HTS. To determine the maximum possible operation temperature of TF coils fabricated of Bi-2223 tapes, the magnetic field distribution at the upper end of the straight part of the inboard leg of the TF coils of ITER has been calculated.

In Fig. 2.5.18 left, the map of the total field above the equatorial plane, inboard leg of the ITER TF coils is shown. The peak field is 11.73T. The largest component is by far in the yz plane, parallel to the broad side of the tape. The field component in x direction is shown in the right hand side of Fig. 2.5.18. A maximum value of 3.38T

for this field component is reached at the lower and upper edge of the winding pack. To estimate the maximum possible operation temperature of a Bi-2223 based ITER type TF magnet system the critical currents for a parallel field of 12T and a perpendicular field of 3.5T have been retained.
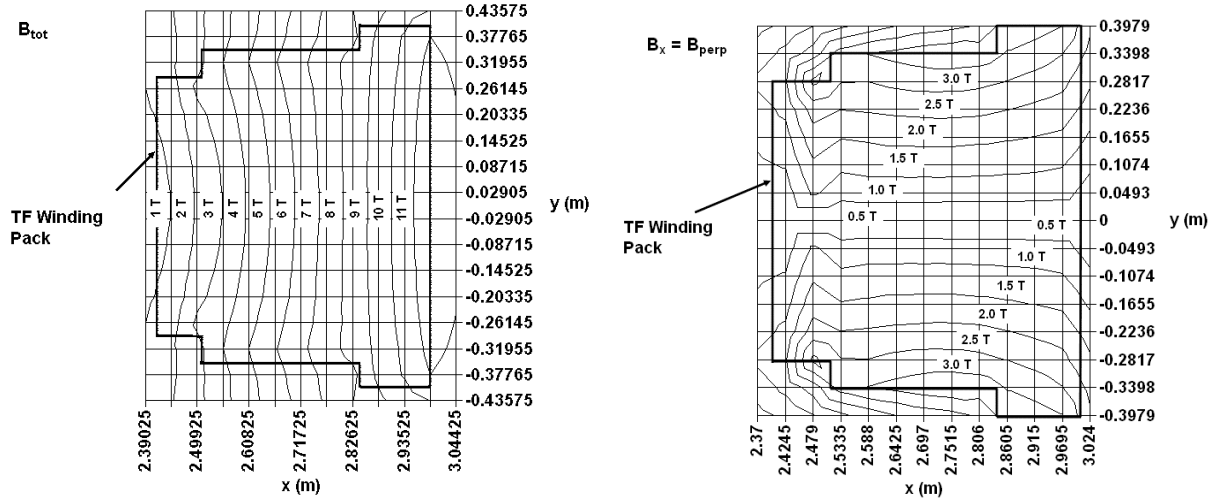
Fig. 2.5.18   *Total magnetic field (left) and component in the x direction (right) at the upper end of the straight part of the inboard leg of the TF ITER coils (z = 3.98m). The peak total field is 11.73T. The peak x-component is 3.38T.*
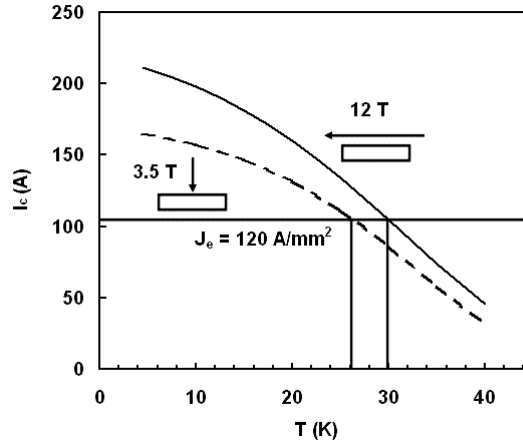
Fig. 2.5.19   *Critical current of Bi-2223 tapes versus temperature for magnetic fields of 3.5T perpendicular and 12T parallel to the broad face of the tapes. The data are based on the performance of Bi-2223 tapes fabricated by EAS. An engineering critical current density of $120A/cm^2$ is reached at temperatures of ≈ 26 K and ≈ 30 K for fields of 3.5T perpendicular and 12T parallel to the broad face, respectively.*

For a retained minimum engineering critical current density of $120A/cm^2$, a maximum operation temperature of 26K is found for the Bi-2223 tapes fabricated by EAS. The operation temperature is limited by the 3.5T field component perpendicular to the broad face of the Bi-2223 tapes, dotted line in Fig. 2.5.19. The use of higher performance Bi-2223 tapes (e.g. Sumitomo high I_c Bi-2223 tapes, see task HTS materials for fusion magnets) would shift the maximum operation

temperature to 34K. As in the case of the EAS tapes the current carrying capacity is limited by the field component perpendicular to the broad face of the tapes.

HTS materials for fusion magnets (TW5-TMSC-HTSPER)

In the framework of this task the performance of Bi-2223 tapes, fabricated by European Advanced Superconductors (EAS) and Sumitomo Electric Industries (SEI), has been investigated. The dimensions of the EAS and SEI Bi-2223 tapes are 4.15mm × 0.212mm and 4.2mm × 0.2mm, respectively. The critical current of the Bi-2223 tapes is defined by a 1μV/cm criterion. The engineering critical current density measured at zero applied magnetic field, are compared in Fig. 2.5.20. The self-field engineering critical current densities are represented by the scaling relation

$$J_{e(T)} = J_e(0)\left(1 - T/T_c\right)^{\alpha}$$

where a critical temperature T_c of 105K has been retained for both Bi-2223 tapes. The scaling exponents α are 1.22 (EAS) and 1.27 (SEI). The engineering critical current densities at T = 0 are 60.48 and 91.68kA/cm^2 for the EAS and SEI Bi-2223 tapes, respectively.
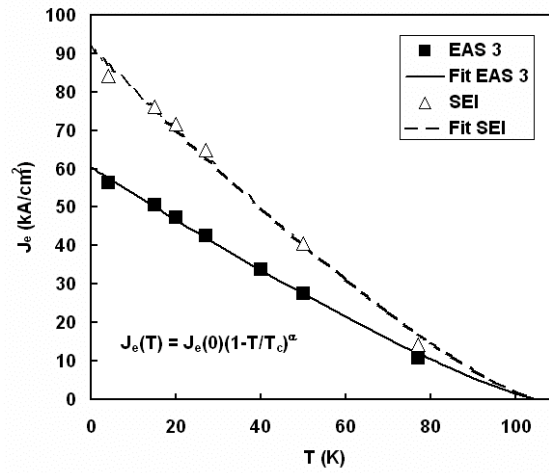
Fig. 2.5.20   *Comparison of the temperature dependencies of the engineering critical current densities of Bi-2223 tapes, fabricated by EAS and SEI, for zero applied field.*

The engineering critical current densities of the EAS and SEI Bi-2223 tapes as a function of the magnetic field applied parallel and perpendicular to the broad face of the tapes are compared in Fig. 2.5.21. For not too small fields, an exponential dependence of the engineering critical current density on the applied magnetic field has been found. The high field engineering critical current density can be represented by the expression

$$J_e(B,T) \;=\; J_{se}(0)\left(1 - \left(T/T_c\right)^{\beta}\right)\exp\!\left(-B/\left(B_{sc}(0)\exp\!\left(-T/T_{sc}\right)\right)\right)$$
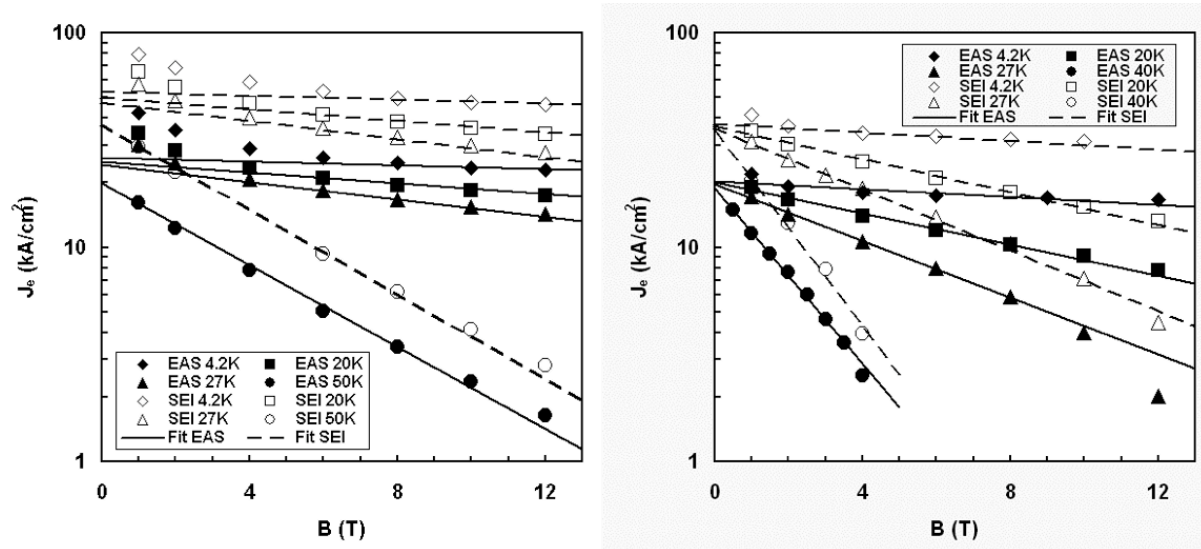
Fig. 2.5.21 *Comparison of the field dependencies of the engineering critical current densities of Bi-2223 tapes, fabricated by EAS and SEI, for fields parallel (left) and perpendicular (right) to the broad face of the tapes at selected temperatures.*

where $J_{se}(0)$, $B_{sc}(0)$, T_{sc} and β are scaling parameters. It has to be noted that $J_{se}(0)$ is considerably smaller than $J_e(0)$ used in the scaling relation for the engineering critical current density at zero applied field. The rapid decline of the engineering critical current density at elevated temperatures in the presence of a magnetic field is mainly caused by the exponential decrease of the scaling field B_{sc} with a scaling temperature T_{sc} much smaller than T_c. The values of the scaling parameters are listed in Table 2.5.5.

Parameter	EAS, parallel	EAS, perpendicular	SEI, parallel	SEI, perpendicular
T_{sc}	14.34K	11.55K	15.03K	11.37K
$J_{sc}(0)$	27.37kA/cm^2	20.24kA/cm^2	53.33kA/cm^2	37.45kA/cm^2
$B_{sc}(0)$	128.8T	67.9T	122.3T	65.3T
β	2.05	2.75	1.63	2.47

Table 2.5.5 *Scaling parameters for engineering critical current density*

Two sub-size samples manufacture and testing (TW6-TMSC-SUBSAM)

In the scope of the project for the construction of a new test facility for ITER conductors (The Dipole) a first milestone is the characterization of the conductor retained for the winding. The design of the superconducting winding of the Dipole foresees four conductor grades, all cable-in-conduit conductors of similar outer size. Short lengths of the highest (HF1) and lowest (LF2) conductor grades were manufactured in Spring 2006 using the same strand and jacket material procured for the full conductor production. The objective of this task is to prepare two SULTAN hairpin samples from short sections of HF1 and LF2 conductors.

Conductor	HF1	LF2
Cable pattern	(3x3)x4x4	(3x3)x3x4
Cu/non Cu (strand)	(0/9)x4x4	(6/3)x3x4
Nb$_3$Sn strand number (ø=0.81 mm)	144	36
Copper wires (ø=0.81 mm)	0	72
Jacket thickness (mm)	1.65	1.5
Outer conductor dimensions (mm)	15.82 x 13.23	12.65 x 12.61
Jacketed length for samples (m)	6.1	6.5
Total length (m)	7.3	7.1
Free cable on ends (m)	0.6 / 0.6	0 / 0.6
Void fraction (%) (calculated)	35	35
Twist pitches (mm)	58 / 95 / 139 / 213	
Heat treatment schedule	48h/210C – 48h/400C – 60h/640C	

Table 2.5.6   *Layout of the two conductors for the SUBSAM samples.*

The two conductor sections are made from the same, high current density OST strand. The conductor layout is gathered in Table 2.5.6. The procedure of bending and termination for the hairpin samples is substantially identical to the one followed for the "dipole pre-prototype sample" in 2005. The heat treatment of both hairpin samples, together with the strand witness samples, see Fig. 2.5.21 is carried out in the CRPP vacuum furnace according to the schedule recommended by the strand supplier, see Table 2.5.6.

Four I_c samples were prepared on "ITER barrels" out of 10 m strand supplied by EFDA. The billet identity is 8712-2. Two out of four samples were tested at liquid helium (4.2 K) in the field of 10, 11 and 12 T. The two samples are named here A and B. A summary of the I_c and n-index result vs. field is gathered in Fig. 2.5.22. Each point on the plots is the average of two identical runs. The scattering between two identical runs is less than 1A (< 0.1%). The results of sample A and B are the same within 0.7% and in good agreement (< 1%) with the supplier data (end of billet 8712-2). As far as n-index is concerned, both samples have high n, sample A is about 10% higher than B.
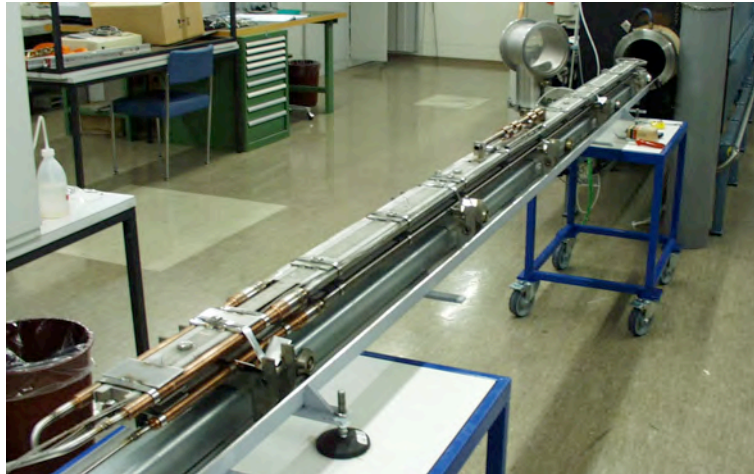
Fig. 2.5.21   *The two hairpin samples entering the furnace for the heat treatment.*
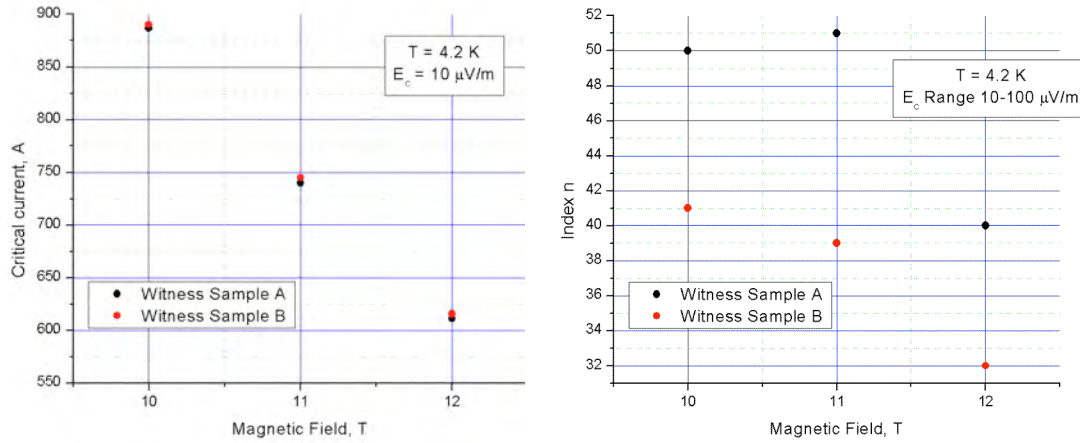
Fig. 2.5.22   *The results of the I$_c$ test (left) and n-index (right) for the witness strands.*

The two hairpins have been taken out of the heat treatment furnace on June 14th 2006. To termination is solder filled with SnAg5 alloy and the jacket is machined for helium inlet, outlet and pressure taps. The thick copper plates for the electrical connection are soldered to the termination. The instrumentation and the clamps are applied.

The test program of the SUBSAM samples was focused on the dc properties, aiming to assess how far the excellent properties of the OST strand are retained in the small size CICC. For the HF1 sample, the current sharing temperature test at 11T background field /16.8kA and at 19kA are of highest interest, because the operating current for the dipole is 16.8kA/12.5kA and the operating load are reproduced by the combination of 19kA/11T (cyclic load).

The most significant dc test results of the HF1 sample are summarized in Fig. 2.5.23. The initial performance is about 30% less than the prediction for the single strand. With cyclic load, the degradation progresses with high rate and does not achieve saturation, even after 800 cycles.
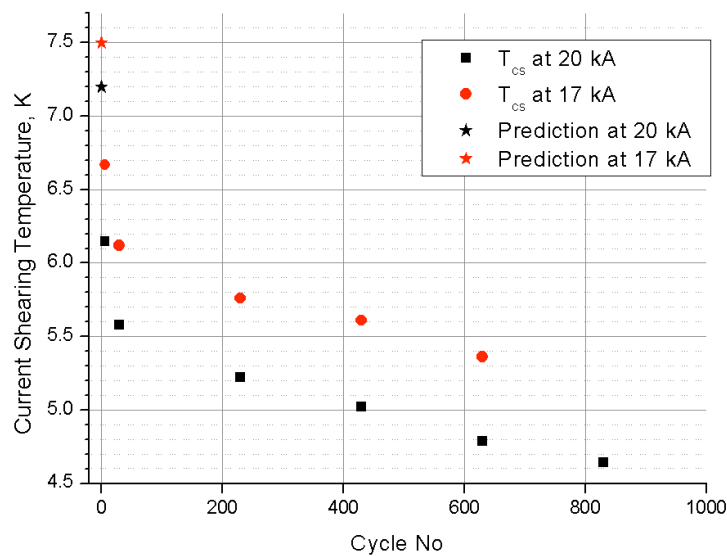
Fig. 2.5.23   *Cyclic load performance (T$_{cs}$) of the HF1 conductor.*

After completing the cycling test, the sample HF1 was lifted in SULTAN to bring into the high field region a sample section which was in lower field during the cycling. The aim was to measure if the moderate load of that section had already induced a significant degradation. The result of the "lifted test" is plotted in Fig. 2.5.24 together with the data collected during cycling. The comparison suggests that the lower BI load (about 95kN/m vs. 209kN/m) had only a minor degrading effect on the conductor, the performance being in the range of the "initial" performance.

Other tests on the HF1 sample included the ac loss in the background field of 2T and the pressure drop as a function of the mass flow meter (in order to deduce the fanning friction factor).
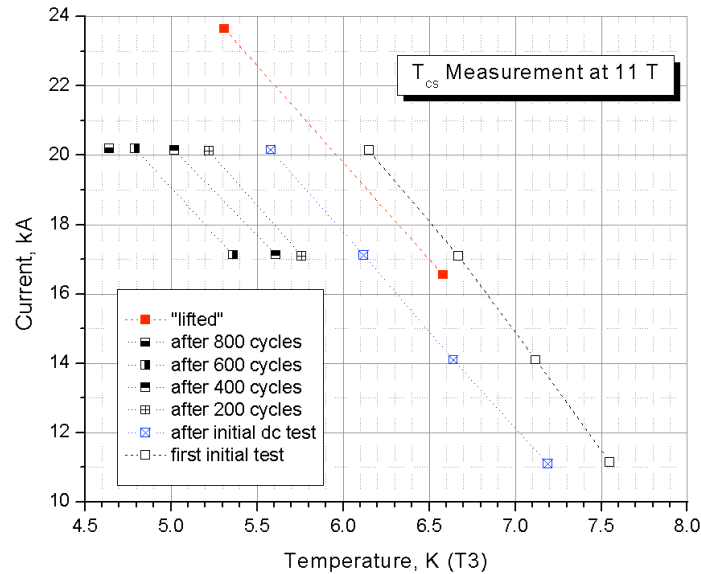
Fig. 2.5.24   *Results of "lifted test". The conductor section exposed to "only" 95kN/m behaves similarly to the initial performance of the section degraded by 209kN/m load.*

The test of the LF2 sample was carried out in the background field of 7T, as the conductor was designed for the low field section of the dipole winding. A few initial tests were also carried out at 11T and confirmed the degradation observed in the HF1 sample: the difference between expected and measured T_{cs} was again in the range of 0.7-0.8K (see for comparison the prediction vs. initial test result in Fig. 2.5.23). Due to the poor performance, the test was terminated before the completion of the original test programme.

Evaluation of test results for full size samples (TW6-TMSC-FSTEST)

An R&D program was launched in Europe in 2003 to qualify the use of high current density Nb_3Sn strands in ITER cable-in-conduit conductors. Two short length samples have been fabricated from conductor sections with the same layout as TFMC, using 0.81mm advanced Nb_3Sn strands supplied by EAS, OST, OCSI and OKSC. The two samples, denoted as TFAS-1 (OST, EAS strands) and TFAS-2 (OCSI, OKSC strands), were tested in SULTAN from December 2005 to May 2006. The main strand (see also section 2.5.2, subsection "Advanced Strand Test") and conductor characteristics are listed in Table 2.5.7. Copper segregation, i.e. replacing one Nb_3Sn strand by a copper wire in the first triplet, is used in both

conductors in the right (R) leg, with the aim to obtain similar critical currents in both legs of the same sample. Polished cross-sections of the four advanced Nb_3Sn strands are shown in Fig. 2.5.25.

The two conductor lengths are cooled in parallel by two circuits with independent regulation of temperature (SULTAN heaters) and mass flow. A sketch of the sample instrumentation is shown in Fig. 2.5.26. It includes one array of six Hall sensors next to the joint, one heater and seven temperature sensors on each leg (the temperature sensors of TFAS-1 had to be replaced at CRPP).

SULTAN Sample	TFAS-1-R	TFAS-1-L	TFAS-2-R	TFAS-2-L
Strand supplier	OST	EAS	OKSC	OCSI
Strand manufacturing technology	Internal tin	Bronze	Internal tin	Internal tin
Diffusion barrier	Ta	Ta	Ta	NbTa
J_c at 4.2K, 12T, 10μV/m [supplier data] (A/mm^2)	1100	780*	1000	950
Steel jacket od/id (mm) - Steel spiral od/id (mm)	40.4/37.2 - 12/10			
Twist pitch sequence (mm)	45/87/126/166/415			
Void fraction (%)	32.7	33.9	33.5	32.5
Number of superconducting strands	720	1080	720	1080
Number of copper wires	360	0	360	0
Total non-Cu cross-section (mm^2)	181	290	181	227

* witness strands 705A/mm^2 for shortened heat treatment

Table 2.5.7   *Conductor layout for TFAS samples*
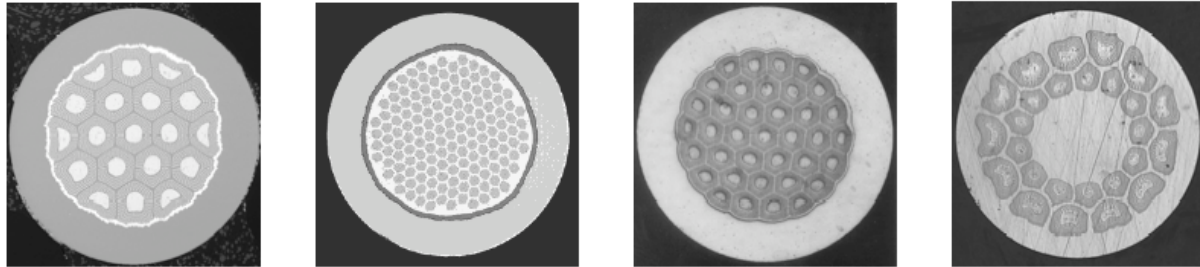
Fig. 2.5.25   *The advanced Nb_3Sn strands supplied by OST, EAS, OKSC and OCSI (from left to right).*
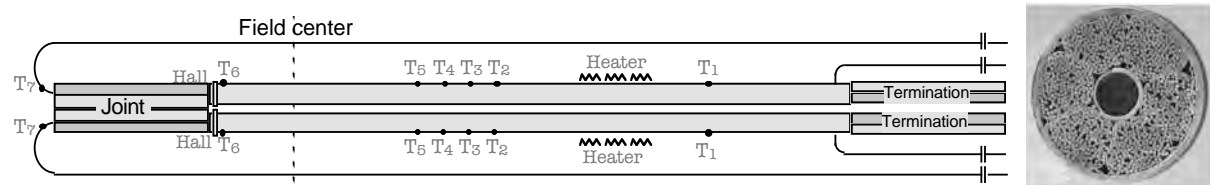
Fig. 2.5.26   *Instrumentation sketch of a TFAS sample. The flow inlet is at the joint for TFAS-2 (bottom-to-top) and at the termination for TFAS-1 (top-to-bottom).*

The dc test includes T_{cs} and I_c runs at 8, 9, 10 and 11T background field. To avoid transverse load in excess of the ITER operation loads, the product field-current is

always limited to BI ≤ 770kA·T. After a first campaign of dc test, cyclic load is applied 1000 times for TFAS-1 and 800 times for TFAS-2 by switching the current between 0-70-0kA in a background field of 11T and the dc test is repeated. The performance evolution is monitored by a "reference" T_{cs} test, periodically carried out at 11T.

The testing group set up by EFDA (including CRPP, CEA, ENEA and Polito) made performance predictions from the individual strand results using the Durham scaling relations normalized to the results of the witness strand sample. In a first prediction, the strand scaling relations are used to calculate the current sharing temperature (T_{cs}) of the four different CIC conductors at a current of 70kA and a SULTAN field of 11T. The thermal strain is retained to be -0.61% (relaxed fully bonded model) and no degradation is accounted for. In additional predictions done by the testing group, the analysts were free to choose other values of the axial strain or to assume a degradation of the current carrying capacity of the strands in the cable accompanied by a reduction of the n factor. The "free" prediction of CRPP maintains the thermal strain at -0.61%, while a reduction of the n factor and the effective non-Cu area account for strand degradation in the cable. Based on the results of the assessment of previously tested sub-size conductors made of similar strands, degradation factors of 0.9 (OST) and 0.7 (EAS, OKSC, OCSI) have been retained. All prediction results for 11T and a current of 70kA are gathered in Table 2.5.8. The values for -0.61% strain and not degraded strands are average values of the predictions of the different labs.

All TFAS conductors are characterized by a very broad transition, with the quench point (I_q or T_q), far away from I_c or T_{cs}, see Fig. 2.5.27. Moreover, a voltage roughly proportional to the current is observed starting at very low current. Such voltage is either positive or negative and depends on the position of the voltage taps, the background field and the cycling history. To process the data, this "linear voltage" is arbitrarily subtracted and only the deviation from the linear voltage is considered evidence of current sharing. The broad transitions in connection with the procedure of the voltage compensation lead to an uncertainty of ±0.15K in the determination of the current sharing temperature.

	TFAS-1-R	TFAS-1-L	TFAS-2-R	TFAS-2-L
Strand supplier	OST	EAS	OKSC	OCSI
Non-Cu current density at 70kA (A/mm^2)	386	241	386	308
T_{cs} at -0.61%, no strand degradation (K)	6.15	6.59	5.46	6.45
CEA free prediction (K)	5.78	6.26	5.10	6.96
CRPP free prediction (K)	5.83	5.7	4.45	5.62
Polito free prediction (K)	5.34	5.84	3.92	4.61

Table 2.5.8 *Summary of performance predictions by the testing group.*

The dc results (T_{cs} and I_c) have been collected at fields of 8, 9, 10 and 11T in the temperature range of 4.5 to 9K for operating currents up to 80kA. In Fig. 2.5.28, the non–Cu critical current densities as a function of current sharing temperature are presented for a field of 11T before and after cyclic loading. The evolution of the current sharing temperature with increasing number of load cycles is illustrated in Fig. 2.5.29. Most of the performance evolution under cyclic load is observed in the first 100 cycles. The OST conductor lost up to 1K during cyclic load. The n index is in the range of 4-8 for all the conductors, without substantial change upon cyclic load. The lowest value is observed for the OKSC.
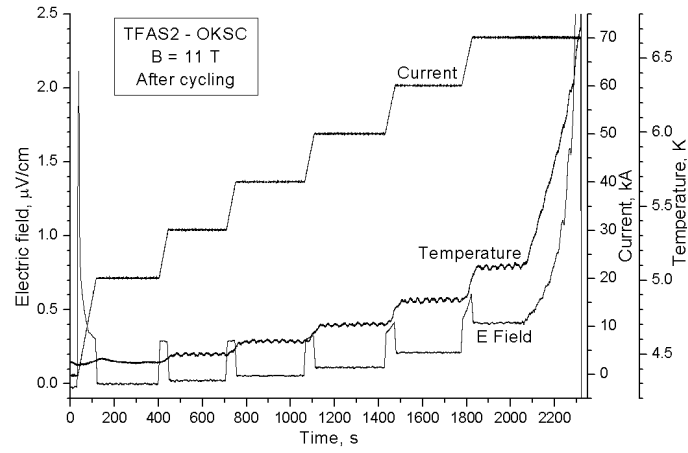
Fig. 2.5.27 *Broad transition observed during current ramp up in steps of 10kA. The temperature is eventually raised till a quench occurs at 70kA/6.6K. The T_{cs} criterion is already largely exceeded at 60kA, 4.8K.*

	ITER specification	TFMC	OST	EAS	OKSC	OCSI
Before cyclic load	5.7K	5.52K	6.63K	4.93K	5.29K	5.77K
After cyclic load	5.7K	-	5.81K	4.72K	5.09K	5.53K
After re-installation	5.7K	-	5.44K	4.57K	-	-

Table 2.5.9 *The T_{cs} results extrapolated at the ITER TF operating current density and average field.*
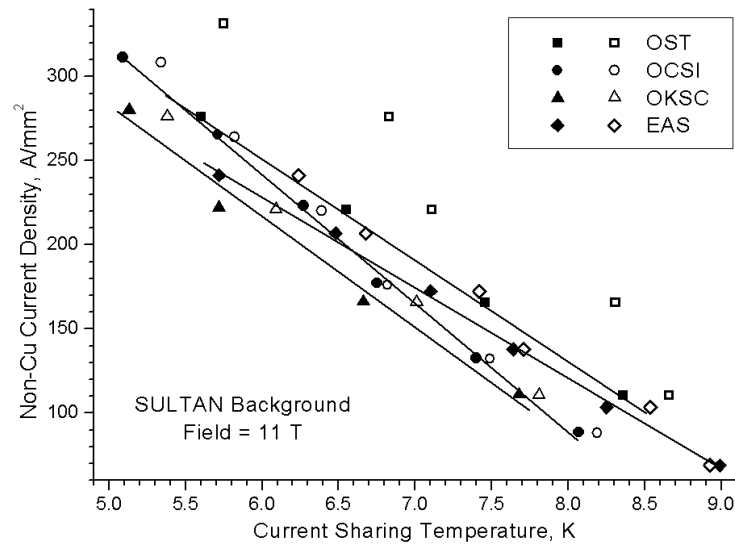
Fig. 2.5.28 *Summary of T_{cs} data at 11T SULTAN field before (open symbols) and after cycling (full symbols). Trend lines are drawn for the data after cycling. The scatter in the data for TFAS-1 is related to an on-going performance degradation.*
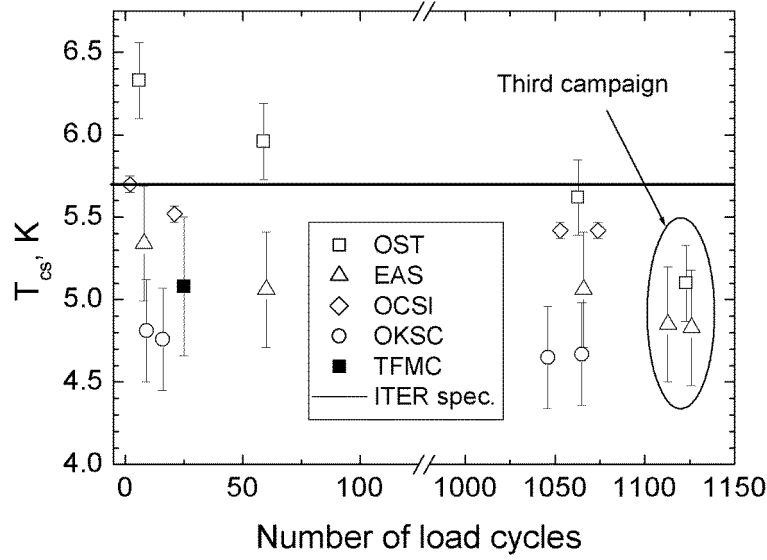
Fig. 2.5.29   *Evolution of the current sharing temperature, measured at 11T and a current of 70kA, with the number of load cycles. For comparison, the results for the TFMC conductor are also included.*

The T_{cs} performance of the four conductors at the ITER operating conditions is interpolated from Fig. 2.5.28 and marginally corrected for 11.15T average field. The results before and after cyclic load are gathered in Table 2.5.9, including also the performance of the TFMC conductor. The analysis of the results has been restricted to the T_{cs} data measured at 11T after cyclic loading. The testing group attempted an analysis of the results by two methods. In a first approach, a load-dependent $\varepsilon=\varepsilon_{th}-\gamma BI$ (I in kA, B in T) is used to fit the results. For each conductor, the set of parameters and the standard deviation, σ, are reported in Table 2.5.10. In a second approach, a constant ε and a reduced filament area (A_0^{cable}/A_0^{strand}) is used to fit the results. For each conductor, both fitting parameters are optimized applying the minimum square sum criterion ($\Sigma\Delta I_c^2$) to the set of results. In a mixed approach, both variables, the strain (ε) and reduced filament cross section ($A_0^{cable}/A_0^{strand}<1$) are varied. As the original strand and CICC have different n indices, the results of the analysis are a function of the electric field criterion retained for the data reduction, i.e. more strict criteria would lead to enhanced values of strain.

		OST	EAS	OKSC	OCSI
First approach $\varepsilon=\varepsilon_{th}-\gamma BI$	ε_{th} (%) γ (%kA^{-1}T^{-1}) σ (%)	-0.54 0.00052 n.a.	-0.51 0.00036 1.6	-0.56 0.00054 7.0	-0.68 0.00019 1.1
Second approach	A_0^{cable}/A_0^{strand} ε (%) n index	0.35 -0.35 6	0.50 -0.42 7	0.45 -0.48 5	0.70 -0.66 n^{strand}
Mixed approach	ε_{th} (%) γ (%kA^{-1}T^{-1}) A_0^{cable}/A_0^{strand}	-0.53 0.00040 0.80	-0.51 0.00033 0.95	-0.55 0.00030 0.72	-0.65 0.00005 0.72

Table 2.5.10   *The parameters obtained by the result analysis of the four conductors.*

The expected improvement of the cable-in-conduit performance using Nb_3Sn strands with high critical current densities could not be achieved in the TFAS conductors. At the ITER non-Cu operating current and field, $J_{op}=286A/mm^2$ and B=11.15T, the current sharing temperature is below 5.7K for all four TFAS conductors, in particular the EAS one made of standard bronze strand fulfilling the present ITER TF bronze strand specification. The very low n index as well as early, linear voltages, affect the accuracy of the measurements, with an error bar of ±0.15K on the T_{cs} results. The substantial evolution of the performance under cyclic load, mostly for the OST conductor, suggests that the degradation is due to the operating load rather than to accidental damage. The analysis, both with "extra strain" and reduced filament cross section, do not provide a satisfactory overall picture, with the fitting parameters broadly varying among the four conductors and, within the same conductor, according to the results, either high or low field.

AC losses computations for ITER magnets (TW5-TPO-ACLOS)

The calculation of ac losses due to the control currents in ITER is a cumbersome task because the control transients require small field changes (0.1T or less) at moderate frequency (up to 10Hz), where effects of partial penetration of the filaments and shielding are important and need to be taken into account. A computation algorithm has been developed for the calculation of ac loss in superconducting magnets after (a) a review of the state of the art of integral formulae for the calculation of the magnetic field in linear and magnetized media, and (b) the conceptual design and programming of a software with a method devised to compute the instantaneous ac loss for an arbitrary field change.

As an example of the use of the above algorithms, calculations of ac loss in the ITER coils for two vertical plasma stabilization scenarios (VS1 and VS2) during high beta operation at start of burn (SOB) are performed. The magnetic model built to this aim includes all CS, PF and TF coils, as well as some 60 axis symmetric passive circuits that represent the conductive wall of the vacuum vessel. The effective filament diameter for Nb_3Sn is 30μm and for NbTi is 6μm and the coupling loss time constant is 25ms in all space directions for all conductors. The current variation during the vertical control scenarios has a wide frequency spectrum and produces field changes of relatively small amplitudes (few tens of mT on the PF coils, up to 0.1T in the CS coils).
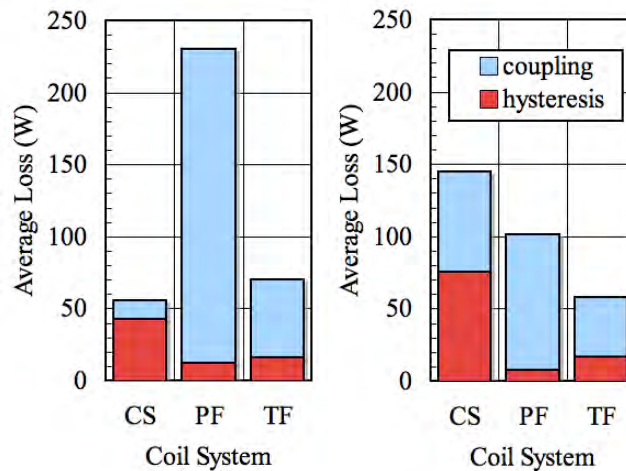
Fig. 2.5.30   *Average ac loss power computed for the vertical stabilization scenario VS1 (left) and VS2 (right) at SOB.*

The calculation provides a quick tool to qualify the controller scenarios in terms of the cryogenic load, as we see a clear distinction in the loss at the level of the CS and PF system. Some results are shown in Fig. 2.5.30, where the bars represent the total loss, split among each of the three main coil systems, and further subdivided in the different mechanisms (coupling and hysteresis). Loads are reported as average power during the time simulated, 10s. We note further that the contribution of the two loss mechanisms in the CS and PF coil systems is massively different in the two scenarios. This is due to the combined effect of the different current amplitudes as well as the different dynamic characteristics of the current waveforms in the CS and PF coils, affecting both hysteresis and coupling loss. Interestingly enough, the situation on the TF coil (close to the plasma) is essentially unaffected by the control scenario, as should have been expected.
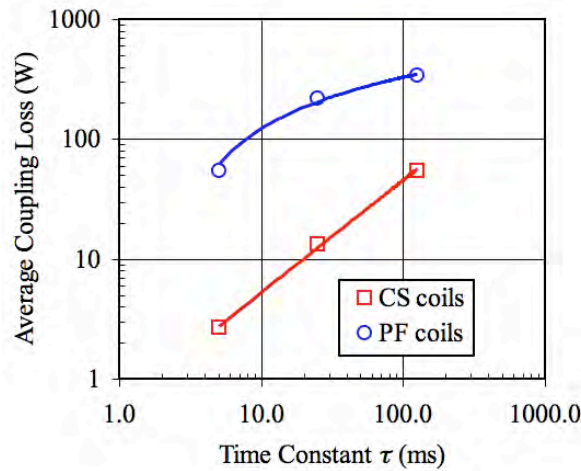
Fig. 2.5.31   *Sensitivity study: effect of time constant on coupling current loss in the CS and PF coil system during the VS1 scenario at SOB.*

The effect of a change of the time constant by a factor $1/5$ to 5, which is the spread measured on the large-scale ITER cables, on the coupling loss is investigated in the scenario VS1 by sensitivity analysis, see Fig. 2.5.31. The scaling of the coupling loss in the CS coil system is approximately linear, which indicates negligible shielding. In the PF coil system, on the other hand, we see the effect of shielding at high values of τ, which results in a coupling loss significantly smaller than would be expected by the low-frequency regime, linear extrapolation.

The above calculation method for ac losses in pulsed superconducting magnets is suitable over a wide regime of field changes (from partial to full penetration) and frequencies (from the low frequency limit to shielding), and the ITER example provides a measure of the flexibility in dealing with complex geometric and powering conditions.

ITER thermo-syphon effect and Central Solenoid Model Coil analysis (TW6-TMSC-ASTSPH)

CRPP regularly evaluates full-size superconducting cables, recently mainly prototypes very close to the ITER specification, in its SULTAN test facility at the PSI in Villigen. Although the cryogenic and magnetic environment provided by SULTAN is very close to the one envisaged for the coil conductors in ITER, the available length in the high field region as well as the imposed vicinity of the lower conductor

joint to this region pose (minor) limits on the relevance of the SULTAN tests. To assess these limits, the results obtained on the large Central Solenoid Model Coil (CSMC) (Layer 1a) in Japan are compared with those obtained on a 3.5m 'short' sample in SULTAN, built of the same conductor (Good Joint sample). Further on, within the same task, a detailed analysis of the so-called thermo-siphon effect, first observed at CRPP in 2002 is carried out at the nominal ITER TF coil operating conditions.

Conductor performance comparison: Central solenoid model coil versus good joint sample

In the late 1990ies, the Central Solenoid Model Coil (CSMC) and three associated insert coils were built with the intention of qualifying long lengths of the full-size ITER conductors at and beyond the ITER operating conditions. In addition to tests on the insert coils, measurements on the innermost layer, layer 1a, provided relevant conductor data because the magnetic field at its location also reaches the high values required by ITER. Layer 1a consists of an Inoloy 908 jacketed cable-in-conduit conductor with 1152 strands bundled into a five stages cable (3×4×4×4×6). Extensive test campaigns in the years 2000–2002 yielded a wealth of complex performance data, which has since been analysed by several groups.

A 9m long section left over from the CSMC conductor production provided the opportunity to test it at SULTAN, at the time with the main aim to evaluate different joint designs. Eventually the dc and ac performance of the so-called "Good-Joint" sample, with a contact resistance below 1nΩ, could be fully determined.

In 2006 CRPP re-analysed the data of the CSMC Layer 1a and the Good-Joint measurements and compared the two with the intention of finding systematic differences arising from the unequal test conditions. The comparison proved to be complex because not only the environments of the two tests are different, but also the state of the conductor: In the solenoid the conductor experiences a tensile stress from the magnetic forces (hoop stress), whereas this stress does not exist in SULTAN samples. With established scaling models it was possible to account for this discrepancy. The analysis will be completed in 2007.

Thermosyphon effect in dual-channel cable-in-conduit conductors

The cable-in-conduit conductors foreseen for the ITER coils consist of two channels (see Fig. 2.5.32 left): an outer annular channel containing more than 1000 cabled and tightly packed superconducting strands (*bundle*) and a central channel containing only helium (*hole*). A steel spiral allowing free exchange of helium and heat between bundle and hole separates the two. The central channel strongly reduces the hydraulic impedance of the conductor, allowing to force significant mass flow of coolant over long cable lengths with moderate pressure drop, and helps to limit the maximum pressure in case of a superconducting transition, a *quench*. However, in 2002 the SULTAN team observed an unexpectedly high local temperature increase in a dual-channel sample during tests involving local heating. If heat is deposited in the bundle region (by e.g. ac losses in the strands or energy deposition by neutrons), the helium density there drops substantially (e.g. by more than 40% if the helium temperature increases from 4.5 to 8.5K). Because the longitudinal pressure drop in the hole and the bundle is the same locally, 'buoyancy' of the lighter helium in the bundle occurs, potentially leading to a flow stagnation and even reversal there, while the flow in the central hole increases to maintain the total helium mass flow. The reduced flow in the bundle in turn leads

to diminishing cooling and potentially to a temperature runaway with ensuing quench of the strands.
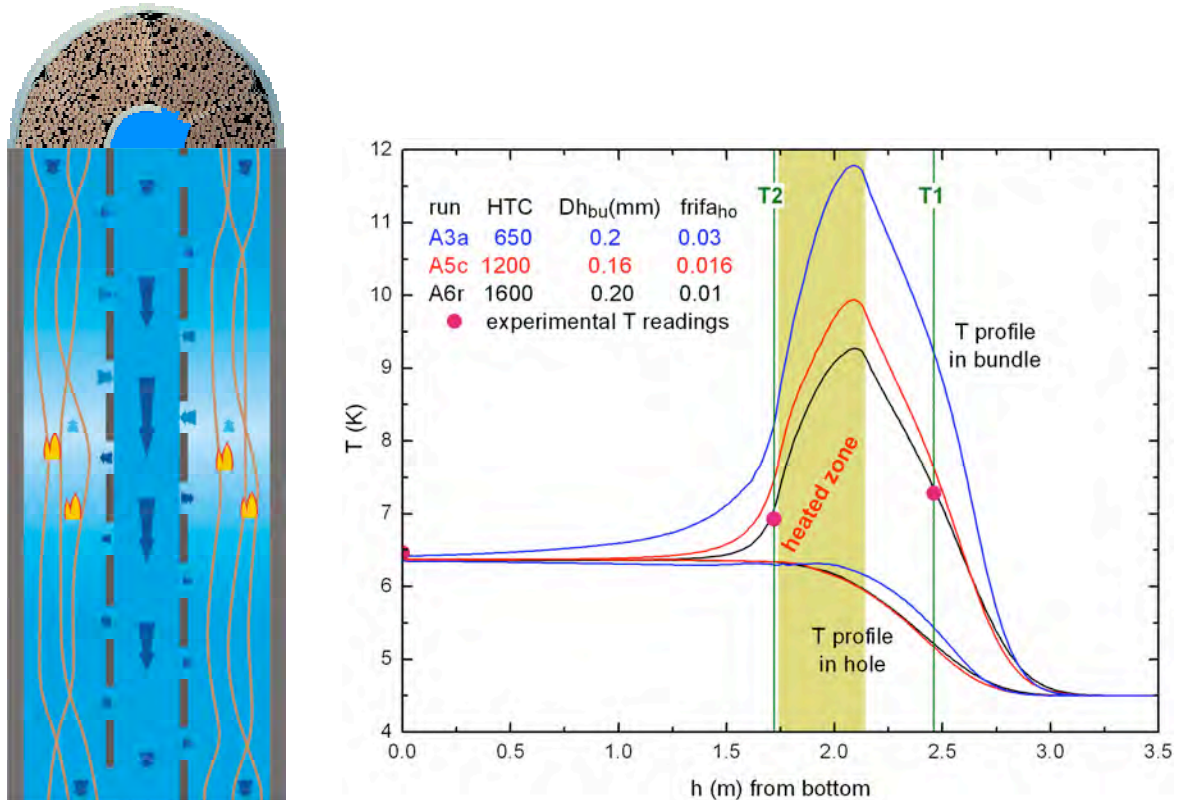
Fig. 2.5.32   *Left: dual-channel CICC with downward He flow and local heat deposition symbolised by small flames. Right: simulation of temperature profiles in the bundle and hole regions of the TFAS2 sample tested in SULTAN in June 2006.*

In the scope of this task, the thermo-hydraulic behaviour of the TFAS2 sample investigated in SULTAN in June 2006 was simulated in detail with an enhanced version of the computer code THEA, specifically taking account of gravity forces for the coolant. Figure 2.5.32 right shows temperature profiles for three sets of simulation parameters, with only the last one (in black) matching the observed temperature values. A detailed parameter study allowed to reproduce the experimental data for all observed mass flows underlining the value and validity of the THEA simulation code for studies of the thermosyphon effect. Consequently the program was used to study the implications of the effect for the ITER toroidal field coils, showing that, at the design heat deposition rate, mass flow rate and current sharing temperature, the erosion of the temperature margin due to the thermo-siphon effect is tolerable, i.e. will likely not drive a runaway with quench.

Review of PF2-PF5 winding design (TW6-TMSP-PFWDES)

This task started in October 2006. The aim of the task is to critically review the design solution adopted for the NbTi, low field poloidal field winding of ITER, including the functionality of the electrical insulation design, the steel plates to block an electric arc propagation, and the general approach of redundance/overload to maintain the operation requirement in case of a fault in a section of the winding. The review work will be supported by risk analysis as well as manufacturing considerations to weigh the demand vs. effectiveness of the design.

European Dipole Facility (TW5-TMS-EDFAC)

In 2006, the activities for the preparation of the European Dipole Facility focused on the interface issues between the dipole winding (to be delivered by EFDA) and the installations of CRPP. Due to the unsatisfactory performance of the dipole prototype conductors, see section 2.5.2, the winding design is not yet frozen. For this reason, the work about the interface issues must be considered as a draft in progress.

The design of the vacuum vessel is carried out in collaboration with the engineering company Hochreuter. Contrary to SULTAN, the winding of the dipole will rest on four gravity supports (feet), rather than be suspended by ropes. The material and size selected for the feet are aimed at limiting the heat conduction and provide a good stability to the large assembly (about 18t of cold mass), see detail in Fig. 2.5.33.
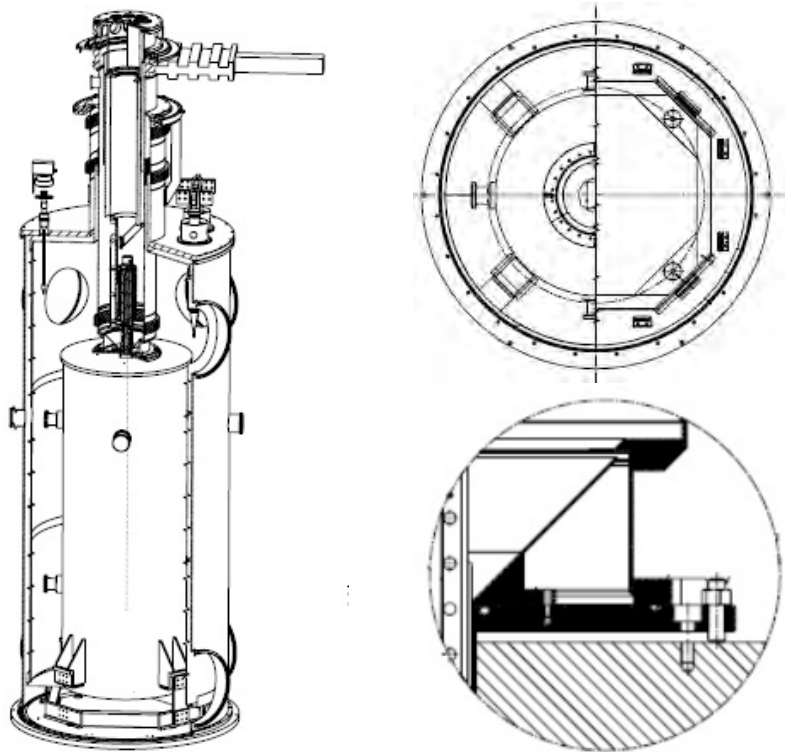
Fig. 2.5.33   *A 3D drawing of the main vacuum vessel with the dipole winding, the vacuum chamber for sample holder and a sample. In the detail inserts, one of the gravity support and the connection between the winding dipole and the sample vacuum chamber.*

Another delicate aspect of the interface is the top of the flange of the winding, where the vacuum chamber of the sample holder (CRPP) must be fitted and welded vacuum tight, see detail in Fig. 2.5.33. The vacuum chamber is also attached to the upper flange of the main vacuum vessel. To accommodate the size change between the top of the main vessel and the top of the winding flange at cool-down, a set of bellows is foreseen. A sophisticated adjustment mechanism is planned also at the top flange to grant the concentricity of the vacuum chamber and dipole winding, for a proper introduction of the sample into the test well of the dipole.

An analysis of the electromagnetic forces between the dipole and the iron screen of SULTAN in the SULTAN hall has shown the need of an additional, heavy iron screen in order to balance the forces. The same material used for the SULTAN screen has already been secured.

Other activities for the Dipole facility include the design of a new, improved transformer unit, the layout of the quench protection for the dipole, the cryogenic supply (transfer lines and heat exchanger), as well as preliminary investigations about power supplies. A 1:1 mock-up of the dipole facility vacuum vessel has been erected in the SULTAN hall close to the actual selected location.

2.6   Industrial process plasmas[*]

The "Swiss Commission for Technology and Innovation" (CTI) projects on large area capacitively coupled RF plasmas for the deposition of thin film solar cells and for flat displays, for many years one of the main activities of the industrial plasma group, have been finished during the last year. Furthermore the economic difficulties and changes of the main industrial partners led to a substantial reduction of the activities of the group. The number of projects and the manpower decreased adapting to the economic situation of the industry. This situation might influence the R&D activities of the group for the next 1-2 years.

The diversification of the R&D activities has been continued and new long-term topics have been initiated. One main topic shall be the research and development of (semi) industrial plasma processes. The group at the CRPP is one of a few laboratories worldwide which can afford to work on industrial sized reactors due to the excellent infrastructure of the CRPP and the EPFL. Design of large plasma reactors and up-scaling of plasma processes are the biggest problems in the industrialisation of the various plasma applications and their successful introduction into production. The up-scaling of small plasma reactors to industrial reactors implies in most cases a considerable increase in electrical power. One of the main problems in industrial reactors is the occurrence of arcing and parasitic discharges, which can hinder a successful introduction into industrial production lines. The study of arc phenomena is one of the oldest topics in plasma physics. In our opinion arcing is at present a key issue in the application of plasma in industry. Arcing starts to be the limiting factor in several applications of plasmas, thus triggering intense research and development on this topic.

First approaches led to investigation of arcing phenomena in large area RF reactors such as the KAI reactor and first contact with industry concerning future projects on this topic were started during the last year. In particular, the arcing in reactors applied for the production of solar cells shall be investigated.

Arcing is also important in space environment and space equipment as underlined by the mandate from Mecanex SA in Nyon undertaken on demand of the European Space Agency (ESA). It is intended to follow up this topic in future.

However arcing or sparking can also be used for precision machining. It is planned to continue or even intensify the activities on micro discharges in particular on the electrical discharge machining (EDM). The very successful TOPNANO project on this topic shall be continued. In addition, basic investigation on a new EDM process shall hopefully be made in a proposed CTI project together with the Ecole

---

[*] Work not belonging to the EURATOM Association's work programme.

d'Ingenieur de Genève, Charmilles Technologies SA and Micron SA. A CTI project continuing the basics and diagnostics is in preparation together with Charmilles SA and Agie. Discharge plasmas physics is the main topic in these interesting projects linked to successful industrial applications.

2.6.1 High rate deposition for microcrystalline silicon for thin film photovoltaic solar cell application

The aim of the present project is to better understand the guiding principles of silicon thin film deposition in large area reactors for the production of photovoltaic (PV) solar cells. This knowledge should provide the basis of the development of an ultimate cost-effective process for industrial PV solar cell production. Ideally this corresponds to a high density RF reactor operating at an elevated plasma excitation frequency allowing industrial high rate deposition of amorphous and microcrystalline silicon with a homogeneity of 5-10% on solar cells relevant to large area substrates, typically around $1m^2$.

The optimization of microcrystalline silicon (μc-Si:H) deposition by Plasma Enhanced Chemical Vapour Deposition (PECVD) is difficult to achieve. This is due to the fact that the transition zone from amorphous silicon (a-Si:H) to μc-Si:H cannot be simply defined as a function of the deposition process parameters (pressure, RF power, frequency, flow rates, …) because of their inter-dependence on the plasma physical properties and chemistry. For example, high dilution of the silane gas with hydrogen is a well-known technique to reach the transition zone, however, depending on the different deposition process parameters and reactor configurations, the transition can occur between silane gas concentrations as low as 3% and as high as 10% and covers the whole intermediate range. Recently, it has been shown that good μc-Si:H at reasonable deposition rate (4Å/s) can be deposited even from pure silane gas. Nowadays, most of the μc-Si:H PECVD optimization has essentially been done by experimental empirical parametric studies, due to the difficulty of applying relevant and simple plasma diagnostics in real deposition conditions. In parallel, self-consistent numerical plasma models including a large number of species and reaction rates have been developed in order to achieve the closest simulation of the complex phenomena occurring in the plasma. However, such models remain very complicated to use and to interpret, and are very time consuming, so that they require dedicated plasma modelling specialists, and are therefore not systematically used. Hence, there is a need to develop a simple methodological approach based on simple plasma measurements in order to better understand the behaviour of the transition zone from a-Si:H to μc-Si:H as a function of the deposition parameters.

In this work, Fourier transform infrared absorption spectroscopy measurements in the exhaust line of a large area industrial reactor have been used to determine the silane concentration in the plasma. It has been shown that the microstructure of the deposited film can be defined as a function of the silane concentration *in the plasma*, independently of the plasma parameters. Figure 2.1.6 shows that μc-Si:H is deposited for silane concentrations lower than 0.5% and that a-Si:H is deposited for concentrations in the plasma higher than 1.2%. These two well-defined regimes are separated by a transition zone where the material can be either amorphous or microcrystalline, because in this zone the plasma composition is not the dominant parameter compared to others such as the substrate roughness.

Based on this result, it has been shown that low silane concentrations necessary to grow μc-Si:H can be reached even from pure silane gas. Moreover, simple analytical plasma chemistry modelling and experiments have shown that for a fixed silane

flow rate, the gas utilization efficiency increased with the silane concentration and has an optimum for pure silane gas. Hence, microcrystalline silicon has been deposited over a large area ($47 \times 37 \mathrm{cm}^2$) from pure silane at a rate of 11.5Å/s with a gas utilization efficiency of 81%.
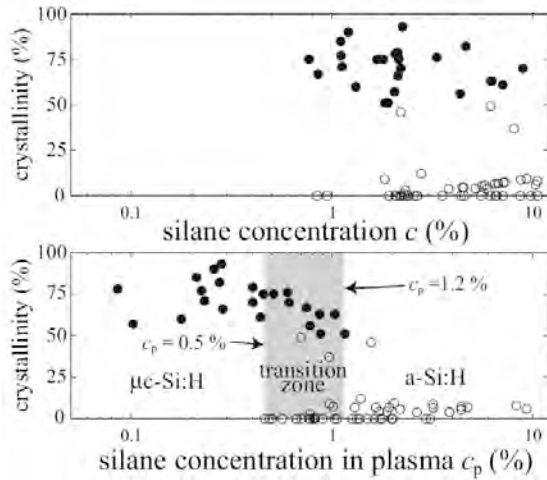
Fig. 2.6.1 *Film crystallinity can be classified as a function of silane concentration in the plasma, but not only as a function of input silane concentration.*
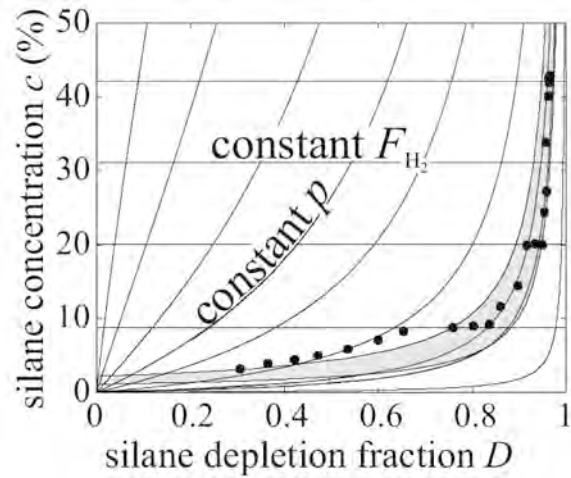
Fig. 2.6.2 *Optimization route from low silane concentration to high silane concentration by varying only the pressure and the hydrogen flow rate.*

Furthermore, an optimization procedure has been developed to determine the optimum plasma conditions in terms of deposition rate, silane utilization fraction and material crystallinity. Results have shown that if the initial plasma parameters are carefully selected, the deposition process can be optimized by varying only the working pressure and the hydrogen flow rate (see Fig. 2.6.2). It has been shown that for the deposition of μc-Si:H, the highest silane utilization efficiency is obtained towards pure silane and not towards the common highly hydrogen-diluted regime. The optimization methodology has been used to reach a deposition rate of 10.9 Å/s of a material with a crystalline fraction of 66% and a silane utilization efficiency of 82.3%. A single junction PV solar cell produced with these parameters has shown a non-optimized light conversion efficiency of 6%.

2.6.2 From conventional Plasma Spraying to Reactive Thermal Plasma CVD

The plasma torch is one of the most elementary plasma sources used in industrial applications. It has brought atmospheric thermal plasma spraying to commercial and economic success. Many daily applications would not be possible without this widespread industrial process. However the applications are limited to relatively porous and thick coatings with respect to vapor deposition techniques, and the spray materials are restricted to substances with a convenient melting point.

Recently the plasma torch has been operated and investigated at very low pressures. Low pressure plasma spraying (LPPS) operates down to pressures in the mbar range and approaches more and more the thin film technology which is mainly dominated by conventional RF plasma sources. This broad operation range

has a large potential for a wide variety of industrial applications and will widen the traditional market of plasma spraying and plasma spray equipment.

The plasma torch up till now is the only plasma source which successfully allows the use of solid, liquid and gaseous precursors. This great advantage is due to the high enthalpy content of the plasma jet. The existing plasma torch is the basis for a new technology of reactive thermal plasma CVD. In reactive thermal plasma CVD, the evaporated solid or liquid precursors and the gaseous components contribute to a complex plasma chemistry which leads to film deposition. With reactive thermal plasma CVD dense layers at high deposition rate can be obtained. However, this needs a completely new development of processes and deeper understanding of the underlying plasma physics and chemistry.

In plasma spraying only solid particle injection is used therefore the injection of liquids into the F4 torch had to be developed and tested. Several different experimental arrangements have been used including commercial nebulisers and capillary tubes. The test clearly showed that injection of the liquid directly into the plasma torch through the existing powder injection hole of the F4 torch is the most favourable. Injection at other places into the plasma jet have been found to be far less favourable. The dependence of the efficiency of the liquid injection on the supersonic flow inside convergent and divergent nozzles has been investigated. Several standard and special nozzles have been equipped with liquid injection holes and pressure measurement taps for injection tests. The local pressure at the injection location has been measured for different nozzle geometries, various plasma conditions, liquid flow rate and chamber pressures. In all these liquid injection investigations, water has been injected into the nozzles and imaging and optical emission spectroscopy has been applied to monitor the behaviour of the plasma jet upon injection. In addition, various modifications to the nozzle have been made and tested. From these tests optimum nozzles have been selected. The investigations and design of the liquid injection led to a patent application by the industrial partner Sulzer Metco.

In the following injections of carbon-containing liquids into the F4 torch were made to study the plasma chemistry in the jet and to investigate the layers formed under different conditions. For various reasons (safety, e.g.) isopropyl alcohol was first chosen as liquid precursor. The injection of isopropyl alcohol shows a very interesting chemistry within the plasma jet. As observed earlier in diamond deposition plasmas, the inside of the plasma jet emits H_α light (red) whereas the plasma boundary emits light originating from C_2 Swan bands (green). First preliminary results from optical emission spectroscopy show that different plasma chemistry occurs in different parts (compression and expansion zones) of the plasma jet (Fig. 2.6.3). First layers were obtained, however at present no detailed characterization of these films has been done.

In order to investigate the behaviour of plasma and plasma chemistry on the different injection locations of gaseous monomers intensive experiments have been performed. To begin with methane and ethylene gases were used. A laser interferometer allowed the in-situ measurement of the deposition rate whereas Fourier-Transform Infrared (FTIR) spectroscopy gave first results on the composition of the obtained films. Film structure was investigated using Secondary Electron Microscope (SEM). These measurements and characterisations were used for a fast development of various carbon-containing films. The first experiments showed clearly that reactive thermal plasma CVD has a very large application potential. In the case of carbon-containing monomers, hard layers (diamond and diamond-like) and soft layers (polymers and amorphous carbon) can be obtained at high deposition rate. This first investigation clearly demonstrated the large potential of reactive thermal plasma CVD using a commercial F4 plasma torch. Various

industrial applications demanding high deposition rate such as textile treatment could be imagined.

Ar (591.20 nm)   H$_\beta$ (486.13 nm)   C$_2$ (516.52 nm)   (In each case)
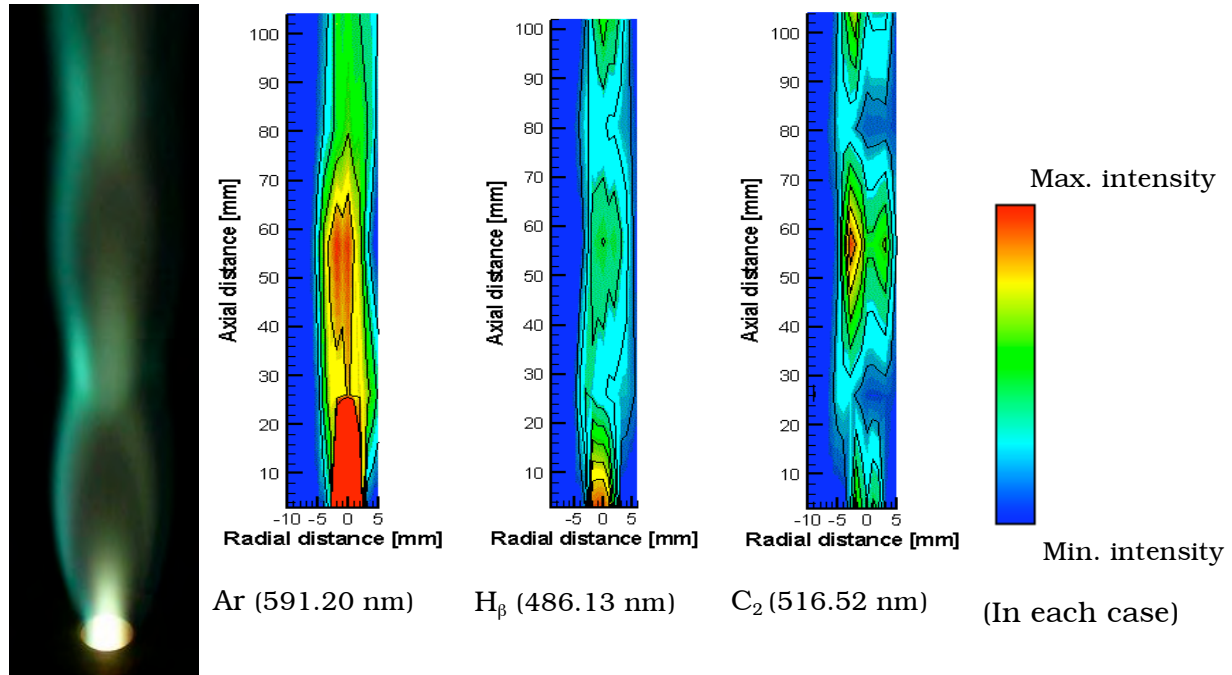
Fig. 2.6.3   *Spatial distribution of the Ar, H$_\beta$ and C$_2$ line intensities as obtained by optical emission spectroscopy (OES).*

2.6.3   Design, characterisation and modelling of a reactive Low Energy Plasma (LEP) Source

Industry needs plasma sources capable of driving high deposition rate processes for high quality coatings. In particular, the semiconductor industry needs high deposition rates in epitaxial processes in order to decrease the production costs of the sources.

The underlying physical principle of the LEP is that an intense low energy plasma can be generated by sustaining a low energy arc discharge by a large electron current emitted from a hot filament. The plasma source contains a tungsten filament heated by a current. The plasma is sustained by applying a voltage of about 20-30V between the grounded chamber walls and the hot filament. Discharge currents in the range 10-100A can easily be obtained. The low energy electrons ionise and excite the argon as well as the admixed gases and therefore create a dense reactive plasma in the chamber. The main advantage of the low energy plasma is the low energy (<12eV) ion bombardment of the substrate leading to interesting industrial applications such as the epitaxial growth of layers such as SiGe.

The first successful applications of the low energy plasma source showed several difficulties which are directly related to plasma physics and chemistry and to the technology of the plasma source design. One major problem inherent in the principle of the plasma source is the influence of the design of the ionisation source on the resulting plasma. Process stability and film inhomogeneity are two other topics which need to be clarified before successful industrialisation of the reactor and process. Therefore, diagnostics of the resulting plasma are needed in order to

optimise the process plasma from the point of view of deposition rate and uniformity.

A detailed noise analysis of the plasma was made by using several measurement techniques: a photomultiplier to detect the plasma light, several multi-Langmuir probes, current probe measurements for the total current and finally a differential voltage probe for the power source output voltage. It was shown that the use of a stabilized dc source instead of an ac source for the filament eliminates all 50Hz noise and its harmonics in the plasma. Finally by also replacing the Unaxis dc source for the plasma discharge by another better-stabilized dc source, the plasma became more stable and nearly free of noise. Filtering of the arc power supply allowed in addition a substantial noise reduction of the plasma.

Using double Langmuir probes, uniformity profiles of the plasma density, electron temperature and floating potential for various conditions (such as different pressures, source configurations, different anode geometries and different magnetic field coil configurations and magnetic field strength) have been measured. At the beginning of the year, the first series of measurements with a multi-Langmuir array were made. The Langmuir probe array contains 59 surface electrical probes for homogeneity measurements which are integrated in a dummy substrate. A multiplexer and a digital multimeter controlled by Labview software read out the probes and enable instantaneous monitoring of plasma uniformity and stability at the substrate surface. The measured electron saturation current leads to the profile of electron density and therefore the plasma uniformity and stability at the substrate surface (see Fig. 2.6.4). With the multi-Langmuir probe it could also be shown, that the installation of an additional magnetic cusp field can increase the homogeneity of the electron density (see Fig. 2.6.5). The plasma stability (the so called plasma flickering) was also investigated under these various conditions.
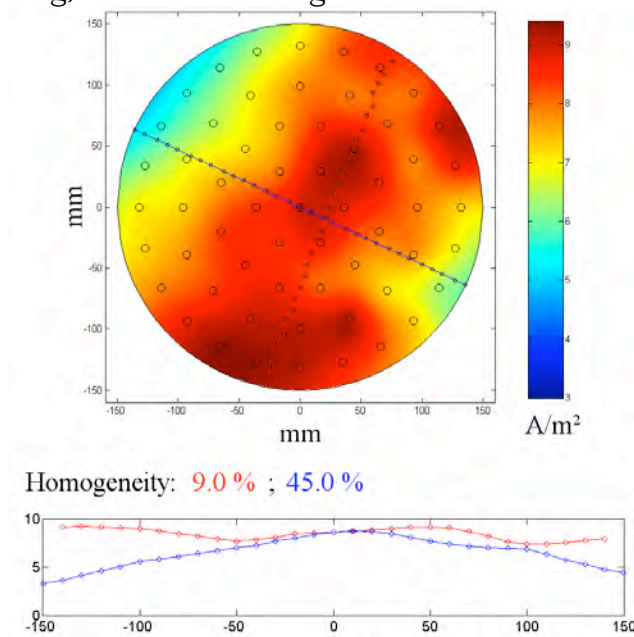
Fig. 2.6.4   *Electron density measurements made with the multi-Langmuir probe.*

The investigation showed that magnetic confinement leads to a stable plasma, whereas a weaker or no magnetic confinement led to instable or asymmetric plasmas. In addition, it was found that the dc discharge current tends to pass on a single spot of the anode, probably due to surface conditioning of the anode. To

analyse this phenomenon a new measurement tool was developed. It consists of a highly sensitive Hall effect probe which measures the B-field created by the plasma current. First measurements and a simple 2D simulation of the system gave very promising results.

Using the Femlab and Matlab software, a fluid model for the argon plasma in a magnetic field was written and is used for comparison with the experiment.
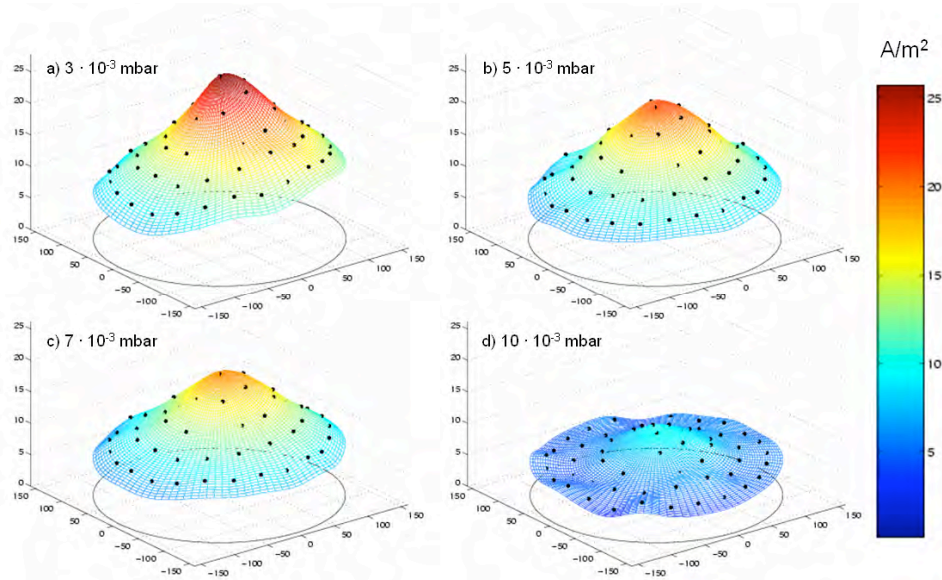
Fig. 2.6.5   *Electron density measurements made with the multi-Langmuir probe at 7×10^{-3} mbar and only 2.5G on the centre axis but with an additional cusp field produced by permanent magnets fixed on the outer reactor wall (x,y coordinates in mm).*

2.6.4   *Low Energy Plasma Processing for Wear Resistant Coatings*

Existing processes for wear resistant coatings have their limitations. The thermal CVD technology is not flexible enough in the selection of the precursors for a given temperature range to compete with PVD because the thermal load is limiting the choice of substrate material. Existing technology for plasma-enhanced CVD for wear resistant coatings has mainly been developed for diamond and diamond-like deposition.

The objective of this project is the deposition of wear resistant coatings by a plasma-enhanced CVD process. The new process approach takes advantage of an existing dc plasma technology. The basis of the process used is the same as for the deposition of diamond and for epitaxial SiGe growth running at the same time at the CRPP. The LEP plasma process is based on a dc arc discharge. The discharge operates at high discharge currents and at low voltages. All gases fed to the discharge are nearly completely dissociated. However, the operating pressure is orders of magnitudes lower than in conventional CVD and also lower than in PECVD for diamond in the same reactor.

The commercial BAI plasma reactor at the CRPP was modified to be run in the Low Energy Plasma (LEP) mode. This implied the addition of a turbo pump with high pumping speed to the device in order to reach working gas pressures down to 10^{-4}mbar. For the deposition of the SiN layer, silane and nitrogen or ammonia gas

mixtures have been used. For the case of the deposition of SiC layer a silane/methane gas mixture was used. As diagnostic, a laser reflectometer was applied in order to obtain in-situ information on the deposition rate, index of refraction and surface roughness of the depositing layer. Optical emission spectroscopy was used to investigate the plasma composition which was then correlated with the layer composition and the layer properties. FTIR spectrocopy was applied as ex-situ characterisation method. FTIR spectroscopy is a simple and fast method which means that results of the layer compostion can directely be used to optimize the plasmas process. Electron microscopy performed at the EPFL also provided information on the structure of the coatings. Selected samples have been sent to the ETHZ to be characterised by means of RBS and first tribological tests have been performed by OC Oerlikon at Balzers.

The obtained coatings clearly show that the dc current reactor is very well suited for the deposition of SiN and SiC layer with an acceptable deposition rate. During the process development all the important process parameters were systematically changed in order to optimize the process window for the two types of coatings. The most important parameters were silane gas flow and silane gas dilution, the gas pressure and the discharge current. The substrate temperature depends on the positon of the samples with respect to the plasma column and the plasma current, and is in the range of 300-400°C for the case here.

In both cases, as determined by RBS measurements, nearly stoichiometric layers have been obtained. However FTIR measurements showed that the SiN as well as the SiC coatings still contain a considerable amount of SiH bonds. Using ammonia for the SiN preparation more NH_x bonds than using silane /nitrogen gas mixture has been found. In addition, SiO contamination was detected, probably originating from small vacuum leaks in the reactor.

The results obtained at the CRPP have been confirmed by investigation from OC Oerlikon in a industrial plasma reactor. The reduction of the SiH bonds reduction in the SiN and SiC coatings is the main problem to obtain coatings for applications.

2.6.5   Atmospheric plasmas for thin film coating

Plasmas at atmospheric pressure are thought to be an alternative way for the production of coatings for various applications. Avoiding vacuum technology for depositing coatings on polymer films is certainly one possible route for cost reduction. However, there are various problems related to the process of RF plasmas operated at atmospheric pressure such as control of the discharge type.

The dielectric barrier discharge is generated between two alumina (Al_2O_3) plates (10cm x 10cm), metallized on their back face, 2mm apart. One is at the high voltage potential; the other is grounded through a 50Ω shunt. The power supply consists of a low frequency function generator, a power amplifier and a high voltage transformer. Gases are injected parallel to the electrodes and the pressure (1-1000mbar) is adjusted with a valve between the chamber and the pump.

A preliminary study of the glow discharge in different neutral gas mixtures (He, N_2, Ar) as a function of the pressure (10^3 to 10^5 Pa) has been done in order to determine the basic characteristics of the plasma. The discharge regime for deposition of SiO_x is of filamentary type because of the large gap used and the adjunction of reactive electronegative species from the HMDSO+O_2 gas mixture plasma. However, at lower pressure, a glow type discharge regime is obtained. The SiO_x layer is deposited on

polyethylene films from a mixture of hexamethyldisiloxane (HMDSO) and oxygen diluted with nitrogen.

At low pressure the plasma is composed of a multitude of discharges during half a period, representative of the multipeak regime. The number of pulses increases with the applied voltage and/or the pressure. A transition from multi-peak to Townsend mode is observed between 160 and 320mbar. This transition is progressive and characterized by discharge pulses becoming closer and closer, overlapping each other, resulting in only one Townsend discharge pulse. An interpretation of this transition could be that at lower gas pressure the ion–electron emission on the dielectric surface is the dominant mechanism which governs the secondary emission resulting in a multipeak mode. The dielectric barrier limits the growth of the pulse, but as the applied voltage continues to increase, a new pulse occurs and so on. By increasing the pressure, the gas density becomes too high for the ions to reach the cathode with sufficient energy and the secondary emission due to the impact of excited molecules prevails resulting in the transition to the single Townsend mode.

The evolution of the current shape during the transition to multi-peak is very similar to what has been observed at atmospheric pressure in nitrogen with an admixture of oxygen. Increasing the amount of oxygen causes a discharge transition from Townsend to multi-peak and finally to filamentary mode. Below the transition pressure, the multi-peak regime is characterized by very stable and identical discharges (number of pulses and amplitudes) from one half period to another and during the entire measurement time. Time-resolved optical emission measurements confirmed this electrical characteristic and high-speed imaging has been used to investigate this particular behaviour in more detail.

The fast exposure images, shown in Fig. 2.6.6, along with the corresponding electrical characteristics, describe the evolution of the light emitted by the discharge during a sequence of multi-peaks in nitrogen at 40mbar. Each image is obtained with a 100ns gate and 100 periods accumulation. These measurements show that although there are spatial nonuniformities, this spatial distribution is very reproducible from one pulse to another. The discharge seems to expand spatially in the gap, like a wave, from the beginning to the end of each pulse. The discharge starts in a preferential region, probably where the gap is smallest and expands transversally, while the charge concentration decreases at the original place and so on until the end of the pulse where a new cycle begins.

In our case, this spatial evolution is certainly due to the geometric imperfections of the discharge cell (parallelism). These images also show that there is still light emission between two pulses (images 1, 4, 7 and 10). In the meantime, the electrical characteristic shows an active component above the displacement current. Thus, the discharge may not be completely quenched between pulses due to the Penning effect which sustains it. The same phenomenon is observable in helium at atmospheric pressure and this may explain why the successive breakdowns occur at lower gas voltages.

The formation of particles in SiO_x deposition plasmas is a real problem in industrial applications of the plasma process. The particle formation in a Dielectric Barrier Discharge (DBD) used for SiO_x deposition has been investigated as a function of pressure and monomer concentration in a $HMDSO/O_2/N_2$ gas mixture. Figure 2.6.7 is an example of results obtained with simultaneous measurements of parallel- and perpendicularly-polarized scattered light by particles formed in the plasma. The particle size evolution at 600mbar is plotted along the gas flow as a function of time and position in the discharge. Particle size is calculated from the evolution of polarization degree. A numerical simulation, based on Mie theory, is used to

calculate the polarization degree as a function of the particle size according to the wave length of the light source (488nm) and particle material (SiO_2).

A periodical powder formation is observable. We suspect a monomer flow variation, inherent to the gas distribution system, to be at the origin of this phenomenon. Particles appear immediately at the entrance of the discharge (pixel 100) then grow before being expelled by the gas flow out of the discharge (pixel 350) where particle accumulation continues until a size of ~0.25µm.
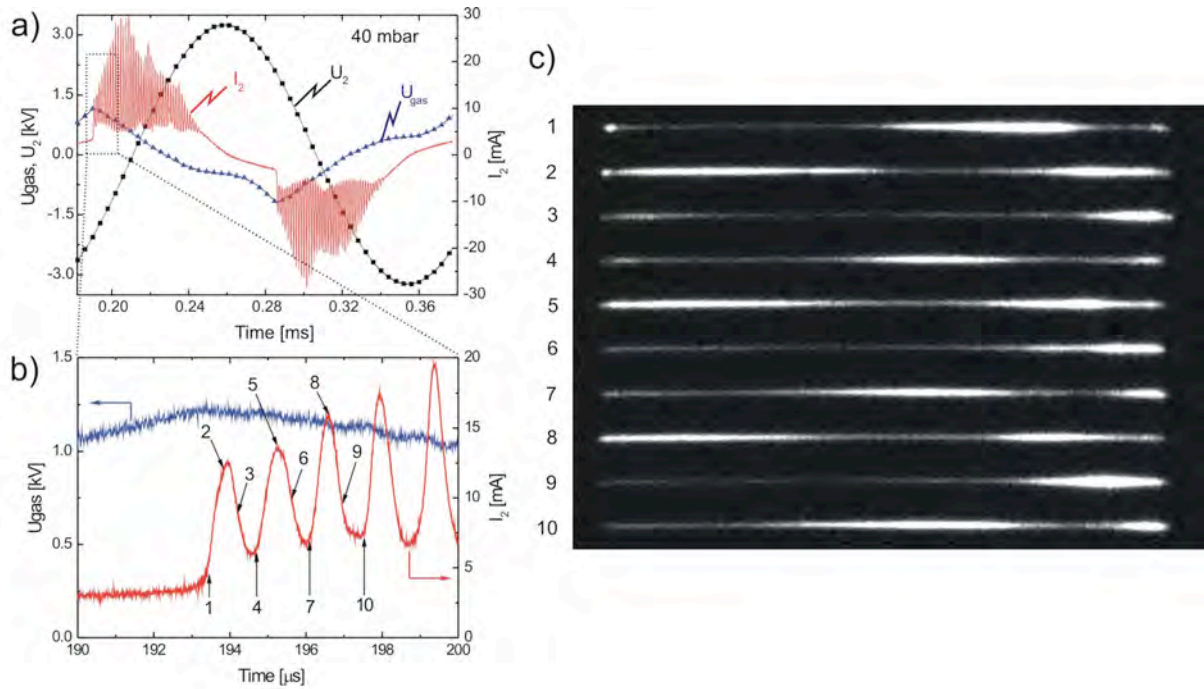
Fig. 2.6.6   a) Electrical signal of a high power DBD at 5kHz with 3slpm gas flow and a 1 mm electrode gap in nitrogen at 40 mbar.
b) Zoom of the first multi-peaks with the number indicating the time when the images were taken.
c) Corresponding 100ns exposure with 100 accumulation images of the electrode gap.

A new experimental arrangement has been built for simultaneous laser light scattering measurements. Two high quantum efficiency CCD cameras have been used and triggered simultaneously in order to acquire the light scattered by particles growing in a $N_2/O_2/HMDSO$ DBD. A polarizer was placed in front of each camera to collect respectively the parallel and perpendicular polarized scattered light, thus avoiding non-repeatable powder dynamic occurring at high pressure. The analysis and calculation made on the images obtained was used to determine the polarization degree and the particle size evolution along the gas flow according to the working pressure, gas composition and monomer concentration.
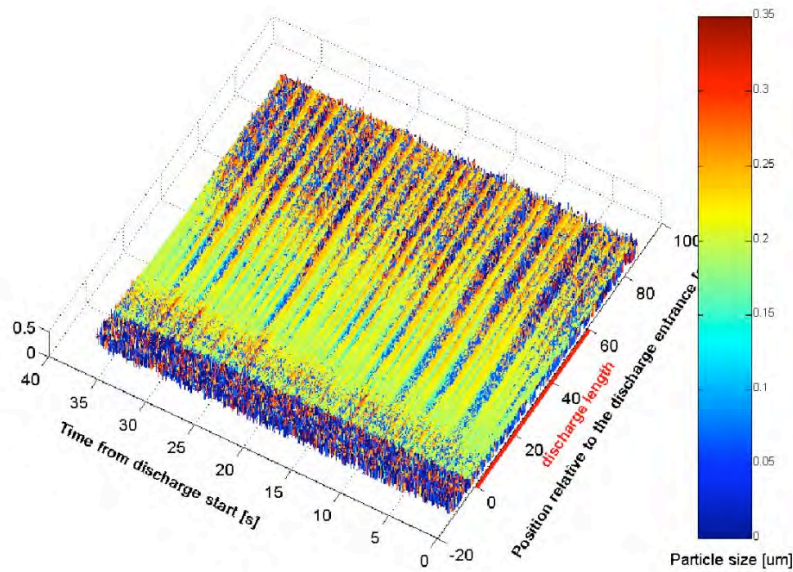
Fig. 2.6.7   *Spatial and time evolution of the particle size in a HMDSO (1.6g/h)/O₂(0.12slm)/N₂(1.8slm) plasma at 600mbar. Discharge length: pixel 100 to 350.*

2.6.6   Nano powder synthesis by thermal plasmas

The goal of this common project between the EMPA Thun and the CRPP is to monitor the process of nanometer particle formation in a thermal RF plasma. The aim is to understand the nano-particle synthesis and growth mechanism and to develop *in-situ* process monitoring for nano-particle processing in inductively coupled RF thermal plasmas. Several in-situ powder and plasma diagnostics have been designed, constructed and have been available at the EMPA Thun for the study of plasma processing of nano-powders.

The nanopowder synthesis system used for this study consists of an induction plasma torch, a synthesis reactor, a filtration unit, and a powder feeder. The induction plasma torch used at a frequency of 13.56MHz is mounted on top of the synthesis reactor and operated with argon and hydrogen gases with a maximum RF power of 35kW. Argon is used as central gas and a mixture of argon and hydrogen as sheath gas. The powder injection probe is connected to a commercial powder feeder being operated by continuous volumetric dosing. Alumina powder was used as precursor material.

Optical emission spectroscopy and laser light extinction measurements are carried out to monitor the on-going process *in-situ*, which gives real-time information on precursor evaporation. Optical emission spectroscopy was used to investigate the thermal decomposition of alumina precursor in the thermal plasma. Figure 2.6.8 shows the changes of the emission line intensities of aluminum vapor Al and gaseous aluminum suboxide AlO. This evolution of the line intensities of Al and AlO gives information on the thermochemical reactions leading to alumina nanoparticle formation. To simplify the analysis, the axial distance is divided into three regions by the two maxima of Al and AlO as illustrated in Fig. 2.6.8. In region (1), the Al line intensity increases and reaches its maximum at z=90mm, indicating the maximum evaporation rate of precursor particles. On the other hand, a steep increase in the line intensity of AlO is found. The low line intensity of AlO near the torch can be

explained by the fact that the temperature at this position is so high that only Al exists. Indeed the plasma temperatures in the center line of the plasma are found to be around 3500K.

The reactions in region (1) of Fig. 2.6.8 can be summarized as heating, vaporizing, and maximal evaporation of the alumina precursor. In region (2), a remarkable decrease in Al line intensity is observed, while the increase in the line intensity of AlO continues reaching a maximum at 130mm. The line intensity decrease of aluminum vapor can be caused by the exothermic oxidation of aluminum with oxygen leading to nucleation and formation of the nano-sized Al_2O_3 particles. In region (3), the vapor phase Al and AlO become unstable with the decreasing temperature and are hence solidified to Al_2O_3 through recombination with oxygen leading to a decrease in line intensities of Al and AlO. From these thermochemical explanations, an axial position of z=95 mm, near to the maximum precursor evaporation, is proposed as the optimum quenching position for the synthesis of the finest particles. It is expected that the nucleation reaction starts at this location, where the line intensity of the main species Al decreases remarkably. In order to ensure the formation of fine particles and to avoid agglomeration, the plasma should be rapidly cooled down to obtain a high saturation rate, once the precursor is evaporated.
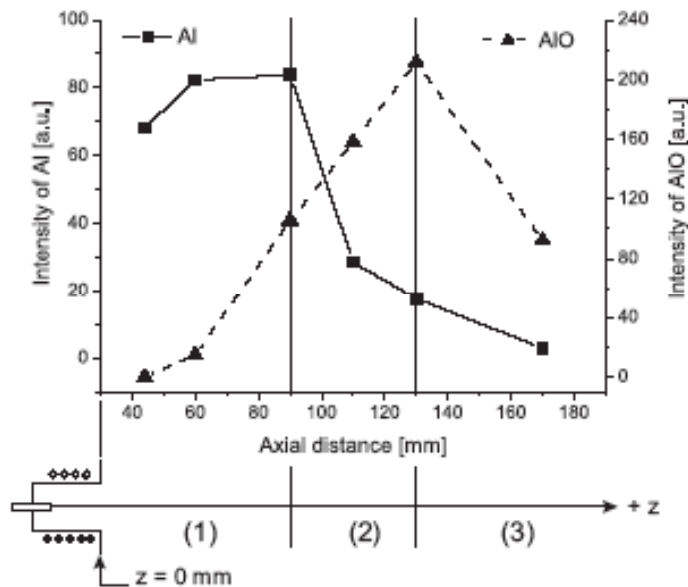
Fig. 2.6.8 *Axial emission line intensities of aluminum vapor Al(g) and aluminum suboxide AlO(g) measured at different axial positions from the torch exit.*

Besides the injection position the influence of the flow rate of the quenching gas was also investigated. Argon as quenching gas with different flow rates was injected through a ring with eight holes. The enthalpy probe measurement showed a remarkable reduction of the plasma enthalpy at the quenching gas flow rates of 28 slpm and higher. The specific surface area (SSA) measurements on the collected nanoparticles showed results consistent with enthalpy probe measurements. Depending on the quenching gas flow rates, different crystallographic phases of the alumina nanoparticles were obtained as measured by X-ray diffraction. The dependence of plasma cooling on the quenching gas flow rates observed by enthalpy probe measurements well explains the occurrence of the different transition aluminas.

The present study demonstrates a better understanding of the process and the possibility that the nanoparticle synthesis process can be optimized by application of the process monitoring technique and its interpretation based on the material properties.

2.6.7 Arc Phenomena in Space Environment and Equipment

In collaboration with Mecanex SA in Nyon and ONERA in Toulouse mandated by ESA (European Space Agency), the necessary fundamentals of small gap arcing have been established and applied to space equipment in order to reduce or suppress arcing in space environment and equipment.

In order to investigate arcing, a micro-plasma device has been mounted in a small UHV vacuum chamber where a controlled atmosphere can be created (Fig. 2.6.9). The distance between two wire electrodes is controlled by a piezo-actuator allowing distance control with nanometre accuracy.
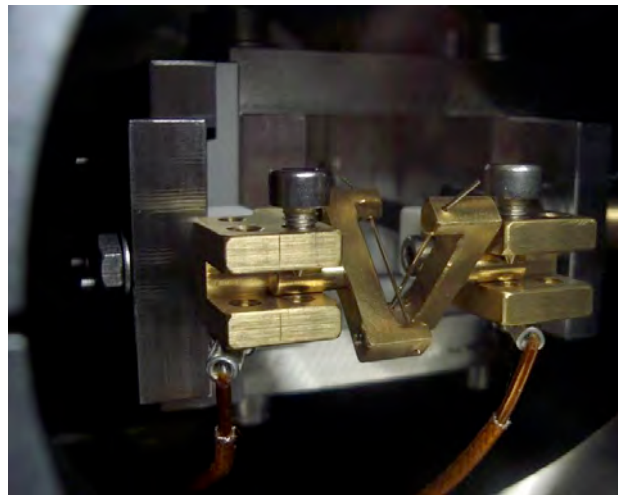
Fig. 2.6.9   *Detail of the crossed wire electrodes.*

Contact openings under various conditions have been investigated at vacuum and atmospheric pressure. As shown in Fig. 2.6.10 it was found that several distinct arc events occur before the final contact opening cuts the current to zero.

The different events were recorded by a fast oscilloscope operated in the sequence triggering mode. This allowed to record the different arcing events of an experiment with high time resolution. Depending on the experimental set up, more than 10 different successive arc events could be observed. During such an experiment the final contact opening was at a separation of about 5-6 microns, occurring 0.5 s after starting the wire movement. Each of these events consists of a series of individual arcs since the voltage traces and the emitted light simultaneously detected by a photomultiplier are correlated (see Fig. 2.6.11).

Before arcing, a liquid bridge is formed between the wires. The ensuing evaporation then leads to the vacuum arc. During such an event, the current delivered from the power supply decreases very rapidly in a first phase (Fig. 2.6.11). The arcing phenomena clearly consist of several spikes indicating that many short time (sub-microsecond) arcs exist. This period finishes suddenly and the current recovers

exponentially to its starting value. During this second part no light is emitted indicating the absence of any plasma. If the separation is large enough, the current decrease in the first phase approaches zero. This arc interruption is followed by exponentially-damped oscillations driven by the energy stored in the different elements of the electrical circuit. A first interpretation of the observations is that the arc melts sufficient material from the wires that a liquid bridge can be reformed between them, establishing full contact again. However, if the separation of the wires is too large the arc interruption is followed by the final contact opening.
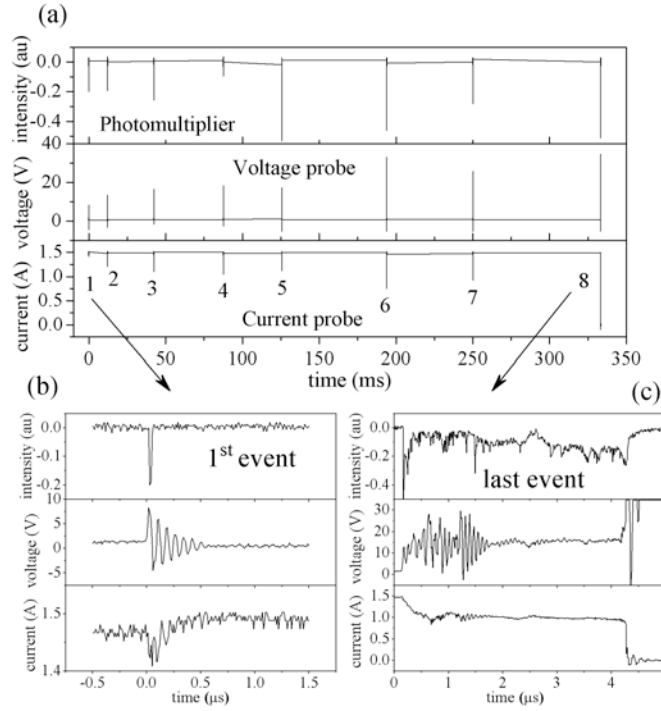
Fig. 2.6.10   *(a) Raw data from the photomultiplier, voltage and current probes, showing 8 arcing events during contact opening at 17 µm/s with a current of 1.5 A and a load resistance of 30 Ω; detail of the first (b) and last (c) events.*
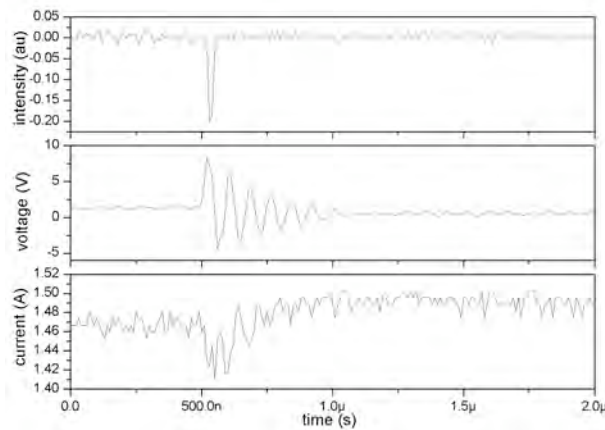
Fig. 2.6.11   *Details of the light intensity, arc voltage and arc current for the event 1(a) of the sequence shown in Fig. 2.6.10. (R=30Ω, I=1.5A).*

The arcing behaviour of the different events during contact opening depends strongly on the external circuit and the surrounding pressure. The voltage/current characteristics as well as the arc duration show roughly the same dependence for all the resistances and inductances (Fig. 2.6.12).

For the very first events the averaged arc voltage is slightly above the load line and approaches the load line around 1A when the interrupting arc takes place. The arc duration varies over 3-4 decades from duration below 100ns up till 100μs.

11.12.22 15:01:22
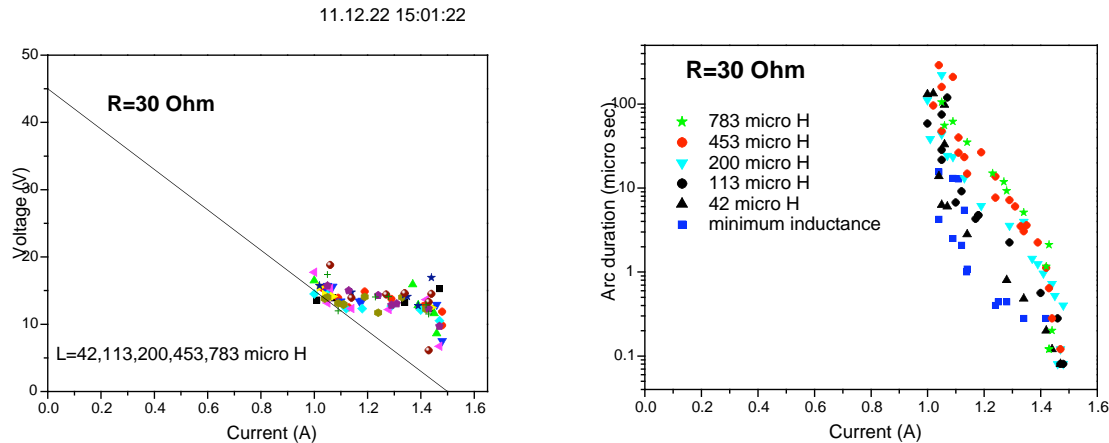
Fig. 2.6.12 *Left) Voltage–current characteristics for different inductances with the corresponding R=30Ω load line.*
Right) Arc duration as a function of the arc current.

Strong effects on the arcing events are obtained by adding an additional capacitance parallel to the contact. The capacitance drastically reduces the arc duration, and the arc voltage remains nearly independent of the arc current.

The current and voltage traces show, in most cases, oscillations particularly visible at the end of the discharge. This ringing comes from the response of the electrical circuit to the perturbation of the arcing. The first arc event leads to a very short light pulse, most probably a very dense plasma as shown in Fig. 2.6.13. This light pulse very quickly reaches a maximum and afterwards decays more slowly. The corresponding voltage and current traces show several distinct oscillations with frequencies higher than 100MHz. The light pulse shows a structure as if the pulse were composed of several light pulses as seen in the beginning of the arcing event. All the different pulses also lead to ringing of the circuit as can be seen on the voltage and current traces. Therefore it seems that the arc events are composed of a few nanosecond discharges which excite the electrical circuit which in turn oscillates leading to the complex voltage and current waveforms.

Preliminary emission spectroscopy measurements have been performed. A first measurement is presented in Fig. 2.6.14. These spectra essentially show line emission from the metals which evaporated from the wire. Therefore the micro plasma consists of a metal vapour plasma. A rough estimate of the electron temperature deduced from the line intensity ratio indicates a rather low electron temperature in the range of one eV.

The metal plasma is probably very dense and therefore a non-ideal plasma is formed. In particular, during the very first nanoseconds of the discharge, an

extremely dense plasma is formed such as can also be observed in electrical discharge machining. The transport properties of such non-ideal plasmas, in particular their electrical conductivity, might explain the observed voltage/current characteristics of the different arc events during an experiment. The contact closing after the arc event extinguished is at present not clearly understood. However, observations indicate that the arc melts sufficient material from the wires so that a liquid bridge could be formed again re-establishing full contact.

a)   b)
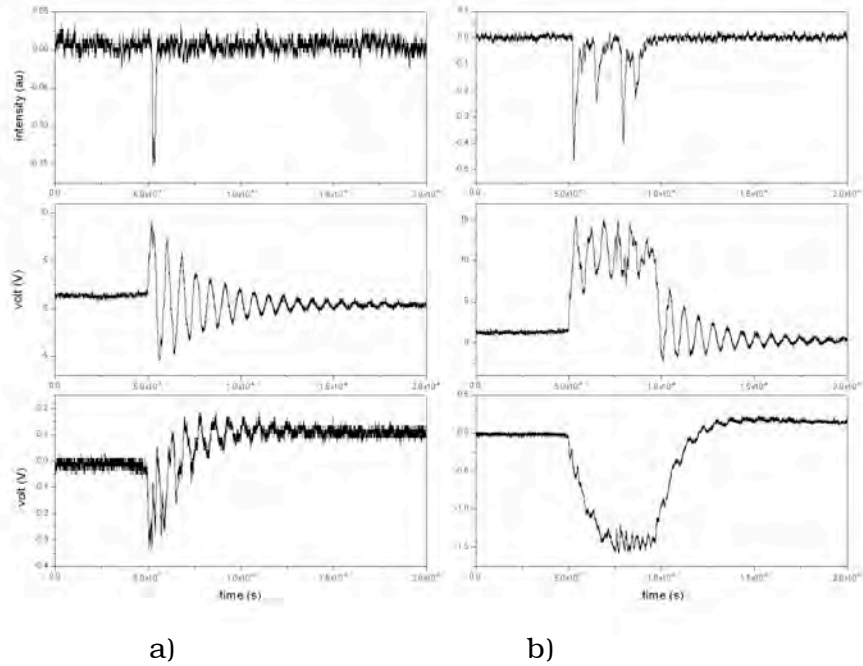
Fig. 2.6.13   *Light intensity, arc voltage and Rogowski probe (signal proportional to the arc current) in the first (a) and in the second (b) event out of four (R=30Ω).*
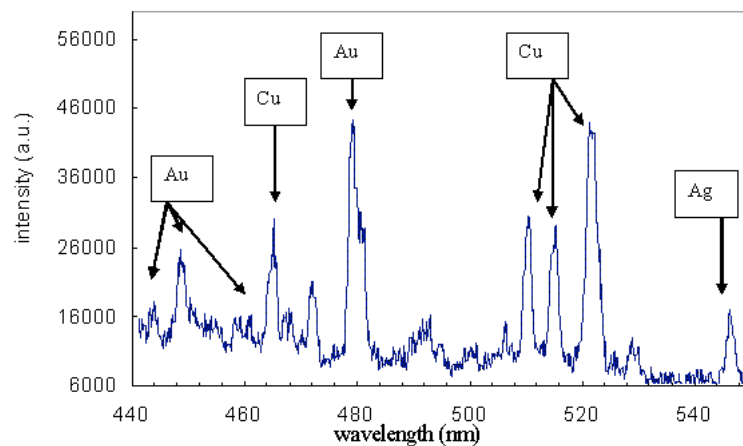
Fig. 2.6.14   *First optical emission spectrum averaged over several arcing events (R=30Ω).*

2.6.8 Influence of a weakly-ionised boundary layer on transonic and supersonic air flow

Dielectric Barrier Discharges (DBD) have been known for more than a century and are widely used in many different applications such as ozone generation, decontamination of gas streams and surface treatments. It is only during the last decade that their applications in aerodynamics, airflow control and plasma assisted combustion have started to be investigated. The present study focuses on the effects of high-speed airflows on dielectric barrier discharge characteristics. The DBD investigated in the common project between the CRPP and Laboratoire de Thermique Applique et de Turbomachines (LTT) and the Laboratoire d'Ingénierie Numérique (LIN) of the Energy Institute (ISE) from the Faculty of Engineering (STI) consists of a 10x10cm alumina plate, on which two electrodes are printed (Fig. 2.6.15). The frequency of the plasma excitation has been varied from 1 to 15kHz and rms voltages of 1 to 15kV have been applied. The use of appropriate materials allowed to achieve a lifetime of more than twenty hours for the DBD plate in air. The DBD plate was then mounted on one of the sidewalls of a Laval nozzle as shown on Fig. 2.6.15. It was demonstrated that a DBD can be maintained for several tens of hours in subsonic and supersonic airflows. The velocities close to the DBD plate, inside the boundary layer formed at the nozzle walls, are smaller than the free stream velocity. For M=1.1Mach in the free stream of the nozzle, corresponding to 343m/s, the velocity at the estimated discharge location d) is about 200m/s.
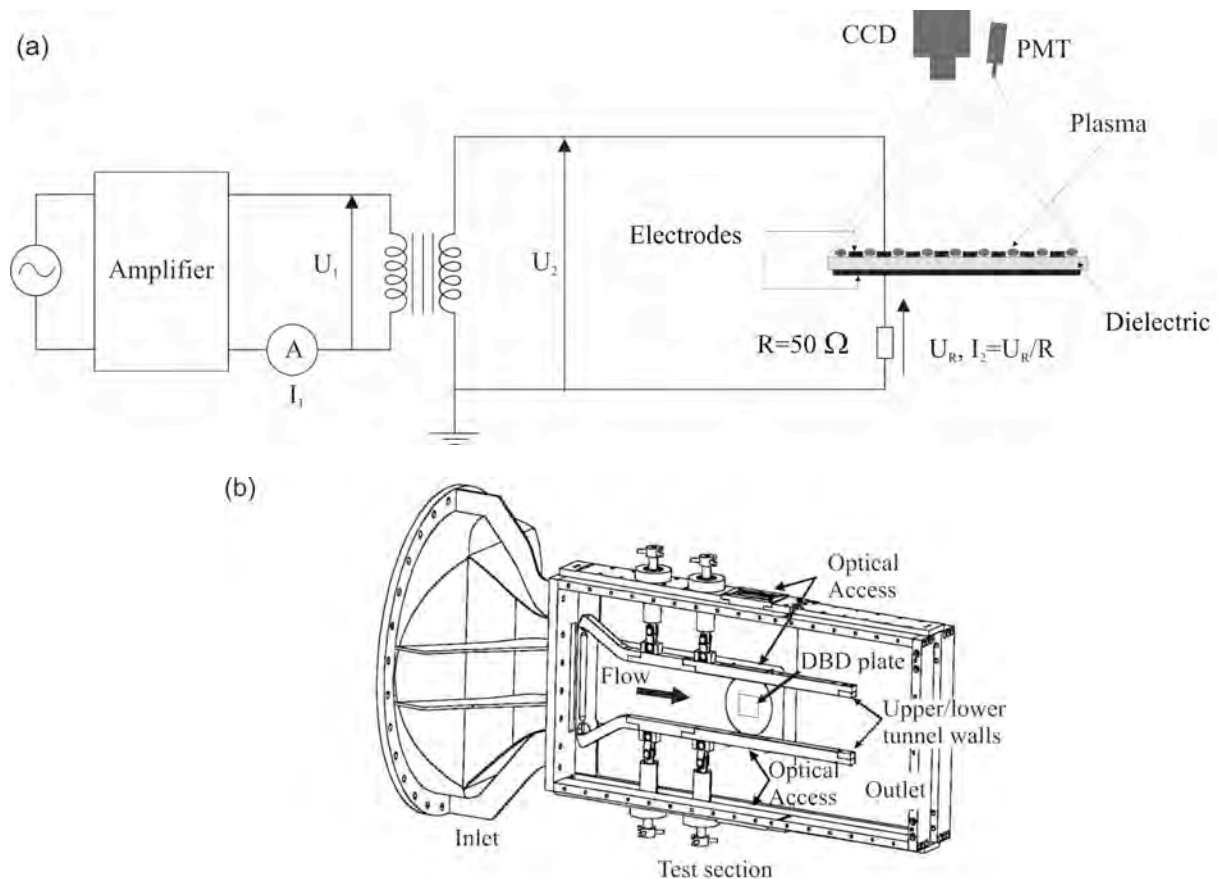
Fig. 2.6.15 *Schematic drawings of the surface DBD configuration, diagnostics and mounting on the Laval nozzle wall.*

Various diagnostics have been evaluated and adapted to study the small-sized and faint plasma: high voltage and current probes are used to measure the input power and estimate the power dissipated in the plasma, photomultiplier signals are correlated to the current signals to investigate the nature of the plasma (which has a glow and a filamentary component), CCD imaging gives information about the plasma geometry and emission integrated over the whole visible spectrum, and finally optical emission spectra are analysed to study the excited species in the plasma.

The DBD has been studied under different airflow velocity, frequency, applied voltage and electrode orientation conditions. Discharge current and time-resolved light emission measurements show that there are modifications in the discharge type at high airflow velocity. The study of the overall discharge shows that the glow component of the plasma is reduced, whereas the discharge becomes more filamentary. Most important are the changes in individual microdischarges: a reduction of the light pulse emission duration by one order of magnitude is found, from 500ns to 50ns, when airflow velocity is increased up to an isentropic Mach number of 0.7. Figure 2.6.16 shows parts of the photomultiplier signals with high time resolution, without airflow (a) and with an airflow at M=0.7 (b) with a direction perpendicular to the electrode stripes. The figure highlights the most significant effect of the airflow on the plasma: the reduction by one order of magnitude of the light pulse duration emitted by individual microdischarges.

These measurements indicate that there is a change in the breakdown mechanism, a transition from Townsend breakdown to streamer breakdown when the airflow velocity is increased. The depletion of N_2 metastable states due to the airflow seems to be the dominant cause, reducing the internal energy and reducing secondary emission processes. The discharge characteristics are also very sensitive to the electrode geometry.
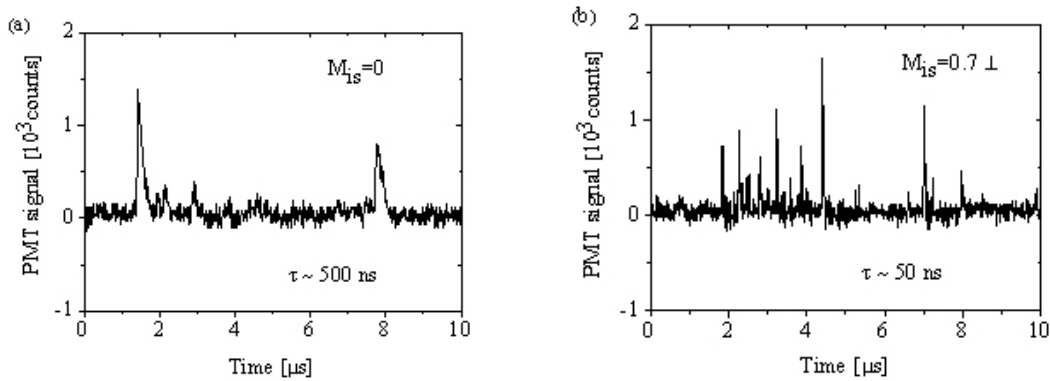
Fig. 2.6.16   *Photomultiplier signal at f=1kHz, P1(rms)=100W, U2(rms)=4.8kV.*

Figure 2.6.17 shows that a strong emission comes from the edges in the form of long filaments. The edge filaments start to appear at M=0.7 and their number increases at Mach 1.1. They were never observed at low speeds. These filaments have the typical shape of streamers, they stretch up to the back electrode boundaries. The difference in shape is clearly visible in comparison with the image at M=0, where the microdischarges remain close to the electrode. The edge effects can be explained by the fact that the electric field is stronger on the outer stripes. Also, the product of the pressure times the distance is larger on the outside because the grounded back electrode stretches about 1cm out of the top electrode

boundaries. The edge effects introduced by a two dimensional geometry, as opposed to a single stripe geometry, are dominant in the measurements. They are a key element in the airflow-plasma interaction. The experiments showed that the discharge and in particular the individual micro-discharges are affected by the surrounding airflow and that the geometry of the electrodes has significant consequences on the airflow-plasma interaction.
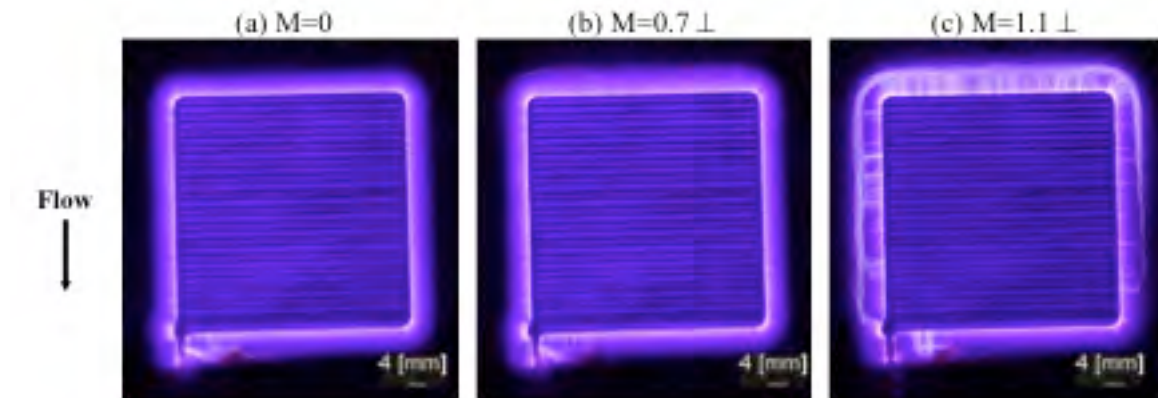
Fig. 2.6.17   *CCD images of the whole discharge area at f=1kHz, P1(rms)=200W, U2 (rms)=7kV, exposure time =0.25 for (a) and (b), 0.2 for (c).*

2.6.9   Plasma Pencil: Application to restoration/conservation of modern art

In modern art, polymers are a widely-used material. Restoration and conservation of these precious objects is often hindered by the low adhesion of these polymers. Plasma assisted surface activation of the polymer could facilitate the delicate restoration and conservation process.

In collaboration with the HKB Bern (Konservierung und Restauration) a plasma pencil operating at atmospheric pressure has been developed and tested in the frame of a BFH project. The plasma pencil consists of a ceramic capillary of about one millimeter in diameter (Fig. 2.6.18). The dielectric barrier discharge is obtained using a high flux of Helium and allows a treatment of the polymer surface in the millimeter range. The discharge is powered by a small high voltage RF power supply.
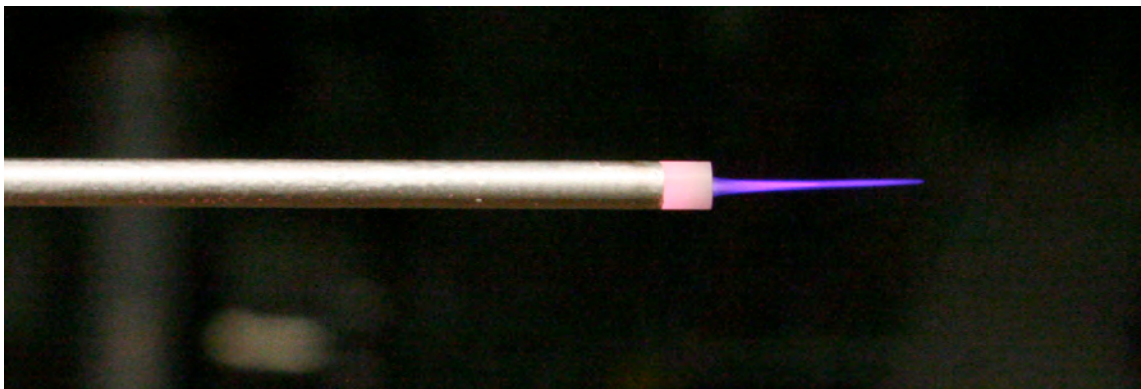
Fig. 2.6.18   *View of the plasma pencil and the plasma flame.*

During the treatment of the polymer surface, radicals are formed which are important for the inclusion of polar groups which in turn lead to an improvement of the adhesion. Extensive tests of the application of the plasma pencil for restoration of modern art have been made. The investigations included variation of the excitation frequency, the helium flow and different polymer materials. Various surface characterisiation methods have been applied to study the mechanism of the surface modification. In future the aging of the modified polymer surface and its relation to the final aim of conservation shall be investigated.

2.6.10   Plasma diagnostics for electrical discharge machining

Electrical Discharge Machining (EDM) is a widely-used machining technique. With this technology, numerous industries produce moulds, dies and finished parts with complex shapes. The process consists in successively removing small volumes of workpiece material, molten or vaporized during a discharge. The sparks are created in a flowing dielectric, generally water or oil. The liquid dielectric plays a crucial role for the electrode cooling and for the material removal: it increases the removing force on the molten metal when the plasma collapses, then it solidifies the molten metal into small particles, and finally it flushes them away. In collaboration with Charmilles SA the plasma, which lies at the heart of the process, has been investigated. Development towards successful micro machining is only possible if the basic physical phenomena of the tool plasma are understood.

The very successful project on the plasma diagnostics of the EMD plasma ended this year. The interesting results obtained during this period have been very promising and new physics about the EDM plasma in particular and its micro discharge have been obtained. Optical emission spectroscopy is one of the only plasma diagnostics applicable to EDM plasma. With this method, the electron temperature, the electron density and the influence of the discharge parameters on the plasma emitted light have been measured. It has also been shown by time-resolved spectroscopy that the EDM plasma is weakly non-ideal, especially in the very beginning of the discharge. Presently the CRPP is leading in the diagnostic and measurement of these extremely fast and dense micro-discharges. For this reason, a continuation of the study of the EDM discharge has been prepared during the last period of 2006. Two projects have been discussed and one in collaboration with Charmilles Technologies SA, the Ecole d'Ingénieur de Genève and Micron SA has already been submitted to CTI. This project is dedicated to the development and investigation of micro EDM milling.

The second project, at present in preparation, shall investigate the important mechanism of erosion of the electrode and the workpieces. Erosion of the electrodes is one of the crucial problems in EDM processing. The dependence of plasma contamination and its influence on the plasma parameters of different electrode materials is intended to be investigated. An additional important point for the future development of EDM is the development of advanced plasma diagnostic methods. Plasma diagnostics of the spark is a challenge since the discharge immersed in a dielectric is small, typically far below a millimetre, complicated by the poor reproducibility from spark to spark. New innovative plasma diagnostic methods are absolutely necessary if the EDM discharge or other micro-discharges shall be understood. Therefore the development of advanced plasma diagnostics is a prime point in future projects.

2.6.11   Other collaborations and industrial mandates

Helyssen SARL, a start-up company at the CRPP

Helyssen SARL, a start-up company, uses a test bed in the laboratories of the industrial plasma group to evaluate the performance of an industrial Birdcage antenna as Helicon source. The magnets and the necessary equipment for benchmarking and infrastructure have been lent to Helyssen SARL by the CRPP. This includes equipment also for plasma diagnostics and equipment and know-how in order to quantify the performance of high power RF plasma sources.

The results of the development and research of Helyssen SARL during the last year resulted in an extremely efficient Helicon source which is of considerable interest to some industries. High RF power operation tests of the Birdcage antenna, important for the industrial application, have been prepared and first tests are planned to start beginning 2007.

The collaboration has been established with the help of the Service des Relations Industrielles (SRI) of the EPFL.

Mandate from the European Project "Flexcellence"

Flexcellence or the EU project "Roll-to-roll technology for the production of high-efficiency low cost thin film silicon photovoltaic modules" is a Specific Targeted Research or Innovation Project (STREP) financed by the Sixth Framework Programme of the EU and is coordinated by the IMT (Prof Ballif) at the University of Neuchatel. The project consortium consists of two SME's (VHF-technologies, Exitech), one industry (Roth & Rau), three Universities (Unine, UBA and UL-FEE), and two research institutions (ECN and FEP). The eight project partners originate from six countries (Slovenia, Spain, Switzerland, Germany, United Kingdom and the Netherlands).

The goal of the project is to develop the equipment and the processes for cost-effective roll-to-roll production of high-efficiency thin-film modules, involving microcrystalline and amorphous silicon. In the frame of this project the CRPP was elected as subcontractor for the analysis, design, construction, and testing of a VHF-PECVD coating electrode for uniform high rate amorphous silicon coating on a 50cm wide moving plastic foil for solar cell application. This new RF electrode is implanted in the new production plant at VHF Technologies at Yverdon.

Flexcell (former VHF Technologies) is a company that manufactures flexible photovoltaic (PV) cells and modules, using Very-High-Frequency plasma technology to deposit thin layers of amorphous silicon onto plastic substrates.

During the year the RF electrode has been modelled, designed and tested by the CRPP in close collaboration with Flexcell. The construction part of the project has been directed by Flexcell. The RF electrodes have been tested on schedule and the obtained electrode performances concerning the homogeneity of the coating are within the specifications demanded by the coordinator of the EU project.

2.6.12 *Future and future projects*

During the last year numerous discussions with interested industries have been held resulting in many small experiments and tests which have been performed on the various plasma reactors at the CRPP.

The economic changes in the industrial landscape within Switzerland will influence the size and the topics of the industrial plasma group at the CRPP. Intense collaboration with the remaining OC Oerlikon (former Unaxis) in the domain of equipment for the production of thin film solar cells is and shall be continued either by direct mandates or with projects such as a project supported by the CCEM or CTI. In addition it is hoped that the successful collaboration with TetraPak in Romont can be continued in the frame of a new CTI project.

The diversification towards new topics such as the problems of arcing in industrial applications, in particular in industrial plasma devices has been started and new contacts for new projects have been initiated. New contacts with interested industries as well as with other institutes such as the PSI have been established. First discussions about common projects, for instance, in the development of the electron source for the free electron laser are under way.

3 Technical achievements of the CRPP in 2006

3.1 TCV Operation

During the year 2006, TCV scientific exploitation for the 2006 campaign started at the end of January and will continue until February 2007 when a major shut-down is planned. Operation was interrupted for 4 weeks in March to do minor maintenance tasks and for 9 weeks in August and September for an upgrade of the X3 mirror launcher (see Section 3.1.3). The machine was operated for an average of 4 days per week, 3 weeks out of 4, corresponding to the average target rate of 60%. Achieved sessions (half days) cover the following topics

Technical work	29 sessions
Transport	14 sessions
Electron internal transport barrier	28 sessions
H-mode	31 sessions
Plasma edge physics	19 sessions
Plasma control	5 sessions
Fast electron physics	5 sessions
Electron Bernstein Waves	16 sessions

3.1.1 X3 System launcher

For the X3 top-launch ECW heating a new focussing mirror generating a non-astigmatic RF beam at its waist (waist: $w_0=19mm$) has been successfully mounted on TCV during the last opening of TCV (summer 2006). According to numerical simulations carried out in the frame of a collaboration with CNR-Milano, this non-astigmatic RF beam with a stronger focussing should significantly improve the single-pass absorption of the X3 wave compared to the absorption levels obtained with the previous version (astigmatic RF beam).

3.2 Diagnostics

Several of the diagnostics launched in 2005 have reached the advanced design or construction phase during 2006. Several new diagnostics are being proposed to tackle the question of measuring the TCV current profile and examining the radial profile and the nature of turbulence in TCV. This is of particular interest in the H-mode and Internal Transport Barrier confinement operational modes which are the subject of increased physics research on TCV. This development activity is, of course, accompanied by continued development/improvement and maintenance of existing diagnostics that must be supported by a strong documentation effort in view of the continuous departure of qualified doctoral students and the arrival of new students.

3.2.1 Thomson scattering

Following the observation of increasingly regular disalignment of the laser path, some of the optical supports were replaced. The system of IR sensitive CCD monitoring cameras using relatively cheap commercial Web-Cams, was improved with up to 5 permanent and other temporary views of selected optics from the laser hall to the TCV device. By determining the position of the laser beams on the guiding mirrors, (some light is scattered by small dust particles on the mirrors), it is now possible to provide an immediate check on the system alignment and even proceed with a simple re-alignment during TCV operation.

3.2.2 Diagnostic neutral beam injector operation

The Diagnostic Neutral Beam Injector (DNBI) was operated throughout the 2006 experimental campaigns following an upgrade of the high voltage (HV) power supply in December 2005 with a nominal energy of 50keV and mean ion current of 2.6A. The beam and control software performed reliably with a beam availability ~94%. The DNBI was operated for 310 TCV discharges.
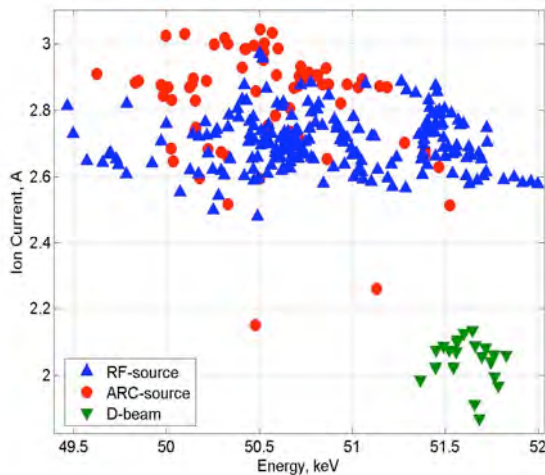
Fig. 3.2.1 *Beam ion current vs. beam energy during the 2006 campaign.*

To increase the beam purity and reduce beam divergence, the RF-plasma generator was upgraded with an Arc plasma source with corresponding arc-power supply and re-optimised ion optical system (IOS) in September 2006 in a contract with the Budker Institute (Novosibirsk, Russia). The H+ (primary energy) fraction was increased from ~50% to ~85% and the beam size in the plasma was reduced from 8 to 5cm (beam radius on 1/e level in the plasma). With this upgrade it is hoped to increase the upper plasma density range of Charge eXchange Recombination Spectroscopy (CXRS) measurements from ~7×10^{19}m^{-3} to 10^{20}m^{-3}.
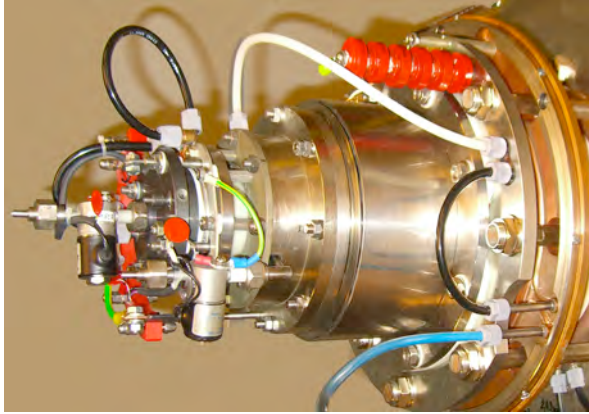
Fig. 3.2.2   *Arc-discharge plasma box of DNBI.*
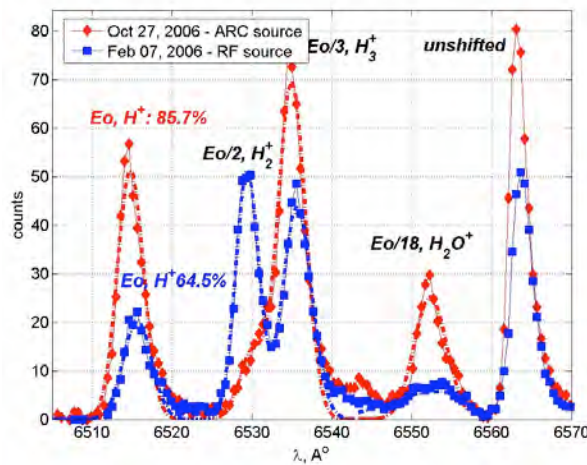
Fig. 3.2.3   *Beam fractions with Arc and RF plasma sources, measured by in situ "Ocean Optics", HR2000 visible light Spectrometer. Here each H_α spectral line is Doppler shifted differently for each energy component. The increase in the peak at 651.5nm demonstrates the increased fraction of the faster neutrals required to penetrate high density discharges.*

3.2.3   Charge exchange spectroscopy

During 2006 the horizontal and the vertical views of the CXRS diagnostic routinely measured ion temperature and rotation profiles (Fig. 3.2.4). Poloidal rotation in the plasma from the vertical system is often ~2km/s, lower than the typical toroidal values ~20km/s. These poloidal rotation values are comparable with the measurement uncertainty, mainly determined by the acquisition noise on the detection system (±50 counts for a typical experimental spectrum).

Two new scientific grade cameras have been installed to improve the sensitivity and to extend the range of plasma conditions available for toroidal rotation measurements. The cameras were procured from XCAM Ltd, and mounted on a back illuminated e2v CCD, with a high nominal quantum efficiency (~80% at the working wavelength of 529 nm) that is expected to improve the S/N ratio by a factor >2.

Fine tuning of the charge transfer timings improved the pattern noise compensation and the minimisation of the stochastic noise component, Fig. 3.2.5
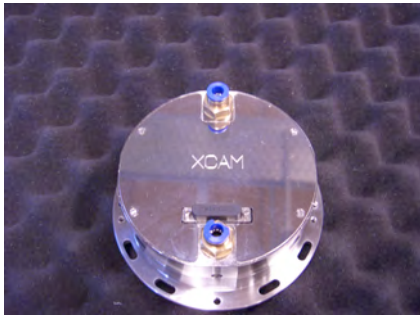
Fig. 3.2.4 *XCAM scientific camera for the CXRS diagnostic upgrade.*
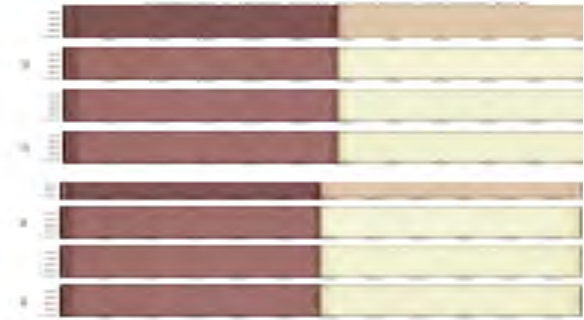
Fig. 3.2.5 *Full frame image of the new CCD cameras. In the bottom image the pattern noise is removed by adjusting the charge transfer timings.*

A new optical transmission line has been designed with increased spatial resolution for both the horizontal High Field Side (HFS) and Low Field Side (LFS) systems. 40 optic fibres (data) will transmit the light from the tokamak to the spectrometer increasing the spatial resolution from 16 to 40 measurement points along the minor radius (Fig. 3.2.6). The configuration was adapted to ensure the full coverage of the plasma radius, without significant loss of signal.
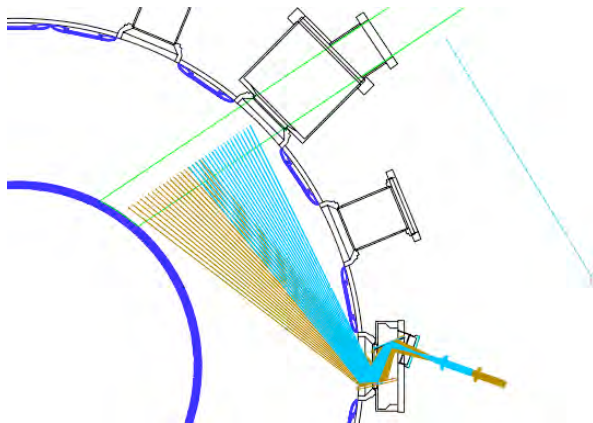
Fig. 3.2.6 *CXRS measurement chords corresponding to the final design of the new 40 fibres trans-mission lines.*

The new transmission lines for the horizontal systems and the installation of the new back illuminated cameras are planned for the 2007 TCV opening.

3.2.4 Neutral Particle analysers

Following repair of the gate-valve between the 5 channel NPA and TCV in June 2006 the routine measurements of escaping high energy neutrals from TCV were continued with this device.

The 10cm thick lead screen surrounding the Compact NPA (CNPA) was completed in August 2006 (lateral walls, further bricks above and below the CNPA) and improved by the installation of a heavy metal block with reduced diameter hole along the line of sight inside the vacuum duct between the analyser and TCV. We estimate the suppression factor of the hard-X-ray driven pollution to the CNPA

detector signals to be ~250. To monitor the influence of light and X-rays on the CNPA measurements two additional detectors outside the particle trajectories were installed in the analyser. One was open to the CNPA chamber to monitor light and the other closed to monitor penetrating radiation (see Fig. 3.2.7).
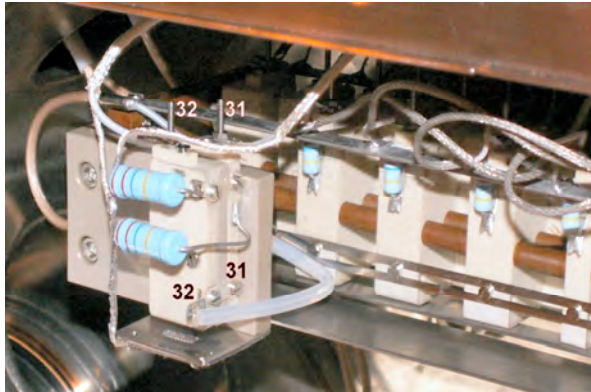
Fig. 3.2.7 *Additional CEM detectors in CNPA: 31 – with screen in front of detector for Hard X-rays, 32 – with open entrance for light detection.*

3.2.5 Correlation ECE diagnostic

Studies of plasma turbulence are important in understanding the nature of transport properties in fusion plasmas. Measurements of electron temperature fluctuations by means of correlation ECE diagnostics have provided information on the micro-turbulence properties both of electrostatic and magnetic origin on many fusion machines. On TCV, correlation ECE with high temporal and spatial resolution will be used to diagnose MHD modes (both small and large-scale), and to probe electron temperature fluctuations in scenarios with eITBs created by strong ECRH/ECCD.

The system was designed early in 2006 and the required components received by July 2006. Completion of the design and construction and installation on TCV is planned for December 2006, permitting preliminary measurements in January 2007.

The RF section of the existing LFS ECE radiometer was upgraded to obtain more amplification for both profile ECE and correlation ECE and the upgraded LFS ECE RF box was re-installed on TCV in September 2006 (Fig. 3.2.8)
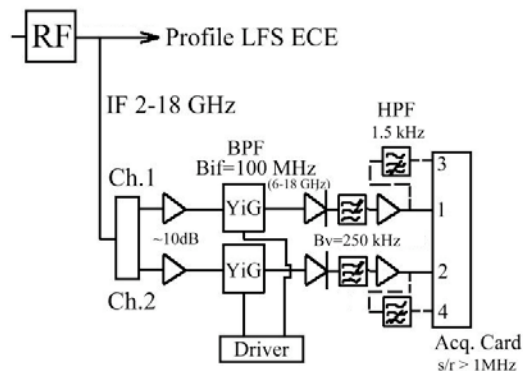
Fig. 3.2.8 Schema of the LFS ECE diagnostic.

3.2.6   FIR polarimeter

A far-infrared (FIR) polarimeter diagnostic for the TCV Tokamak is under construction at the CRPP. It is designed to measure the poloidal magnetic field and hence the current density profile of TCV plasmas. There is particular interest in low density plasma discharges with non-monotonic q-profiles, which are associated with internal transport barriers. The system has been designed to measure the current density profile using the Faraday rotation angle of FIR laser beams along 10 vertical lines of sight across the poloidal cross section of TCV. By the end of 2006, the diagnostic layout will be finalised and all the detailed component design will be in progress. The diagnostic will be installed on TCV in 2007.

1) Lenses
2) Waveguides
3) Half-wave plate
4) Mirrors
5) Wire grid
6) Mylar foil
7) Pyroelectric detectors
8) Reference detector
9) Choppers
10) Quarter-wave plates
11) Meshes
12) Quartz windows
13) Dichroic filter
14) Waveguide detectors
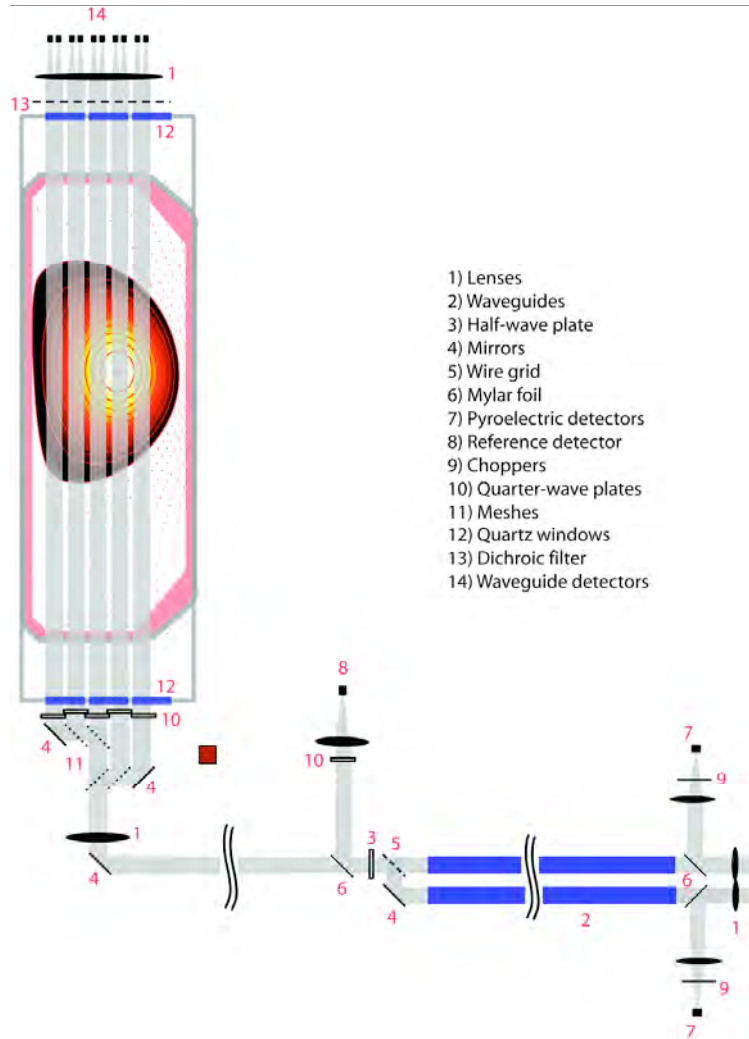
Fig. 3.2.9   *Polarimeter setup on TCV. Each of the 5 parallel beams traversing the plasma are sampled by 2 detectors (Schottky barrier diodes) to obtain 10 separate chords.*

A specific polarimetric technique has been chosen, which employs 2 FIR laser cavities operating at 432.5µm and optically pumped by a 120W continuous wave CO_2 laser. The FIR cavities will be detuned in length to obtain a difference frequency of 750kHz. Combining the beams of perpendicular polarisation and passage through a quarter-wave plate results in a beam with a linear polarisation vector rotating at the difference frequency. For measurements across the minor radius of

TCV, this beam will be split into 5 sub-beams, each equipped with two waveguide Schottky diode detectors with a sensitivity of ~400mV/mW. Using this scheme, the Faraday rotation angle will be obtained as a phase shift with respect to a reference signal, making the measurement insensitive to amplitude fluctuations. The lower limit for the measurable rotation angle is estimated to be ~1mrad. In order to optimise the sensitivity of the polarimeter in the parameter range of interest, we have chosen a longer wavelength than for the actual FIR interferometer operating at 214µm. As shown in Fig. 3.2.9, this has led to substantial simplifications in both the mechanical design and signal processing.

Since the purpose of the diagnostic is to measure the current density profiles in plasmas with internal transport barriers, high bootstrap current fraction and reversed magnetic shear profiles, it is important to detect differences in the Faraday rotation between monotonic q profiles, reversed magnetic shear profiles, and current hole plasmas. Figure 3.2.10, shows typical q-profiles and the resulting simulated Faraday rotation angle for plasmas with given total current I_p=80kA, central electron density n_{e0}=1.1x10^{19}m^{-3}, and shape representing the lowest plasma currents and electron densities of interest on TCV. In these low current, low density discharges, the Faraday rotation angle will be small. With a maximum value of 10mrad, the resolution of the system for this discharge will be marginal. Nevertheless, the differences between the two reversed shear q profiles ought to be detectable. The slope of the Faraday rotation around the plasma axis being proportional to the central current density, the central value of q should be both measurable and distinguishable for the cases shown in the figure.
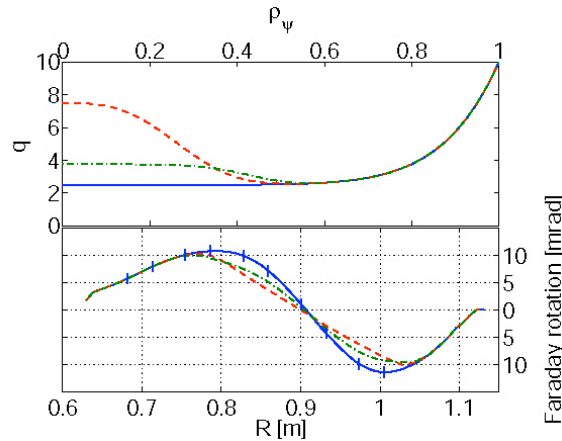
Fig. 3.2.10 *Top: Profiles of the safety factor q for 3 representative cases: monotonic (blue), slightly reversed shear (green), strongly reversed shear (red). Bottom: Simulated measurements of the Faraday rotation angles. The small vertical bars indicate the position of the detectors. The bars heights indicate the expected detection resolution of 1mrad. The main plasma parameters are I_p=80kA, n_{e0}=1.1x10^{19}m^{-3}, elongation=1.4, and triangularity=0.25.*

3.2.7   Tangential X-ray detector array

A tangential X-ray diagnostic has been designed in collaboration with the RRC-Kurchatov Institute (Moscow, Russian Federation). The instrument has been constructed in Moscow and is in the final assembly process. Installation on TCV is planned for the next major machine opening early in 2007. The diagnostic features

six movable, tangentially viewing CdTe detectors providing fast (10µs) and radially localised (2cm) measurements of 2-200keV bremsstrahlung emission in the direction parallel to the magnetic field, from a chosen location in the plasma, using a collimator arrangement. These measurements are expected to provide insight into the physics of magnetic island formation, of runaway electron production and of electron acceleration associated with electron cyclotron current drive.
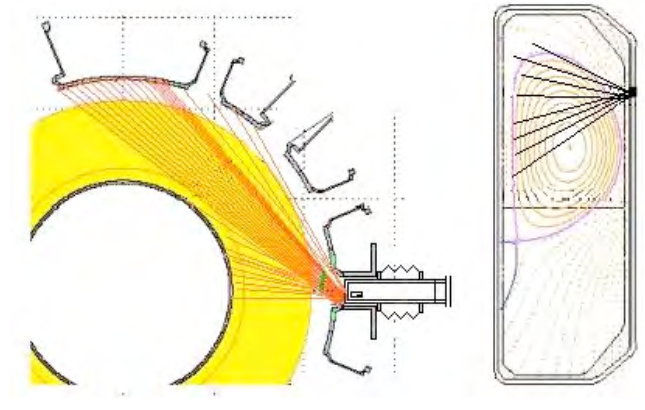
Fig. 3.2.11   *Tangential X-ray diagnostic: toroidal (left) and poloidal (right) projections of the possible lines of sight.*

3.2.8   *Tangential phase contrast imaging*

We are currently designing a diagnostic to investigate core fluctuations in TCV employing a CO_2 laser beam launched through the plasma in a direction approximately tangential to the magnetic field. The transmitted beam is processed through a phase contrast filter and an additional spatial filter to image the density fluctuations with a chosen wave-vector direction onto a detector array. The tangential geometry results in a very fine spatial resolution, of the order of 1% of the minor radius. The accessible wave-number range, from 0.1 to 7cm^{-1}, spans the spectrum of ion- to electron-dominated turbulence (ITG, TEM and ETG modes), opening the possibility of a thorough study of core turbulence in plasmas with very strong electron heating.

The design of the in-vessel components has been completed and the system will be installed on TCV in the first half of 2007.
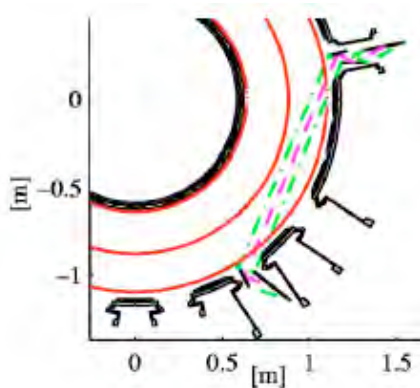
Fig. 3.2.12   *Geometry of the planned tangential phase contrast imaging diagnostic for TCV (top view).*

3.2.9　Microwave reflectometer

A single-frequency, 70GHz homodyne reflectometer was installed on TCV during 2006. The reflectometer is connected to a unused 2nd harmonic steerable ECRH launcher, which can orient the launch wave vector in a wide variety of directions. The reflected wave is collected along the same path as the launched wave and is separated inside the instrument. The diagnostic is undergoing final tests and is expected to become operational in 2006. It will be used for single-point density fluctuation measurements and for plasma flow measurements using the Doppler reflectometry method.

3.2.10　SPRED UV-spectrometer

The SPRED UV spectrometer was mounted on the test bench for the first part of 2006 where the detector electronics was repaired following damage from water exposure. The hollow cathode calibration lamp was used to focus the spectrometer and obtain an updated absolute intensity calibration. Following re-installation on TCV, it was concluded that the micro-channel plate based detector was being influenced by the TCV magnetic field resulting in spectra displacement across the detector surface and an increase in the spectral line width (reduced spectral resolution).

3.2.11　Fast imaging visible camera

A Photron Ultima APS-RX fast framing camera, shown in Fig. 3.2.13 was installed on TCV. This camera is equipped with a 10bit CMSOS monochrome sensor with 17 μm sized pixels featuring extreme light sensitivity (up to 6400 ASA) in the visible range. At the full chip resolution (1024x1024 pixels) the framing rate can be varied in the range 50fps-3kfps for plasma surveying whereas at reduced pixel acquisition (down to 16x128 pixels) the framing rate may be increased up to 250kfps permitting fluctuation and turbulence measurements of visible light emission from the plasma edge. The camera is equipped with 2.6Gbyte of on-board memory which allows the acquisition 4.2s of images at the maximum frame rate.

On TCV, the optical system comprises a fibre bundle and a fish eye lens providing a wide angle view of the plasma along an approximately tangential line of sight. This view was optimised to study filament dynamics during ELMs in H-mode plasmas. The camera control and acquisition systems are fully integrated into the TCV cycle through a client-server technology which is based on the MDS+ package in the frame of a collaboration with the MAST Tokamak. Following a TCV discharge, the data locally stored in the camera are downloaded to a Window XP based computer that also controls the camera. A 50MB/s transfer rate Ethernet link ensures a download time compatible with the repetition rate of TCV discharges. Preliminary operation during H-mode discharge with 15kfps of 482x482 pixels images have shown the presence of filaments during ELMs.
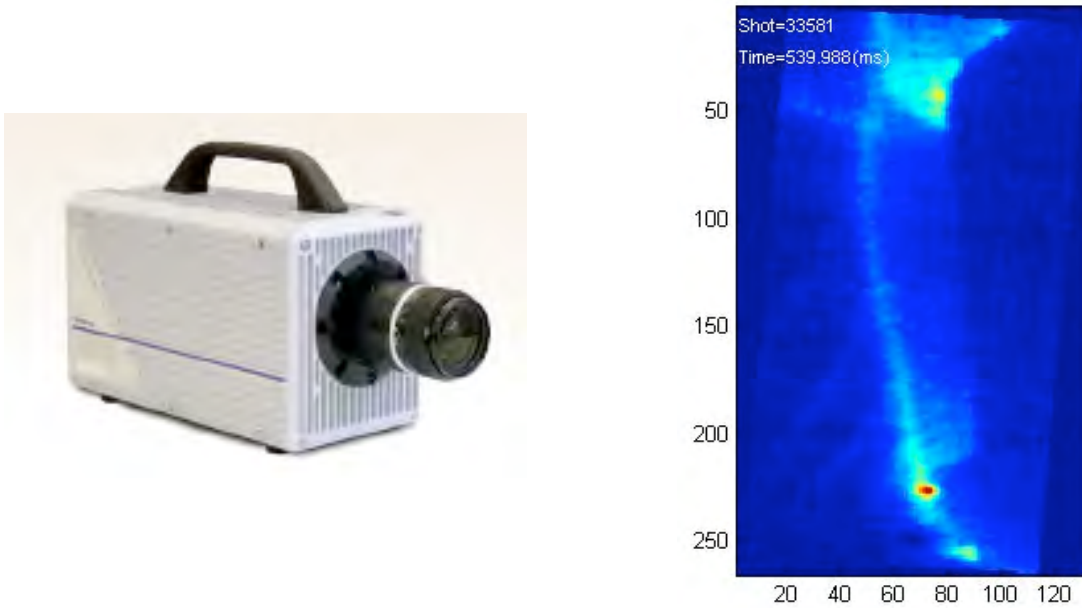
Fig. 3.2.13   *Ultima APS-RX fast framing camera showing poloidal wide angle view on TCV.*

3.2.12   Lower-hybrid parametric instability probe

A Lower-Hybrid Parametric decay Instability probe (LHPI probe) is being designed for operation close to the TCV plasma. It will consist of a magnetic loop-antenna for the detection of lower-hybrid waves (LHW) and a spectrum analyser. This probe is intended to assist in the optimisation of Electron Bernstein Wave Heating (EBWH) using the O-X-B double mode conversion scheme. The measurement of LHW generated by parametric decay around the conversion from X- to Bernstein-mode of EC waves at the upper-hybrid layer will provide an additional monitor of the O-X conversion. The LHPI probe is also of interest for suprathermal ions physics studies.

3.3   Control and acquisition

3.3.1   Plant control and data acquisition

For the period of this report there have been 2200 TCV shots, each generating around 250MB of data, which are compressed and stored on disk.

All the TCV data, acquired and calculated, are kept on-line on hard disks, for immediate access. At the end of the year they occupy 860GB, backed up entirely on another set of hard disks and, separately, on tape.

3.3.2   Plasma control system

The advanced plasma control system, built in collaboration with IST Lisbon (Portugal), is ready and preliminary conformity tests have been carried out during November before delivery to CRPP in December.

3.4   Heating Systems

3.4.1   X2 heating system

In October 2005, 2 gyrotrons which had previously been repaired broke down again and were returned to the factory for repair under warranty. In April 2006 a spare tube was installed, aligned, calibrated and conditioned, and made available for operation on TCV. The repaired tubes were returned from the factory in May. The acceptance tests of both tubes were carried out from mid August to mid October resulting in the removal of the least reliable of the 5 operating tubes on TCV and installation of the two repaired tubes. Both repaired tubes successfully passed the on-site acceptance test and were aligned with respect to their respective transmission lines and launchers. The output powers were calibrated as a function of beam voltage and the calibration data entered into the ECH control system.

The full X2 system (2.7MW in the plasma) was operational at the start of campaigns in October, following the summer shut-down.

A new control system interface allows easier shot preparation for TCV physicists.

3.4.2   X3 heating system

The three X3 gyrotrons have been successfully operated on TCV since 2000. These gyrotrons have been designed to operate in continuous mode and are equipped with a cryogenically cooled sapphire window. This type of window was the state of the art at the time of the gyrotron design (1993) but the operation on TCV has shown that it is actually the weakest element since two window failures occurred during this time. The second one occurred in May 2005, and therefore reduced the X3 ECH injected power to 0.9MW (2 gyrotrons). The first failure (2003) was repaired with a new cryogenically cooled sapphire window.

The present state of the art for a gyrotron of this power level and pulse length includes the implementation of a Chemical Vapor Deposition (CVD) diamond window, which improves its performance with respect to two main aspects:

- With a CVD diamond window the window reliability is significantly improved since the window cooling system is simplified compared to the cryogenically cooled sapphire window (water cooling instead of liquid nitrogen).

- For the cryogenically cooled sapphire window, the maximum RF power achievable with the gyrotron is limited by the window itself due to a thermal runaway instability related to the thermal properties of the cryogenically cooled sapphire. With a CVD diamond window, due to the significantly improved thermal properties, the maximum RF power achievable, with the exact same gyrotron components (apart from the window), can be increased

by approximately 20-30%, therefore possibly increasing the X3 ECH power injected into TCV.

A CVD diamond window with parameters compatible with the gyrotron to be repaired was procured during the R&D phase of this gyrotron by the Forschungszentrum Karlsruhe (FZK) but actually never implemented on a gyrotron. Since FZK is offering the unbrased window for free, the gyrotron repair, including the CVD window, allows to improve its performances at a relatively moderate cost considering the value of the CVD window itself.

The gyrotron is presently being repaired by THALES and will be delivered to CRPP, equipped with a CVD window, by the end of 2006. The guaranteed specifications of the repaired gyrotron in terms of RF power level are the same as the previous version, i.e 500kW at the gyrotron window for a 2s pulse length. Tests of the gyrotron operational capabilities at higher RF power than the guaranteed 500kW will be performed in short pulse at the beginning of 2007. The results of these tests will be the basis for the decision concerning a possible future X3 power upgrade in TCV which is essentially based on the replacement of all the cryogenically cooled windows with CVD windows.

3.5   Superconductivity

3.5.1   The SULTAN facility

After the maintenance work in October 2005, re-cooling and operation of SULTAN started November 9th 2005 and continued without major interruptions till next yearly maintenance in December 2006. In October, the Service Pack 2 for Windows XP was installed in the SULTAN control system Sattline.

A number of technical failures caused a total of about 10 days of either shut-down or stand-by for the facility:

- Two current dumps were triggered in February by a voltage offset in the quench detection electronic
- In the hot July, several tyristors of the 13kA power supply failed because of high temperature
- On August 2nd, one of the two Hall probes used to sense the sample current failed because of a broken wire in a connector. The failure was not immediately noticed. As a consequence, the tests carried out between August 2nd and August 29th recorded a "wrong" current signal, which had to be re-scaled to the correct value in September.
- On October 30th, the electronic unit for the conditioning of the Hall sensors had a major failure and all the active components (amplifiers) had to be replaced

In the scope of the design activity for the superconducting transformer of the Dipole facility, the layout and operation range of the primary winding of the SULTAN transformer was reviewed. It was found that the original design correctly set the operating range at ±200A, but the actual operation was extended up to ±300A. Although the winding actually does not quench at this extended range, the coil is not adequately protected for currents higher than 200A (too high hot spot temperature). The operating range has now been reduced to the original ±200A.

The quench detection of the primary winding of the transformer was also improved by an accurate balance of the voltages of the half windings. The result is a better compensation of the inductive voltages, i.e. an improvement of the maximum allowable ramp rate in the primary winding. Thank to this measure, the cycling rate is expected to improve up to 20%.

An upgrade of the data acquisition system for the sample test has been considered and various options have been inquired. An order for an upgraded system is placed at the end of 2006 and most components are delivered.

3.5.2   A new 15T solenoid for small size experiments

The existing, 12T test station for strand characterization has been upgraded to 15T. A new solenoid has been ordered at Oxford, with the same free bore (80mm) as the old system to allow the use of all the existing insert cryostats.

The new solenoid and its dewar have been delivered in October 2006. The commissioning was successfully carried out in December 2006. The higher field imposes tighter requirements on screening. A section of the second floor of the SULTAN hall, where the new solenoid will be installed, had to be replaced by a stainless steel plate. The distance from walls also had to be increased.

3.6   ITER 170GHz gyrotron and its test facility

For the electron cyclotron wave system of ITER the European Party plans to deliver 2MW cw 170GHz sources. Compared with the reference design of ITER based on 1MW sources, a higher power source (2MW) allows a lower system cost. During 2006, CRPP members participated regularly in meetings with EFDA and other participating Associations (FZK, Karlsruhe, Germany, CNR, Milano, Italy) as well as the contract follow-up concerning all elements of the project. The test facility at CRPP with all the auxiliaries under CRPP responsability needed for operating the gyrotron underwent testing and are operational. The gyrotron prototype has been delivered in December. However, the experimental campaign will only start in mid-2007 due to the late delivery of the superconducting magnet.

In 2006 EFDA placed two new contracts with CRPP a) for the operation of the ITER gyrotron test facility and b) for the scientific coordination of the experimental program on the prototype tube.

3.6.1   Gyrotron components

The first prototype of the 170GHz/2MW/CW has been delivered in December 2006, after the occurrence of some minor delays during the assembly phase. A picture of the tube before baking is presented here after.

CRPP is the leading Association, responsible for the contract follow-up, as well as the organization of the regular bimonthly progress meetings. and will host the tests of the tube. The target performances of the first prototype are 2MW/1s, although the system, and in particular the cooling, has been designed to be compatible with cw operation.
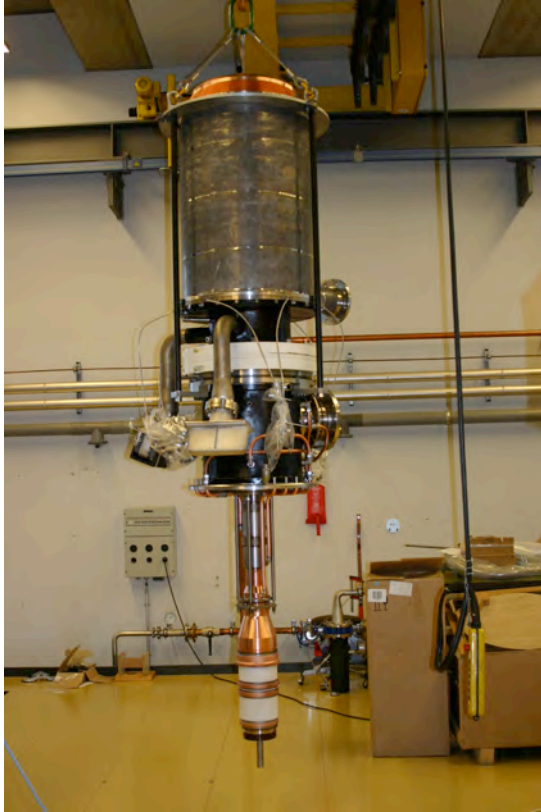
Fig. 3.6.1   *Picture of the 170GHz/2MW first prototype after delivery to CRPP.*

The tests are scheduled to begin early 2007, and will last 9 months. Scientists from FZK, CNR, TED and other Associations are expected to participate in the experiments. After this period, an opening and an inspection of the tube are foreseen to detect any trace of misbehavior. In parallel to a redesign phase which will lead to the production of the second prototype, the first tube will be refurbished and tests continued further. In particular, an updated version of the mode launcher will be tested.

Superconducting 7T magnet

The construction of the 7T magnet is nearly terminated and the assembly of all the subsystem composing the magnet is presently underway. A the level of the test stand, most of the auxiliaries and sub-systems needed to perform the acceptance test are operational. The magnetic field measurement system has been designed within CRPP and is presently in construction with a completion date for mid-January 2007.
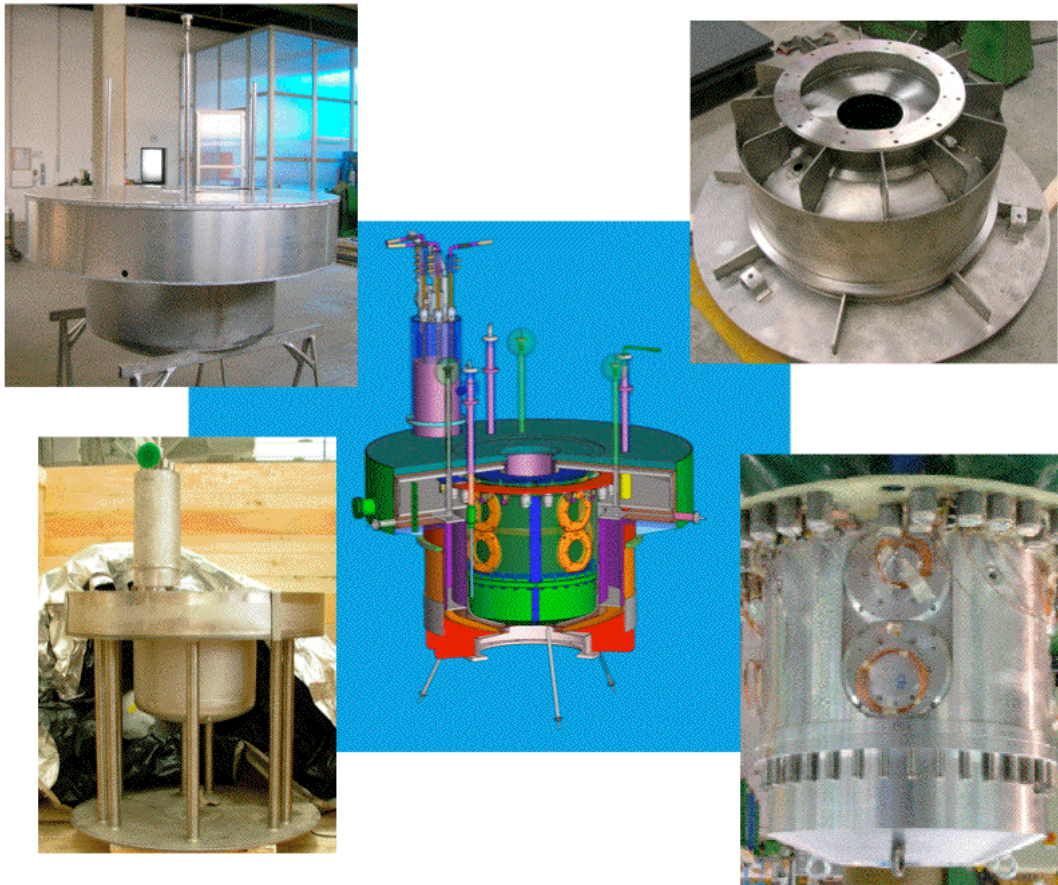
Fig. 3.6.2   *Centre part: 3D view of designed magnet. Four pictures in the corners: different sub-systems which are in the process of being assembled.*

3.6.2   C-GT170 test facility

Power supplies

During 2006 the work on the power supply structure for the gyrotron C-GT170 has continued. Two power supplies, the Main High Voltage Power Supply (MHVPS) and the Body Power Supply (BPS), providing together the beam voltage required for the RF waves generation, have been contracted by the EU Commission to OCEM (I, Bologna) in May 2005. CRPP has followed the contracts through several progress meetings at OCEM premises, where both the technical choices and the interface of these supplies with the Test Facility in preparation at Lausanne have been decided.

The BPS has been manufactured during the first half of 2006. A CRPP representative participated in the factory tests applied to the transformer, which is a particular design made of 50 secondaries. After it has been delivered to OCEM premises to be connected and mounted with the other parts of the power supplies, the factory acceptance tests on the complete power supply took place at the end of September. These tests were successful and the BPS was delivered to Lausanne. The installation, the commissioning and the final tests on-site have been passed during the second week of October. Figure 3.6.3 shows a picture of the BPS installed in the HV room located in the CRPP buildings.

Fig. 3.6.3 *BPS equipment installed inside the HV zone in the CRPP buildings. In front, the frame with the 50 power modules grouped in 5 rows and connected to the HV transformer behind.*

The MHVPS contract has been amended in order to include the High-Voltage Solid State Switch (HVSSS) requirements in addition to the ones to be fulfilled per specifications. Thus, the contract has been delayed and the delivery would take place in October 2007. A CRPP representative has followed the contract in collaboration with EFDA. The design is now practically frozen and a draft design report has been provided by OCEM in November 2006.

Since the gyrotron test will start in January 2007, the existing CRPP HV power supply used on the electron cyclotron heating for TCV will be shared with the C-GT170 test facility during the first prototype tests. Due to this new requirement, the existing hardware has been adapted in order to supply the power from the existing installation to the new test facility. The control has also been modified to allow driving the power supplies from the two experiments. This new functionality has been tested and is now ready to start with the test facility operation.

Infrastructure

The work on the infrastructure of the test facility has continued in 2006. Most of the required equipment is installed and tested, only some minor adjustments will be necessary when the gyrotron and its auxiliaries (SCM, collector power supplies, RF load) will be delivered.
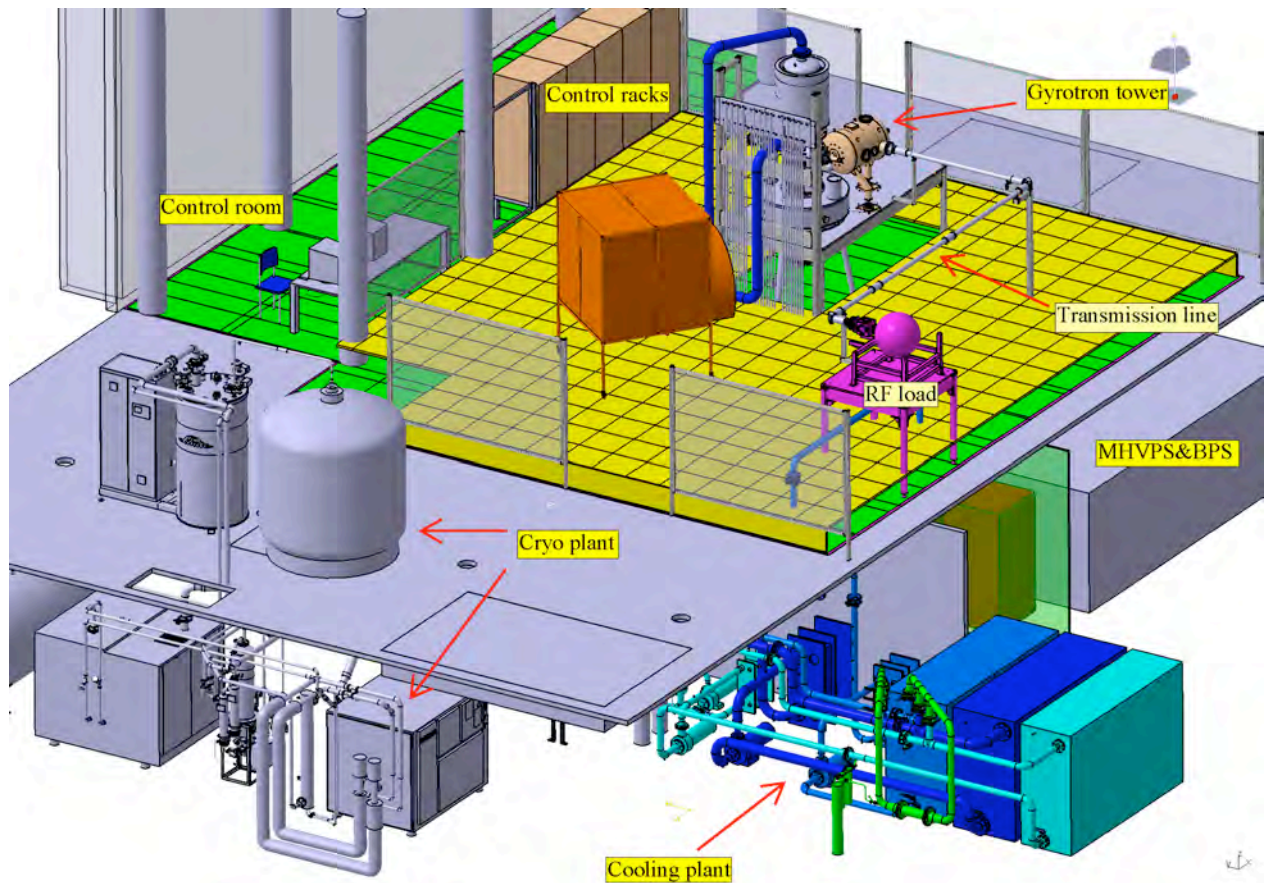
Fig. 3.6.4   *3D view of the infrastructure installed for the gyrotron test facility.*

A complete overview of the infrastructure installed for the test facility is shown in the Fig. 3.6.4. The design of the gyrotron tower has been finalized and the tower infrastructure is mounted. It includes: the table supporting the gyrotron, the tripod required to support the SCM and to ensure a correct alignment, the collector water pipes support and the auxiliary water pipes distribution. Figure 3.6.5 is a picture of the tower. The table is also foreseen to support the RFCU box connected to the gyrotron window. In addition, a table has been mounted, on which the RF load will be installed. This table will be movable and can be placed where required depending on the RF measurements to be performed. The power distribution has been installed for the BPS power supply provided by OCEM and for the thyristors crowbar delivered by JEMA (E). The associated racks receiving the control electronics units have been mounted and cabled. The control hardware made of several units developed by the CRPP electronics group has been installed and tested.

Effort has been placed in the definition of the safety concept, which will be applied to the test facility operation. Four documents have been provided defining:

- The potential dangers which can be encountered in the framework of the test facility
- The construction rules to be followed to ensure a safe operation
- The exploitation rules to be followed during the operation of the test facility
- The operation team required

Fig. 3.6.5   *View of the gyrotron tower.*

Cooling water system

Three separate cooling circuits are actually installed to allow for heat loss removal of the gyrotron collector, of the gyrotron auxiliaries and of the microwave load. These three circuits are designed to dissipate a maximum total power of 5MW in continuous mode. The construction of the circuits was finalized early in 2006. After completion of the leakage tests, the complete piping has been insulated in order to reduce the heat exchange with the air and allow for accurate measurement of the gyrotron losses and efficiency.

Insertion of provisional piping and valves in place of the gyrotron collector, the microwave load and the gyrotron auxiliaries has allowed for commissioning of the complete system with the flows and pressure drops expected. Running tests, summing up to more than 600 hours of operation, have permitted to demonstrate the robustness and availability of the system.

Fig. 3.6.6   *Left: Collector circuit with collector simulation valve and hoses of the auxiliary circuits ready to be connected. Right: Main piping to and from the tanks, disinfection unit.*

The heat dissipated in the water by the pumps has been measured and can be taken into account if required for the calorimetric measurements on the gyrotron. All the measurement transducers are now in operation. The primary circuit, delivered and installed by the EPFL has also be commissioned. The regulation of the primary water flow which controls the secondary circuit temperature has also been commissioned and tested, despite the lack of high heat loads to be evacuated. The gyrotron auxiliaries circuit is the only one which will cool down elements subject to high voltage. Thus, its water has to be deionized (low conductivity) and its bacterial content limited without use of disinfection liquids which may degrade the water conductivity. An ultra-violet light disinfection unit is installed and commissioned for this aim. An oil pump with its oil-water heat exchanger is also installed to provide oil flow and heat removal capacity for the gyrotron oil circuit.

Fig. 3.6.7   *Left: Distribution for the auxiliaries and pumps of the three circuits in the background.*
Right: Oil pump and heat exchanger ready to be connected to the gyrotron oil circuit.

Transmission line

All waveguide components for the transmission line were ordered in 2004 and received in 2005. A few additional waveguide components (additional straight waveguide, CF flange adapters, and coupling units) have been purchased during 2006 from the contract associated with the ITER EC Upper Launcher development. These components will be shared between the CGT170 test facility and the Upper Launcher high power tests. Some components associated with the transmission line support structure have been manufactured during the later half of 2006. The transmission line will be installed only after initial high power gyrotron tests and installation of the calorimetric load in its final position, which should occur near the end of 2007.

Data acquisition and control

Data acquisition modules for the gyrotron test stand were installed and the hardware tested on site in mid 2006. Software development and sequencing scripts for long pulse and short pulse operation have been developed and tested in collaboration with DTACQ Solutions Limited. An MDS plus data tree structure has been constructed and tested and MDS plus will be used throughout the test stand for data storage and access.

Software has been developed to allow continuous transfer of data to the V-SYSTEM hardware control and surveillance system for overview and surveillance purposes and sequencing scripts have been developed that allow mode switching between surveillance, out with gyrotron shots, and data acquisition during gyrotron pulses.

The hardwired state machine has been defined and is under construction at the CRPP. The state machine will be completed during 2007.

Cryogenics

The Helium recovery and liquefaction system for the entire EPFL is operational since the 1st of February 2006. As shown in Fig. 3.6.8, nearly 60'000 liters of liquid helium have been delivered to different laboratories within FSB during the period February-December 2006. It has to be noticed that without this new liquefaction system, during the period October-December 2006 most of the research activities within EPFL requiring liquid helium would have been stopped due to important worldwide difficulties in purchasing liquid helium on the external market. During this period, CRPP staff has operated the system and also designed and constructed the first part of the gas recovery data acquisition system. This acquisition system has been operational since September 2006 and allows data acquisition and remote monitoring of the main high-pressure recovery system installed at CRPP. With the acquisition system it is now possible to determine the global helium recovery efficiency.
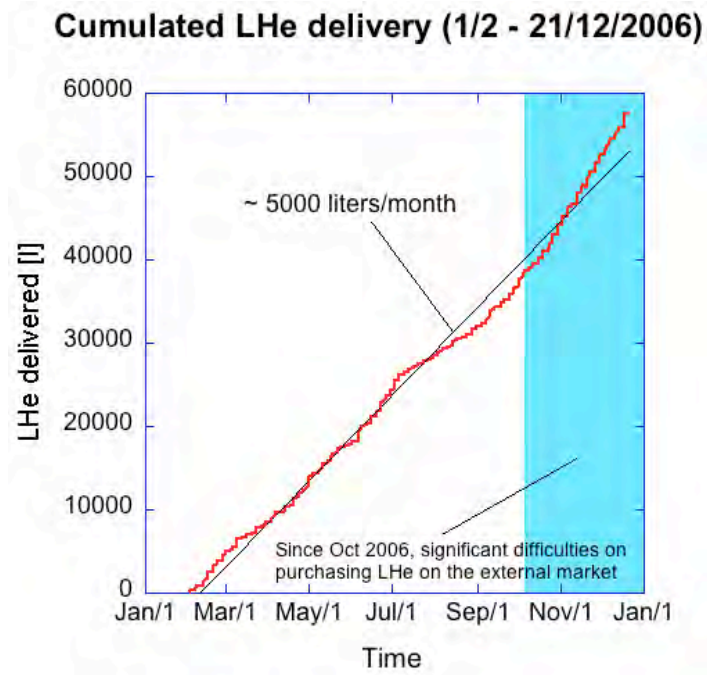
Fig. 3.6.8 *Liquid helium deliveries for the FSB institutes during the period February-December 2006.*

During 2007, the data acquisition and control system for the helium recovery will be completed with two subsystems to be installed in the two recovery systems located in the FSB-PH and FSB-BSP buildings.

4 International and national collaborations

4.1 *Exploitation of the JET facilities*

4.1.1 *Density Profiles in Low Collisionality H-modes in JET and ASDEX Upgrade*

Studies of density peaking in JET H-modes in the previous two years have clearly shown that density peaking cannot be explained by the Ware pinch, nor the particle source, although the latter can be a significant contributor in neutral beam (NB) heated discharges. In 2006 the profile database resulting from this work has been combined with an independently established database on AUG, which has allowed us to reduce correlations between physics parameters, especially correlations between the NB source and collisionality. In order to allow comparisons between the two devices that are not biased by machine dependent differences between diagnostics and analysis procedures, we devised and tested a method allowing interferometer inversions in a consistent way in the two devices.

Results from the combined database, which comprises some 600 samples in H-mode, show that the density peaking factor $n_{e0}/\langle n_e \rangle$ increases to above 1.5 as the effective collisionality drops to values close to those expected for ITER. Fully RF-heated H-modes in JET and AUG show that neutral beam fuelling is not the dominant contributor to density peaking. Multiple regression analyses are performed which show that the most important parameters for peaking are collisionality, the beam source (where applicable) and the Greenwald fraction. An example of a scaling relation (Fig. 4.1.1) without N_{GR} is given as

$$n_{e2}/\langle n_e \rangle = (1.35\pm0.015) - (0.12\pm0.01)\ln\nu_{eff} + (1.17\pm0.01)\Gamma^* - (4.3\pm0.8)\beta$$

Importantly, the increased density peakedness at low collisionality results in an increased peakedness of the pressure profile and of the merit factor $<p^2>/<p>^2$. For fixed average pressure, this merit factor is proportional to the thermonuclear fusion power in the optimum temperature range (7-20keV) for the D-T reaction. Scaling expressions including collisionality predict fairly peaked density profiles for ITER $n_{e0}/\langle n_e \rangle > 1.4$, providing a fusion power increase of near 30% at fixed average pressure. Although clearly anomalous, many observations of density profile behaviour are still challenges for physics based theoretical modelling. These include the apparent lack of correlation of density peaking with magnetic shear in H-mode (albeit observed in L-mode in JET and TCV) and with temperature peaking and the abrupt collisionality dependence of pinches in gyrokinetic models. The relatively broad scatter of the regression fits, which exceeds experimental errors, also suggests the existence of factors influencing density peaking, which have yet to be experimentally identified. [In collaboration with members of the AUG Team, IPP Garching]
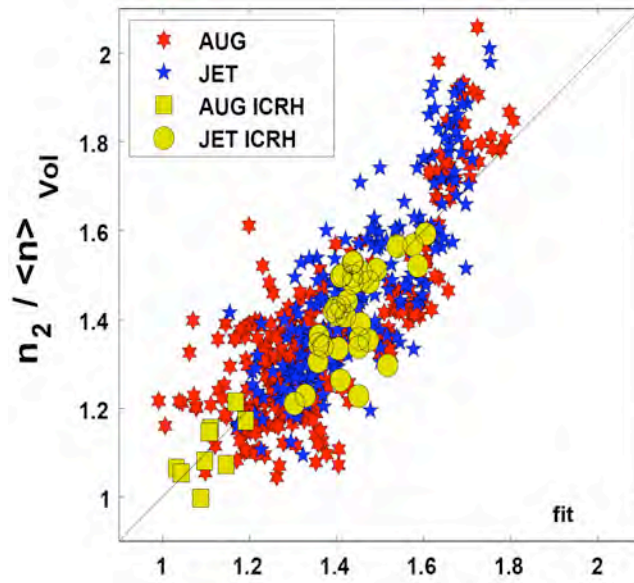
Fig. 4.1.1   *Experimental density peaking versus fit for JET and AUG H-modes.*

4.1.2   Collaboration with the JET-EFDA Task Force E (Exhaust)

Strong support for JET Task Force Exhaust (TF-E) by CRPP has continued, as in previous years, throughout 2006. This has been in the form of Task Force Leadership (TFL) and the provision of infra-red thermography expertise for the analysis of divertor target ELM power loads. The delays to the JET programme have meant that the principal TF-E session in the C17-C19 programme to be coordinated by CRPP will not occur until 2007. Considerable effort has nevertheless been expended in Task Force management and re-planning of the various campaigns following the technical difficulties. In addition, the usual TFL duties have continued unabated with significant effort devoted to organisation and chairing of regular TF meetings and participation in all scientific activities of the Task Force.

4.1.3   CRPP – JET collaboration on Alfvén waves and fast particles studies

The study of Alfvén waves and their interaction with fast particles is an important topic in the JET programme. During 2006, JET has only been partially in operation, with a large fraction of this time devoted to additional shutdown and restart tasks. Our activities have mainly focused on installation and commissioning of the new Alfvén Eigenmodes Diagnostic system (KC1T), designed and built by CRPP, and on the analysis of previous experimental results.

Commissioning of the new AE diagnostic system – KC1T

The previous antenna geometry limited the active AE excitation to low toroidal mode numbers, $n=0 \div 2$, whereas intermediate toroidal mode numbers characterise the most unstable AEs, which are already detected in JET and are similarly predicted for ITER. Hence, a direct excitation and tracking of modes is of clear interest for preparing the next burning plasma experiments. To this end, two antenna

structures optimised for the excitation and detection of AEs with n≈5-15 were designed and built by CRPP.

In 2005, CRPP completed the manufacturing and the testing of the two new AE antenna frames and of the related control and protection electronics, which were delivered to the JET facilities on schedule. However, due to delays in the procurement of the feedthroughs only one antenna frame could be installed during the 2005 shutdown. This was then followed by the installation of the ex-vessel hardware, completed by the end of September 2005. The second antenna frame (and the associated ex-vessel hardware) will be installed during the next shutdown, scheduled for the 2007 spring/summer period.
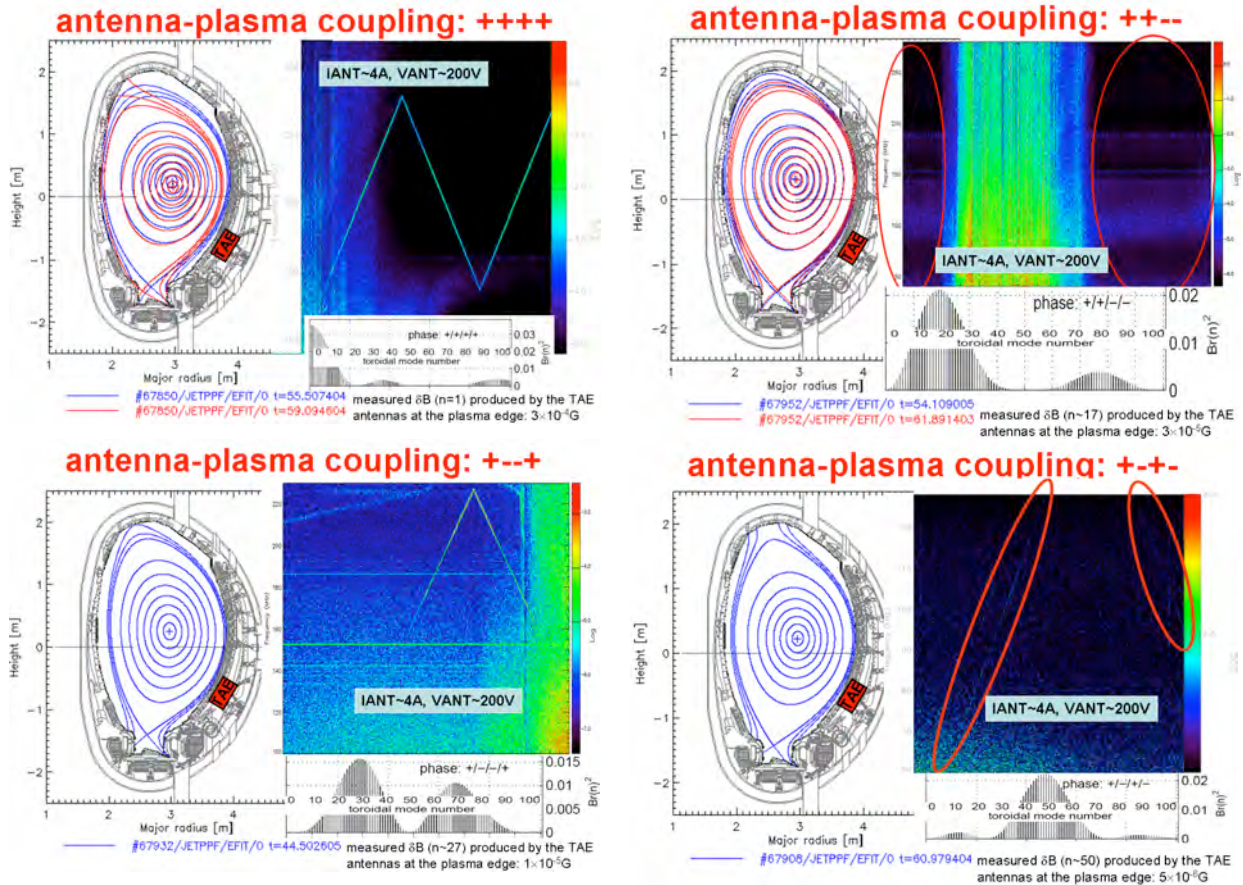
Fig. 4.1.2   *Examples of the excitation spectra obtained in the plasma using different antenna configurations.*

CRPP has also been responsible for the modifications and upgrades to a significant fraction of the ex-vessel hardware: amplifier, isolation and distribution unit, control and protection electronics, and the data acquisition modules. CRPP has also significantly participated in the design, testing and assembly of the new link boxes, connecting the transmission lines to the antenna systems. The installation of ex-vessel hardware and electronic for the octant 8 antennas has been performed mostly by CRPP staff seconded to the JET facilities.

The commissioning of the new KC1T diagnostic system started in November 2005. This work has been slowed down by difficulties in accessing the ex-vessel hardware at JET, and by the multiple interruptions to the JET operation that occurred until August 2006. The technical commissioning of the system, including plasma operation, could only be completed in early October 2006. Figure 4.1.2 shows

various excitation spectra that were obtained in the plasma for different antenna configurations, driving both low-n and high-n modes. First significant scientific results using this new diagnostic system are expected for the next few months.

Regarding data analysis, work has focused on a new approach for the development of disruption protection and avoidance tools and on measurements and simulation of high-energy deuteron tails produced by close collisions (knock-on effect) with He^3 ions accelerated to MeV-energy by Ion Cyclotron Resonance Heating (ICRH).

Furthermore, CRPP also contributed to the analysis of the data obtained with a new fast digitiser system (KC1M), with particular focus on the measurements of the mode amplitude and radial eigenfunction combining external magnetics and internal (core-localised) X-mode reflectometry data.

A new approach to disruption protection and avoidance

Previous disruption predictors were based on neural networks, whereby a large number of input data are collected and processed to derive a suitable alarm signal for a specific type of disruption. In this new approach a minimal subset of input data to drive a neural network is considered: the choice for this reduced subset is given by the identification of the physical mechanisms driving the disruption, which can be extracted from the understanding of the main observable(s) for the event. In particular the density limit and radiative limit disruptions representing about 2/3 of the total number of disruption events during JET operation have been considered. These events are initially caused by an increase in the impurity radiation to a level at which it equals the input power, the difference being the cause for this increase in the radiative power fraction (density rise or impurity accumulation). This causes a contraction of the temperature profile, which produces a strongly destabilizing current gradient inside the q=2 surface, therefore bringing the plasma towards/into an MHD-unstable configuration. At this point a severe disruption with a rapid energy quench can/will occur. Both these events cause a significant increase in the loop voltage V_{LOOP} over a millisecond time scale: hence a sudden increase in the (signed) value of the V_{LOOP} signal is their main observable. Starting from this simple description of the dynamic of such disruptions, this work addresses the problem of recognising in real-time the sequence of these events using the data signals available at JET. The main observable (an increase in the loop voltage V_{LOOP} over a typical millisecond time scale) can readily be associated with an increase in the plasma toroidal resistivity $\eta_{||}$, which can be monitored via the corresponding decrease in the electron plasma temperature T_e and/or an increase in the effective charge Z_{EFF}.

The knowledge about the dynamic of these disruptions has been used to detect their onset by means of two simple algorithms. The first algorithm is based on the assumption of a constant edge current profile during the pre-disruption phase, whereby an increase in the plasma toroidal resistivity $\eta_{||}$ would cause a corresponding increase in the loop voltage. The second algorithm associates the increase in $\eta_{||}$ (hence V_{LOOP}) to a temperature quench at the plasma edge. In both cases the results demonstrate that the model is compatible with the experimental data, and the onset of the disruption could be predicted in real-time with a sufficient warning delay to trigger a disruption avoidance scheme. This leads to a much simpler and more effective neural network predictor for density and radiative limit disruptions, and, as a by-product, also allows us to remove the artificial distinction between density limit and radiative limit events in L-mode and H-mode plasmas.

Table 4.1.1 gives a summary of the main plasma observable for three individual density limit cases in the database that was constructed for this study: the time of disruption, the time when the alarm is triggered using the loop voltage and using the temperature, and the time of the so-called "soft stop" termination of the discharge, which is the current JET protection system based on an implementation of the mode-lock detection algorithm. In all cases the two algorithms trigger the alarm almost at the same time instant, and always at least 50ms in advance with respect to the soft stop time, therefore providing a tool to improve the safety of the machine. In particular, it is worth noticing that in one of these cases the current JET protection system completely failed to produce an alarm.

Pulse Nr.	Disruption Time [s]	V_{LOOP} Alarm [s]	T_{EDGE} Alarm [s]	Soft Stop Time [s]
#58718	67.205	67.090	67.090	*Failed*
#55974	63.075	63.000	63.006	63.079
#59648	63.340	63.280	63.281	63.329

Table 4.1.1   *Comparison between the time of disruption, the alarm time triggered by the loop voltage, the alarm time triggered by the quench in the edge temperature and the so-called "soft stop" time (the alarm provided by the present JET protection system) for three representative cases.*

For the database analysis, the algorithm based on the loop voltage does not trigger the alarm for the non-disruptive pulses and for those pulses that cannot be considered density/radiative limit disruptions. For all the 54 discharges recognised as density/radiative limit disruptions, the V_{LOOP} algorithm always triggers the alarm: in 52 of these cases the algorithm triggers the alarm before the traditional mode lock protection system raises a "soft-stop" termination. It is also important to note that, within these 52 cases, in 20 cases the mode lock protection system has completely failed to detect a forthcoming disruption, therefore the V_{LOOP} algorithm proposed here generally improves the performance of the actual alarm system installed at JET. The V_{LOOP} algorithm triggers the alarm on average 144ms before the disruption, with a 70% probability that the alarm would precede the disruption by [40ms to 240ms]. Such variation in the "alarm time" generated by the V_{LOOP} algorithm can be explained by the large difference in the plasma background parameters for the L-mode and H-mode discharges included in our database. By separating the L-mode from H-mode cases, the 70% confidence level for the alarm time is now reduced [100ms to 240ms] for L-mode discharges and to [40ms to 100ms] for H-mode discharges. The faster dynamical evolution for the H-mode density limit disruptions can be associated with the much larger plasma energy content. It is also important to underline that for all the disruptions correctly detected the alarm time corresponds to a collapse of the edge temperature, as seen on the post-processed pulse data. This also confirms the accuracy of the proposed T_e*Z_{EFF} algorithm. Work is now underway to fully test a real-time implementation of algorithm based on the detection of a temperature quench at the plasma edge.

Measurement and simulation of high-energy deuteron tails produced by close collisions with He^3 ions accelerated to MeV-energy by Ion Cyclotron Resonance Frequency heating.

Collisions between charged particles are usually considered as Coulomb collisions with small fractional energy exchange and small scattering angles. However, high-energy particles can participate in close collisions with a large energy exchange when the minimum distance of approach between particles is such that the strong nuclear force comes into play. Theoretical and experimental studies of this effect

showed that Nuclear Elastic Scattering (NES) of energetic α-particles with thermal ions forms MeV energy range deuterium and tritium tails, which can give a significant contribution to the α-particle signal on a Neutral Particle Analyser (NPA). Experimental data on the NES knock-on deuterium was collected on JET for discharges with ICRF-heating of He_3 minority, where close collisions between fast He_3 ions and thermal deuterons produced a non-thermal deuterium energy tail (the so-called knock-on effect). Interpretation of such experiments and understanding of the underlying processes require accurate modelling of both the He_3 and deuterium populations. The complexity of the problem is determined by the strong anisotropy of ions in velocity and spatial coordinates and the necessity to solve a 3D kinetic problem accounting for the large orbit widths, friction and diffusion in velocity space, pitch angle scattering, neo-classical radial transport and NES.

Figure 4.1.3 shows the calculated and measured He_3 and deuterium Line Integrated Distribution (LID) functions. It is seen how both the He_3 distribution function and the knock-on deuterium tail broadly agree between the NPA data and the calculation. The magnitude of the knock-on effect is somewhat lower than it was observed for α-particles in the JET DTE1 experiment, but it is still very important for the correct interpretation of the NPA data. An agreement between experiment and simulation is seen from the slope of the LID curves, showing the tail temperature of both He_3 and knock-on deuterons.

Phase space regions contributing most to the NPA signal were determined. The analysis of pulses with different ICRH localisation showed the sensitivity of the deuterium distribution function along the NPA chord to the anisotropy in the He_3 distribution function. The importance of the large orbit width effect for the NES perturbed deuterium distribution function was also clearly demonstrated. Due to the magnitude of the charge exchange probability for D and He_3 ions, it can become less complicated to measure deuterium rather than He_3 directly. Taking into account the localisation in phase space of the He_3 distribution, the dominance of local regions in the NPA signal and the known law for the He_3 spread, one can try to solve the inverse problem for obtaining properties of the He_3 distribution using measurements of the NES deuterium.
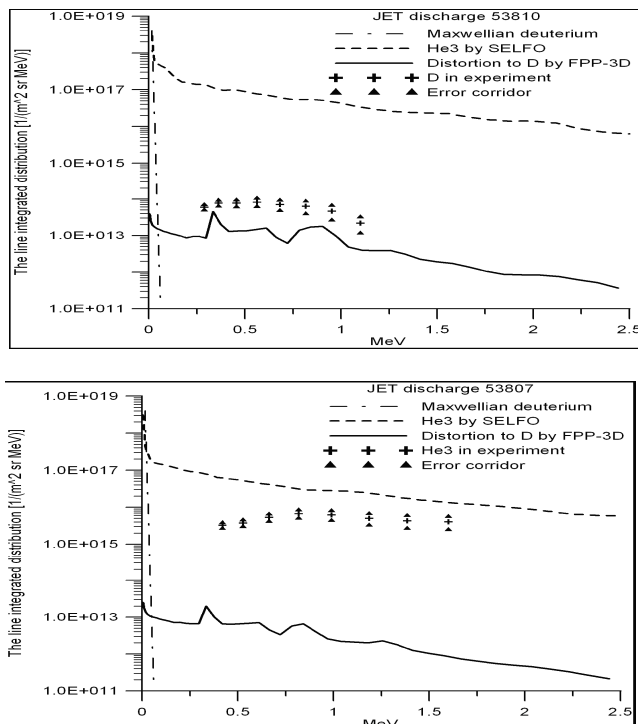
Fig. 4.1.3 *a) D-He$_3$ knock-on effect: comparison between the measured and simulated deuterium and He$_3$ LIDs.*
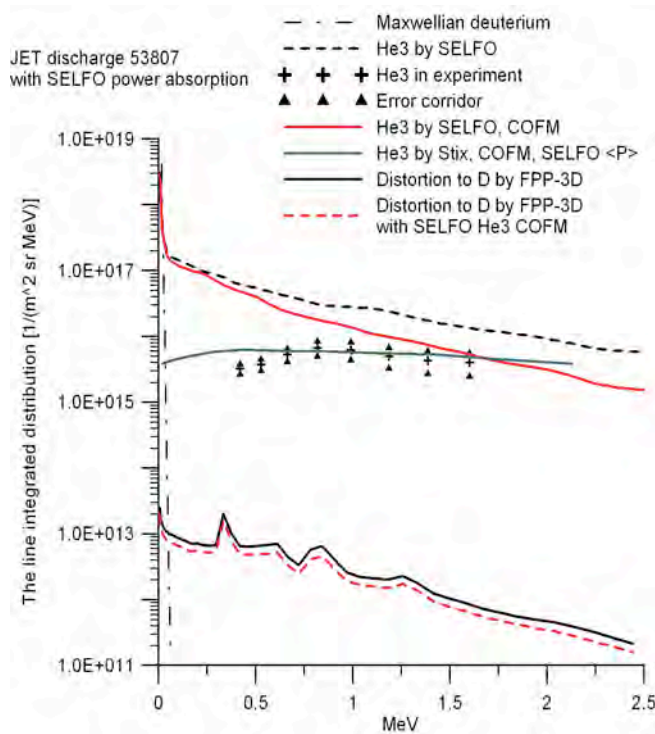
Fig.4.1.3 *b) Comparison of the effect on the simulated LIDs of different models for the ICRF power deposition profile.*

4.2 ITER

4.2.1 ITER Tasks

EFDA/04-1208 Diagnostic Design for ITER: Magnetic Diagnostic (Task Coordination and Design Analysis)

The ITER magnetic diagnostic system provides the main electromagnetic parameters of the plasma, the position or vertical speed of the plasma centroid, the shape of the plasma boundary, supplemented by some internal parameters and the amplitude and mode number of MHD fluctuations. It is therefore of primary importance for machine performance, experimental analysis, control and safety.

As ITER host, the EU will supply the magnetic diagnostic for ITER; CRPP has bid for the leadership for this procurement package. During this year, CRPP participated in the EFDA contracts 04-1208 and 05-1345, designing sensor types that are currently underdeveloped, developing models for electromagnetic effects and vacuum vessel movement, defining methodologies for performance analysis, refining the work plan for full implementation, assessing the existing documentation and supporting the ITER International Team in writing the procurement package. In addition, the CRPP is responsible for co-ordinating the activities within the participating EU Fusion Associations, namely ENEA-RFX (Italy), CEA (France) and CIEMAT (Spain).

Divertor equilibrium coils

To avoid spurious effects in the measurements related to temperature gradients in the magnetic sensor volume, for example radiation induced thermoelectric

sensitivity, the temperature must be kept constant in the sensor within 10°C. The divertor is one of the components being exposed to the highest heat loads in a fusion reactor, and that also applies to the components mounted in the divertor. An assessment of the present design for the magnetic sensors in the divertor and thermal simulations showed that this requirement cannot be reached with a passively cooled sensor. A design for actively cooled sensors was proposed and fluid dynamics computations based on finite element method were used to quantify the temperature distribution in this new design (Fig. 4.2.1). The conclusion is that the temperature variation can be brought down to 4°C.
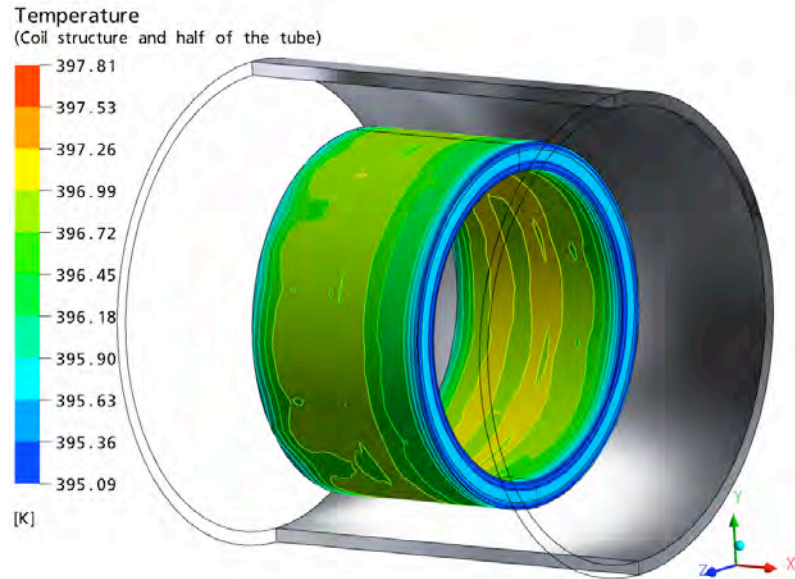
Fig. 4.2.1   *Temperature distribution in ¼ of the actively cooled coil (°K) using a shear stress turbulence transport model.*

MHD noise on the vertical observer

The magnetic field oscillation associated to MHD instabilities such as ELMs, sawteeth and modes on rational surfaces can propagate in the observer for the vertical position of the plasma since this observer is based on the measurement of the magnetic field. This effect must be reduced to improve vertical stability and power consumption for the stabilising coils. A study of the magnetic field structure produced by these instabilities can be combined with a judicious combination of individual magnetic measurements in order to cancel the effect of MHD while keeping an adequate position observer (Fig. 4.2.2). This method was applied to TCV plasmas and showed that it should be sufficient for safely controlling the vertical position in ITER.
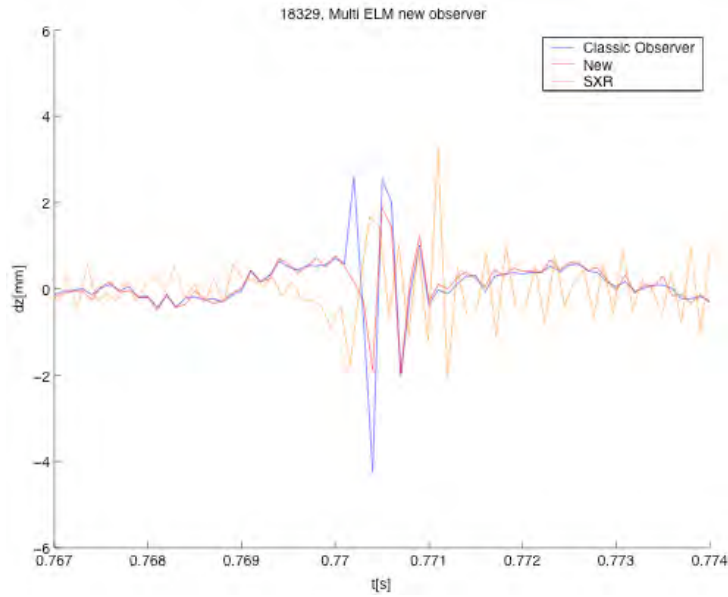
Fig. 4.2.2   *Vertical position excursion during an ELM obtained from the classic observer, the new ELM resilient observer and the soft X-ray tomography.*

Specifications for the electromagnetic modelling of the vacuum vessel

During a recent review of the design and implementation of the magnetic diagnostic systems in ITER, procedures to assess either the sensor characteristics or the measurement performances of the system were established. It clearly appeared that several of these procedures rely on the availability of an adequate modelling of the electro-magnetic properties of the vacuum vessel and any mechanical elements made of conducting, ferro-magnetic or dielectric material. The first steps in the development of such a model are to identify the specific needs for its application to the assessment of the magnetic diagnostic performances, to define the scope of the modelling and then to draw out the detailed specifications for its implementation. Then follows a survey of available software and the functionalities in view of a reduced scale preliminary tests of the modelling schemes.

High frequency probe and MHD saddle loop performance analysis

The main goal for the high frequency probes and the MHD saddle loops is to detect MHD instabilities in the plasma and to identify their spatial structure. Two aspects are considered: first the optimisation of the probe positions to reach the measurement requirements in terms of mode number identification, then the calibration of the system to guarantee an adequate calibration of the transfer function of the probes and the transmission lines.

Performance analysis of the equilibrium reconstruction

The equilibrium reconstruction method is used to derive in particular the outer plasma shape. It combines many magnetic measurements. High performance of the device relies on the quality of this analysis, in particular concerning the distance between the plasma and the first wall components. The equilibrium reconstruction capability of the ITER magnetic diagnostic is assessed using an equilibrium code and studying the propagation of realistic measurement errors or failure of certain

sensor subsets. The ultimate goal is to derive sensor performance specifications that can guarantee to meet the ITER measurement requirements.

4.2.2 International Tokamak Physics Activities (ITPA)

The participation of CRPP in the ITPA activities involves several contributions, like in the field of MHD and fast particles, in conjunction with the recent installation on JET of a high-n Alfvén Wave antenna and the related Alfvén Eigenmode measurements. Empirical scaling laws of spontaneous plasma rotation and momentum transport have been obtained, i.e in absence of momentum injection. In the area of diagnostics, the progress on the magnetic diagnostics of ITER has been presented, as well as measurements of deposition and erosion rates for different materials. Important results have been obtained in the analysis of density peaking from different machines.

The management of the International H-mode Threshold Power Database is still ensured by a member of the CRPP. ITER H-mode threshold power predictions based on power law scalings only give the required power to access the H-mode. Hysteresis effects were then assumed to access 'good' H-mode such as H-mode with type I ELMs. The analysis of the power required to access such 'good' H-mode regime in the contributing devices has started, in order to determine whether this assumption can be maintained for ITER.

4.2.3 ITER upper port ECH front steering launcher

CRPP is responsible for the mm-wave design of the front steering (FS) ITER ECH launcher for the upper port plug, see Fig. 4.2.3. This work is directed by the EFDA-CSU Garching along with several other associations concentrating on the optical design (CRPP, CNR and IPF), port plug structure (FZK), nuclear aspects (FZK) and physics (IPP, CNR, CRPP).
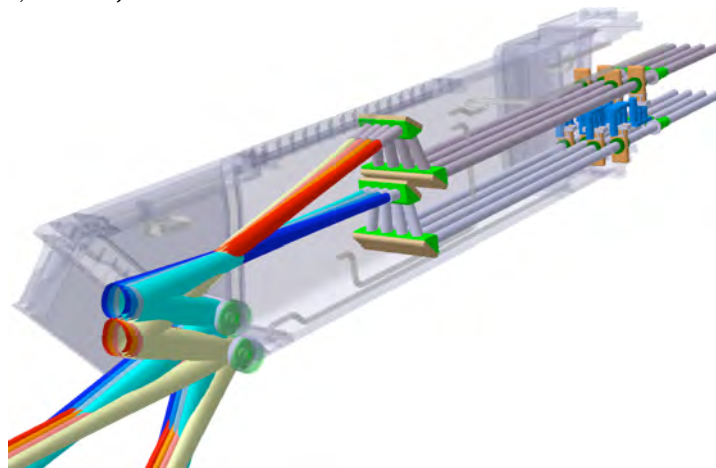
Fig. 4.2.3   *Present design of the FS launcher compatible with injecting eight 2.0MW RF beams.*

CRPP initiated the FS design in 2004 as an alternative to the remote steering (RS) design being investigated by FOM, CNR and IPF. The FS launcher was shown to be more efficient than the RS system for stabilizing NTM (factor of 3.7 averaged over the reference flux surface), which led ITER-IT to change the reference design in

2005 to the FS system. The design activities during the year 2006 has focused on four main areas:

- Resolve remaining critical design issues
- Advance from a conceptual to a detailed design
- Promote modifications to the ITER EC system for improved performance and/or capabilities
- Establish collaboration with other ITER partners working on similar EC sub-systems

Critical Design Issues

Early in 2005, CRPP made a list of the critical design issues that had to be resolved in order to demonstrate the feasibility of a front steering launcher system in the ITER upper port plug. There were 23 issues identified, and solutions to all but one were presented to ITER-IT at the end of 2005 to demonstrate the FS systems reliability. The one open issue was the fatigue on the bellows used in the pneumatic actuator controlling the steering mechanism system. ITER-IT requires that the number of cycles prior to cyclic fatigue are determined using the Expansion Joint Manufacturer's Association (EJMA) codes. These codes evaluated the FS bellows (Nickel) for ~8'000 full cycles based on the 2005 steering mechanism design. CRPP estimated that 21'000 full cycles would be needed for stabilizing the NTMs during the ITER lifetime. ITER-IT provisionally accepted the FS launcher expecting further optimization would increase the longevity of the steering mechanism. CRPP investigated bellows of different materials (Nickel-Cobalt, Inconel 718 and 625), manufacturing processes and shapes along with improvements to the bellows configuration within the steering mechanism. As a result, the number of full cycles has been improved to >35'000 cycles based on the 2005 required steering range of ±7° as shown in Fig. 4.2.4. Note that in parallel an alternative optical design has been proposed that reduces the steering range to ±5.5°, while it increases the deposition range in which the EC beam can be applied in the plasma cross section. Reducing the steering range has increased the longevity to ~200'000 full cycles well beyond the physics requirements. Thus resolving all remaining critical design issues left unresolved during the 2005 design analysis.
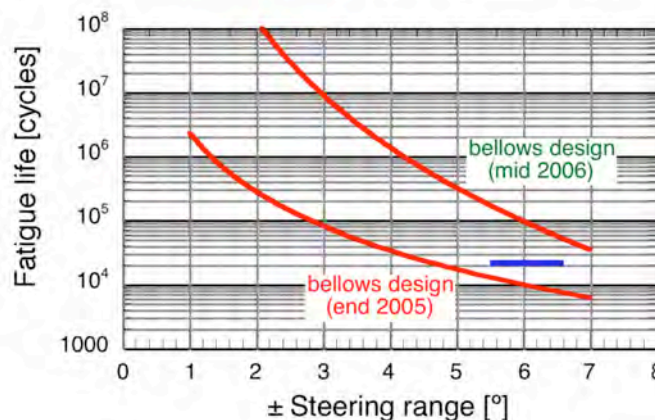
Fig. 4.2.4 *The number of full compression and expansion cycles for the steering mechanism bellows versus steering range based on the EJMA code. The steering mechanism is expected to undergo 21'000 full cycles, which the new bellows design obtains for either the former (2005) or enhanced performance (2006) launcher designs.*

Detailed Design Status

CRPP has been awarded an EFDA contract for the continuation of the FS launcher work that advances the conceptual design of 2005 to a near build-to-print ready design at the end of 2008. Progress has already been made in updating the design of all mm-wave components used in the FS launcher based on the revised optical design of 2006, new design shown in Fig. 4.2.4. In parallel, the design and manufacturing process of the mirrors and some waveguide components are being progressed with the collaboration of Swiss industrial partners. A perfect example is the steering mirror design, which is to be made of a copper reflecting surface and a stainless steel backing. The copper surface minimizes the absorbed RF power and maximizes the thermal conductivity from the surface to the cooling channels, while the higher resistive steel backing minimizes the magnitude of induced currents during vertical disruption events in the plasma. Manufacturing of test assemblies is under progress. It uses Hot Isostatic Pressing to assemble the copper and stainless steel layers. In parallel, CRPP is working with LANOS (Laboratory of Nonlinear Systems) of the EPFL to model the induced currents in the mirror body and optimize the copper and stainless steel quantity to reduce the currents, while maintaining adequate thermal conductivity.

Enhanced performance EC system

A FS system in the upper launcher not only offers a large safety margin for NTM stabilization, but also the possibility to increase the steering range to alleviate the imbalance of physics applications between the EL (Equatorial Launcher) and UL (Upper Launcher). The ITER EC H&CD system (as of 2005) had many shortcomings mainly due to the fact that the EL had to do all physics applications aside from the NTM stabilization. The EL could not adequately provide a narrow deposition profile needed for sawtooth control (in the region of $0.4 \leq \rho_\psi \leq 0.6$). In addition, not all power could be distributed over the region $0.0 \leq \rho_\psi \leq 0.6$. Neither could pure heating and counter current drive useful for controlling the current profile be provided, as illustrated in Fig. 4.2.5 under 'Present EC Capabilities'. A synergestic EC system was proposed by CRPP in collaboration with EFDA-CSU, CNR and IPP, that repartitioned the physics applications based on the functionalities specific to the two launcher designs. The UL is optimized for providing a narrow and peaked current deposition profile off-axis, while the EL was optimized for driving a maximum current with more central deposition. This led to a natural division of the applications with the UL applied to control MHD activity (NTM, FIR, sawteeth, etc.) and the EL to applications requiring centralized deposition of a significant fraction of driven current. Realistic modifications to both launcher designs were proposed that could provide the increased steering range of the UL and relax the steering range of the EL, which could then be modified to provide counter ECCD and pure heating to satisfy all physics requirements for an optimized ITER EC system as illustrated in Fig. 4.2.5 under 'Synergistic EC System'.

These concepts and the related modifications to the UL and EL have been presented to ITER-IT, JAEA (responsible for the EL), the related ITPA groups and the EC international community, with the majority of the concepts well received. As a result of these actions, CRPP also volunteered to revise some of the EC related ITER documents such as the Project Integration Document (PID) and the Design Description Document (DDD). A nearly complete revision of the PID's EC section has been made in collaboration with EFDA-CSU and submitted and accepted by ITER-IT in the Version 3 soon to be released.
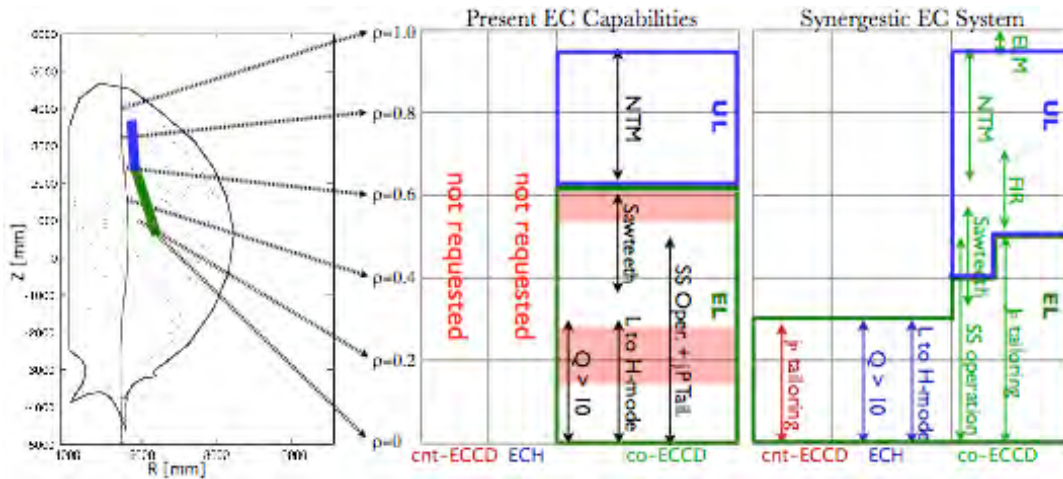
Fig. 4.2.5 *The EC capabilities of the two launcher ITER system based on the present capabilities (center) with the dark bands representing limited performance or access from the EL, and (right) from the synergetic design proposed by the UL design team.*

CRPP in collaboration with FZK and EFDA-CSU also revised roughly half of the EC section of the DDD during the first part of 2006. The revisions made brought the design and technical specifications up to date based on the launcher reference design change and advances in the EC technology and physics since the last upgrade prior to 2002. The revision included modifying other aspects of the overall EC H&CD system reflecting the progress made in all sub systems (gyrotrons, transmission lines, power supplies, equatorial launcher and physics priorities.). The progress is on going, but placed at a lower priority relative to the revision of other more critical documentation such as the PID and the ITER Issue Cards for the ITER design review.

International collaboration

With the change of the UL to a front steering system, ITER-IT encouraged the strengthening of the collaboration between the teams involved with the UL (Europe) and EL (Japanese). CRPP and JAEA had already started informal collaboration prior to 2005. During 2006, this collaboration has advanced to include the synergistic EC system design described above, common component designs and performing high power tests needed for both systems. For example, CRPP initiated the testing of a sample mitre bend test programme with JAEA and GA (US). A sample mitre bend was purchased jointly by CRPP/EFDA and GA (US) and is to be delivered to JAEA for testing in their 170GHz 1MW long pulse test stand at the start of 2007. Two mitre bend mirrors will be tested, one of pure copper and a second of a copper body coated with nickel. The nickel coating will have a similar power deposition to the 2MW in the launcher port plug, and thus simulates the mitre bend used in both the UL and EL when a 2MW beam is applied. The highest power density occurs on the mitre bend and demonstrating its feasibility at an equivalent of 2MW indirectly verifies the other mirrors.

Informal discussion has occurred between CRPP, EFDA, FZK and ITER-US related to the optimization of the EC system. In particular, design modifications to the transmission line and launchers were discussed that improved the performance of the overall EC system without significantly increasing the cost (or more likely offering a cost reduction).

Participation between CRPP and GA in developing an improved RS launcher system that is aimed at a DEMO like machine has advanced. The design was applied to an ITER like remote steering (RS) system and shown to out perform previous RS designs made for the RS launcher. This work has been submitted for publication.

4.2.4 CODAC conceptual design

Under EFDA 5.1b task CRPP-TW5-TPO-CODAC, CRPP seconded a Visiting Researcher to ITER to conduct a revision of the ITER COntrol, Data Access and Communication (CODAC) design. Part of this task was to coordinate voluntary contributions within the fusion community, including an EFDA 5.1a task uniting 6 Associations, but also including contributions from Japan and US. The major challenges in the ITER CODAC were identified and agreed on, and appropriate approaches for meeting these challenges were developed. Where possible, strawman solutions to the CODAC Systems were identified, leading to a conclusion that there are no significant risks associated with any of the novel challenges. The challenge which is the most different from present work in the fusion community is to guarantee an exceptional level of availability during the 25 years of operation.

The critical path is associated with the procurement of plant systems, to define the communications with these systems, and to prescribe the instrumentation and control within them. The standards defining these features are being elaborated.

Concurrently, the CODAC document has been revised, with a new Project Integration Document, a philosophy overview document, and a detailed breakdown of the CODAC Systems.

Certain elements of the CODAC design attracted specific attention, including the user interface to ITER data, data storage, data compression, appropriate middleware solutions for "data plumbing", methods for encapsulating the description of the many ITER Plant Systems, and an approach to the organisation of operation and plasma control. Additional activities included the requirements and design of the main control room and interactions with the licensing procedure.

4.2.5 Superconductivity

The following EFDA tasks have been worked on during this period:

TW5-TMSC-HTSPER. HTS materials for fusion magnets.
TW5-TMSC-HTSMAG. Scoping study of HTS fusion magnets.
TW4-TDS-CLDES. Final design of HTS current leads for ITER.
TW6-TMSC-FSTEST. Participation to conductor tests and evaluation of test results.
TW6-TMSC-ASTSPH. ITER thermosyphon effect and CSMC analysis.
TW6-TMSC-TFPRO. ITER TF prototype conductor sample manufacture.
TW5-TMSC-NEFSS. TF conductor qualification.
TW6-TMSC-SUBSAM. Sub size sample manufacture and testing.
TW5-TPO-ACLOS. ac losses computations for ITER magnets.
TW6-TMSC-SULT. SULTAN operation and testing 2006.
TW5-TMS-EDFAC. European dipole facility.
TW6-TMSC-LTPSAM. Long Twist Pitch Sultan Sample Manufacture and Solder Filling of Joints
TW6-TMSC-PITSAM. Manufacturing of Subsize Cable-in-Conduit Conductors
TW6-TMSP-PFWDES1. Review of PF2-PF5 Winding Design (ITA 11-88).

4.2.6   Materials

See "Task Next Step" in section 2.4.4.

4.3   Collaborations on other tokamak experiments

4.3.1   Intermediate mode number Alfvén Eigenmodes in Alcator C-mod

Collaboration with the Alcator C-Mod group at MIT continues on the topic of the damping rate of intermediate n toroidal mode number Alfvén Eigenmodes.

Such activity constitutes part of a combined experiment in the framework of the International Tokamak Physics Activities, which includes JET and MAST. In 2006 several experiments have been conducted on Alcator C-mod, using the active MHD antenna, driven with oscillating currents in the TAE frequency range up to 25A, and exciting a large toroidal mode number spectrum including intermediate n values (FWHM of the n-spectrum is 16). Several plasma resonances associated with TAEs have been detected, and the dependence of the TAE damping rates on a number of plasma parameters (e.g. shape, collisionality, beta, normalised Larmor radius) has been reconstructed. Although a clear determination and identification of the toroidal mode number was not always possible, these experiments indicate that the damping rate of ITER relevant intermediate mode numbers scales differently from the low mode numbers previously investigated on JET.

4.4   Plasma surface interactions in collaboration with the University of Basel

Mirror samples made from a variety of different materials of interest to ITER (Mo, W, Si...) have been prepared at the University of Basel and installed in pairs on a specially designed manipulator allowing sample insertion in the divertor floor region of the TCV tokamak. Samples are recessed behind the front surface of the divertor tiles to avoid direct plasma ion impact. Sample exposures are integrated across short campaign periods of 2-3 weeks, including regular helium glow discharge conditioning. Under identical exposure conditions the mirror substrate can strongly influence the deposit thickness found on the sample: the carbon layer thickness on a Si sample is found to be five times higher than on a Mo substrate. The reflection coefficients of carbon and deuterium atoms from a Mo substrate are higher than from a Si substrate. In addition, while being reflected from a Mo substrate an incoming particle may re-sputter some already deposited material thus decreasing the deposition rate on a high-Z material. These assertions were confirmed by numerical simulations using the Monte-Carlo code TRIDYN.

In ITER, it is expected that the SOL plasma flow to the divertor may contain a Be fraction in the range 1-10%. Recent results obtained in the PISCES-B linear plasma simulator indicate that the erosion of a graphite target exposed to Be-containing D_2 plasma is suppressed and that the formation of Be-rich layers is observed in line-of-sight locations from the target. Therefore, experiments have been initiated in PISCES-B to evaluate the effect of Be deposition on the surface of metallic mirrors

made from Cu and Mo. First experiments were made in June-July 2006. It has been observed that the deposition of a thin Be layer (about 20 nm thick) onto the mirror surface strongly affects its reflectivity. Moreover for Cu mirrors exposed to 250°C, diffusion of Be into the Cu bulk has been noticed which may complicate the possible mirror cleaning. Analysis of the data obtained during the first experimental campaign is ongoing.

The growing interest about the use of Rh as a material for the first mirrors in ITER and the necessity of using it as a thin film deposited on a polished substrate has raised the necessity of the development of a robust deposition technique for the preparation of high-reflectivity mirrors. Preparation of Rh-coated mirrors by magnetron sputtering has been studied in Basel, and Rh layers with a thickness of 2 microns have been produced so far with a negligible amount of impurities in the layers. Experiments are planned in the TEXTOR tokamak to check the resistance of such mirrors under erosion conditions.

4.5   Socio-Economic Studies

4.5.1   TW5-TRE-FESO/C (Art.5.1a): Fusion and energy scenario options (performed by LASEN/EPFL)

Potential Role of Fusion Power in Long Term Electricity Supply Scenarios Worldwide: Quantitative Assessment with a Least Cost Electricity System Planning Model PLANELEC-PRO

The main task of this research project consisted in the formulation of multi-regional long-term electricity market scenarios for 2100 and an estimation of the global potential for deployment of fusion power plants. Quantitative evaluation of fusion technology was performed using the least cost electricity systems expansion planning model PLANELEC-Pro in terms of potential impact of fusion power on the levelised system electricity cost as well as the total discounted cost and CO_2 emissions of the electricity generation systems in different world regions. Various scenarios were examined, including "reference" (without fusion) and several explorative scenarios presuming different market shares of fusion, nuclear fission and coal with CO_2 capture and sequestration technologies.

It was found that controlled thermonuclear fusion could become an important electricity supply option attaining the maximum share in total regional electricity generation in case of the North American region (22.9%) and providing the maximum contribution to CO_2 emission abatement in case of the Western European region (16.7%). In moderate "Fusion Introduction" scenario (330 GWe of fusion power capacities by 2100 worldwide) the deployment of fusion allows reducing global CO_2 emissions from power generation by ≈ 1.8 % and in more ambitious "Fusion Massive" scenario (950 GWe of Fusion capacities by 2100) the CO_2 emissions reduction is estimated at ≈ 4.3 % compared to the "reference" case. In all world regions the deployment of Fusion power entails a slight increase of the levelised system electricity cost. In general, the higher deployment rates result in greater increment of levelised electricity cost, in the range 0.3-0.4‰€cent/kWh in Western Europe, North America and Pacific OECD regions and not exceeding 0.1€cent/kWh in less developed world regions.

As regards the economic performance of fusion, it was found that in the second half of the century power could become competitive compared to natural gas-fuelled technologies, mainly due to a significant increase of the natural gas price.

Furthermore, during the period 2080 – 2100 it can equalise the production cost of coal-based technologies with carbon capture and sequestration, which will be gradually facing the problem of exhaustion of most affordable sites for geological sequestration. While fusion technology is expected to remain more costly than advanced nuclear fission power plants, its deployment may be favoured by the public distrust in nuclear fission and the risk of proliferation of fissile materials from breeder reactors. Furthermore, the case of Western Europe demonstrates that introduction of a stringent CO_2 tax (€ 50/tCO_2) allows Fusion power to be massively deployed practically without any change of the levelised system electricity cost compared to the "reference" scenario.

4.5.2 TW5-TRE-FESS/C (Art.5.1a): Fusion Economic and Social Studies (performed by CEPE/ETHZ)

Estimating Spillover Benefits and Social Rate of Return of Fusion Research, Development, Demonstration and Deployment Programme

This project is aimed at developing an integrated assessment framework that will allow to evaluate the Fusion research, development, demonstration and deployment (RDDD) programme on the basis of the social rate of return taking into account both internal and external costs and benefits. The main challenge consists of elaboration of a robust methodology for measurement of positive externality effects represented by knowledge, technology, network and market spillovers. These positive externalities represent the side benefits of the RDDD process of any innovative technology, and they usually reveal through publications, patents, technological spin-offs, learning due to industry accession to publicly funded procurement contracts, lowering of the product cost, increased customer satisfaction and other ancillary and macroeconomic benefits. The Fusion RDDD programme may yield substantial amount of spillovers, which will have a positive impact on other energy technologies, related industries and the whole society as well. Accordingly, a proper estimation of spillover benefits within an integrated evaluation framework should allow for optimising public support to current fusion R&D and future demonstration and deployment activities.

The research projects are the following:

- Specification and analysis of spillover effects from basic & applied R&D basing on the examples of high energy physics (CERN), nuclear power development program, space exploration program etc.; definition of specific types of spillovers that can emerge from fusion RDDD program;
- Identification of technology clusters and industrial sectors which can benefit from spillover effects of fusion R&D; estimation of the realised and potential economic benefits due to industry accession to fusion-related procurement contracts;
- Elaboration of the methodology allowing to trace statistical relationship between fusion R&D funding and the produced knowledge stock (publications, patents, trained staff, etc.); estimation of the magnitude and direction of knowledge spillovers;
- Development of an integrated evaluation framework based on energy systems – engineering – economic model allowing to assess the role of different technologies, including fusion, in future energy systems and to optimise the amount of public funding subject to the expected social rate of return of fusion RDDD programmes.

4.5.3   Socio-economic studies

The Centre for Energy Policy and Economics, CEPE, of the ETH Zurich had started a project named "Agenda for Social Science Research Related to Long-term Energy Options (ASRELEO)" in 2005 to, among other goals, give a "new impulse to social studies for fusion: enlargement to and reflection by a wider social science community". In 2006 the organising committee was enlarged to include specialists in political science, sociology (science-technology studies), economy, and research policy (from British Petroleum Ltd.) to provide a fuller range in order to tackle non-technical aspects of long-term energy research. Three dozens of researchers participated in Workshop I in October 2006. Twelve presentations and one dinner talk were given in four sections: key issues, policy and governance, innovations systems, and everyday life issues. An initial inventory of research topics could be established. This is incorporated into an interim report, which will be reviewed in Workshop II in 2007 with a wider audience of researchers, practitioners and research policy officers.

4.6   Collaborations with other EURATOM Associations

J-F. Artaud, V. Basiuk, Association EURATOM-CEA, France, *"Coupling of the DINA-CH and CRONOS codes to simulate the ITER hybrid scenario"*

X. Bonnin, LIMHP, CNRS-UPR 1311, Université Paris, France, *"SOLPS5 (B2.5-Eirene) modelling of parallel scrape-offlayer flows in TCV"*

S. Cirant, F. Gandini, EURATOM-ENEA-CNR Association, Italy, *"Electron transport studies on TCV via shear modulation experiments with ECCD"*

G. Conway, IPP Garching, Germany, *"Planning of a reflectometer diagnostic for TCV"*

A. dellaCorte, Association EURATOM-ENEA, Italy, **D. Ciazynski**, Association EURATOM-CEA, France, *"Participation to conductor test and evaluation of test results"* (TW6-TMSC-FSTEST).

O. E. Garcia, A. Nielsen, Association EURATOM–Risø National Laboratory, Roskilde, Denmark, *"Modelling and simulation of turbulence interchange dynamics in the TCV tokamak scrape-off layer"*

R. Heller, Association EURATOM-FzK, Germany, *"Final design of HTS current leads for ITER"* (TW4-TDS-CLDES, TW5-TMSC-HTSPER, TW5-TMSC-HTSMAG).

J. Horacek, Association EURATOM/IPP.CR, Czech Academy of Sciences, Praha, Czech Republic, *"Electrostatic turbulence measurements in the TCV tokamak scrape-off layer"*

Y. Ilyin and **A. Nijhuis**, University of Twente, The Netherlands, *"Assessment of ac losses results from tests in SULTAN"*

H.P. Laqua, IPP Greifswald, Germany, *"Electron Bernstein Waves on TCV"*

E. Lazzaro, **M. Lontano**, **G. Grosso**, EURATOM-ENEA-CNR Association, Italy, *"Development of a linear plasma device for basic wave-particle interactions studies"*

S. Nowak, EURATOM-ENEA-CNR Association, Italy, *"Modelling of X3 top-launch on TCV with beam-tracing code ECWGB"*

Y. Peysson, J. Decker, Association EURATOM-CEA, France, *"Quasilinear Fokker-Planck simulations and modelling of hard X-ray emission in TCV"*

V. Piffl, IPP Prague, Czech Republic, *"Study the carbon ionisation equilibrium using Charge Exchange Spectroscopy and infer transport coefficients for carbon ions"*

A. Rodrigues, L.A. Pereira, C. Varandas, CFN Lisbon, Portugal, *"Advanced plasma control for TCV"*.
This project consists in upgrading the central analogue controller of the TCV plasma control system with a system based on an array of DSP boards connected together to provide about 32 inputs and 32 outputs.

S. Shibaev, Association UKAEA Fusion, UK, *"Data acquisition for fast framing camera on TORPEX and TCV"*

I. Tigelis, S. Mallios, Association Euratom Hellenic Republic, Greece, *"Modelling of the EM field distribution at 2.45GHz in the empty TORPEX torus"*

I. Tigelis, G. Latsas, Association Euratom Hellenic Republic, Greece, *"Instability calculations in the 170GHz coaxial-cavity-gyrotron beam-duct"*

A.D. Turnbull, General Atomics, San Diego, USA, *"Stability studies of ARIES stellarator configurations"*

G. Veres, S. Kalvin, M. Berta, A. Bencze, Association EURATOM-HAS, KFKI Research Institute for Particle & Nuclear Physics, Budapest, Hungary.
This is a continuous collaboration under an Article 1.1b staff movement agreement (from HAS to CRPP). A number of projects are being pursued: design and fabrication of a fast gas injection valve for disruption mitigation and impurity transport studies, analysis and tomographic inversion of foil bolometer and AXUV fast diode camera arrays, analysis of ELM structure and turbulence using in-vessel, tile embedded Langmuir probes and 1D STRAHL modelling of impurity transport.

M. Windridge, Association UKAEA Fusion, UK, *"Non-linear modelling of MAST"*

M. Wischmeier, *IPP*- Garching, Germany, *"SOLPS5 modelling of the effect of parallel flows on detachment thresholds in TCV"*

4.7   Other international collaborations

J. Egedal, W.Fox, M.Porkolab, PFSC, MIT, USA, *"Investigation of the physics of magnetic reconnection in the collisionless regime in a dedicated laboratory device, the Versatile Toroidal Facility"*

R. Gruber, EPF-Lausanne, Switzerland, **S.P. Hirshman**, ORNL, USA, **K.Y. Watanabe, H. Yamada, S. Okumara, Y. Narushima, S. Sakakibara, C. Suzuki, T. Yamaguchi**, NIFS, Japan, **K. Yamazaki**, Nagoya Univ., Japan, *"3D anistropic pressure equilibrium and fluid magnetohydrodynamic stability"*

R.W. Harvey, A.P. Smirnov, E. Nelson-Melby, CompX, San Diego, CA, USA, *"Development of a fully relativistic ray tracing solver for study of mode conversion and electron Bernstein wave propagation in TCV"*

W. Heidbrink, H. Boehmer, UC Irvine, USA, *"Sources for energetic ions for a simple magnetized torus"*

M.Yu. Isaev, Russian Research Centre Kurchatov Institute, Moscow, Russia *"Development of the VENUS-df Code for Bootstrap Current and Neoclassical Transport in Stellarators"*

M.Yu. Isaev, Kurchatov Inst. Moscow, Russia, **H. Maassberg, C. Beidler, J. Nuehrenberg, M. Schmidt, J. Geiger**, IPP-Greifswald, Germany, **A. Bergmann**, IPP Garching, Germany, *"Montecarlo-delta_f neoclassical transport in 3D systems"*

K. Kim, KBSI, South Korea, **K. Okuno**, JAERI, Japan, **J. Miller**, ORNL, USA, **S. Egorov**, Efremov Inst., Russian Fed., and **P. Weng**, CAS, China, *"Preparation of ITER conductor qualification samples"*

S.Yu. Medvedev, A.A. Martynov, A.A. Ivanov, Yu.Yu. Poshekhonov, Keldysh Institute of Applied Mathematics, Moscow, Russia, **M.Yu. Isaev, V.D. Shafranov, A.A. Subbotin**, RRC Kurchatov Institute, Moscow, Russia, *"Equilibrium and Stability of 2D and 3D plasma configurations"*

M. Mikhailov, A. Subbotin, V.D. Shafranov, M.Yu. Isaev, M. Samitov, Russian Research Centre Kurchatov Institute, Moscow, Russia; J**. Nuehrenberg**, Max Planck Institut fuer Plasma Physik, Greifswald *"Optimisation of Advanced Stellarator Systems"*

G. Moritz, GSI Darmstadt, Germany, and **V. Vysotsky**, All-Russia Scientific Cable R&D Institute, Moscow, Russian Fed., *"INTAS Project"*

V. Naulin, Risoe, Denmark (with S.Mueller), *"Adaptation of the ESEL fluid code for modelling of turbulence in the TORPEX device"*

J. Nührenberg, A. Koenies, V. Kornilov, A. Mishchenko, S. Sorge, IPP Greifswald, Germany, **A. Bottino, A. Peeters**, IPP Garching, Germany, **R. Hatzky**, Rechenzentrum MPG Garching, Germany
"Linear and nonlinear gyrokinetic code developments and simulations"

V. Pantsyrny, ASRIIM, Russian Fed., *"Preparation of ITER conductor qualification samples"* (EFDA Task NEFSS)

L. Rossi, CERN, Switzerland, N4 - CARE *"Coordination of studies and technical R&D for high energy high intensity hadron beams"*

P. Savrukhin, A. Sushkov, RRC Kurchatov Institute, Moscow, Russian Federation, *"Planning of tangential X-ray measurements in TCV"*

F. Skiff, Univ. of Iowa, USA, *"Basic wave-particle interactions and turbulence studies in TORPEX"*

P. Smeibidl, HMI, Berlin, Germany, *"Design of superconductor for 30 T Hybrid Magnet"*

J. Snipes, R. Parker, M. Porkolab, J. Freidberg, J.Sears, PFSC, MIT, USA, *"Fast particle physics, Alfven waves, and active MHD mode excitation on the Alcator C-Mod tokamak plasma"*

A. Sushkov, Nuclear Fusion Institute, Kurchatov, Moscow, Russia, "Electron heat transport at switch-off in sawtooth-less TCV discharges", and *"Development, commissioning and use of DMPX soft X-ray wire chamber towards Te measurements"*

E. Valeo, Princeton University, USA, and **R. Berger**, Lawrence Livermore National Laboratory, USA, *"Development of numerical methods for Vlasov simulations"*

K. Yamazaki, K. Y. Watanabe, S. Okamura, T. Yamaguchi, Y. Narushima, H. Yamada, S. Sakakibara, C. Suzuki, National Institute for Fusion Science, Toki, Japan; S.P. Hirshman, Oak Ridge National Laboratory, USA, *"Model Anisotropic Pressure Equilibria in Stellarators with Tangential Neutral Beam Injection"*

J. Yu, Institute of Plasma Physics, Chinese Academy of Sciences, Hefei, P.R. China, 'Effects of irradiation in SINQ on the Chinese Low Activation Martensitic steel (CLAM)'.

4.8   *Other collaborations within Switzerland*

Besides the activities in the field of plasma wall interaction with the University of Basel, of the socio-economics with the LASE (EPFL) and CEPE (ETHZ), the CRPP also collaborates with the PSI in the field of material under irradiation.

The Industrial Plasma Group has close collaborations with the following Swiss Industries: Charmilles SA, Oerlikon SA (Unaxis), Ruag (before Mecanex), Sulzer Metco and Tetra Pak.

P. Ott, S. Pavon, Laboratoire de Thermique Appliquée et Turbomachines, EPFL, **P. Leyland**, Laboratoire d'Ingénierie Numérique, EPFL, Swiss National Science Foundation Project: *"Influence of a weakly ionised boundary layer on transonic and supersonic air flows"*.

5 The Educational Role of the CRPP

The CRPP plays a role in the education of undergraduate and postgraduate students, particularly in the Faculté des Sciences de Base (FSB) of the EPFL. Advanced education and training in fusion physics and technology and plasma physics topics is carried out as part of the research activities of the Association. Section 5.1 presents the 6 courses given to physics undergraduates and to engineering undergraduates. In their fourth and final year, physics undergraduates spend time with a research group at the EPFL, typically 12 hours per week for the whole year. During this period, they perform experimental or theoretical studies alongside research staff, discovering the differences between formal laboratory experiments and the "real" world of research. After successful completion of the first year of the Master Programme (4th year of studies), physics students are required to complete a "master project" with a research group, lasting a full semester. This master project is written up and defended in front of external experts. The CRPP plays a role in all of these phases of an undergraduate's education, detailed in Sections 5.2 and 5.3.

As an academic institution, the CRPP supervises many Ph.D. theses, also in the frame of the Physics Section of the EPFL. 7 PhDs were awarded in 2006. At the end of 2006 we had 35 PhD students supervised by CRPP members of staff, mostly in Lausanne but also at the PSI site in Villigen. Their work is summarised in Section 5.4.

5.1 Undergraduate courses given by CRPP staff

S. Alberti, *Chargé de cours – "Plasma Physics I"*
This course is an introduction to plasma physics aimed at giving an overall view of the essential properties of a plasma and at presenting the approaches commonly used to describe its behaviour. We study single particle motion, the fluid description and the kinetic model. The relation between plasma physics and developing a thermonuclear reactor is presented and illustrated with examples.

N. Baluc, *Chargée de cours – "Materials Physics"*
Basic course on materials physics, presented as an option to 3rd year Physics students. The course covers the theory of diffusion, dislocations and plasticity as well as the characterization of materials. Ways of production, structures, microstructures, physical and mechanical properties are presented for pure metals, intermetallic alloys, superalloys, shape memory alloys, steels, quasicrystals, glasses, gels, liquid crystals, aggregates, ceramics, composites, polymers, and nuclear materials for fission and fusion reactors.

A. Fasoli, Associate Professor – *"Plasma physics II"*
One semester option course presented to 4th year Physics students, introducing the theory of hot plasmas via the foundations of kinetic and magnetohydrodynamic theories and using them to describe simple collective phenomena. Coulomb collisions and elementary transport theory are also treated. The students also learn to use various theoretical techniques like perturbation theory, complex analysis, integral transforms and solutions of differential equations.

A. Fasoli, Associate Professor – *"General Physics II"*
This course completes the introduction to mechanics provided in the first semester with the basic concepts of statics, oscillations and special relativity. It also covers the whole of thermodynamics, from the introduction to heat, temperature and kinetic theory to the first and second principles, including entropy and thermal engines, ending with a treatment of transport and non-equilibrium phenomena in open systems.

J.B. Lister, *Maître d'Enseignement et Recherche (MER)* – *"Plasma Physics III"*
An introduction to controlled fusion, presented as a one semester option to 4th year Physics students. The course covers the basics of controlled fusion energy research. Inertial confinement is summarily treated and the course concentrates on magnetic confinement from the earliest linear experiments through to tokamaks and stellarators, leading to the open questions related to future large scale fusion experiments.

M.Q. Tran, *Professor - "General Physics III"*
This course, given to the Mathematics Section, covers hydrostatic, hydrodynamics waves and electromagnetism.

L. Villard, *Professeur Titulaire* – *"Numerical Physics I-II"*
Full year course given to students in their 2nd year in Physics. The course covers various time and space integration techniques for ordinary and partial differential equations, and is applied to various physics problems ranging from particle dynamics, hydrodynamical equilibrium, electromagnetism and waves. It includes a strong practical work aspect.

5.2   Undergraduate work performed at the CRPP

EPFL 4th year students

Pierre-Henri Chevalley, *"Characterisation of a Vacuum Photodiode (VDP) for X-ray detection"*. As a result of an EFDA contract for monitoring the development of VDP's by the Kurchatov Institute in view of a potential application for X-ray tomography on ITER, CRPP obtained an early model made from Beryllium sheets for testing. The student used a small vacuum chamber for the detector used a biasing circuit to measure the response characteristics on our X-ray test source, obtaining results consistent with those obtained earlier at Kurchatov. The device can also be operated as a gas detector, providing a signal 500 times stronger with air at atmospheric pressure.

Lucia Federspiel, *"Calibration of the pixels of the Photron Fastcam-APX RS camera"*. In this pratical work, the camera pixels have been calibrated using an integrating sphere. The signal intensity on each pixel (1024x1024) has been measured as a function of the light intensity in the integrating sphere, the camera gain and the exposure time. A similar calibration has been performed directly using the plasma light in various experimental conditions on TORPEX.

Pierre Kikudji, *"Disruptions in TCV"*. The lower bound of the current quench time during a disruption is described, from the ITPA group, by a very simple expression including the plasma cross-section area only. In TCV disruptions happened in a wide variety of plasma shapes. The TP work consists in searching for more refined dependencies in our large dataset.

Etienne Küng, *"Design, construction and calibration of a Rogowskii probe for the TORPEX experiment"*. In order to measure over a poloidal cross-section, the induced plasma current during the ohmic operation, two new Rogowskii probes have been designed, constructed, calibrated during this practical work period. They differ by the material used as support (copper and teflon) and by the effective detection area. Both have been successfully tested on plasmas but nevertheless the probe with a teflon core gives a signal ten times larger than the other one and therefore will be used routinely on TORPEX now.

External students

Michael Brunmayr, *"Analysis of plasma fluctuations in TORPEX using non-pertubative optical methods"*. In this experimental diploma work, photons emitted by an Argon plasma, at a particular wavelength ($\lambda = 461nm$) have been counted using a gated photomultiplier as detector. Two methods have been used to estimate the excited ion population in the plasmas which give substantial different results. (ERASMUS student)

Robert Patterson, *"Optical System for Correlation ECE Diagnostic on TCV"*. The task set was to use and improve upon existing horizontal viewing arrangements on the ECE diagnostic installed on the TCV to obtain a very highly spatially resolved measurement of the ECE intensity at two different frequencies, and to use advanced data analysis to probe fluctuations in the electron temperature profile of the plasma. (ERASMUS student)

Julian Piatek, worked on the focussing characteristics of our Ultra-Violet SPRED spectrometer installed on TCV. After repairing a water damaged main board, a Hollow Cathode lamp was used to set the focal depth and the detector slope to maximise the system resolution. Following re-installation on TCV, it was concluded that an increase in the detector's magnetic shielding would be required before the improved resolution could be obtained. A preliminary design of the dimensions of such a system was passed to the drawing office for further design and construction. (ERASMUS student)

Robert Tye, "Improvement of diamagnetic measurement on TCV". Development of a discrete Rogowsky coil to measurement the toroidal field coil current for the compensation of the the diamagnetic loop measurement. Design requirements include adequate sensitivity and bandwidth and a geometrical set-up that makes the measurement insensitive to the current distribution in the bus bars of the toroidal field coils. (ERASMUS student)

5.3   EPFL Master degrees awarded in 2006

Mathieu BERNARD: *"Mesure de la charge effective et de la concentration d'impuretés dans le plasma de TCV"*
The aim of this work is to compare the Z_{eff} measurement calculated with three different methods: the soft X-Ray, the neoclassical conductivity and the charge exchange spectroscopy (CXRS).
The implementation of the absolute calibration of the CXRS and programme for calculation of carbon density and Z_{eff} was performed. The programme for Z_{eff} with conductivity was ameliorated. An automatic FIR correction for the soft X-ray measurement was implemented.

The second part the work is the study of the principal plasma parameters effect on Z_{eff}. The plasma parameters studies are the electronic density and temperature, the toroidal magnetic field, plasma elongation and triangularity, plasma current and ECRH power.

The third part of the work is a study of the carbon density profile. A comparison between the electron density peaking factor and the carbon density peaking factor was done. The effect of ECRH power deposition and EITB was also studied for a small number of shots.

Loïc CURCHOD: *"Electron Bernstein Wave Heating in the TCV Tokamak at EPFL"*
Electron Cyclotron Heating (ECH) with the second harmonic X-mode (X2) is possible for plasmas typically only up to 10% of the Greenwald density limit in TCV. Electron Bernstein Waves (EBW) don't encounter a density limit and EBW Heating (EBWH) through the O-X-B double mode conversion was recently demonstrated in TCV. Further investigations of higher harmonics ECH (X3) and of high power EBW injection and their effects on the plasma are thus important to extend TCV operation to high-density plasma regions. EBW Emission (EBE) studies with a newly commissioned receiving steerable antenna, as well as a loop-antenna being designed to monitor the lower-hybrid waves generated by parametric decay instability at the X-B conversion of injected EC waves, will both help to optimize mode coupling and power absorption of EBWH. A Duplex Multiwire Proportional X-ray detector (DMPX) with high spatial and temporal resolution is used to determine the location of power deposition, with the potential of yielding the electron temperature profile. Simulations with the fully relativistic code GENRAY will support initial EBW Current-Drive (EBCD) experiments. Heating of high-density plasmas opens the possibility of heat transport studies in highly collisional plasmas with $T_e/T_i \sim 1$ and domination of Ion Temperature Gradient modes (ITG).

Martin JUCKER: *"Self-consistent model of magnetic electron drift wave turbulence"*
This work elucidates the creation and stability of large scale magnetic field structures in an unmagnetised inhomogeneous plasma. Non-linear model equations for magnetic electron drift mode turbulence are derived and it is shown that gradients in electron density and temperature serve as energy source for magnetic drift waves, which in their turn generate larger scale structures of higher symmetry. The latter are in their description similar to the large scale flows known in the theory of electrostatic drift wave turbulence, but they show a higher complexity due to a two-field model (temperature and magnetic field) compared to the one-field model (electric potential) in electrostatic drift wave turbulence.

Furthermore, the newly derived self-consistent description is used for an extensive stability study of these large scale magnetic structures in interaction with small scale drift turbulence.

Nicolas SAGE: *"Calibration et mesure de cohérence dans l'expérience toroidale de plasma TORPEX"*
In this work, a frequency calibration of the imaging probe HEXTIP was performed, using two complementary methods. Such calibration allows one to reconstruct accurately the spatio-temporal plasma behaviour over the whole device cross-section, and in particular the dynamics of turbulence and related structures, with a good time resolution.

Measurements of cross-correlation and coherence of the fluctuations along the direction of the magnetic field were performed. The electrostatic turbulence in TORPEX appears to be dominated by long parallel wavelength modes. Similarly, the turbulence generated structures are observed to have a filamentary character and to be practically uniform along the magnetic field.

Master studies presently underway (Winter semester 2006)

Karim DAOUK: *"Simulation du transport électronique d'énergie et de particules"*

Michaël CHESEAUX: *"Déposition de silicium microcristallin par plasma dc à haut courant d'arc"*

5.4   *Postgraduate studies*

Postgraduate courses given in 2006

Nadine BALUC, Robin SCHAUBLIN, Philippe SPÄTIG: *"Multiscale Approach of Plastic Deformation of Metals and Alloys"*
This 28-hour course is part of the EPFL Doctoral School in Materials Science and Engineering (PY-16 course). It is aimed at introducing the fundamental phenomena of plastic deformation of metals and alloys, and at providing the necessary background to understand the multi-scale nature of the plastic deformation from the atomistic scale up to the continuum one. The course is divided into eight chapters: 1) elasticity, 2) plasticity, 3) finite element simulations, 4) dislocations, 5) strain hardening model, 6) molecular dynamics simulations, 7) kinetic Monte-Carlo simulations, 8) discrete dislocation dynamics simulations.

Ch. Hollenstein and **A.A.Howling** *"Diagnostic des Plasmas"* (PY-11) Doctoral school EPFL, winter semester 2005-2006

Ch.Hollenstein, Vakuum Kurs of Swiss Vacuum Society 18./19. Mai 2006 at CERN

Ch.Hollenstein, *"Introduction to plasma physics and its application in industry"* Course for the Swiss Vacuum Society 25. and 26. Nov 2005 in LeLocle

Y. Martin, *"Demain, quelles énergies ? - Fusion"*, Course on Plasma Physics given to physics professors at the Yverdon Gymnasium organised by the Commission Romande de Physique.

Doctorate degrees awarded during 2006

Paolo ANGELINO: *"The role of the electric field in simulations of plasma microturbulence"* (EPFL Thesis 3559(06))
The ultimate goal of magnetic confinement fusion research is to develop an electricity producing power plant based on thermonuclear fusion reactions. Among the most promising magnetic confinement devices, as leading concepts for future power plants, are tokamaks. Plasma turbulence typically produces much larger rates of particle and energy diffusion than one would otherwise expect (for example taking into account only collisions between particles), and is a main source of present-day difficulties in achieving controlled fusion. Large scale flows induced by radial electric fields (E×B flows) are known to act as a regulating agent on the plasma turbulence. This thesis focuses on the study of the effects of an E×B flow on

plasma turbulence driven by microinstabilities. These plasma instabilities are characterized by small spatial scales compared to the size of the device. The corresponding plasma turbulence is named microturbulence. The gyrokinetic model has been derived to describe microinstabilities. The gyroaveraged potential allows for a dimensional reduction of the problem. A numerical computation of the solution of the full nonlinear electromagnetic gyrokinetic equations is still behind the computational capabilities of modern supercomputers. Further approximations have to be introduced. In this thesis two schemes are presented which include the effects of E×B flows into two different global gyrokinetic codes. The first is a linear electromagnetic code which solves the gyrokinetic equation with a spectral approach. The linear approximation excludes the self-generation of electric fields which have then to be imposed as external equilibrium fields. The second is a nonlinear electrostatic code which solves the gyrokinetic equations with a Particle in Cell scheme. The nonlinear model allows us to study the self-generated radial electric field and the corresponding axisymmetric flows, also known as zonal flows. In this thesis, a formulation of the gyrokinetic equations is derived which includes E×B terms in a form suited for numerical implementation in both the linear and nonlinear schemes. The code implementations are described together with several numerical optimizations, in particular devoted to the execution of the two codes on parallel machines. Simulations have been run on electrostatic and electromagnetic microinstabilities driven by temperature gradients (ITG, Ion Temperature Gradient, and AITG, Alfvén Ion Temperature Gradient modes). The main results include a linear stability analysis of the effects of an equilibrium E×B flow on AITG and ITG modes and a study of the nonlinear interactions of ITG turbulence, zonal flows and poloidally asymmetric zonal flow oscillations, known as GAMs. As a consequence of these linear and nonlinear effects, the radial ion heat flux is found to scale linearly with the total plasma current. Besides these main results, the implemented models allow for other interesting analyses of the microinstabilities which are also presented in this thesis.

Antoine DESCOEUDRES: *"Characterisation of electrical discharge machining plasmas"* (EPFL Thesis 3542(06))
Electrical Discharge Machining (EDM) is a well-known machining technique for more than fifty years. Its principle is to use the eroding effect on the electrodes of successive electric spark discharges created in a dielectric liquid. The different phases of the EDM process and the properties of the EDM plasma have been systematically investigated with electrical measurements, with imaging and with time- and spatially-resolved optical emission spectroscopy.
Analysis of the pre-breakdown duration shows that the breakdown is of stochastic nature. Due to presence of gas bubbles created by electrolysis, the breakdown mechanism in water could be different from the one in oil. After the breakdown, the plasma develops very fast (<50ns) and then remains stable. While the gap distance is estimated around 10-100µm, the plasma excites a broad volume around the electrode gap, between 50 and 400µm in diameter depending on the discharge current. After the discharge, light is still emitted by incandescent metallic particles coming from erosion of the workpiece. Their temperature is measured around 2200K, demonstrating that they are still in a liquid state in the beginning of the post-discharge.
Typical spectra show a strong H_α and continuum radiation, with many lines emitted by impurities coming from electrode and workpiece materials. Hydrogen atoms come from the cracking of the dielectric molecules. The plasma contamination from the electrodes, measured with spatially-resolved spectroscopy, is found to be mostly concentrated in their vicinity. The contamination from the workpiece increases during the discharge probably due to vaporization. Time-resolved spectroscopy shows that the plasma density reaches $2 \cdot 10^{18} cm^{-3}$ at the beginning of the discharge. This extreme density causes merging of lines, strong Stark broadening and shift of

the H$_\alpha$ line. The density decreases afterwards rapidly with time, remaining nevertheless above 10^{16}cm^{-3} after 50µs. During the whole discharge, the density is slightly higher in the plasma centre. The EDM plasma has such a high density because it is formed from a liquid, and because it is constantly submitted to the pressure imposed by the surrounding liquid. The electron temperature remains roughly constant around 0.7eV (8100K).

The low temperature and the high density measured prove that the EDM plasma is weakly non-ideal (Γ≈0.45). In this plasma, the Coulomb interactions between the charged particles are thus of the same order as the mean thermal energy of the particles, which produces coupling phenomena. The EDM plasma has thus extreme physical properties, and the physics involved is astonishingly complex.

Yann CAMENEN: *"Etude du transport d'énergie thermique dans les plasmas du Tokamak à Configuration Variable au moyen de chauffage électronique cyclotronique"* (EPFL Thesis 3618(06))

This thesis work, performed on TCV, covers the implementation and exploitation of a multi-channel soft X-ray detector, the optimisation of a current profile broadening method based on temperature profile modification and a detailed study of radial electron heat transport in L-mode plasmas.

The soft X-ray detector, comprised of two superposed wire chambers, has been tested and calibrated using an X-ray source and then installed onto the tokamak. Tomographic inversion routines have been developped for data analysis. The position of the detector was chosen such as to observe the whole plasma cross-section with maximum spatial resolution leading to high quality tomographic inversions. A mobile absorber holder was installed between the plasma and the wire chambers. The energy range of the soft X-ray emission observed by the detector was thus chosen by selecting the appropriate absorber. These various features have made possible the use of the detector for numerous studies and in particular for the spatial and temporal characterisation of the plasma internal transport barrier formation.

Plasma shaping abilities covering a wide range of plasma elongations and triangularities, including negative values, are one of the strengths of the TCV tokamak. For instance, plasmas with elongated cross-sections offer higher energy confinement as well as higher plasma current and pressure limits. However, the increase of the plasma vertical instability growth rate with elongation makes the vertical control of elongated plasmas difficult, in particular if the plasma current profile is too peaked. As the current profile is usually peaked for low plasma currents, current profile broadening is required there to achieve high elongation. During this thesis, a current profile broadening method based on temperature profile modification by localised EC heating has been studied in detail. The mechanism of this method has been documented and the optimal conditions for the EC power deposition determined. Using these conditions, the TCV operational space has been extended towards higher elongation at low current by over 25% permitting the exploration of the plasma transport properties in this regime.

The flexibility of the TCV EC heating system has also been used to investigate radial electron heat transport in L-mode plasmas. For the first time, the normalised temperature gradient has been varied by a factor of four and its influence on electron heat transport has been separated from that of the electron temperature. Electron heat transport increases strongly with the normalised temperature gradient, for values between 6 and 10, and then becomes independent of this parameter. In addition, electron heat transport increases with increasing electron temperature, decreasing density and increasing effective charge. The electron heat transport dependence on these three parameters can be cast as a single dependence on the plasma collisionality. TCV shaping abilities have then been used to test the influence of plasma triangularity. The main variations of the level of electron heat transport are described by a decrease of the electron heat diffusivity

towards negative triangularity and high collisionality. At constant collisionality, electron heat transport is two times lower at a negative triangularity of -0.4 than at a positive triangularity of +0.4. Gyro-fluid and gyro-kinetic simulations indicate that trapped electron modes (TEM) and ion temperature gradient modes (ITG) micro-instabilities are at play in these plasmas, the predominant instabilities beeing the TEM. The good qualitative agreement between the observed experimental dependencies and the predictions of simulations suggests strongly that the TEM instabilities are involved in the transport of electron heat. The experimental study provides dependable scaling of the electron heat transport on plasma parameters that can now be used to test the prediction of transport simulations. New elements such as the saturation of electron heat transport at high values of the normalised temperature gradient and the decrease of electron heat transport towards negative triangularities have been demonstrated.

Jan HORACEK: *"Measurement of edge electrostatic turbulence in the TCV tokamak plasma boundary"* (EPFL Thesis 3524(06))
Cross-field particle transport in the tokamak scrape-off layer (SOL) has long been known to be highly anomalous, exceeding classical (diffusive) rates by several orders of magnitude. This thesis aimed to investigate the fundamental nature of this transport using a fast reciprocating Langmuir probe inserted into a wide range of TCV ohmic plasmas (deuterium, helium plasma, L and H-mode, forward and reversed toroidal field, varying density and plasma current), concentrating on providing high quality measurements at high frequency of the density and cross-field particle flux turbulent fluxes and quantifying the turbulence in terms of statistical analysis of the time series. A remarkable degree of similarity across the database has been found, with the significant observation that the probability distribution functions (PDFs) of density fluctuations can be well approximated, across the entire SOL, by known analytic functions (Gamma or Lognormal analytic PDFs). This eliminates (at least for TCV) a whole class of possible origins for the turbulence characterised by extreme value distributions. A consequence of the universality of the observed PDFs in the vicinity of the main chamber plasma-wall interaction region (the wall radius) is that the local turbulent driven particle flux is directly proportional to the local density, itself found to increase with the square of the line averaged plasma density, thus demonstrating that the quadratic dependence of the total radial particle outflux with line averaged density observed on other tokamaks is a direct consequence of the turbulent transport.
Careful comparison of the results from one particular TCV discharge with those of 2D fluid turbulence simulations of the TCV SOL using the two dimensional fluid turbulence code ESEL (developed at Risø, Denmark) has shown a remarkable level of quantitative agreement, providing the first ever agreement between a turbulence simulation and experimental data in the tokamak SOL. Theory agrees with experiment in radial profiles of mean values, fluctuation levels, PDF shapes, timescales and power spectra of both density and of turbulence-driven flux throughout the SOL. This demonstrates quantitatively, for the first time, that convective interchange motions are the driver for the edge density and particle flux fluctuations observed in the tokamak SOL. By operating the probe simultaneously to measure turbulence and as a Mach probe, parallel SOL flows have also been investigated throughout the thesis study, providing the first ever measurements of such flows on TCV and, notably, careful studies of the flow magnitudes and directions with varying density and toroidal field direction. The data show clearly the presence of two main components to the flow in the outboard midplane vicinity: a field direction dependent contribution, with magnitude and direction quantitatively as expected on the basis of neoclassical Pfirsch-Schlüter return parallel flows compensating poloidal electric and diamagnetic drifts and a small, field direction independent, "offset" flow which is shown to be a direct consequence

of over-pressure on SOL flux tubes due the ballooning-like turbulent interchange motions.

Stefan MUELLER: *"Turbulence in Basic Toroidal Plasmas"* (EPFL Thesis 3673(06))
This thesis work contributes to the improvement of the experimental assessment of turbulence in fusion-relevant toroidal plasmas via the construction and dedicated exploitation of the TORPEX basic toroidal plasma experiment. Several contributions to the construction phase of TORPEX between November 2001 and March 2003 are presented, including design studies of the magnetic-field configurations and the concept and realization of the IT system.
For the studies of fluctuations and turbulence, a toroidal magnetic field complemented by a small vertical component is used in rf-driven discharges. An analytical model of the particle confinement mechanism in this topology is developed and experimentally verified. The basic plasma properties are characterized as a function of the available control parameters, namely the toroidal and vertical magnetic field, the injected microwave power, and the neutral gas type and pressure.
The fluctuations and turbulence in TORPEX are investigated via the specifically developed plasma-imaging probe HEXTIP, which employs a hexagonal disposition of 86 Langmuir probes, covering the entire poloidal cross section. Established one- and two-point Fourier-space analysis techniques are generalized to be suitable for such a 2D diagnostic.
A novel real-space analysis method for fluctuating spatiotemporal structures is developed based on a pattern-recognition approach combined with a massive statistical analysis of measurements of many realizations of turbulent structures, permitting to assess the probabilistic properties of the turbulent fluctuations directly with convincing detail and statistical accuracy.
The combined force of the generalized Fourier-space and the probabilistic real-space analysis techniques, applied automatically to a wide variety of discharges, is used to characterize the fluctuations in the TORPEX plasma in detail. Structures are observed to occur mostly on the low-field side, in patterns expected for drift-interchange type instabilities. The magnitude of the fluctuations is generally comparable to the time-average density level and the areas occupied by the structures extend over a significant fraction of the poloidal cross-section.
The development of a 3D fluid simulation code, ESELTPX, is initiated in the framework of this thesis, aiming at performing global nonlinear simulations of TORPEX plasma discharges for detailed experiment-theory comparison. The present state of the project is summarized and future development strategies are outlined.

Andrea SCARABOSIO: *"Stability and toroidal rotation properties of highly shaped plasmas in the TCV tokamak"* (EPFL Thesis 3609(06))
The work in this thesis may be divided into two parts. In the first part, we focus on plasma instabilities appearing in three different TCV scenarios. These instabilities limit the achievable maximum pressure and current density. In the second part of this thesis, we experimentally study the plasma rotation properties and their relation with the plasma parameters and MHD activity.
During the initial plasma current rise, edge MHD instabilities are commonly observed in most tokamaks when the edge safety factor q_a approaches low rational values. These instabilities may lead to plasma disruptions and can effectively limit the edge safety factor to $q_a > 3$, which is above the well-known operational limit $q_a > 2$. We report on a detailed analysis of the MHD modes leading to disruptions and show experimental evidence of the key role of mode coupling in agreement with resistive MHD theory. In this thesis we characterise the effect of the plasma shape on the instability, showing how plasma elongation and triangularity (positive and negative) act as stabilising factors and help in avoiding disruptions. Different stabilising

mechanisms linked with plasma shaping are considered and shown to be important for TCV and, in some cases, to other tokamaks.

Sawteeth, which are central relaxation oscillations common to most tokamak scenarios, also have a significant effect on central plasma parameters. In highly elongated TCV discharges heated with far off-axis ECRH, the sawtooth oscillations are observed to disappear and to be replaced by a continuous MHD mode resonant on the q=1 surface. The combination of a flat current profile and small q=1 radius determines the change in the plasma stability, which we study using ideal and resistive MHD models.

Plasmas with internal transport barriers (ITBs) are routinely produced in TCV using high power ECRH and current drive. A variety of MHD activity is observed during these discharges including classical m/n=3/1 and neoclassical m/n=2/1 tearing modes, and q=2 pseudo-sawteeth central relaxations. Disruptive modes are observed in ITB plasmas with strong reverse magnetic shear. In general, the MHD instabilities limit the maximum achievable plasma pressure. The experimental β–limit in this scenario is observed to depend strongly on the peaking of the electron pressure profile, in agreement with the ideal MHD theory.

The properties of the toroidal carbon impurity rotation in Ohmic limited L-mode plasmas are studied in detail in stationary conditions. We show that the toroidal rotation in TCV is generally directed in the counter-current or electron diamagnetic drift direction. The rotation profile is peaked up to sawtooth inversion radius and flat inside. We find that, in these conditions, the toroidal velocity scales as $v_\varphi[km/s]=-12.5T_i/I_p[eV/kA]$. We also compare the experimental results with the neoclassical prediction for stationary toroidal rotation in absence of external momentum input.

Angular momentum re-acceleration is observed in TCV Ohmic plasmas, following a breaking due to MHD activity. We show that we can reproduce the time evolution of rotation profiles observed in TCV Ohmic plasmas with a phenomenological momentum transport model. We then infer transport coefficients such as the momentum diffusivity, which results to be much larger than neoclassical prediction.

Hannes SCHMIDT: *"Characterization of a high-density large-area VHF plasma source"* (EPFL Thesis 3495(06))

The objective of this thesis was a feasibility study of a novel, large-area capacitively coupled RF plasma reactor for thin film production of amorphous and microcrystalline silicon, based on a shaped electrode technique ("lens") to compensate non-uniformity due to the electromagnetic standing wave effect.

In a first phase a cylindrical reactor was designed and constructed to show the "proof of principle" of the novel electrode design. The cylindrical geometry of the reactor was chosen in order to allow easier comparison with theory and simulations already performed before by the CRPP. The main reactor parameters were an electrode 1m in diameter and an excitation frequency of 67.8MHz. It was demonstrated that a uniform electric field can be obtained, a necessary condition for plasma homogeneity, and subsequently it was shown that the shaped electrode design can compensate the standing wave effect at very high plasma excitation frequencies.

The "proof of principle" for the cylindrically shaped electrode paved the way for the rectangular electrode. A process compatible in-situ optical uniformity measurement system enabled the measurement of the standing wave effect in an industrial rectangular, parallel plate electrode reactor design at typical industrial frequencies (13.56MHz, 27.12MHz, 40.68MHz, 67.8MHz, 100.0MHz). The operation of the reactor at 100.0MHz required the construction of a triple stub tuner, which is an interesting way of impedance matching at VHF for PECVD. In spite of parasitic edge plasmas, the measurements carried out with the rectangular shaped electrode corroborated the conclusions of the cylindrical test reactor experiments.

Ph.D. Theses supervised by CRPP staff at the end of 2006

Mathieu BERNARD: *"Confinement time of impurities and energies in JET plasma"*
The aim of this work is to calculate the confinement time of an injected impurity with laser ablation and to compare this value with the energy confinement time. Two X-Ray diagnostics are used, the Soft X-Ray cameras and the X-Ray Crystal Spectrometer.
The confinement time of impurities is calculated using the exponentially decreasing signal of the X-Ray and the hypothesis of stationary plasma.
The confinement time of the energy is measured with the Principal Magnetic Diagnostics and is compared with the confinement time of the electron's energy.

Alessandro BORTOLON: *"Plasma rotation and momentum transport studies in the TCV Tokamak based on Charge Exchange Spectroscopy measurements"*.
During this year the study of intrinsic toroidal plasma rotation in L-mode confinement regime has been extended from limited to diverted magnetic configurations. In particular, the dependence of stationary rotation profiles on n_e has been investigated using a shot by shot density scan at fixed I_p. In diverted configuration discharges, for central density up to $n_{e0}=6\times10^{19}m^{-3}$, the plasma column rotates in the co-current direction, with central velocities of $\omega_\phi\approx+20krad/s$. The outer CXRS measurements at $\rho=0.85$ indicate that rotation is positive with values of $\omega_\phi=7\text{-}12krad/s$. With increasing density, the whole rotation profile rigidly decreased, with a decrease in the edge rotation not observed in the limited case (12 to 5krad/s, passing from 4 to $8\times10^{19}m^{-3}$ on axis). This suggests that the edge rotation, possibly coupled to parallel flows in the scrape-off layer, may act as a boundary condition for the ω_ϕ profile. Whereas, with a limiter, the plasma wall interaction constrains the edge rotation to values close to zero, in diverted configurations edge rotation is freer to adapt to the plasma processes. Increasing the density further to $n_{e0}=8\times10^{19}m^{-3}$ resulted in an inversion of the rotation profile, which now becomes similar to those measured with a limiter. This observation, repeated in both positive and negative current discharges, is under investigation but does not disagree with observations in the Alcator C-mod tokamak, for similar plasmas.

Loïc CURCHOD: *"Heating of High Density Plasmas in the TCV Tokamak"*
Electron Cyclotron Heating (ECH) with the second harmonic X-mode (X2) is possible for plasmas typically only up to 10% of the Greenwald density limit in TCV. Electron Bernstein Waves (EBW) do not encounter a density limit and EBW heating (EBWH) through the O-X-B double mode conversion was recently demonstrated in TCV. Further investigations of higher harmonics ECH (X3) and of high power EBW injection and their effects on the plasma are thus important to extend TCV operation to the high-density plasmas region. EBW emission (EBE) studies with a newly commissioned receiving steerable antenna, as well as a loop-antenna being designed to monitor the lower-hybrid waves generated by the parametric decay instability at the X-B conversion of injected EC waves, will both help to optimize mode coupling and power absorption of EBWH. Simulations with the fully relativistic code GENRAY supported initial EBW current-drive (EBCD) experiments. Heating of high-density plasmas opens the possibility of heat transport studies in highly collisional plasmas with $T_e/T_i\sim1$ and domination of Ion Temperature Gradient modes (ITG).

Lukas DERENDINGER: *"Design of low-energy plasma sources"*
At the beginning of 2006, the first series of measurements with a multi-Langmuir probe were made. The measured electron saturation current leads to the profile of electron density and therefore the plasma uniformity and stability at the substrate surface. With the multi-Langmuir probe it has also been shown, that the installation of an additional magnetic cusp field can increase the homogeneity of the electron density.

During the first few weeks with the new probe and anode, a relatively strong magnetic confinement (5.4G) gave stable plasmas, whereas a weak or no magnetic confinement led to instable or asymmetric plasmas. This was already observed before with another circular anode. But after several hours of experiments the plasma became even unstable with a maximum B-field.

Because of that a complete noise analysis of the plasma was made by use of several measurement techniques: a photodiode with photomultiplier, several of the multi-Langmuir probes, a current measurement of the total current through a 0.1Ω resistance and a differential probe for the power source output voltage. It was shown that the use of a HP 6469C dc source instead of an ac source for the filament eliminates all 50Hz harmonics in the plasma. And by replacing also the Fronius dc source for the plasma discharge by another HP source (6472C) the plasma became much more stable and nearly noise free.

But a remaining problem is the symmetry of the plasma. Probably due to a surface conditioning of the anode, the dc current tends to pass on a single spot of the anode. To analyse this phenomenon a new measurement tool was developed. It consists mainly of a highly sensitive hall probe which measures the B-field created by the plasma current. First measurements and a simple 2D simulation of the system gave very promising results.

Emiliano FABLE: *"Simulation of plasma transport"*
Electron internal transport barriers in TCV have been analysed from the point of view of particle transport to study the behaviour of the density profile in these advanced scenarios. The main result is that the normalized density gradient scales as 0.5 times the normalized electron temperature gradient, with no evident dependence on the q profile. Therefore a peaked density profile is observed, despite the strong electron heating, contrary to what is normally observed in Ohmic L-mode plasmas with ECH heating.

Transient phenomena in eITB have been analysed and the particle diffusivity has been estimated as 10 times higher than the neoclassical prediction, indicating that anomalous transport is still active, although at lower levels, i.e. 5-10 times smaller than diffusivity in Ohmic L-modes . Modelling with gyrofluid and gyrokinetic codes show that the mechanism that sustain this thermodiffusive particle transport might come from the non-adiabatic passing electron response to parallel electrostatic fluctuations.

Silvano GNESIN: *"Design of a tomographic set of hard X-ray detector arrays for the TCV tokamak"*
The TCV plasma is routinely heated by means of ECRH; moreover ECCD is extensively used to tailor the current profile. During ECRH and ECCD operation a suprathermal electron population is generated in an energy range from a few tens to a few hundred keV, resulting in hard X-ray (HXR) bremsstrahlung emission. The study of suprathermal formation and dynamics is of capital importance for understanding the spatial deposition of ECRH and ECCD, the wave-particle interaction, and the confinement of high-energy electrons. This thesis addresses the development of a new set of hard X-ray cameras in order to investigate suprathermal dynamics in TCV with unprecedented spatial and temporal resolution. A preliminary design for up to nine cameras has been carried out, based

on a novel tungsten collimator design adapted from the Soller collimator concept. The detectors chosen are CdTe semiconductor diodes.

Our aim is to open the possibility of a full 2D reconstruction of the HXR emission in the plasma cross-section. A minimum of 3 HXR cameras are foreseen; the number of cameras may be increased further depending on the available TCV ports and the effective improvements that can be derived from each additional camera.

At present tomographic simulations are in progress in order to optimize the geometry and the number of cameras to be employed.

Alexandr GUDOZHNIK: *"Numerical and experimental validation of sawtooth control using ECCD"*

A numerical code for the determination of the period of sawtooth oscillations using two different methods was developed. Applicability of these two methods to different types of signals (noise, sawtooth form, etc.) was analized in terms of best results.

Measurements of losses in two lines of sight of LFS ECE radiometer were performed.

Several mm-wave components for the ITER ECH launcher low-power test were tested.

Barbora GULEJOVA: *"Exploitation of the new AXUV diagnostic"*

First attempts have been made to model the scrape-off layer (SOL) and pedestal plasma of ohmic Type III ELMing H-mode discharges on TCV using the SOLPS5 coupled fluid-Monte Carlo code package (without drifts) beginning with simulations of the inter-ELM phase constrained by careful upstream Thomson scattering, fast reciprocating probe (RCP) and Langmuir probes profiles. Results of this successful first phase have been presented at the Plasma Surface Interactions conference (PSI 17) in Hefei, China and accepted for publication in the Journal of Nuclear Materials. To account for the very differing transport rates in the edge pedestal and main SOL regions, radial variation of the edge transport coefficients have been introduced in the simulation. Similarly, it has been found that the transport in the main chamber and divertor regions must be separately adjusted to provide an acceptable code-experiment match. The encouraging overall model-experiment agreement for steady state phase provides a good basis for the more complex time dependent modelling of the ELM itself. This is being performed by transiently increasing the SOL transport coefficients for the ELM duration (fixed at $100\mu s$) according to a specified poloidal variation (a facility which has been added to he code during a mobility visit to IPP Garching in late 2005). The inter-ELM solution is used as the starting point for the time dependent ELM simulation. Initial results are providing encouraging agreement with experimental measurements of divertor particle fluxes. During a 4 week visit of SOLPS5 expert X. Bonnin (LIMHP, CNRS) in Nov-Dec of this year, drifts have been introduced into the SOLPS5 TCV inter-ELM simulations.

Careful investigation of the problem of the $140L_\alpha$ filtered AXUV diodes installed on TCV in 2004 has been performed using laboratory tests of cameras removed during the summer shutdown. Scratches on the L_α filter have been identified as the source of light seen on the few working camera lines of sight. The unfortunate conclusion of these tests is that the low peak transmission of the L_α absorption filters (10%) and the strong angular dependence of this emission (only 1% with incidence angle 60°), means that insufficient L_α emission is produced from even the highest density TCV plasmas for the filtered diodes to be useful. Moreover a strong ageing effect (due both to exposure to boronisation and plasma operation) has been observed on the complementary set of 140 unfiltered diodes. Discussions are now underway with regard to replacing the L_α filters with D_α analogs (although plasma D_α emission is considerably lower than L_α, D_α filters have much higher transmission) and possible solutions for the ageing.

Seyed Masood HAFEZ HAGHIGHAT: *"Molecular dynamics modelling of cavity strengthening in irradiated iron"*
One of the most important problems in the field of nuclear industry is the relationship between irradiation-induced damage and the resulting induced mechanical response of the target. Ferritic base steels are being extensively studied since these alloys are considered to be first candidate materials for the blanket and first wall of fusion reactors. Multiscale modelling appears nowadays as a major tool for the description of plasticity of materials. The molecular dynamics is used to simulate the nanoscale interaction between a moving dislocation and a defect, such as a cavity, a void or a He bubble. The stress-strain curves are obtained under imposed strain rate condition using the interatomic potentials based on the Fe-Fe potential of Ackland 1997, Mendelev 2003, and Dudarev-Derlet 2005 for a void and He bubble as a function of He content, temperature and cavity size. It appears that with increasing temperature the release stress and strain decrease. Furthermore it is proved that with increasing He content the cavity can either become softer or stronger as an obstacle. At the highest He content of 5 He atoms per vacancy loop punching occurs, which strongly increases the cavity resistance to the passage of the dislocation. But in general it could be stated that a low content He bubble is a softer defect whereas a high content He bubble is much stronger than an empty cavity.

Davoud IRAJI: *"Turbulence imaging in a toroidal magnetised plasma"*
Calibration of fast camera to take images from plasma. Determination of optical parameters of camera and developing some matlab routines for vigneting and distortion correction of images. Installing the fast camera on TCV using an optical fiber.

Sudheer Kumar JAWLA: *"Phase Retrieval of Gyrotron Microwave Beam from Intensity Measurements"*
An analysis based on the iterative phase reconstruction algorithm was made (on the beam profile of 170GHz gyrotron microwave beam) to resolve the effects of fundamental issues like scan separation, plane dimensions, number of planes used and measurement accuracies, etc. on the reconstructed phase using intensity measurements in different planes. It was found that correct phase evaluation can be obtained by a careful and optimized selection of measurement parameters. The irradiance moment approach was also studied for the phase reconstruction which gives a good estimate of the phase for fundamental gaussian modes but fails in providing the correct phase profile if the beam contains higher order mode contents. Efforts are underway to develop an optical model mainly focussing on the reconstruction of phase from amplitude measurements made at several locations from the gyrotron window, so that the method can be extended to shaping mirrors as phase-correcting surfaces.

Sébastien JOLLIET: *"Non-linear gyrokinetic simulations including kinetic electrons"*
Gyrokinetic theory is a useful tool for studying microinstabilities, such as ITG and TEM modes, which are commonly held responsible for anomalous transport observed in tokamaks. From a numerical point of view, simulating TEM and ITG simultaneously is a difficult task due to disparate spatial and time scales. The aim of this work is the implementation of kinetic electrons in the nonlinear, global PIC code ORB5. The PIC method unavoidably suffers from numerical noise and leads to the loss of energy conservation for long simulations. Therefore several numerical algorithms have been developed and implemented in the code. The perturbed

density is filtered with a field-aligned Fourier filter, which removes the unphysical high $k_{//}$ modes from the simulation. This technique allows us to increase the time step and to reduce the number of markers in the simulation, leading to a speed-up of two orders of magnitude. The ORB5 code has been successfully benchmarked against the CYCLONE test case. Excellent scalability properties have been obtained up to 4096 processors on the BlueGene/L cluster of the EPFL. Kinetic electrons are now implemented in ORB5. First studies will determine the influence of the mass ratio and the time step on the linear growth rates.

Martin JUCKER: *"Extension of the VENUS code to include anisotropic effects"*
The VENUS code is originally a numerical drift orbit code using a Hamiltonian description for an isotropic plasma, using the 3D magnetic field and pressure distribution given from VMEC/TERPSICHORE. A first goal is to implement new Hamiltonian equations of motion that include pressure anisotropy self-consistently for the investigation of energetic particle effects in magnetically confined plasmas. Then, as a first application, the code is used to confirm analytical results for the toroidal drift frequency in the tokamak geometry.

Sun Hee KIM: *"Full tokamak discharge simulations using DINA-CH"*
A free-boundary evolution code, DINA-CH, has been combined with an advanced transport modelling code, CRONOS, for the full tokamak discharge simulation. The combined tokamak simulator has been upgraded resolving some difficulties in its first version. The equilibrium information requested by CRONOS is directly substituted by a free-boundary equilibrium from DINA-CH and an undesirable time-step delay in the data exchange between the two codes is removed. ITER H-mode and hybrid mode have been simulated with the upgraded simulator. From the recently attempted study of free-boundary features, additional requirements for the combined simulator are now recognized concerning the plasma heating and current drive modules in CRONOS. The power coupling physics between launched waves and plasma should be considered for the study of free-boundary features during the plasma evolution. The update time-step of heating and driven current profiles should be time-variable to optimize the computational performance of the combined simulator. For the control of plasma shape parameters, a simple control algorithm has been developed using a plasma response identification method and tested for the design of a shape controller. Although this algorithm could to be applicable for the profile control of steady-state plasma, the control robustness which is necessary for the safe operation of ITER is one of the big challenges of this work.

Xavier LAPILLONNE: *"Gyrokinetic Simulations using Eulerian Approach"*
With the purpose of developing a grid based code for solving the 5 dimensional gyrokinetic equations in toroidal geometry, the 4D code, CYGNE, is being developed for solving the electrostatic drift-kinetic equations in cylindrical geometry. This code uses a semi-Lagrangian approach based on cubic spline interpolation. In this approach the distribution function f is computed on a fixed grid and is updated from time t-Δt to time t using its invariance along particle trajectories. One of the main advantages of this method is that it provides a grid description of f, with no stability restriction on the time step such as the Courant Friedrichs Lewy condition. The code simulates well the linear phase. In the non-linear regime however, when fine scale structures start to appear, simulations exhibit development of negative value regions of the distribution function, as well as bad energy conservation, which have been investigated. In addition, some simple 1d and 2d models have been studied, which still contain some of the key issues found in the 4D code, providing a better understanding of CYGNE behaviour.

Bin LONG: *"Liquid Pb-Bi embrittlement effects on T91 steel after different heat treatments"*
Liquid metal embrittlement (LME) refers to the reduction or loss of ductility of a ductile material when it contacts with a liquid metal under stress. The susceptibility to liquid Pb-Bi eutectic (LBE) embrittlement effects of martensitic steel T91 was studied by performing slow-strain-rate tensile (SSRT) and 3-point bending tests at temperatures ranging from 150°C to 450°C in LBE. Parallel tests were performed in Ar environment for comparison. In order to obtain different strengths, the T91 steel was tempered at different temperatures, 500, 600 and 750°C, after normalizing at 1050°C. LME has been observed for specimens of all the three tempering conditions. Furthermore, it is much more pronounced for specimens tempered at 500 and 600°C. The SEM analysis shows the fracture mode of these specimens is brittle with cleavage fractures. The results of 3-point bending tests show the LME effects on the J_{IQ} of the steel.

Alessandro MARINONI: *"Experimental study of plasma fluctuations in tokamaks"*
The aim of this work is to investigate plasma density fluctuations in the edge region of the tokamak JET and in the core region of the tokamak TCV.
The first project relies on the microwave reflectometry diagnostic, mainly on the X-mode correlation reflectometer, which should be able to yield the fine scale spatial correlation structure of the turbulence. Since a recent upgrade of the diagnostic has considerably raised the signal to noise ratio, new data are being currently analysed with software previously developed.
The second project is mainly focused on the installation in the TCV tokamak of a core turbulence diagnostic which, on the basis of a previous feasibility study, has been chosen to be based on the tangential Phase Contrast Imaging technique. The design is presently being finalized.
The gyrokinetic codes GS2 and KINEZERO, which had been used to calibrate the diagnostic design, are now run to investigate specific turbulence issues concerning the TCV tokamak.

Janos MARKI: *"TCV divertor infrared measurements"*
Work started last year on a comparison of data from a vertically viewing micro-bolometer infrared camera and an array of tile-embedded Langmuir probes has been continued and a small database of the sheath heat transmission coefficient of the floor tiles has been established. Values in the range of 4-8 were found on TCV, which are somewhat lower than expected, though agree within experimental errors with those from simple sheath theory. These results have been presented at the 17th PSI conference in Hefei, China, and have subsequently been accepted for publication in JNM. Serious efforts were made to quantify and reduce experimental error levels, nevertheless, the typical errors are of the order of 60-70%. In order to reduce these, two measures will be taken: The deviations of the floor tiles from the horizontal plane will be measured in-situ to reduce errors on the magnetic field line incidence angle calculation, and new, thermally well-coupled thermocouples will be fitted into 3 tiles in the centre of the field of view, so that an evaluation of the emissivities of the tile surfaces can be performed in the cool-down phase of each pulse. Over the course of 2006, the old Merlin system has been replaced with the Thermosensorik CMT256. This involved installing new relay optics and a magnetic shielding box, creating a remotely controlable triggering unit, integrating the system into the TCV shot cycle and setting it up for automatic acquisition, as well as a calibration for a range of integration times (a wide range of acquisition frequencies are available as a function of the size of the sub-array acquired). The first shot was acquired with the new system on 13th October 2006; since that date, the system is ready for scientific exploitation, nevertheless, a number of features are still to be implemented such as fully automatic data acquisition in the TCV shot cycle as well

as establishing an automatic data backup procedure (each experiment produces 600-700 MB of data).

Mikhail MASLOV: *"Particle transport and confinement in TCV and JET"*
The aim of this work is to identify the key parameters which influence the particle transport properties in tokamaks (diffusion and convection) in order to predict the density profile behaviour in burning plasma devices.
The current work has provided substantial backing to the existence of the anomalous convention in H-mode in the TCV and JET tokamaks and has been reported at the 33rd EPS Conference on Plasma Physics as an oral contribution.
Thorough analysis of various JET 2006 H-mode experiments was carried out using more advanced diagnostic measurements (comparing to the previous years). That work will be continued in 2007.
A variety of experiments on TCV with 3rd harmonic ECRH heating in H-mode plasma were done, achieving very different density profiles, from very peaked to nearly flat. The reasons for such contrasting behaviour are under investigation. TCV sessions dedicated to particle transport studies are also planned to be done in 2007-2008, since early 2007 already passed without any continuation of experiments.

Nicolas MELLET: *"Extension of the LEMAN code to include finite temperature effects in the dielectric tensor to resolve singular mode structures and study effects of mode conversion without having to include gyroradius effects as in the PENN code"*
The LEMan code has been further optimised. The Gauss decomposition is now performed during the computation of the matrix allowing that only one instead of three matrix blocks has to be stored for each magnetic surface. Such a modification makes it possible to compute IC cases in the LHD stellarator. But it is still insufficient for more complicated geometries like W7X. The modelisation of the antenna has been also improved adding the possibility of a helical shape or a localisation in both toroidal and poloidal directions. The latter is fully parallelised taking advantage of the absence of coupling between Fourier modes with different toroidal wave numbers in a tokomak. Several scenarios have been studied in a JET-like equilibrium with the warm model, for example broadening of the resonance with the temperature or presence of the ion-ion hybrid resonance. Finally, comparisons with different approximations of the parallel wave vector have been performed with the LEMan code and a version of PENN keeping terms only up to the 0th order in the Finite Larmor radius expansion. A good correspondence is found.

Pablo MUELLER: *"Study of the fracture properties of two reduced-activation tempered martensitic steels, F82H and Eurofer97"*
A promising local criterion model with the potential of predicting cleavage fracture toughness has been studied. Notched tensile specimens of Eurofer97 steel were tested from room temperature down to -165°C. Finite element simulations of these specimens were undertaken. For each tested temperature, the calculated load-displacement curves were found to reproduce very well those of the tests. The local criterion model states that, when the stress is larger than a critical stress within a critical volume ahead of the crack tip, cleavage is triggered leading to macroscopic failure of the specimen. It was shown that this model is able to predict the fracture load of the notched specimens with the same values of critical stress and critical volume that were calibrated for compact specimens.
Eurofer97 and F82H steels show different fracture properties despite of having very similar composition, fabrication process, and heat treatment. Eurofer97 has a steeper brittle-to-ductile transition, and the F82H has low toughness points even at

relatively high temperatures. Scanning and transmission electron microscope as well as optical microscope observations were performed to find differences in the microstructure and possible explanations. It was found that Tantalum in Eurofer97 formed small carbides up to 1 micron, while in F82H it formed large oxides up to 30 microns. These big particles are believed to be responsible for the low toughness data points. Since the tantalum did not form carbides, it could not stabilize the pre-austenite grain size in the F82H, which was observed to be about eight times as large as the pre-austenitic-grain size in Eurofer97

Theodoros PANIS: *"Study of the Alfvén instability in tokamak plasmas"*
By studying the properties of stable Toroidal Alfvén Eigenmodes (TAE's), high performance regimes of tokamak reactor operation avoiding unstable fast particle driven modes can be found. To this end, a system consisting of eight antennas which excite TAE's with high toroidal mode number (n~10) was designed and built at CRPP and installed on the JET device.
The purpose of this work was the optimization of the efficiency of the antenna system, with the goal of maximizing the current driven in the antenna in the frequency range 30kHz–500kHz, under a voltage limitation of 600V maximum. A (lumped) LC circuit was considered to be used as a matching unit. In order to perform this optimization process, simplified system models were used in the environment of a radio-frequency design software.
The results when one antenna is at the end of the transmission system include various sets of values of the matching unit elements for several bands of frequencies, allowing a current between 4 and 11A for the frequency range 25–230kHz

Ilya PAVLOV: *"Study of the SAWTOOTH impact on MECH and ELM's induced perturbation on TCV Tokamak Plasmas"*
Perturbation experiments for studying electron heat transport were performed on the TCV tokamak in various plasma conditions. Data from different diagnostics (ECE, MPX) were analysed to demonstrate the simultaneous propagation and non-linear interaction of heat pulses induced by Modulated Electron Cyclotron Heating (MECH) and sawtooth activity. One needs a long data set to quantitatively characterize the effect of the nonlinear coupling of these heat waves on the measured temperature perturbation. In the experiment the sawtooth behaviour could vary significantly during discharge. For example it is very hard to control the sawtooth frequency, which makes the Fourier based data analysis hard to perform. A modelling of the TCV sawtoothing discharges with the ASTRA transport code was used to get more controllable sawteeth and to test different approaches to model the ST-MECH interaction. The perturbed temperature profiles from experiment and modelling have been compared. Since in the modelling we fixed the sawtooth frequency the experimental temperature profiles are not identical to the profiles from modelling but both of them show the same effect of phase coupling.
Another experimental topic is studying a strong correlation between sawteeth & ELMs on TCV. We use the technique based on Higher Order Spectral Analysis to quantitatively characterize the effect of phase coupling which is observed in H-mode with X3 heating.

Francesco PIRAS: *"Plasma shape control of TCV"*
A new Digital System Processor (DSP) will be installed in TCV, allowing the design of a modern system for the control of the plasma shape. In order to develop a powerful feedback algorithm, the system will be optimized by means of simulations in order to find the optimal architecture and parameters for the control loop. The

breakdown model will also be studied, to improve precision in reconstructing the plasma behavior during this phase.

Andreas PITSCHKE: *"Investigations of the spatial resolution of the Thomson scattering diagnostic at the TCV tokamak in order to characterize electron temperature and density gradients of eITB plasmas"*
Internal transport barriers in tokamak plasmas are explored in order to improve confinement and stability beyond the ITER reference scenario and to achieve higher bootstrap current fractions as an essential part of non-inductive current drive. Internal transport barriers are produced by modifications of the current profile using external heating and current drive effects.
For a first examination mathematical profile deconvolution methods, especially the Thikonov regularization method, were applied on characteristic eITB electron temperature and density profiles. However, the lack of sufficient data points due to the low spatial resolution of the diagnostic did not allow to reliably apply the deconvolution methods onto the given profiles. Thus a new arrangement of the viewing chords, using the existing hardware, has been designed to be suitable for future eITB experiments at a vertical plasma position of z=0.

Gennady PLYUSHCHEV: *"Interaction of turbulence with suprathermal ions in a simple magnetized toroidal plasma"*
For this investigation the suprathermal ions will be produced by a small size fast ion source which will be directly placed inside the vacuum vessel. The design of the source was developed and optimized in order to increase the fast ion current. The fast ion detector, which consists of two gridded energy analysers (one of them is used for background subtraction), was constructed. A theoretical investigation of the fast ion beam behaviour in the TORPEX plasma was started. The first results show that despite a relatively narrow energy distribution, significant beam spreading appears after one toroidal turn. The detector and the source will be installed on a recently developed two-dimensional poloidally moving system. The first prototype of the 2D moving system was constructed and installed on TORPEX with a new mobile Rogowski coil. This will enable plasma current profile measurements in the plasma scenario in which an ohmic transformer is used. In such scenario plasma currents up to 1kA have already been achieved. A theoretical investigation showed that, in order to obtain equilibrium in such TORPEX regimes with circular cross-section plasmas, modifications of the coil system are needed.

Mario PODESTA: *"Experimental studies of transport properties in toroidal plasmas"*
In the past year I have investigated the particle source and the loss mechanisms in the toroidal magnetised device TORPEX, where plasmas are generated and sustained by microwaves in the electron-cyclotron (EC) frequency range. In particular, the electron energy distribution function resulting from the interaction of the injected EC waves with the plasma has been characterised. I have applied techniques based on the Fourier and Laplace analysis of the plasma response to a modulation of the injected microwave power to determine the particle flux responsible for the particle loss. A 2D reconstruction of the particle flux based on the Conditional Average Technique has been carried out. The link between the local fluctuation-induced particle loss across B, determined by drift-interchange plasma instabilities, has thus been established. To achieve this goal, the hardware control of the microwave source installed on TORPEX has been conveniently modified. A feedback loop, which enhances the stability properties of the microwave source, has been introduced in the original control system. The discharge duration has been increased up to a continuos operation.

Francesca Maria POLI: *"Investigation of instabilities and turbulence in a simple toroidal plasma"*
Instabilities develop in TORPEX in the bad curvature region, at the location of maximum pressure gradient. The nature of instabilities has been investigated in an experimental configuration with low level of fluctuations, where the frequency spectrum is dominated by coherent modes. The dispersion relation, measured at different locations across the plasma cross-section, is consistent with a drift-wave dispersion relation. From the comparison with a linear, kinetic, analytic model in slab geometry, it has been shown that the curvature of the magnetic field is the dominant mechanism for the destabilization of these modes. The wavenumber and frequency spectrum is coherent at the location where the instabilities are generated, then broadens during propagation, indicating development of turbulence. Higher order spectra, measured along the direction of convection, show that the transition from a coherent mode to a turbulent spectrum is due mainly to three-wave interaction processes, during which the spectral power is redistributed from the unstable mode to the whole spectrum.

Amuthan RAMAR: *"On the Relationship Between the Microstructure and The Mechanical Properties of an ODS Ferritic/Martensitic Steel"*
Oxide dispersion strengthened (ODS) ferritic/martensitic (F/M) steels are candidate structural material for the future fusion reactors due to their good high temperature strength, good thermal conductivity, swelling resistance and low radiation damage accumulation. A new ODS F/M steel with the EUROFER 97 RAFM steel as matrix material and Y_2O_3 particle as reinforcement material is being developed through the classical powder metallurgy technique. The Eurofer 97 atomized powder with particle sizes around 45μm is ball milled in argon atmosphere in a planetary ball mill together with Y_2O_3 particles with sizes about 10 to 30nm. The milled powders are canned in a steel container. They are degassed at 650°C for 3 hours in vacuum of 10^{-5}mbar. The canned sample is sealed and finally compacted by hot isostatic pressing (HIP) in an argon atmosphere under a pressure of 180MPa at 1150°C for 2 hours. Electron microscopy and X-ray diffraction observations are done at regular intervals during ball milling to identify changes in the particle and crystallite size and in the solubility of yttria in the matrix. In a next step, the microstructure and mechanical properties of the final compacted material will be assessed and the size, shape and spatial distribution of dispersed oxide particles will be determined.

Christian SCHLATTER: *"Fast ions studies on TCV and JET"*
The modelling of the charge exchange (CX) spectrum in ohmic TCV plasmas was completed with a proof of principle to reconstruct the ion temperature profile from single chord NPA measurements a) experimentally by a vertical plasma scan or b) without plasma displacement but with convergent modelling of the NPA CX spectrum by iterating the parameters of a functional ion temperature profile (for more details see 2.1.4 under "Reconstruction of ion temperature profiles using a Neutral Particle Analyser). In plasmas with ECCD and ECH, anomalous energy and momentum transfer from the electrons to the ions is generally observed on TCV. The measured time scales suggest a wave-particle interaction mechanism, able to resonate with the electrons and ions simultaneously. For the experiments carried out last year it was theoretically shown that the current-driven ion-acoustic instability (propagating at frequencies close to the plasma ion frequency, excited in plasmas with drifting electrons) is a possible candidate. To conclude, further modelling is necessary, but this requires more experimental data, for example the spatial localization of the fast ions (experiment under way) or information about

the electromagnetic spectrum of the plasma (an RF antenna is planned to be installed in 2007).

The numerical tools for the simulation of suprathermal plasmas (data analysis codes, ion neutralization code DOUBLE) were continuously improved. A new code for the simulation of the electron-cyclotron emission NOTEC was implemented and extensively tested for TCV plasmas. The code recovers the properties of the suprathermal electrons from the ECE measurements, whose parameters are essential for the understanding of the formation of the suprathermal ion population.

For new experiments to be carried out in the winter 2006/2007, the shield of the Compact NPA against hard X-ray photons emitted by runaway-electrons was further optimized (for more details see the section 3.2.4).

On JET, a new campaign started in early 2006 and the high energy NPA KF1 has been prepared for the new experiments. Various calibration issues and the anomalous response of some scintillators were analysed and possible solutions were proposed. A further stay was devoted to the analysis of NPA data in tornado mode (toroidal Alfvén eigenmode inside the q=1 surface) experiments. Tornado modes are considered to be a possible reason for expelling fast ions from the q=1 region and causing monster sawtooth crashes due to the loss of fast ion stabilization. Indeed it was found that the neutral fluxes originating from the plasma core and measured by the NPA start to drop before the crash.

Benjamin STRAHM: *"Thin film technology for solar cells"*

Microcrystalline and amorphous silicon are both used for photovoltaic solar cells technology. The growth of the amorphous microstructure is nowadays well controlled, but it is not the case of the growth of microcrystalline silicon which is more complicated and difficult to achieve. The analytical plasma chemistry model developed earlier has shown that to grow microcrystalline silicon, the silane concentration *in the plasma* has to be very low (<0.5%). This condition is sufficient even to deposit microcrystalline silicon from pure silane gas, as confirmed by experiments. Modelling and experiments in a large area industrial PECVD reactor have shown that deposition from pure silane gas has also the advantage to be the optimum of the silane gas utilization efficiency compared to deposition with lower silane gas concentration. Hence, microcrystalline silicon has been deposited at high rate (11.5Å/s) over a large area with a gas utilization efficiency of 81%. The knowledge gained from this model and these experiments helped us to develop a reactor independent optimization methodology for microcrystalline silicon deposition. This optimization methodology has been used to reach an ultimate cost-effective process with a deposition rate of 10.9Å/s of a material with a crystalline fraction of 66% and a silane gas utilization efficiency of 82.3%. A single junction PV solar cell produced with these parameters has shown a non-optimized light conversion efficiency of 6%. All these results have been detailed in three submitted papers and one conference paper. Further work is on-going to study the effect of the early stage of plasma ignition on the plasma composition, hence, on the deposited material microstructure.

Alban SUBLET: *"Study of atmospheric and near atmospheric pressure dielectric barrier discharges for SiOx deposition on polymer films"*

A new experimental arrangement has been built for simultaneous Laser Light Scattering measurements. Two high QE CCD cameras have been used and triggered simultaneously in order to acquire the light scattered by particles growing in a $N_2/O_2/$HMDSO Dielectric Barrier Discharge (DBD). A polarizer was placed in front of each camera to collect respectively the parallel and perpendicular polarized scattered light. This avoids fast and non repeatable powder dynamic occurring at high pressure. The analysis and calculation made on the images obtained allow us

to determine the polarization degree and the particle size evolution along the gas flow according to the working pressure, gas composition and monomer concentration. This study finalizes the Ph. D experimental work.

Moreover, fast imaging measurements of a multipeak DBD in helium and nitrogen have been made to complete a more fundamental study of DBDs in non reactive gases. These measurements showed a clear distinction between each multipeak discharge and spatial inhomogeneities of the plasma in the electrode gap.

Gang YU: *"SANS analysis of irradiation-induced defects in metals and alloys"*
SANS measurements were performed on series of specimens of reduced activation tempered martensitic (RAFM) steels, irradiated with high-energy protons in the PIREX facility or with a mixed spectrum of high-energy protons and spallation neutrons in the SINQ target station, at the Paul Scherrer Institute. Different irradiation temperatures and doses were investigated, ranging from 50°C to 350°C and from 1 to 20dpa, respectively. The ratio A of the nuclear plus magnetic scattering intensity for $\phi=90°$ to the nuclear scattering intensity for $\phi=0°$, where ϕ is the angle between the applied magnetic field direction and the projected observation direction onto the plane perpendicular to the neutron beam, was found much higher than that calculated for He bubbles, for instance.
In order to identify the irradiation-induced defects, molecular dynamics (MD) simulations were used to create a number of microstructural features typical of the irradiation-induced damage in Fe, the latter being considered as a model alloy representing typical RAFM steels. These features include dislocation loops, voids and helium bubbles with various He contents. A defect database was generated for various defect sizes.
A methodoly has been established to simulate the scattering intensity obtained with neutrons. We recently developed and validated the codes for the case of neutron diffraction. It is planned to use our experience in MD simulations to simulate the neutron scattering intensity as a function of the defect types that are expected in the matrix.

Alexandra ZHUCHKOVA: *"Faraday rotation measurements of the poloidal magnetic field in the TCV Tokamak, using a far-infrared polarimeter"*
A new far-infrared (FIR) polarimeter diagnostic for the TCV Tokamak is under construction at CRPP. It will allow to measure the poloidal magnetic field and hence the current density profile in TCV plasmas. The current density j(r) is linked to the safety factor q which is a key parameter for the transport models as well as for the magnetohydrodynamic (MHD) stability theory of tearing modes, sawteeth and disruptions. The Faraday rotation measurements will also improve the accuracy of the equilibrium reconstruction by the LIUQE equilibrium code. The diagnostic will measure the Faraday rotation angle of FIR laser beams along 10 vertical lines of sight across the poloidal cross section of the tokamak. At the time of writing the conceptual design of the diagnostic is almost finished: the scheme, optical components and their supports, electronics, detection system. Most of the components of the polarimeter have been tested, namely the stability of the CO_2 and FIR lasers, the characteristics of the recently acquired waveguide Schottky diode detector, the optical properties of the materials at the laser wave length 432.5 μm (FIR laser) and 9.27 μm (CO_2 laser), optical components: mirrors, lenses, meshes, wave guides, half wave and quarter wave plates, polarizers and quartz windows. In 2007 the diagnostic will be installed on TCV and used for the physical research.

Costanza ZUCCA: *"Studies of electron transport and current diffusion in switched ECCD experiments on TCV"*

Understanding the physical connection behind electron confinement and plasma current density profile is of primary importance for the exploitation of a future fusion reactor. These two quantities were found to be strongly related by a variety of dedicated experiments in many tokamaks: in TCV, it was shown that the electron confinement improves by modifying the steady-state current density from peaked to hollow. Such behaviour is believed to be due to the suppression of plasma turbulence in the presence of a negative magnetic shear and a finite Shafranov shift. Generation of a Switched ECCD (SECCD) has been done in TCV L-mode plasmas, i.e. driving alternatively co- or counter-ECCD at constant total input EC power during a single discharge. The idea underlying these experiments is to decouple the contributions of specific heating oscillations from those of the current density tailoring, so that any modification in the transport properties of the plasma is to be ascribed only to the shear profile modulation realized by the ECCD switching. Modelling of the plasma current density profile has been carried out with the ASTRA code employed in both interpretative and predictive modes, with two shear-dependent transport models. In this model the modulation of ECCD is the only actuator for the transport properties modifications. The plasma response has thus been studied in presence of SECCD to understand the differences in time scales and transient behaviours between the various models employed and with different experimental conditions, such as changes in period and deposition location, confirming the synergy between electron transport and magnetic shear, both of which are modulated around the EC deposition region. This modelling also allows to completely decouple the effects of the current profile modification from those of slight plasma heating imbalance or non-constant plasma elongation, which are key concepts at the basis of SECCD and can be a rather delicate experimental issue. The numerical results moreover validated a previous rough model based on electrodynamics calculations.

6 Public relations activities in 2006

Generalities

Outreach activities presenting the progress in fusion and plasma science at different levels of education have been largely pursued, especially in organised meetings for high school & gymnasium physics teachers. CRPP also received undergraduate students, university students, government officials and the general public.

Coordinated with the various announcements concerning ITER and the setting up of the European Domestic Agency, a particular effort was made to inform the Swiss industry by formal meetings, contacts and a website. We maintained the contact with radio and TV broadcasting teams.

A special day on ITER and fusion was set-up in Ticino in July 2006 to present the industrial opportunities.

Organised visits to the CRPP

Following established practice, we welcomed about 1100 visitors to the CRPP in Lausanne, mostly in groups of about 20 to 80 people. About 50% of the visitors came from schools, high schools or universities, 85% of the visitors were from Switzerland, the rest from different countries, among them: Italy, the Czech Republic, France, Holland... All these participants visited TCV, but also other experiments, i.e. the Torpex basic plasma physics experiment – and plasma processes.

Conferences and talks

Members of the CRPP gave several talks on fusion in Switzerland and in Europe. Preparations for the AIEA 2008 Conference in Geneva started, with a special involvement of CRPP, as well as of the « Education & Research » Secretariat of State. This conference represents the 50th anniversary of the « Atom for Peace » conference which was located in the UN buildings in Geneva, and the anniversary will be organised in those same buildings, from 12th to 18th October 2008.

Web activities on http://crppwww.epfl.ch
The main CRPP website is regularly kept up to date, including links to other, mainly fusion oriented, sites.

Articles of general interst

R. A. Pitts, R. J. Buttery, S. Pinches, *"Fusion: the way ahead"*, Physics World, Vol 19, March 2006 pages 20-26. *From a CRPP lead author, this is a commissioned article for the headlight magazine of the British Institute of Physics, with a circulation of over 50,000 worldwide to physicists in industry, research and education. It introduces fusion and tokamak research, describing how the physics programme on the Joint European Torus (JET) in the UK is concentrating on critical issues for the next step ITER project.*

P.J.Paris, *"La fusion thermonucléaire : 100 MWh à partir d'un gramme de combustible"*, Bulletin SEV/VSE 9/06

APPENDICES

APPENDIX A   *Articles Published in Refereed Scientific Reviews During 2006*

(see CRPP archives at http://crppwww.epfl.ch/archives)

P. Angelino, A. Bottino, R. Hatzky, S. Jolliet, O. Sauter, T.M. Tran, L. Villard, *Effects of plasma current on nonlinear interactions of ITG turbulence, zonal flows and geodesic acoustic modes,* Plasma Physics and Controlled Fusion 48, 557-571 (2006)

P. Angelino, A. Bottino, R. Hatzky, S. Jolliet, O. Sauter, T.M. Tran, L. Villard, *On the definition of a kinetic equilibrium in global gyrokinetic simulations,* Phys. Plasmas 13 (5), 052304 (2006)

A. Anghel, P. Bruzzone, M. Vogel, *Results of contact resistance distribution in ITER conductor termination,* IEEE Trans. Appl. Supercond. 16(2), 779-782 (2006)

D. Backes, L.J. Heyderman, C. David, R. Schaublin, M. Klaui, H. Ehrke, U. Rudiger, C.A.F. Vaz, J.A.C. Bland, T. Kasama, R.E. Dunin-Borkowski, *Fabrication of curved-line nonostructures on membranes for transmission electron microscopy investigations of domain walls,* Microelectronic Engineering 83(4-9), 1726-1729 (2006)

N. Baluc, *Materials for fusion power reactors,* Plasma Phys. and Contr. Fusion 48 (2006) B165-B177

P. Blanchard, R. Behn, H. Weisen, A. Zhuchkova, *A 10-channel far-infrared polarimeter for the TCV tokamak,* Rev. Sci. Instrum. 77, 10F101 (2006)

A. Bortolon, B. P. Duval, A. Pochelon, A. Scarabosio, *Observation of Spontaneous Toroidal Rotation Inversion in Ohmically Heated Tokamak Plasmas,* Phys. Rev. Lett. 97, 235003 (2006)

A. Bottino, O. Sauter, et al., *Linear stability analysis of microinstabilities in electron internal transport barrier noninductive discharges,* Plasma Phys. & Contr. Fusion 48, 215-233 (2006)

L. Bottura, P. Bruzzone, C. Marinucci, B. Stepanov, *Transverse heat transfer coefficient in CICC's with central cooling channel,* Cryogenics 46, 597-605 (2006)

P. Bruzzone, *30 Years of conductors for fusion: a summary and perspectives,* IEEE Trans. Appl. Supercond. 16(2), 839-844 (2006)

P. Bruzzone, B. Stepanov, R. Wesche, A. Portone, E. Salpietro, A. Vostner, A. Della Corte, *Test results of a small size CICC with advanced Nb3Sn strands,* IEEE Trans. Appl. Supercond. 16(2), 894-897 (2006)

P. Bruzzone, B. Stepanov, E. Zapretilina, *A critical review of coupling loss results for cable-in-conduit conductors,* IEEE Trans. Appl. Supercond. 16(2), 827-830 (2006)

P. Bruzzone, B. Stepanov, R. Zanino, R.L. Savoldi, *Results of buoyoncy-gravity effects in ITER cable-in-conduct conductor with dual channel,* Adv. Cryo. Eng. 51, 1749-1756 (2006)

P. Bruzzone, B. Stepanov, R. Wesche, *Transverse load degradation in Nb3Sn cable-in-conduit conductors with different cable pattern,* Adv. Cryo. Eng.: Trans. Int'al Cryo. Material Conf. ICMC 52, 558-565 (2006)

Y.L. Chiu, N. Baluc, R. Schaeublin, *Nanostructured tungsten-iron alloy prepared by electrodeposition,* International Journal of Modern Physics B, 20 (2006) 4195-4200

S. Coda, I. Klimanov, S. Alberti, G. Arnoux, P. Blanchard, A. Fasoli, the TCV Team, *The effect of ECRH on the electron velocity distribution function,* Plasma Physics and Controlled Fusion 48 (2006) B359

W.A. Cooper, J.P. Graves, T.M. Tran, R. Gruber, T. Yamaguchi, Y. Narushima, S. Okamura, S. Sakakibara, C. Suzuki, K.Y. Watanabe, H. Yamada, K. Yamazaki, *Stability Properties of Anisotropic Pressure Stellarator Plasmas with Fluid and Noninteractive Energetic Particles,* Fusion Science and Technology, 50, 245 (2006)

W.A. Cooper, J.P. Graves, S.P. Hirshman, T. Yamaguchi, Y. Narushima, S. Okamura, S. Sakakibara, C. Suzuki, K.Y. Watanabe, H. Yamada Yamazaki, *Anisotropic Pressure Bi-Maxwellian Distribution Function Model for Three-Dimensional Equilibria,* Nuclear Fusion 46, 683 (2006)

W.A. Cooper, J.P. Graves, M. Jucker, M. Yu Isaev, *Relativistic Hamiltonian Guiding Center Drift Fomalism in Anisotropic Pressure Magnetic Coordinates,* Physics of Plasmas 13, 092501 (2006)

L.-G. Eriksson, T. Johnson, M.-L. Mayoral, S. Coda, O. Sauter, R.J. Buttery, D. McDonald, T. Hellsten, M.J. Mantsinen, A. Mueck, J.-M. Noterdaeme, M. Santala, E. Westerhof, P. de Vries, JET-EFDA contributors, *On ion cyclotron current drive for sawtooth control,* Nucl. Fusion 46, S951-964 (2006)

E. Fable, O. Sauter, S. Coda, T. P. Goodman, M. A. Henderson, H. Weisen, A. Zabolotsky, C. Zucca and the TCV team, *Inward thermodiffusion particle pinch in electron internal transport barriers in TCV,* Plasma Physics and Controlled Fusion, 48 (2006) 1271

A. Fasoli, B. Labit, M. McGrath, S.H. Mueller, G. Plyushchev, M. Podesta, F.M. Poli, *Electrostatic turbulence and transport in a simple magnetized plasma,* Phys. Plasmas 13, 055902 (2006)

W.H. Fietz, R. Heller, R. Lietzow, V.L. Tana, G. Zahn, R. Wesche, E. Salpietro, A. Vostner, *High temperature superconductor current leads proposal for ITER,* IEEE, 1-4244-0150-X/06 (2006)

W. Fundamenski, R. A. Pitts, and JET-EFDA contributors, *A model of ELM filament energy evolution due to parallel losses,* Plasma Phys. Contr. Fusion 48 (2006) 109

I. Furno, T. P. Intrator, D. D. Ryutov, S. Abbate, T. Madziwa-Nussinov, A. Light, L. Dorf, and G. Lapenta, *Current-Driven Rotating-Kink Mode in a Plasma Column with a Non-Line-Tied Free End,* Physical Review Letters PRL 97, 015002 (2006)

I. Furno, T.P. Intrator, D.D. Ryutov, S. Abbate, T. Madziwa-Nussinov, A. Light, L. Dorf, and G. Lapenta, *Current driven rotating kink mode in a plasma column with a non-line-tied free end,* Physical Review Letters PRL 97, 015002 (2006)

O.E. Garcia, J. Horacek, R.A. Pitts, A.H. Nielsen, W. Fundamenski, J.P. Graves, V. Naulin, J. Juul Rasmussen, *Interchange turbulence in the TCV scrape-off layer,* Plasma Phys. & Contr. Fusion 48, L1 (2006)

V. Grangirard, M. Brunetti, P. Bertrand, N. Besse, X. Garbet, P. Ghendrih, G. Manfredi, Y. Sarazin, O. Sauter, E. Sonnendruecker, J. Vaclavik, L. Villard, *A drift-kinetic semi-Lagrangian 4D code for ion turbulence simulation,* J. Comput. Phys. 217(2), 395-423 (2006)

S. Hacquin, et al., D. Testa, *X-mode reflectometry measurements in the JET plasma core region,* Rev. Sci. Instrum. 77, 10E925 (2006)

R. Heller, W.H. Fietz, R. Lietzow, V.L. Tanna, A. Vostner, R. Wesche, G.R. Zahn, *70kA high temperature superconductor current lead,* IEEE Trans. Appl. Supercond. 16(2), 823-826 (2006)

F. Imbeaux, G. Giruzzi, P. Maget, J.L. Segui, V.S. Udintsev, et al., *Giant Oscillations of Electron Temperature during Steady-State Operation on Tore Supra,* Phys. Rev. Letters 96, 045004 (2006)

M. Jucker, Zh.N. Andrushchenko, V.P. Pavlenko, *Large scale magnetic fields and coherent structures in nonuniform unmagnetized plasma,* Phys. Plasmas 13, 072308 (2006)

A.N. Karpushov, B.P. Duval, Ch. Schlatter, V.I. Afanasyev, F.V. Chernyshev, *Neutral particle analyzer diagnostics on the TCV tokamak,* Rev. Sci. Instrum. 77, 033504 (2006)

Giovanni Lapenta, Ivo Furno, Thomas Intrator, Gian Luca Delzanno, *Kink instability of flux ropes anchored at one end and free at the other,* Journal of Geophysical Research, vol. 111, A12S06, 2006

N.P. Lazarev, C. Abromeit, R. Schaeublin, R. Gotthardt, *Temperature-controlled martensitic phase transformations in a model NiAl alloy,* J. Appl. Phys. 100(6), 063520-10 (2006)

A.W. Leonard, N. Asakura, J.A. Boedo, et al., R.A. Pitts, for the Pedestal and Edge Physics ITPA Topical Group, *Survey of Type I ELM dynamics measurements,* Plasma Phys. & Contr. Fusion 48, A149 (2006)

R. Lindau, N. Baluc, R. Schaeublin, et al., *Present development status of EUROFER and EDS-EUROFER for application in blanket concepts,* Fusion Eng. Design 75-79, 1037 (2005)

M.F.F. Nave, H.R. Koslowski, S. Coda, J. Graves, M. Brix, R. Buttery, C. Challis, C. Giroud, M. Stamp, P. de Vries, JET-EFDA contributors, *Exploring a small sawtooth regime in Joint European Torus plasmas with counterinjected neutral beams,* Physics of Plasmas, 13 (2006) 014503

P. Maget, F. Imbeaux, G. Giruzzi, V.S. Udintsev, et al, *Temperature Oscillating Regimes in Tore Supra diagnosed by MHD activity,* Nucl. Fusion 46 (2006), 797-806

A. Marinoni, P. Mantica, D. Van Eester, et al., *Analysis and modelling of power modulation experiments in JET plasmas with internal transport barriers,* Plasma Phys. & Contr. Fusion 48, 1469-1487 (2006)

A. Marinoni, S. Coda, R. Chavan, G. Pochon, *Design of a tangential Phase Contrast Imaging diagnostic for the TCV tokamak,* Review of Scientific Instruments 77 (2006) 10E929

S. Yu Medvedev, A.A. Martynov, Y.R. Martin, O. Sauter, L. Villard, *Edge Kink/Ballooning Mode Stability in Tokamaks with Separatrix,* Plasma Phys. Controlled Fusion 48, 927 (2006)

S.H. Mueller, A. Diallo, A. Fasoli, I. Furno, B. Labit, G. Plyushchev, M. Podesta, F.M. Poli, *Probabilistic analysis of turbulence structures from 2D plasma imaging,* Phys. Plasmas 13, 100701 (2006)

R.A. Pitts, W. Fundamenski, S.K. Erents, Y. Andrew, A. Loarte, C. Silva, and JET-EFDA contributors, *Far SOL ELM ion energies in JET,* Nuclear Fusion 46 (2006) 82

R.A. Pitts, R.J. Buttery, S. Pinches, *Fusion: the way ahead,* Physics World 19, (2006) 20

G. Plyushchev, A. Diallo, A. Fasoli, I. Furno, B. Labit, S.H. Mueller, M. Podesta, F.M. Poli, H. Boehmer, W.W. Heidbrink, Y. Zhang, *A new fast ion source and detector for investigating the interaction of turubulence with supra-thermal ions in a simple magnetized toroidal plasma,* Rev. Sci. Instrum. 77, 10F503 (2006)

M. Podesta, A. Fasoli, B. Labit, M. McGrath, S.H. Mueller, F.M. Poli, *Experimental characterization and modeling of the particle source in a Electron-Cyclotron wave driven toroidal plasma,* Plasma Phys. & Contr. Fusion 48, 1053-1062 (2006)

F.M. Poli, S. Brunner, A. Diallo, A. Fasoli, I. Furno, B. Labit, S.H. Mueller, G. Plyushchev, M. Podesta, *Experimental investigation of drift-interchange instabilities in a simple toroidal plasma,* Phys. Plasmas 13, 102104 (2006)

P. Popovich, W.A. Cooper, L. Villard, *A Full-Wave Solver of the Maxwell's Equations in 3D Plasmas,* Computer Physics Communications 175, 250 (2006)

A. Portone, E. Salpietro, L. Bottura, P. Bruzzone, W. Fietz, R. Heller, J.M. Rifflet, J. Lucas, F. Toral, S. Raff, P. Testoni, *Conceptual design of the 12.5T superconducting EFDA dipole,* IEEE Trans. Appl. Supercond. 16(2), 1312-1315 (2006)

A. Portone, E. Salpietro, L. Bottura, P. Bruzzone, et al., *Design and optimization of the 12.5T EFDA dipole magnet,* Cryogenics 46, 494-506 (2006)

H. Reimerdes, I. Furno, F. Hofmann, An. Martynov, A. Pochelon and O. Sauter, *Sawtooth behaviour in highly elongated TCV plasmas,* Plasma Phys. Control. Fusion 48 (2006) 1621

M.J. Rubel, G. De Temmerman, J.P. Coad, et al., R.A. Pitts, and JET EFDA contributors, *Mirror test for International Thermonuclear Experimental Reactor at the JET tokamak: An overview of the programme,* Rev. Sci. Instrum. 77, 063501 (2006)

D.D. Ryutov, I. Furno, T.P. Intrator, S. Abbate, T. Madziwa-Nussinov, *Phenomenological theory of the kink instability in a slender plasma column,* Physics of Plasmas 13, 032105 2006

A. Salmi, et al., D. Testa, *JET experiments to assess the clamping of the fast ion energy distribution during ICRF heating due to finite Larmor radius effects,* Plasma Phys. and Contr. Fusion 48, 717 (2006)

L. Sansonnens, H. Schmidt, A.A. Howling, Ch. Hollenstein, Ch. Ellert, A. Buechel, *Application of the shaped electrode technique to a large area rectangular capacitively-coupled plasma reactor to suppress standing wave nonuniformity,* J. Vac. Sci. Technol. A24(4), 1425 (2006)

L. Sansonnens, A.A. Howling, Ch. Hollenstein, *Electromagnetic field nonuniformities in cylindrical, large area high-frequency capacitive plasma reactors,* Plasma Sources, Sci. Technol. 15, 302 (2006)

M.I.K. Santala, M.J. Mantsinen, L. Bertalot, S. Conroy, V. Kiptily, S. Popovichev, A. Salmi, D. Testa, Yu Baranov, P. Beaumont, P. Belo, J. Brzozowski, M. Cecconello, M. deBaar, P. deVries, C. Gowers, J.-M. Noterdaeme, C. Schlatter, S. Sharapov, *Proton-triton nuclear reaction in ICRF heated plasmas in JET,* M I K Santala et al 2006 Plasma Phys. Control. Fusion 48 1233-1253

A. Scarabosio et al., *Toroidal plasma rotation in the TCV tokamak,* Plasma Phys. and Contr. Fusion 48 (2006) 663-683

R. Schaeublin, *Nanometric crystal defects in transmission electron microscopy,* Microscopy Res. & Techn. 69(5), 305-316 (2006)

R. Schaeublin, A. Ramar, N. Baluc, V. de Castro, M.A. Monge, T. Leguey, N. Schmid, C. Bonjour, *Microstructural development under irradiation in European ODS ferritic/martensitic steels,* J. Nucl. Mater. 351(1-3) 247-260 (2006)

Ch. Schlatter, B.P. Duval, A.N. Karpushov, *Reconstruction of ion temperature profiles from single chord NPA measurements on the TCV tokamak,* Plasma Phys. Control. Fusion 48, 1765-1785, (2006)

J.-W. Shin, H. Miyazoe, M. Leparoux, S. Siegmann, J.-L. Dorier, Ch. Hollenstein, *Influence of process parameters on an inductively coupled thermal plasma used for powder synthesis,* Plasma Sources, Sci. Technol. 15, 441 (2006)

A.A. Subbotin, M.I. Mikhailov, V.D. Shafranov, M. Yu. Isaev, C. Nuehrenberg, J. Nuehrenberg, R. Zille, V.V. Nemov, S. Kasilov, V.N. Kalyuzhnyj, W.A. Cooper, *Integrated Physics Optimization of a Quasi-Isodynamic Stellarator with Poloidally Closed Contours of the Second Adiabatic Invariant,* Nuclear Fusion 46 (2006) 921-927

A. Sublet, C. Ding, J-L. Dorier, Ch. Hollenstein, P. Fayet and F. Coursimault, *Atmospheric and sub-atmospheric dielectric barrier discharges in helium and nitrogen,* Plasma Sources Sci. Technol. 15, 627-634 (2006)

V.L. Tanna, W.H. Fietz, R. Heller, A. Vostner, R. Wesche, G.R. Zahn, *Conceptual design of a high temperature superconductor current feeder system for ITER,* J. of Physics: Conference Series 43, 1023-1026 (2006)

D. Testa, A. Fasoli, C. Boswell, and JET-EFDA contributors, *Measurement of the instability threshold for toroidal Alfvén eigenmodes in JET plasmas with forward and reversed magnetic field,* Nucl. Fusion 46, pp 829-836 (2006)

V.S. Udintsev, M. Goniche, G. Giruzzi, G.T.A. Huysmans, F. Imbeaux, P. Maget, X. Garbet, R. Sabot, J.L. Segui, F. Turco, T.P. Goodman, D. Molina, H. Weisen, *Studies of high frequency hot ion instabilities by means of correlation ECE on Tore Supra,* Plasma Phys. Control. Fusion 48 L33-L44

V.S. Udintsev, M. Goniche, et al, *First Results of Correlation ECE on Tore Supra,* Fusion Sci. & Technol. 50(4) (2006) 508-520

J. Wang, Y. Wang, R. Schaublin, C. Abromeit, R. Gotthardt, *The effect of point defects on the martensitic phase transformation,* Materials Science and Engineering A, 438-440 (2006) 102-108

H. Weisen, A. Zabolostky, M. Maslov, et al., and JET EFDA contributors, *Scaling of density peaking in JET H-modes and implications for ITER,* Plasma Phys. & Contr. Fusion 48, A457 (2006)

R. Wesche, B. Stepanov, P. Bruzzone, *Comparison of the DC performance of full and sub-size NbTi cable-in-conduit conductors,* IEEE Trans. Appl. Supercond. 16(2), 819-822 (2006)

R. Wesche, *High-temperature superconductors,* Springer Handbook of Electronic and Photonic Materials, ISBN 0-387-26059-5; e-ISBN: 0-387-29185-7

G. Yu, N. Nita, N. Baluc, *Thermal creep behaviour of the EUROFER 97 RAFM steel and two European ODS EUROFER 97 steels,* Fusion Eng. Design 75-79, 1037 (2005)

A. Zabolotsky, H. Weisen, A. Karpushov, TCV Team and JET-EFDA contributors, *Influence of particle sources on electron density,* Nucl. Fusion 46, 594-607 (2006)

R. Zanino, M. Bagnasco, W. Baker, et al., P. Bruzzone, *Implications of NbTi short-sample test results and analysis for the ITER poloidal field conductor insert,* IEEE Trans. Appl. Supercond. 16(2), 886-889 (2006)

R. Zanino, P. Bruzzone, R.L. Savoldi, *A critical assessment of pressure drop design criteria for the ITER magnet conductors,* Adv. Cryo. Eng. 51, 1765-1772 (2006)

APPENDIX B Conferences and Seminars

(see CRPP archives at http://crppwww.epfl.ch/archives)

B.1 Conference and conference proceedings published in 2006

P. Angelino, A. Bottino, R. Hatzky, S. Jolliet, O. Sauter, T.M. Tran and L. Villard, *Plasma elongation and magnetic shear effects in nonlinear simulations of ITG-zonal flow turbulence,* 33rd European Physical Society Conference on Plasma Physics, Rome, Italy, 19.06. - 23.06.2006

C. Angioni, et al., M. Maslov, H. Weisen, A. Zabolotsky, *Particle and impurity transport in ASDEX Upgrade and JET, experimental observations and theoretical understanding,* 48th Annual Meeting of the APS Division of Plasma Physics, Philadelphia, Pennsylvania, 30.10. - 03.11.2006

E. Asp, O. Sauter, S. Coda, E. Fable, T.P. Goodman, G. Turri, V.S. Udintsev and C. Zucca, *On the ECCD current density profile with particle diffusion in eITBs and its impact on the q-profile,* Theory of Fusion Plasmas, Varenna, Italy, 28.08. - 01.09.2006

N. Baluc, et al., *Status of R&D activities on materials for fusion power reactors,* 21th IAEA Fusion Energy Conference, Chengdu, China, 16.10. - 21.10.2006

N. Baluc, D.S. Gelles, S. Jitsukawa, et al., *Status of reduced activation ferritic/martensitic steel development,* Proc. 12th Int. Conference on Fusion Reactor Materials (ICFRM-12), Santa Barbara, USA, December 2005

N. Baluc, *ITER: un soleil prometteur sur terre,* Women in Nuclear (WIN) Annual Conference, Cassis, France, May 2006

N. Baluc, M.Q. Tran, *About R&D on fusion reactor materials in Switzerland,* Sino-Swiss Symposium on Material Science, ETH-Zuerich, Switzerland, October-November 2006

N. Baluc, *Materials for Fusion Reactors,* 33rd European Physical Society Conference on Plasma Physics, Rome, Italy, 19.06. - 23.06.2006

R. Berger, S. Brunner, E. Valeo, L. Divol, C. Still, *The nonlinear evolution of driven nonlinear ion acoustic waves with kinetic electrons,* 48th Annual Meeting of the APS Division of Plasma Physics, Philadelphia, Pennsylvania, 30.10. - 03.11.2006

P. Blanchard, R. Behn, H. Weisen, A. Zhuchkova, *A 10-channel far-infrared polarimeter for the TCV tokamak,* 16th Topical Conference on High-Temperature Plasma Diagnostics, Williamsburg, Virginia, 07.05. - 11.05.2006

R. Bonadé, P. Spaetig, N. Baluc, *Fracture toughness properties in the transition of the EUROFER97 tempered martensitic steel,* Proc. 12th Int. Conference on Fusion Reactor Materials (ICFRM-12), Santa Barbara, USA, December 2005

R. Bonadé, P. Spaetig, *The evolution of the mobile dislocation density during successive stress relaxation transients,* Proc. 14th Int. Conf. on the Strength of Materials (ICSMA14), 4-9 June 2006, Xi'an, China

A. Bortolon, A. Scarabosio, B.P. Duval, *Spontaneous plasma rotation in limited and diverted TCV ohmic discharges,* 33rd European Physical Society Conference on Plasma Physics, Rome, Italy, 19.06. - 23.06.2006

A. Bottino, P. Angelino, R. Hatzky, S. Jolliet, A.G. Peeters, E. Poli, O. Sauter, T.M. Tran, L. Villard, *Global nonlinear gyrokinetic simulations of ETG turbulence using particles,* 33rd European Physical Society Conference on Plasma Physics, Rome, Italy, 19.06. - 23.06.2006

L. Bottura, P. Bruzzone, J.B. Lister, C. Marinucci, A. Portone, *Computations of AC losses in the ITER magnetics during fast field transients,* Proc. of ASC 2006, Seattle, USA, August 2006

L. Bottura, P. Bruzzone, R. Herzog, C. Marinucci, *Simulation of the thermosyphon effect in dual channel CICC for ITER,* Proc. of CHATS-AS 2006, Berkeley, USA, September 2006

S. Brunner, R. Berger, E. Valeo, L. Divol, C. Still, *Effect of non-adiabatic electron dynamics on the non-linear evolution of ion acoustic waves,* 48th Annual Meeting of the APS Division of Plasma Physics, Philadelphia, Pennsylvania, 30.10. - 03.11.2006

P. Bruzzone, R. Bagnasco, D. Ciazynski, et al., R. Herzog, B. Stepanov, R. Wesche, *The results of two ITER TF conductor short samples using high current density Nb3Sn strands,* Proc. of ASC 2006, Seattle, USA, August 2006

P. Bruzzone, R. Herzog, B. Stepanov, M. Vogel, R. Wesche, *Test results of a large size, forced flow Nb3Sn conductor, based on a design alternative to the cable-in-conduit,* Proc. of ASC 2006, Seattle, USA, August 2006

P. Bruzzone, B. Stepanov, R. Dettwiler, F. Staehli, *Test results of contact resistance distribution in NbTi and Nb3Sn ITER conductor termination,* Proc. of ASC 2006, Seattle, USA, August 2006

P. Bruzzone, B. Stepanov, R. Wesche, M. Vogel, *Design, manufacture and first results of a novel, large size, Nb3Sn force flow conductor,* Proc. ICMC 2006, Prague, Czech Rep., July 2006

Y. Camenen, A. Pochelon, R. Behn, A. Bottino, A. Bortolon, S. Coda, A. Karpushov, O. Sauter, G. Zhuang and the TCV team, *Impact of Plasma Shaping on Electron Heat Transport in TCV L-mode Plasmas at Various Collisionalities,* 21th IAEA Fusion Energy Conference, Chengdu, China, 16.10. - 21.10.2006

R. Chavan, M. Henderson, R. Bertizzolo, J.-D. Landis, F. Sanchez, H. Shidara, *The ECH front steering launcher for the ITER upper port,* SOFT 2006, 24th Symposium on Fusion Technology, Warsaw, Poland, 11.09. - 15.09.2006

R. Chavan, R. Bertizzolo, F. Dolizy, M.A. Henderson, J.-D. Landis, G. Saibene, F. Sanchez, O. Sauter, H. Shidara, *The ITER ECH FS Upper Launcher mm-wave design,* 21th IAEA Fusion Energy Conference, Chengdu, China, 16.10. - 21.10.2006

S. Cirant, S. Alberti, R. Behn, F. Gandini F., T.P. Goodman, O. Sauter, C. Zucca, TCV team, *Modulated ECCD experiments on TCV,* 21th IAEA Fusion Energy Conference, Chengdu, China, 16.10. - 21.10.2006

J.P. Coad, P. Andrew, S.K. Erents, D.E. Hole, J. Likonen, M. Mayer, R. Pitts, M. Rubel, J. D. Strachan, E. Vainonen-Ahlgren, A. Widdowson, and JET EFDA contributors, *Erosion and Deposition in the JET Mk IISRP Divertor,* International

Conference on Plasma Surface Interactions in Controlled Fusion Devices, Hefei Anhui, China, 22.05. - 26.05.2006

S. Coda, TCV team, *The effect of ECRH on the electron velocity distribution function,* 33rd European Physical Society Conference on Plasma Physics, Rome, Italy, 19.06. - 23.06.2006

S. Coda, E. Asp, E. Fable, T.P. Goodman, O. Sauter, V.S. Udintsev, R. Behn, M.A. Henderson, A. Marinoni, G.P. Turri, C. Zucca, TCV team, *The Physics of Electron Internal Transport Barriers in the TCV Tokamak,* 21th IAEA Fusion Energy Conference, Chengdu, China, 16.10. - 21.10.2006

W.A. Cooper, M. Drevlak, M.Yu Isaev, M. Mikhailov, J. Nuehrenberg, V.D. Shafranov, A.A. Subbotin, R. Zille, *Magnetic Coils for a High-Beta Quasi-Isodynamic Stellarator,* 33rd European Physical Society Conference on Plasma Physics, Rome, Italy, 19.06. - 23.06.2006

W. A. Cooper, *Kinetic and Fluid Ballooning Stability with Anisotropic Energetic Electron Layers,* Theory of Fusion Plasmas, Varenna, Italy, 28.08. - 01.09.2006

A. Descoeudres, Ch. Hollenstein, G. Waelder, R. Demellayer, R. Perez, *Experimental characterization of electrical discharge machining plasmas,* 3rd International Workshop on Microplasmas 2006, Greifswald, Germany, 09.05. - 11.05.2006

A. Diallo, A. Fasoli, I. Furno, B. Labit, S.H. Mueller, G. Plyushchev, M. Podesta, F.M. Poli, *Excitation and detection of drift waves in the TORPEX toroidal plasma,* 48th Annual Meeting of the APS Division of Plasma Physics, Philadelphia, Pennsylvania, 30.10. - 03.11.2006

T. Eich, A. Kallenbach, S. Jachmich, P.L. Andrew, J.C. Fuchs, W. Fundamenski, A. Herrmann, R.A. Pitts, J. Neuhauser, ASDEX Upgrade Team and JET EFDA contributors, *Divertor Power Deposition and Target Current Asymmetries during Type-I ELMs in JET and ASDEX Upgrade,* International Conference on Plasma Surface Interactions in Controlled Fusion Devices, Hefei Anhui, China, 22.05. - 26.05.2006

A. Encheva, J.-M. Moret, D. Testa, R. Chavan, A. Karpouchov, Ph. Moreau, *Progress on the design of various magnetic sensors for ITER: diamagnetic and flux loops, high frequency coils, in-vessel and divertor coils, ex-vessel coils, and external Rogowskis,* 10th Meeting of the ITPA Topical Group on Diagnostics, Moskow, Russia, 10.04. - 14.04.2006

J.W. Farthing, M. Greenwald, J.B. Lister, I. Yonekawa, *The conceptual design of the ITER CODAC system,* SOFT 2006, 24th Symposium on Fusion Technology, Warsaw, Poland, 11.09. - 15.09.2006

D. Fasel, S. Alberti, T. Bonicelli, E. Droz, T. Goodman, M.-A. Henderson, J.-P. Hogge, X. LLobet, B. Marletaz, Ph. Marmillod, A. Perez, L. Porte, U. Siravo, M.Q. Tran, *Installation and commissionning of the EU test facility for ITER gyrotron,* SOFT 2006, 24th Symposium on Fusion Technology, Warsaw, Poland, 11.09. - 15.09.2006

A. Fasoli, A. Diallo, I. Furno, B. Labit, S.H. M˛ller, G. Plyushchev, M. Podesta and F.M. Poli, *Basic investigations of electrostatic fluctuations, turbulence and transport in the TORPEX toroidal plasma,* 11th EU-US Transport Task Force Workshop, Marseille, France, 04.09. - 07.09.2006

A. Fasoli for the TCV Team, *Overview of TCV Results,* 21th IAEA Fusion Energy Conference, Chengdu, China, 16.10. - 21.10.2006

L. Feitknecht, F. Freitas, C. Bucher et al., B. Strahm, A.A. Howling, L. Sansonnens, Ch. Hollenstein, *Fast growth of microcrystalline silicon solar cells on LP-CVD ZnO in industrial KAI PECVD reactors,* EPSEC Conference, Dresden, Germany, September 2006

J. Fikar, R. Schaeublin, *Molecular dynamics simulation of radiation damage in bcc tungsten,* Computer Simulation of Radiation Effects in Solids (COSIRES), Richland, Washington, USA; 18.06-23.06.2006

W. Fundamenski, R. A. Pitts, *ELM filament interaction with outboard limiters on JET and ITER,* International Conference on Plasma Surface Interactions in Controlled Fusion Devices, Hefei Anhui, China, 22.05. - 26.05.2006

I. Furno, A. Diallo, A. Fasoli, B. Labit, S.H. Mueller, G. Plyushchev, M. Podesta and F.M. Poli, *Effect of the magnetic configuration on fluctuations and turbulence in the TORPEX toroidal plasma,* 11th EU-US Transport Task Force Workshop, Marseille, France, 04.09. - 07.09.2006

G. Gantenbein, S. Alberti, A. Arnold et al., J.-P. Hogge, M.Q. Tran, *Experimental results of the 1-MW, 140-GHz, CW gyrotron for W7-X,* 21th IAEA Fusion Energy Conference, Chengdu, China, 16.10. - 21.10.2006

O.E. Garcia, R.A. Pitts, J. Horacek, A.H. Nielsen, W. Fundamenski, J.P. Graves, V. Naulin, J.J. Rasmussen, *Turbulent transport in the TCV SOL,* International Conference on Plasma Surface Interactions in Controlled Fusion Devices, Hefei Anhui, China, 22.05. - 26.05.2006

D.S. Gelles, G.R. Odette, P. Spaetig, J.W. Rensman, *Examination of crack tip microstructures in F82H on the lower shelf,* Proc. 12th Int. Conference on Fusion Reactor Materials (ICFRM-12), Santa Barbara, USA, December 2005

T.P. Goodman, I. Kimanov, A. Mueck, V.S. Udintsev O. Sauter and the TCV Team, *First measurements of oblique ECE with a real-time moveable line-of-sight on TCV,* EC - 14, 14th Joint Workshop on Electron Cyclotron Emission and Electron Cyclotron Resonance Heating, Santorini island, Greece, 09.05. - 12.05.2006

J. P. Graves, S. Coda, W. A. Cooper, L.-G. Eriksson, T. Johnson and JET-EFDA Contributors, *Modelling ICCD Experiments for Sawtooth Control in JET,* Theory of Fusion Plasmas, Varenna, Italy, 28.08. - 01.09.2006

B. Gulejova, R. A. Pitts, M. Wischmeier, R. Behn, D. Coster, J. Horacek, J. Marki, *SOLPS5 modelling of ELMing H-mode on TCV,* International Conference on Plasma Surface Interactions in Controlled Fusion Devices, Hefei Anhui, China, 22.05. - 26.05.2006

S. Hacquin, et al., D. Testa, *X-mode reflectometry measurements in the JET plasma core region,* 16th HTPD Topical conference on High Temperature Plasma Diagnostics, Williamsburg, USA, 07-11 May 2006

S.M. Hafez Haghighat, R. Schaeublin, *Molecular dynamics modeling of cavity strengthening in irradiated iron,* MMM Multiscale Materials Modeling, 3rd Int. Conference, Freiburg, Germany, 18.09. - 22.09.2006

R.W. Harvey, J.R. Cary, G. Taylor, D.C. Barnes, T.S. Bigelow, S. Coda, J. Carlsson, J.B. Caughman, M.D. Carter, S. Diem, P.C. Efthimion, R.A. Ellis, N.M. Ershov, R.J. Fonck, E. Fredd, G.D. Garstka, J. Hosea, F. Jaeger et al., *Electron Bernstein Wave Studies: Emission and Absorption with Nonthermal*

Distributions; Current Drive; Delta-F Particle in Cell Simulations, 21th IAEA Fusion Energy Conference, Chengdu, China, 16.10. - 21.10.2006

M.A. Henderson, G. Ramponi, D. Campbell, R. Chavan, D. Farina, E. Poli, G. Saibene, K. Sakamoto, O. Sauter, A. Serikov, H. Shidara, K. Takahashi, H. Zohm, *Synergy study of the Equatorial and Upper port ITER ECH Launchers for an enhanced Physics Performance,* EC - 14, 14th Joint Workshop on Electron Cyclotron Emission and Electron Cyclotron Resonance Heating, Santorini island, Greece, 09.05. - 12.05.2006

M.A. Henderson, R. Chavan, R. Bertizzolo, D. Campbell, I. Danilov, F. Dolizy, D. Farina, K. Kleefeldt, R. Heidinger, J.-D. Landis, E. Poli, G. Ramponi, G. Saibene, F. Sanchez, O. Sauter, A. Serikov, H. Shidara, P. Spaeh, H. Zohm, *The ITER ECH FS Launcher design for an optimized Physics Performance,* EC - 14, 14th Joint Workshop on Electron Cyclotron Emission and Electron Cyclotron Resonance Heating, Santorini island, Greece, 09.05. - 12.05.2006

M.A. Henderson, et al., *EU Developments of the ITER ECRH System,* SOFT 2006, 24th Symposium on Fusion Technology, Warsaw, Poland, 11.09. - 15.09.2006

M.A. Henderson, D. Campbell, R. Chavan, D. Farina, E. Poli, G. Ramponi, G. Saibene, O. Sauter, H. Shidara, H. Zohm, C. Zucca, *An Enhanced ITER ECH Upper Port Launcher for an Extended Physics Programme,* 21th IAEA Fusion Energy Conference, Chengdu, China, 16.10. - 21.10.2006

M.A. Henderson, R. Chavan, R. Bertizzolo et al., *The ITER ECH FS Upper Launcher mm-wave Design based on a Synergy Study with the Equatorial Launcher,* 21th IAEA Fusion Energy Conference, Chengdu, China, 16.10. - 21.10.2006

J. Horacek, O.E. Garcia, R.A. Pitts, W. Fundamenski, J.P. Graves, V. Naulin, A.H. Nielsen, Juul J. Rasmussen, *On the origin of anomalous radial transport in the tokamak SOL,* 21th IAEA Fusion Energy Conference, Chengdu, China, 16.10. - 21.10.2006

G.T.A. Huysmans, L. Appel, A. Bécoulet, B. Guillerminet, C. Konz, H. Leggate, J.B. Lister, H. Luetjens, P.J. Mc Carthy, M.F.F. Nave, O. Sauter, E.R. Solano, P. Strand, E. Strumberger, L. Villard, W. Zwingmann and EFDA contributors, *Integrated tokamak modeling taskforce: the integrated modeling project on equilibrium and linear MHD stability,* 33rd European Physical Society Conference on Plasma Physics, Rome, Italy, 19.06. - 23.06.2006

Y. Idomura, M. Ida, S. Tokuda, L. Villard, *Conservative gyrokinetic Vlasov simulation using Morinishi scheme,* 33rd European Physical Society Conference on Plasma Physics, Rome, Italy, 19.06. - 23.06.2006

S. Jachmich, T. Eich, W. Fundamenski, A. Kallenbach, R. A. Pitts, and JET EFDA contributors, *Divertor Particle and Power Deposition Profiles in JET ELMy H-Mode Discharges,* International Conference on Plasma Surface Interactions in Controlled Fusion Devices, Hefei Anhui, China, 22.05. - 26.05.2006

S. Jolliet, A. Bottino, P. Angelino, T.M. Tran, B.F. McMillan, R. Hatzky, A.G. Peeters, E. Poli, O. Sauter and L. Villard, *Ion and Electron Dynamics in Nonlinear PIC simulations,* Theory of Fusion Plasmas, Varenna, Italy, 28.08. - 01.09.2006

M. Jucker, Zh.A. Andrushchenko, V.P. Pavlenko, *Large scale magnetic field structures in nonuniform unmagnetized plasma,* 33rd European Physical Society Conference on Plasma Physics, Rome, Italy, 19.06. - 23.06.2006

A.N. Karpushov, B.P. Duval, T.P. Goodman, Ch. Schlatter, *Non-Maxwellian Ion Energy Distribution in ECH-heated plasmas on TCV,* 33rd European Physical Society Conference on Plasma Physics, Rome, Italy, 19.06. - 23.06.2006

S.H. Kim, J-F. Artaud, V. Basiuk, V. Dokouka, R.R. Khayrutdinov, J.B. Lister, V.E. Lukash, *Free-boundary simulation of ITER hybrid scenario,* 48th Annual Meeting of the APS Division of Plasma Physics, Philadelphia, Pennsylvania, 30.10. - 03.11.2006

A. Kirschner, V. Philipps, M. Balden, X. Bonnin, S. Brezinsek, J.P. Coad, D. Coster, S.K. Erents, H.G. Esser, W. Fundamenski, A. Huber, J. Likonen, H. Maier, G.F. Matthews, M. Mayer, R.A. Pitts, M. Roedig, M.J. Rubel, U. Samm, *Material erosion and redeposition during the JET MkIIGB-SRP divertor campaign,* 21th IAEA Fusion Energy Conference, Chengdu, China, 16.10. - 21.10.2006

A. Klein, D. Testa, A. Fasoli, J. Snipes, *Active MHD spectroscopy at JET,* 48th Annual Meeting of the APS Division of Plasma Physics, Philadelphia, Pennsylvania, 30.10. - 03.11.2006

B. Labit, A. Fasoli, A. Diallo, I. Furno, S.H. Müller, G. Plyushchev, M. Podesta and F.M. Poli, *Local statistical properties of electrostatic fluctuations in the TORPEX experiment,* 33rd European Physical Society Conference on Plasma Physics, Rome, Italy, 19.06. - 23.06.2006

J.-D. Landis, R. Chavan, R. Bertizzolo, M. Henderson, F. Sanchez, *Design of the critical components in the ITER ECH upper launcher steering mechanism,* SOFT 2006, 24th Symposium on Fusion Technology, Warsaw, Poland, 11.09. - 15.09.2006

X. Lapillonne, M. Brunetti, S. Brunner, T.-M. Tran, *Development of a Grid-Based Gyro-Kinetic Simulation Code,* Theory of Fusion Plasmas, Varenna, Italy, 28.08. - 01.09.2006

X. Lapillonne, M. Brunetti, T.-M. Tran, S. Brunner, *Development of a grid-based gyro-kinetic simulation code,* 48th Annual Meeting of the APS Division of Plasma Physics, Philadelphia, Pennsylvania, 30.10. - 03.11.2006

P. Libeyre, D. Ciazynski, P. Decool, et al., P. Bruzzone, *New results and remaining issues in superconducting magnets for ITER and associated R&D in Europe,* 21th IAEA Fusion Energy Conference, Chengdu, China, 16.10. - 21.10.2006

Y. Liu, J.B. Lister, *Oprimization of Sensor Signals for Resistive Wall Mode Control in ITER,* 21th IAEA Fusion Energy Conference, Chengdu, China, 16.10. - 21.10.2006

A. Loarte, G. Saibene, R. Sartori, D. Campbell, V. Riccardo, P. Andrew, G.F. Matthews, J. Paley, W. Fundamenski, T. Eich, A. Herrmann, G. Pautasso, A. Kirk, G. Counsell, G. Federici, G. Strohmayer, M. Merola, K.H. Finken, J. Linke, *ELMs and disruptions in ITER: Expected Energy Fluxes on Plasma Facing Components from Multi-machine Experimental Extrapolations and Consequences for ITER Operation,* 21th IAEA Fusion Energy Conference, Chengdu, China, 16.10. - 21.10.2006

A. Loarte, G. Saibene, R. Sartori, V. Riccardo, P. Andrew, J. Paley, W. Fundamenski, T. Eich, A. Herrmann, G. Pautasso, A. Kirk, G. Counsell, G. Federici, K.H. Finken, G. Maddaluno, D. Whyte, A. Leonard, M. Fenstermacher, R.A. Pitts, *Transient heat loads in current fusion experiments, extrapolation to next step devices and consequences for their operation,* 11th

International Workshop on Plasma-Facing Materials and Components for Fusion Applications, Greifswald, Germany, 10.10. - 12.10.2006

G.E. Lucas, G.R. Odette, H. Matsui, A. Moeslang, P. Spaetig, J. Rensman, *The role of small specimen test technology in fusion materials development,* Proc. 12th Int. Conference on Fusion Reactor Materials (ICFRM-12), Santa Barbara, USA, December 2005

V.E. Lukash, J-F. Artaud, V. Basiuk, V. Dokouka, R.R. Khayrutdinov, S.H. Kim, J.B. Lister, *Progress on Combined DINA-CH and CRONOS Simulator,* 33rd European Physical Society Conference on Plasma Physics, Rome, Italy, 19.06. - 23.06.2006

P. Maget, F. Imbeaux, G. Giruzzi, V.S. Udintsev, et al, *MHD issues in Tore Supra steady-state fully non-inductive scenario,* 21th IAEA Fusion Energy Conference, Chengdu, China, 16.10. - 21.10.2006

A. Marinoni, S. Coda, R. Chavan, G. Pochon, *Design of a tangential Phase Contrast Imaging diagnostic for the TCV tokamak,* 16th Topical Conference on High-Temperature Plasma Diagnostics, Williamsburg, Virginia, 07.05. - 11.05.2006

C. Marinucci, L. Bottura, P. Bruzzone, B. Stepanov, *Analysis of the transverse heat transfer coefficients in a dual channel ITER-type cable-in-conduit conductor,* Proc. of CHATS-AS 2006, Seattle, USA, August 2006

J. Marki, R.A. Pitts, T. Eich, A. Herrmann, J. Horacek, F. Sanchez, G. Veres, *Sheath heat transmission factors on TCV,* International Conference on Plasma Surface Interactions in Controlled Fusion Devices, Hefei Anhui, China, 22.05. - 26.05.2006

A.A. Martynov, S. Yu. Medvedev, L. Villard, *Axisymmetric Mode Stability in Tokamaks with Reversed Current Density,* 33rd European Physical Society Conference on Plasma Physics, Rome, Italy, 19.06. - 23.06.2006

S. Yu Medvedev, A.A. Ivanov, A.A. Martynov, Yu.Yu. Poshekhonov, R. Behn, S.H. Kim, J.B. Lister, Y.R. Martin, O. Sauter, L. Villard R.R. Khayrutdinov, *Edge Stability of TCV Plasma,* 33rd European Physical Society Conference on Plasma Physics, Rome, Italy, 19.06. - 23.06.2006

N. Mellet, P. Popovich, W.A. Cooper, L. Villard and S. Brunner, *Three-dimensional warm plasma simulations for low-frequency waves,* Theory of Fusion Plasmas, Varenna, Italy, 28.08. - 01.09.2006

M.I. Mikhailov, M.Yu. Isaev, A.A. Subbotin, V.D. Shafranov, C. Nuehrenberg, J. Nuehrenberg. R. Zille, A. Cooper, *Quasi-isodynamic Configuration with N=12 and High beta,* Theory of Fusion Plasmas, Varenna, Italy, 28.08. - 01.09.2006

A. Mueck, Y. Camenen, S. Coda, L. Curchod, T.P. Goodman, H.P. Laqua, A. Pochelon, TCV Team, *Electron Bernstein Wave Heating in the TCV Tokamak,* EC - 14, 14th Joint Workshop on Electron Cyclotron Emission and Electron Cyclotron Resonance Heating, Santorini island, Greece, 09.05. - 12.05.2006

A. Mueck, Y. Camenen, S. Coda, L. Curchod, T.P. Goodman, H.P. Laqua, K. Mason, R. Patterson, A. Pochelon, L. Porte, V. Udintsev, *Electron Bernstein Wave Heating and Emission in the TCV Tokamak,* 33rd European Physical Society Conference on Plasma Physics, Rome, Italy, 19.06. - 23.06.2006

P. Mueller R. Bonadé P. Spaetig, *Fracture Properties of Notched and Pre-Cracked Specimens of a Tempered Martensitic Steel at Low Temperature,* 14th International Conference on the Strength of Materials (ICSMA14), 4-9 June 2006, Xi'an, China

S.H. Mueller, A. Fasoli, A. Diallo, I. Furno, B. Labit, G. Plyushchev, M. Podesta, F.M. Poli, *Real space statistical characterization of turbulence and transport in the TORPEX experiment,* 33rd European Physical Society Conference on Plasma Physics, Rome, Italy, 19.06. - 23.06.2006

S. Pavon, J.-L. Dorier, Ch. Hollenstein, P. Ott, P. Leyland, *Effect of transonic airflows on a dielectric barrier discharge,* Gordon Research Conference on Processing Plasmas, July 16-21, 2006, Mount Holyoke College, South Hadley, MA, USA

R.A. Pitts, J. Horacek, W. Fundamenski, A.H. Nielsen, O.E. Garcia, V. Naulin, J.J. Rasmussen, M. Wischmeier, *Parallel flow in TCV,* International Conference on Plasma Surface Interactions in Controlled Fusion Devices, Hefei Anhui, China, 22.05. - 26.05.2006

R.A. Pitts, W. Fundamenski, P. Andrew, G. Arnoux, X. Bonnin, D. Coster, T. Eich, E. Gauthier, A. Huber, S. Jachmich, J. S. Loennroth, C. Silva, F. Subba, D. Tskhakaya and JET EFDA Contributors, *ELM transport in the JET scrape-off layer,* 21th IAEA Fusion Energy Conference, Chengdu, China, 16.10. - 21.10.2006

R.A. Pitts, P. Andrew, G. Arnoux, T. Eich, W. Fundamenski, E. Gauthier, A. Huber, S. Jachmich, C. Silva, D. Tskhakaya, and JET EFDA Contributors, *ELM Transport in the JET Scrape-Off Layer,* 21th IAEA Fusion Energy Conference, Chengdu, China, 16.10. - 21.10.2006

G. Plyushchev, H. Boehmer, A. Diallo, A. Fasoli, I. Furno, W.W. Heidbrink, B. Labit, S.H. Mueller, M. Podesta, F.M. Poli, Y. Zhang, *A new fast ion source and detector for investigating the interaction of turbulence with supra-thermal ions in a simple magnetized toroidal plasma,* 33rd European Physical Society Conference on Plasma Physics, Rome, Italy, 19.06. - 23.06.2006

G. Plyushchev, H. Boehmer, A. Diallo, A. Fasoli, I. Furno, W.W. Heidbrink, B. Labit, S.H. Mueller, M. Podesta, F.M. Poli Y. Zhang, *A new fast ion source and detector for investigating the interaction of turbulence with supra-thermal ions in a simple magnetized toroidal plasma.,* 16th Topical Conference on High-Temperature Plasma Diagnostics, Williamsburg, Virginia, 07.05. - 11.05.2006

A. Pochelon, A. Mueck, Y. Camenen, S. Coda, L. Curchod, B.P. Duval, T.P. Goodman, I. Klimanov, H. Laqua, Y. Martin, J.-M. Moret, L. Porte, A. Sushkov, V.S. Udintsev, F. Volpe and the TCV Team, *Electron Bernstein Wave Heating of Overdense H-mode Plasmas in the TCV Tokamak via O-X-B Double Mode Conversion,* 21th IAEA Fusion Energy Conference, Chengdu, China, 16.10. - 21.10.2006

M. Podesta, A. Diallo, A. Fasoli, I. Furno, B. Labit, S.H. Mueller, G. Plyushchev, F.M. Poli, *Experimental studies of particle transport in the TORPEX toroidal plasma,* 48th Annual Meeting of the APS Division of Plasma Physics, Philadelphia, Pennsylvania, 30.10. - 03.11.2006

F.M. Poli, A. Diallo, A. Fasoli, I. Furno, B. Labit, S.H. Mueller, G. Pliushchev, M. Podesta, *Linear and nonlinear drift-interchange instabilities in the TORPEX toroidal plasma,* 11th EU-US Transport Task Force Workshop, Marseille, France, 04.09. - 07.09.2006

L. Porte, S. Coda, S. Alberti, G. Arnoux, P. Blanchard, A. Bortolon, A. Fasoli, T.P. Goodman, I. Klimanov, Y. Martin, M. Maslov, A. Scarabosio, H. Weisen, *Plasma Dynamics with Second and Third Harmonic ECRH on TCV Tokamak,* 21th IAEA Fusion Energy Conference, Chengdu, China, 16.10. - 21.10.2006

A. Ramar, N. Baluc, R. Schaeublin, *effect of irradiation on the microstructure and the mechanical properties of oxide dispersion strenghtened EUROFER 97 steel,* Proc. 12th Int. Conference on Fusion Reactor Materials (ICFRM-12), Santa Barbara, USA, December 2005

J. E. Rice, A. Ince-Cushman, J. S. deGrassie, L.-G. Eriksson, Y. Sakamoto, A.Scarabosio, A. Bortolon, K. H. Burrell, C. Fenzi-Bonizec, M. J. Greenwald, R. J.Groebner, G. T. Hoang, Y. Koide, E. S. Marmar, A. Pochelon and Y. Podpaly, *Inter-Machine Comparison of Intrinsic Toroidal Rotation,* 21th IAEA Fusion Energy Conference, Chengdu, China, 16.10. - 21.10.2006

M.J. Rubel, J.P. Coad, R.A. Pitts, R. Dejarnac, J.P. Gunn, R. Panek, and JET EFDA Contributors, *Overview of Co-deposition and Fuel Inventory in Castellated Structures at JET,* 21th IAEA Fusion Energy Conference, Chengdu, China, 16.10. - 21.10.2006

K. Rummel, M. Czerwinski, et al., P. Bruzzone, B. Stepanov, M. Vogel, *Test results from the full size prototype test of W7-X joint,* SOFT 2006, 24th Symposium on Fusion Technology, Warsaw, Poland, 11.09. - 15.09.2006

L. Sansonnens, H. Schmidt, A.A. Howling, Ch. Hollenstein, Ch. Ellert, A. Buechel, *Application of the shaped electrode technique to a large area rectangular capacitively-coupled plasma reactor to suppress standing wave nonuniformity,* AVS Conference, November 2005 (ID 749, PS-ThA2)

O. Sauter, M.A. Henderson, H. Zohm, C. Zucca, *Partial Stabilization and Control of Neoclassical Tearing Modes in Burning Plasmas,* 21th IAEA Fusion Energy Conference, Chengdu, China, 16.10. - 21.10.2006

A. Scarabosio, A. Bortolon, B.P. Duval, A. Pochelon, *Comparison of MHD-mode and Plasma Rotation Frequencies in TCV Ohmic and ECH Discharges,* 33rd European Physical Society Conference on Plasma Physics, Rome, Italy, 19.06. - 23.06.2006

R. Schaeublin, N. Baluc, *Radiation damage in Ferritic/Martensitic steels for fusion reactors: a simulation point of view,* 21th IAEA Fusion Energy Conference, Chengdu, China, 16.10. - 21.10.2006

R. Schaeublin, S. M. Hafez Haghighat, Y.L. Chiu, *Effet de l'hélium sur le durcissement induit par irradiation dans le Fe,* Colloque Plasticité 2006, Sévrier (Annecy), France, 27.03-29.03.2006

R. Schaeublin, Y. L. Chiu, *Effect of helium on irradiation-induced hardening of iron: A simulation point of view,* European Materials Research Society conference (E-MRS), Nice, France, 29.05-02.06.2006

R. Schaeublin, G. Yu, A. Harjunmaa, G. Drudis Solé, *Nanometric defects in Fe in Transmission Electron Microscopy,* International Microscopy Conference (IMC-16), Sapporo, Japan, 03.09-08.09.2006

Ch. Schlatter, B.P. Duval, A.N. Karpushov, E. Asp, S. Coda, V.S. Udintsev, *Conditions for anomalous energy and momentum transfer from electrons to ions in ECCD discharges on TCV,* 33rd European Physical Society Conference on Plasma Physics, Rome, Italy, 19.06. - 23.06.2006

S.E. Sharapov, B. Alper, V.G. Kiptily, S. Hacquin, Ch. Schlatter et al, *Energetic Ion-driven instabilities on JET and on MAST,* 48th Annual Meeting of the APS Division of Plasma Physics, Philadelphia, Pennsylvania, 30.10. - 03.11.2006

H. Shidara, M.A. Henderson, R. Chavan, D. Farina, E. Poli, G. Ramponi, *ECRH beam Optics optimization for ITER upper port launcher,* EC - 14, 14th Joint

Workshop on Electron Cyclotron Emission and Electron Cyclotron Resonance Heating, Santorini island, Greece, 09.05. - 12.05.2006

J.-W. Shin, H. Miyazoe, M. Leparoux, S. Siegmann, J.-L. Dorier, Ch. Hollenstein, *In-situ process monitoring for plasma synthesis of alumina nanoparticles,* 5th World Congress on Particle Technology, April 23-27, 2006 Orlando, Florida, USA

P. Spaetig, R. Bonadé, G.R. Odette, J.W. Rensman, N. Campitelli, P. Mueller, *Plastic flow properties and fracture toughness characterization in the low transition of unirradiated and irradiated tempered martensitic steels,* Proc. 12th Int. Conference on Fusion Reactor Materials (ICFRM-12), Santa Barbara, USA, December 2005

J.D. Strachan, J. P. Coad, G. Corrigan, J. Spence, G. F. Matthews, J. Likonen, M. Rubel, R. A. Pitts, A. Kirschner, A. Kallenbach, and JET EFDA contributors, *Carbon Migration during JET 13C Injection Experiments,* 48th Annual Meeting of the APS Division of Plasma Physics, Philadelphia, Pennsylvania, 30.10. - 03.11.2006

G. De Temmerman, R.A. Pitts, V.S. Voitsenya, L. Marot, M. Maurer, P. Oelhafen, *First mirror tests for ITER: influence of material choice on the deposition/ erosion mechanisms affecting optical reflectivity,* International Conference on Plasma Surface Interactions in Controlled Fusion Devices, Hefei Anhui, China, 22.05. - 26.05.2006

G. Turri, O. Sauter, A. Scarabosio, V.S. Udintsev, I. Furno, C. Zucca, T.P. Goodman, *Towards q-profile reconstruction through fast-MHD analysis on TCV,* 33rd European Physical Society Conference on Plasma Physics, Rome, Italy, 19.06. - 23.06.2006

V.S. Udintsev et al, *Progress in ECE diagnostics development on TCV,* EC - 14, 14th Joint Workshop on Electron Cyclotron Emission and Electron Cyclotron Resonance Heating, Santorini island, Greece, 09.05. - 12.05.2006

V.S. Udintsev, T.P. Goodman, G.P. Turri, S. Coda, et al, *Oscillations of Electron Temperature and Their Interplay with MHD in the Presence of Internal Transport Barriers on TCV,* 33rd European Physical Society Conference on Plasma Physics, Rome, Italy, 19.06. - 23.06.2006

V.S. Udintsev, T.P. Goodman, G.P. Turri, O. Sauter, E. Asp, S. Coda, E. Fable, I. Klimanov, A. Mueck, R. Patterson, A. Pochelon, H. Weisen, G. Giruzzi, F. Turco, TCV team, *Oscillations of Electron Temperature and Their Interplay with MHD in the Presence of Internal Transport Barriers on TCV,* 33rd European Physical Society Conference on Plasma Physics, Rome, Italy, 19.06. - 23.06.2006

G. Veres, R.A. Pitts, M. Wischmeier, B. Gulejova, J. Horacek, S. Kalvin, *Radiation distributions in TCV,* International Conference on Plasma Surface Interactions in Controlled Fusion Devices, Hefei Anhui, China, 22.05. - 26.05.2006

L. Villard, P. Angelino, A. Bottino, R. Hatzky, S. Jolliet, B.F. McMillan, O. Sauter, T.M. Tran, *Plasma Shape Effects on Geodesic Acoustic Oscillations,* Theory of Fusion Plasmas, Varenna, Italy, 28.08. - 01.09.2006

H. Weisen, P.J. Paris, *ITER und der Weg zur Nutzung der Fusionsenergie,* Internationale Fachtagung "Europas Energieszenario der Zukunft", Gemeinschaftstagung der Energietechnischen Gesellschaften der Electrosuisse, des VDE und des OVE, Salzburg, 8/9 November 2006

H. Weisen, M. Maslov, A. Zabolotsky, L. Porte, C. Angioni, M. Beurskens, TCV team and JET-EFDA contributors, *Density peaking in TCV and JET H-modes,* 33rd

European Physical Society Conference on Plasma Physics, Rome, Italy, 19.06. - 23.06.2006

H. Weisen, A. Zabolotsky, M. Maslov, M. Bernard, A. Bortolon, B.P. Duval, E. Fable, A. Karpushov, O. Sauter, V. Piffl, Ch. Schlatter, G. Veres, *Particle and impurity transport in electron-heated discharges in TCV,* 21th IAEA Fusion Energy Conference, Chengdu, China, 16.10. - 21.10.2006

H. Weisen, C. Angioni, M. Maslov et al, *Peaked Density Profiles in Low Collisionality H-modes in JET, ASDEX Upgrade and TCV,* 21th IAEA Fusion Energy Conference, Chengdu, China, 16.10. - 21.10.2006

R. Wesche, F. Roth, P. Bruzzone, *Comparison of the dc performance of various Nb3Sn strands used in cable-in-conduit for fusion,* Proc. of ICMC 2006, Praha, Czech Rep., July 2006

R. Wesche, R. Heller, P. Bruzzone, W.H. Fietz, A. Vostner, *Design of high-temperature superconductor current leads for ITER,* SOFT 2006, 24th Symposium on Fusion Technology, Warsaw, Poland, 11.09. - 15.09.2006

A. Zabolotsky, M. Bernard, V. Piffl, H. Weisen, A. Bortolon, B.P. Duval, A. Karpushov, *Carbon transport in TCV,* 33rd European Physical Society Conference on Plasma Physics, Rome, Italy, 19.06. - 23.06.2006

A. Zabolotsky, M. Bernard, A. Bortolon, B.P. Duval , E. Fable, A. Karpushov, M. Maslov, O. Sauter, V. Piffl, Ch. Schlatter, G. Veres, H. Weisen, *Particle and Impurity Transport in Electron-Heated Discharges in TCV,* 21th IAEA Fusion Energy Conference, Chengdu, China, 16.10. - 21.10.2006

F.S. Zaitsev, et al., D. Testa, *Simulation of deuteron tails produced by close collisions with ICRH accelerated He3 ions in JET,* 33rd European Physical Society Conference on Plasma Physics, Rome, Italy, 19.06. - 23.06.2006

L. Zani, D. Ciazynski, B. Stepanov, R. Dettwiler, F. Roth, *Analysis of critical electrical properties and current distribution of the first two full size conductor samples using Nb3Sn advanced strands developed for ITER,* Proc. of ASC 2006, Seattle, USA, August 2006

R. Zanino, L. Savoldi Richard, F. Bellina, P. Bruzzone, N. Mitchell, P.L. Ribani, *Assessment of the effect of current non-uniformity on the Nb3Sn good joint short sample DC performance,* Proc. of ASC 2006, Seattle, USA, August 2006

R. Zanino, M. Astrov, R. Bagnasco, et al., R. Wesche, *The ITER poloidal field conductor insert (PFCI) test program and predictive analysis,* Proc. of ASC 2006, Seattle, USA, August 2006

M.K. Zedda, D. Testa, Cannas B., Fanni A., Piccolo F., Sartori F., Sonato P., *A new approach for the development of disruption protection-avoidance tools for JET,* SOFT 2006, 24th Symposium on Fusion Technology, Warsaw, Poland, 11.09. - 15.09.2006

C. Zucca, S. Alberti, R. Behn, S. Cirant, E. Fable, F. Gandini, T.P. Goodman, O. Sauter, *Studies of Electron Transport and Current Diffusion in Switched ECCD experiments on TCV,* 33rd European Physical Society Conference on Plasma Physics, Rome, Italy, 19.06. - 23.06.2006

C. Zucca, O. Sauter, S. Alberti, T.P. Goodman, S. Cirant, R. Behn, E. Fable, F. Gandini, *Studies of Electron Transport and Current Diffusion in Switched ECCD experiments on TCV,* 33rd European Physical Society Conference on Plasma Physics, Rome, Italy, 19.06. - 23.06.2006

B.2 Seminars presented at the CRPP in 2006

Dr. C. Angioni, Max-Planck-Institut für Plasmaphysik, Garching, Germany, *"Direction of impurity pinch and auxiliary heating in tokamak plasmas"*

M. Jucker, Dept. of Space Physics and Astronomy, Uppsala Univ., Sweden, *"Self-consistent model of magnetic electron drift wave turbulence"*

J. Kim, Korea Advanced Inst. Of Science and Technology, Dept. of Physics, Daejeon, Korea, *"R&D activities of soft X-ray array diagnostics for KSTAR"*

Dr. M. Peres Alonso, Univ. Técnica de Lisboa, Inst. Superior Técnico, Centro de Fusao Nuclear, Portugal, *"A review of Thomson scattering diagnostics"*

Dr. A. Vostner, EFDA, Close Support Unit Garching, Germany, *"The ITER high amperage cable in conduit conductors"*

A. Eivani, Dept. of Materials Science and Engineering, Sharif Univ. of Technology, Tehran, Iran, *"Strengthening of an Al-Mg-Si-Cu alloy using equal channel angular extrusion and precipitation hardening"*

Dr. I. Klimanov, CRPP-EPFL, Switzerland *"Reconstruction of the electron distribution function during ECRH/ECCD and magnetic reconnection events in a tokamak plasma"*

Prof. O.F.J. Martin, Nanophotonics & Metrology Lab. EPFL, Switzerland, *"Negative refraction: revisiting electromagnetics from microwave to optics"*

Dr. V. Krivenski, Milano, Italy, *"Electron temperature measurements in the presence of non-Maxwellian bulks"*

L. Curchod, CRPP-EPFL, Switzerland, *"Electron Bernstein wave heating in TCV"*

Dr. M. Calvi, CERN, Geneva, Switzerland, *"Training quenches in the LHC superconducting dipole magnets"*

Dr. M. Endler, IPP Greifswald, Germany, *"Status of the W7-X project"*

Dr. B. McMillan, CRPP-EPFL, Switzerland, *"Global kinetic ballooning modes in Stellarators"*

Dr. G. Tynan, Univ. of California at San Diego, USA, *"Observation of turbulent-driven shear flow in a cylindrical plasma device"*

M. Bernard, CRPP-EPFL, Switzerland, *"Mesure de la charge effective et de la concentration d'impuretés dans le plasma de TCV"*

Th. Panis, National Technical Univ. of Athens, Greece, *"Steady-state fitted models for composite loads and subtransmission networks"*

P.L. Khilar, Inst. For Plasma Research, Bhat, Gujarat, India, *"Power supply system for RF systems of SST-1"*

Dr. W.A. Cooper, CRPP-EPFL, Switzerland, *"Relativistic guiding centre drifts in anisotropic pressure magnetic coordinates: Hamiltonian formulation and direct verification"*

Dr. J. Horacek, CRPP-EPFL, Switzerland, *"Measurement of edge electrostatic turbulence in the TCV tokamak plasma boundary"*

F. Turco, CEA Cadarache, France, *"Localised current perturbation experiments by electron cyclotron current drive on Tore Supra"*

D. Iraji, Urmi University-Urmia, K.N. Toosi Univ. of Technology, Tehran, Iran, *"Runaway electrons in Damavand Tokamak"*

Dr. J.B. Lister, CRPP-EPFL, Switzerland, *"The conceptual design of the ITER CODAC"*

Dr. P. Romatschke, Univ. Bielefled, Germany, *"A Weibel instability in quark-gluon-plasmas"*

L. Rehorek, Inst. Of Physics of Materials, Brno, Czech Republic, *"Mechanical properties at high temperatures of a model glass matrix material reinforced with alumina platelets"*

F. Piras, Politecnico di Torino, Italy, *"Analysis of plasma control system in RFX machine"*

L.V. Veleva, IPMC-EPFL, Switzerland, *"Internal friction in C-C composites"*

J. Berrino, Univ. Milano, Italy *"A system for automatic detection and control of magnetic islands in a tokamak"*

Dr. T. Intrator, Los Alamos National Laboratory, USA, *"High pressure field reversed configuration with anomalous resistivity"*

R. Tye, ERASMUS student at EPFL, Switzerland, *"Improvement of diamagnetic measurement on TCV"*

Dr. C.A. Michael, National Inst. For Fusion Science, Toki, Japan, *"Fluctuation and particle transport studies on LHD with 2d phase contrast imaging"*

Dr. B.A. Hammel, Lawrence Livermore National Laboratory, USA, *"The NIF ignition program: progess and planning"*

A. Hasnaoui, CNRS, Université de Bourgogne, France, *"Structure and growth of thin passive oxide films on aluminium surfaces at low temperatures - Variable-charge molecular dynamics simulations"*

G. Lucas, Laboratoire de Métallurgie Physique, Univ. de Poitiers, France, *"Ab initio molecular dynamics determination of threshold displacement energy in silicon carbide and recombination"*

Dr. A. Bottino, Max-Planck-Institut für Plasmaphysik, Garching, Germany, *"Global nonlinear simulations of ETG turbulence using particles"*

Dr. H. Sugama, National Institute for Fusion Science, Toki, Japan, *"Gyrokinetic studies of plasma turbulence and zonal flows in tokamaks and helical systems"*

Dr. J. Jin, Forschungszentrum Karlsruhe, Germany, *"Quasi-optical mode converter for high power gyrotron"*

F. Militello, Univ. of Texas at Austin, USA, *"Interaction between magnetic island and electrostatic turbulence"*

P. Colsters, CRPP-EPFL (exchange student), Switzerland, *"Time-resolved study of SiH4/H2 plasma ignition"*

S. Mueller, CRPP-EPFL, Switzerland, *"Turbulence in basic toroidal plasmas"*

Dr. I. Pagonakis, CRPP-EPFL, *"Electron beam numerical simulation"*

F. Felici, Techn. Univ. Delft, NL, *"System identification, subspace methods and applications in plasma modelling"*

B. Legradic, Inst. für Allgemeine Physik, Vienna Univ., Austria, *"Plasma parameters and electron energy distribution functions of inductively coupled low-pressure argon plasmas in simulation and Langmuir-probe measurements"*

M. Ricci, Univ. of Bari, Italy, *"Deposition of silicon nitride and oxynitride thin films from plasmas fed by dimethylaminosilanes"*

Y. Camenen, CRPP-EPFL, *"Electron heat transport studies in TCV"*

Dr. O.E. Garcia, Risö National Lab., Denmark, *"Radial interchange motions of plasma filaments"*

Dr. X. Bonnin, Lab. d'ing. des Matériaux et des Hautes Pressions, Univ. Paris, France, *"Carbon dust growth in plasmas: experiment and modelling"*

Dr. P. Angelino, CRPP-EPFL, *"The role of the electric field in simulations of plasma microturbulence"*

Dr. A. Scarabosio, CRPP-EPFL, *"Stability and toroidal rotation properties of highly shaped plasmas in the TCV tokamak"*

Prof. H. Keppner, HE-Arc, Le Locle, Switzerland, *"Spectacle plasma"*

B.3 Other external presentations in 2006

N. Baluc, *EMPA, Duebendorf, Switzerland, 15 Jan 2006,* "Materials for fusion reactors"

N. Baluc, *IRA, Lausanne, Switzerland, 15 Mar 2006,* "Materials for fusion reactors"

N. Baluc, *ETH-Zuerich, Switzerland, 15 May 2006,* "Effects of radiation on Metals and Alloys, Day in honor of Prof. G. Kostorz"

N. Baluc, *EPF-Lausanne, Switzerland, 20 May 2006,* "Materials: A key issue on the path to fusion pwer reactors, Day in honor of Dr. R. Gotthard"

M. Brunetti, X. Lapillonne, S. Brunner, T.M. Tran, *Colloque numérique EPF-Lausanne, Switzerland, 01 Apr 2006,* "Comparison of Semi-Lagrangian and Eulerian Algorithms for solving Vlasov-type equaitons"

Y. Camenen, *IPP Garching, Germany, 29 Nov 2006,* "Electron heat transport studies in TCV"

A. Fasoli, *JET, Culham, UK, 24 Feb 2006,* "Basic investigations of electrostatic turbulence and transport in a simple toroidal plasma"

A. Fasoli, *MIT, Cambridge, USA, 10 Mar 2006,* "Basic investigations of electrostatic turbulence and transport in a simple toroidal plasma"

M. Henderson et al., *US-EU-Japan Workshop "RF Heating Technology" & US-Japan Workshop "RF Heating Physics", Nara, Japan, 26 Sep 2006,* "Status of the ITER Upper Port FS Launcher"

M.A. Henderson et al., *US-EU-Japan Workshop "RF Heating Technology" & US-Japan Workshop "RF Heating Physics", Nara, Japan, 26 Sep 2006*, "Possible modifications to the ITER ECH system for enhanced performance"

S. Jolliet, *Max-Planck-Institute fuer Plasmaphysik, Garching, Germany, 01 Dec 2006,* "A global collisionless PIC code in magnetic coordinates"

J.B. Lister, *EDF/SEPTEN, Lyon, France, 06 Jun 2006,* "ITER - Rendez-vous avec un défi planétaire"

Y. Martin, *Yverdon, 22 Nov 2006,* "Demain, quelles énergies? Introduction"

Y. Martin, *Yverdon, 22 Nov 2006,* "Demain, quelles énergies? Fusion I"

Y. Martin, *Yverdon, 22 Nov 2006,* "Demain, quelles énergies? Fusion II"

Y. Martin, *Yverdon, 22 Nov 2006,* "Demain, quelles énergies? Fusion III"

M.Q. Tran, *FEDRE. Forum Int. sur "La production d'énergie électrique", session 2, Geneva, Switzerland, 24 Jan 2006,* "La Fusion"

M.Q. Tran, *Energy Science Colloquia, ETH-Zentrum, Zuerich, Switzerland, 15 Jun 2006,* "The role and challenges of ITER within the future fusion program"

M.Q. Tran, *Univ. Zuerich-Irchel, Zuerich, Switzerland, 03 May 2006,* "ITER: its physics and technologyical challenges and role in the roadmap towards a fusion reactor"

M.Q. Tran, *Alstom (Switzerland) Ltd, Birr, Switzerland, 09 Sep 2006*, "Fusion, a challenge for high technology"

M.Q. Tran, *Energieforum "Life needs power", Hannover Messe 2006, germany, 15 Jun 2006,* "Visionen in der Energietechnik"

M.Q. Tran, *Société Fribourgeoise des Sciences Naturelles, Unvi. Fribourg, Suisse, 06 Apr 2006,* "La Fusion sera-t-elle prête pour satisfaire les besoins en énergie de l'humanité?"

M.Q. Tran, The nuclear Forum in Beznau, Suisse, Oct. 2006, *"Liefermöglichkeiten für die Konstruktion des Fusionsreaktors ITER"*

M.Q. Tran, *Univ. Genève, Switzerland, 15 Nov 2006*, "ITER and the way towards a fusion reactor"

H. Weisen, P.J. Paris, *Int. Fachtagung "Europas Energieszenario der Zukunft, VDE und OVE, Salzgurg, Austria, 08 Nov 2006,* "ITER und der Weg zur Nutzung der Fusionsenergie"

APPENDIX C   External activities of CRPP Staff during 2006

C.1   National and international committees and ad-hoc groups

MEMBERSHIP

N. Baluc   Scientific and Technical Advisory Committee, Euratom
International Organizing Committee of the SOFT Conference (Symposium on Fusion Technology)
International Advisory Committee of the ICFRM Conference (International Conference on Fusion Reactor Materials)
IEA Annex II Executive Committee
IEA Fusion Materials Agreement Executive Committee
Steering Committee Association Euratom-Confederation Suisse
Steering Committee CRPP-PSI
Steering Committee PSI-CRPP on Materials for Nuclear Applications (SCMATNUC).
Swiss Society for Optics and Microscopy (SSOM)
Task Coordinator of the Euratom Task TTMS-003 entitled 'Compatibility of Steels with Hydrogen and Liquids' of the Tritium Breeding and Materials Programme of EFDA
Task Coordinator of the subproject entitled 'Radiation-Resistant Materials' of the EXTREMAT Integrated Project (IP) of the 6th European Framework Programme

P. Bruzzone   International Magnet Technology Conference Organizing Committee
ITER Magnet Expert Group
EFDA Dipole Design Advisory Group
Wendelstein 7-X Magnet Advisory Group
GSI Magnet Advisory Group

W.A. Cooper   Chairman, CSCS Large users assembly, Switzerland

J.-L. Dorier   Member of the commitee of the Swiss Vacuum Society
Member of the scientific commitee of the 7th Workshop on Frontiers in Low Temperature Plasma Diagnostics, Beverley (UK), April 2007

A. Fasoli   Visiting Professor, MIT Physics Department
Scientific and Technical Advisory Committee, Euratom
ASDEX Upgrade Programme Committee, Germany
Scientific Expert for Switzerland at Fusion Power Coordination Committee of the International Energy Agency
International Tokamak Physics Activities: MHD and Energetic Particles Topical Group
Chairman of ad-hoc group of STAC for the monitoring of 2004 activities and 2006 work program of JET
Scientific Committee, 10th IAEA Technical Meeting on Energetic Particles in Magnetic Confinement Systems, 2006
Committee for 'Bourses Ecole Doctorale', EPFL
Education Committee, EPFL FSB
President of Doctoral School Examination Committee, University of Milan, Italy
Audit Committee, Laboratory for Ion and Molecular Interactions, Université de Provence, France

Ch. Hollenstein   Expert for Deutsche Forschungsgemeinschaft (DFG) for the funding proposal 2007-2010 of the SFB591 (Sonderforschungsbereich) at the Ruhr University of Bochum

Expert for the Deutscher Wissenschaftsrat (WR) for the audit of the
Bundesanstalt fuer Materialforschung und -pruefung (BAM) in Berlin
Member of the Wissenschaftlicher Beirat Leibniz-Institut für
Oberflächenmodifizierung Leipzig
Comite d'evaluation du LASEP (Laboratoire d'analyse spectroscopique et
d'eneeretique des plasmas Universite d'Orleans Bourges
Editorial Board Plasma Chemistry and Plasma Processing Kluwer
Academic/Plenum Publisher
Member of the IUVSTA Plasma Division
President of the Swiss Vacuum society

J.B. Lister — International Tokamak Physics Activities: MHD, Disruption and Control
Topical Group
33rd EPS Conference Programme Committee, Roma 2006
34th EPS Conference Programme Committee, Warsaw 2007
Member of the STAC ad hoc group on EU modelling requirements

C. Marinucci — CHATS-AS, Board

P.J. Paris — Member of the CCEF

R.A. Pitts — Leader of the EFDA Plasma Edge Task Force
CRPP Representative of the EFDA EU Task Force on Plasma-Wall
Interactions
Member of the Diagnostic Working Group for JET EPII diagnostics.
Member of the jury for the thesis of G. De Temmerman, Université de
Basle, "On the lifetime of the First Mirrors in the diagnostic systems of the
International Thermonuclear Experimental Reactor"

A. Pochelon — Member of the Committee of the Swiss Nuclear Forum
Member of the Commission for Training and Formation of the Swiss
Nuclear Forum

O.Sauter — Scientific Committee of the 13th European Fusion Theory Conference 2007
Chairman of the scientific committee of the Joint Varenna-Lausanne
International Workshop on Theory of Fusion Plasmas
Member of ITPA on Transport Physic

R. Schäublin — Member of the board of the Swiss Society for optics and microscopy

M.Q. Tran — Director of the Inst. of Physics of Energy and Particle, EPFL
Electron Cyclotron Wave Task Area Leader
Chairman of the Electron cyclotron Wave-Coordinating Committee
Consultative Committee for the Euratom Specific Research and Training
Programme in the field of Nuclear Energy, Fusion (CCE-FU)
Chairman of the Scientific and Technical Advisory Committee, Euratom
(STAC)
Chairman of the STAC Ad'hoc Group, Phase I of Compass in Prague
Chairman of the CCE-FU Ad'hoc Group on Expenses Overrun
Member of the Ad'hoc Group on the Statutes of the European Legal Entity,
Euratom
Standing Committee of the International Symposium on Fusion Nuclear
Technology
Scientific Committee of the IAEA Technical Meeting on ECRH Physics and
Technology for ITER
Expert on the IAEA International Fusion Research Council
Chairman of the Fusion Staffing Committee created by the CCE-FU
Member of the Steering Committee of the Center of Competence on Energy
and Mobility of the the CEPF
Member of the "Strategy Committee" of the Faculty of Basic Science, EPFL
Swiss delegate at the Fusion Power Coordinating Committee

L. Villard	Scientific and Technical Advisory Committee, Euratom, member until STAC-17, observer since
	Conseil Scientifique du Département de Recherche sur la Fusion Contrôlée – CEA, France
	Member of the jury, PhD thesis, Nicolas Dubuit, Université Henri Poincaré, Nancy and CEA, Cadarache, Transport turbulent d'impuretés dans un plasma magnétisé
H. Weisen	Coordinator for particle transport at the JET Transport Task Force
	Coordinator for particle transport ('spokesperson') of the working group on partcile transport within the ITPA database and modelling workgroup
	Member of the Diagnostics Working Group within the ITPA
	Member of the ad'hoc expert group for the application for preferential support for the proposal "Enabling a programme of ITER relevant plasma studies by transferring and installing COMPASS-D to the Institute of Plasma Physics AS CR, Association EURATOM-IPP.CR".

PARTICIPATION

N. Baluc	Ah Hoc Group on 'Support measures for theory and modelling activities under EFDA'
B. Duval	Remote Participation Users Group, EFDA-JET
	33nd EPS Local Organising Committee
Y.R. Martin	International Tokamak Physics Activity: Confinement Database and Modelling Topical Group
R.A. Pitts	International Tokamak Physics Activity: SOL & Divertor Topical Group
L. Villard	Ad-Hoc Group for the assessment of an application for a Cost-Sharing Action by the Bulgarian Academy of Sciences

C.2   Editorial and society boards

S. Coda	Editorial Board of Plasma Physics and Controlled Fusion
A. Fasoli	International Tokamak Physics Activities group on MHD and Energetic Particles
Ch. Hollenstein	Editorial Board Plasma Chemistry and Plasma Processing Kluwer Academic/Plenum Publisher
J.B. Lister	Chairman of the European Physical Society Plasma Physics Division
	Deputy Editor of Plasma Physics and Controlled Fusion
Y.R. Martin	Chairman of the Association Vaudoise des Chercheurs en Physique
P.J. Paris	EFDA Information Network
	"Fédération Romande de l'Energie" Committee
	Chairman of the "International Association of Specialists in Energy" (AISEN)
A. Pochelon	Auditor of the Swiss Physical Society Committee
O. Sauter	Co-Editor of "Theory of Fusion Plasmas", proceedings of the above, AIP Conference Proceedings Volume 87

C.3   EPFL committees and commissions

N. Baluc   Commission Ecole Doctorale en Science et Génie des Matériaux

J-L. Dorier   Commission du Doctorat de la Section de Physique, FSB-EPFL

A. Fasoli   Commission d'Enseignement de la Section de Physique, FSB-EPFL

J-Ph. Hogge   Commission du Doctorat de la Section de Physique, FSB-EPFL

M.R. Siegrist   Commission du Doctorat de la Section de Physique, FSB-EPFL

M.Q. Tran   Commission du Doctorat de la Section de Physique, FSB-EPFL
                  Commission stratégique de la Section de Physique, EPFL
                  Membre du Comité de Sélection du Prix de la meilleure thèse EPFL

T.M. Tran   Groupe de travail technique du Comité de Pilotage HPC/MPC, EPFL

L. Villard   Délégué à la mobilité, Section de physique, FSB-EPFL
                  Conseiller d'Etudes, Section de physique, FSB-EPFL
                  Commission d'Enseignement de la Section de Physique, FSB-EPFL
                  Groupe de travail technique HPC (High Performance Computing) – EPFL
                  Steering Committee, HPC (High Performance Computing) – EPFL
                  Steering Committee, Blue Gene Project - EPFL

APPENDIX D   Lausanne Reports (LRP)

(see CRPP archives at http://crppwww.epfl.ch/archives)

P. Angelino, The role of the electric field in simulations of plasma microturbulence (EPFL Thesis 3559(06)), LRP 819/06

G. Arnoux, Chauffage de plasma par ondes électromagnétiques à la troisième harmonique de la fréquence cyclotron des électrons dans le tokamak TCV (EPFL Thesis 3401(05)), LRP 812/06

A. Bortolon, B. P. Duval, A. Pochelon, A. Scarabosio, Observation of Spontaneous Toroidal Rotation Inversion in Ohmically Heated Tokamak Plasmas, LRP 825/06

L. Bottura, P. Bruzzone, C. Marinucci, B. Stepanov, Analysis of the transverse heat transfer coefficients in a dual channel ITER-type cable-in-conduit conductor, LRP 822/06

Y. Camenen, Etude du transport d'énergie thermique dans les plasmas du Tokamak à Configuration Variable au moyen de chauffage Électronique cyclotronique (EPFL Thesis 3618(06)), LRP 821/06

A. Descoeudres, Characterization of electrical discahrge machining plasmas (EPFL Thesis 3542(06)), LRP 818/06

M.A. Henderson, R. Chavan, R. Heidinger, G. Saibene, Interface issues related to the ITER ECH system, LRP 828/06

J. Horacek, Measurement of edge electrostatic turbulence in the TCV tokamak plasma boundary (EPFL Thesis 3524(06)), LRP 817/06

C. Marinucci, L. Bottura, ac losses computations for ITER magnets (EFDA ref. TW5-TPO-ACLOS/Contract No. 05-1307, Deliverable No. 2 and 3), LRP 823/06

P. Marmy, Low cycle fatigue and creep-fatigue of Eurofer 97 (EFDA technology workprogramme 2003 - Final report on task TW3-TTMS-05/Del No. 1), LRP 826/06

S. Mueller, Turbulence in basic toroidal plasmas (EPFL Thesis 3673/06), LRP 827/06

H. Reimerdes, I. Furno, F. Hofmann, An. Martynov, A. Pochelon, O. Sauter, Sawtooth behaviour in highly elongated TCV plasmas, LRP 820/06

A. Scarabosio, Stability and toroidal rotation properties of highly shaped plasmas in the TCV tokamak, LRP 824/06

H. Schmidt, Characterization of a high-density large-area VHF plasma source (EPFL Thesis 3495(06)), LRP 816/06

R. Wesche F. Roth P. Bruzzone, Final report on "Tests of advanced Nb3Sn Strands", EFDA Reference: ASTEST Contract 03-1121, Deliverable 4.3, LRP 815/06

A. Zabolotskiy, Particle transport in tokamak plasmas (EPFL Thesis 3252(05)), LRP 814/06

APPENDIX E   The basis of controlled fusion

E.1   Fusion as a sustainable energy source

Research into controlled fusion aims to demonstrate that it is a valid option for generating power in the long term future in an environmentally, politically and economically acceptable way. Controlled fusion is a process in which light nuclei fuse together to form heavier ones: during this process a very large amount of energy is released. For a fusion reactor it is planned to use the two isotopes of hydrogen: deuterium (D) and tritium (T), which fuse together much more readily than any other combination of light nuclei according to the following reaction:

$$D^2 + T^3 \rightarrow He^4 + n + 17.6\text{MeV}$$
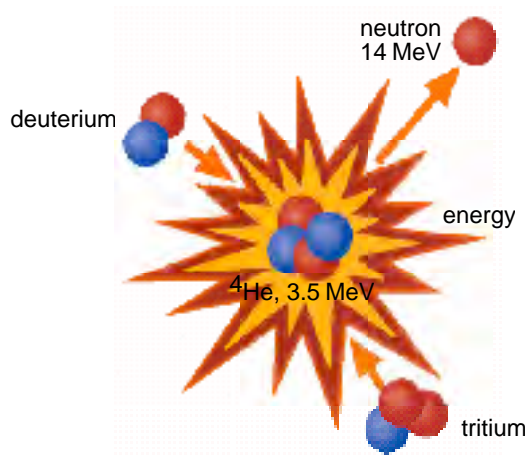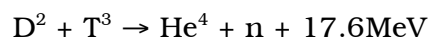
Fig. E.1   *Schematic of a fusion reaction between deuterium and tritium nuclei. The products are 3.5MeV ^{4}He, the common isotope of helium, and a 14MeV free neutron.*

The end products are helium and neutrons (n). The total energy liberated by fusing one gram of a 50:50% mixture of deuterium and tritium is 94000kWh, which is 10 million times more than from the same mass of oil. 80% of this energy is carried by the neutrons with an energy of 14MeV while the remaining 20% is carried by the helium nucleus. Most of this energy eventually becomes heat to be stored or converted by conventional means into electricity.

The temperature at which fusion reactions start to become significant are above a few tens of millions of degrees. For the D-T reaction, the optimal temperature is of the order of 70-200 million degrees. At such temperatures the D-T fuel is in the plasma state.

Deuterium is very abundant on the earth and can be extracted from water (0.034g/l). Tritium does not occur naturally, since its half-life is only 12.3 years, but it can be regenerated from lithium using the neutrons produced by the D-T fusion reactions. The two isotopes of natural lithium contribute to this breeding of tritium according to the reactions:

$$Li^6 + n \rightarrow He^4 + T^3 + 4.8MeV$$

$$Li^7 + n \rightarrow He^4 + T^3 + n - 2.5MeV$$
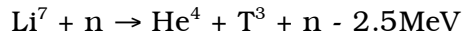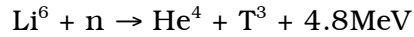
The relative abundance of the two lithium isotopes Li^6 and Li^7 are 7.4% and 92.6%, respectively. The known geological resources of lithium both in the earth and in the sea water are large enough to provide energy for an unlimited time.

E.2 *Attractiveness of fusion as an energy source*

The inherent advantages of fusion as an energy source are:

- The fuels are plentiful and their costs are negligible because of the enormous energy yield of the reaction;
- The end product of the reaction is helium, an inert gas;
- No chain reaction is possible: at any time only a very small amount of fuel is in the reacting chamber and any malfunction would cause an immediate drop of temperature and the reaction would stop;
- No after-heat problem can lead to thermal runaway;
- None of the materials required by a fusion power plant are subject to the provisions of the non-proliferation treaties.

Its further potential advantages are:

- Radioactivity of the reactor structure, caused by neutrons, can be minimised by careful selection of low-activation materials resulting in a manageable quantity of long lived radioactive waste;
- The release of tritium in normal operation can be kept at a very low level. The inventory of tritium in the breeding section of the reactor and on the site can be sufficiently small so that the worst possible accident could not lead to a harmful release to the environment requiring evacuation of the nearby population.

APPENDIX F Glossary

A general purpose glossary for the field of controlled fusion and plasma physics is provided in the CRPP Annual Report every two years. Since it was part of the Annual Report 2005, it will not be provided here.

APPENDIX G   Sources of Financial Support

The CRPP is the Host of Euratom Fellows:

- Dr. A. Mueck, who's fellowship is entitled *"Electron Bernstein wave studies in TCV"*,
- Dr. I. Pagonakis whose fellowship is entitled *"Design of the collector system for the coaxial gyrotron 170GHz/2MW/CW"*,
- Dr. J. Paley, whose fellowship is entitled *"Real-time control of multi-beam ECRH-ECCD in the TCV tokamak"*,
- Dr. P. Ricci, whose fellowship is *entitled "Plasma turbulence: comparison between theory simulations and the basic plasma physics experiments TORPEX"*, and
- Dr. G. Turri, whose fellowship is entitled *"MHD spectroscopy in the TCV tokamak, in particular to determine current density profiles"*.